# Adequately Safe and Efficient Design of Orthogonally Stiffened Cylinders

R.F. Lennon

The Department of Naval Architecture and Ocean Engineering

The University of Glasgow

Masters Thesis

May 1997



ProQuest LLC.
789 East Eisenhower Parkway
P.O. Box 1346
Ann Arbor, MI 48106 – 1346

# *ABSTRACT*

The buckling resistance of orthogonally stiffened cylinders is investigated by using a general purpose finite element program (ABAQUS). The effects of residual stresses arising from shell cold forming the cylinder and welding frame components are considered in the analysis of two stiffened cylinder models with similar material weights and different geometric parameters. A static axial load is applied to the models prior to a non-linear elasto-plastic limit point buckling step which produces large displacement compartment buckling. Residual stress simulation has a reducing effect of approximately 25% on buckling resistance.

Cylindrical boundary conditions for Finite Element analysis are formulated that allow torsional displacement and buckling of a sector of a cylinder of half axial height, and of a circumferential arc angle that will divide into 360°.

## Acknowledgements :

This thesis is the result of 13 months work as an EPSRC funded Research Assistant at the Department of Naval Architecture and Ocean Engineering at the University of Glasgow. I am grateful to EPSRC for their support, to the programme supervisor, Dr P.K. Das for his guidance and to the head of the Department, Professor N.D.P. Barltrop for taking a keen interest and for providing important insights to the project.

This research was a continuation of research carried out at the department of Naval Architecture and Ocean Engineering into stiffened cylinders over the years by many people. The more recent work by Professor D.Faulkner, Dr Moradi and others was the starting point and was essential to the momentum of the work at times when it was directly referenced and probably also at times when it was not apparent.

I wish to thank Professor J.M.Rotter at the Department of Civil Engineering in the University of Edinburgh for providing our final year structures group of '95 with a firm foundation and a keen interest in Finite Element theory and practice, I sincerely regret missing the opportunity to collaborate with the Silos group on this project.

Thanks also to the other staff and students at the Department of Naval Architecture for their support and friendliness and to my family and friends in Dublin for calling me when I forget.

# Contents

**List of figures :**

# Notation :

| | |
|---|---|
| E | Young's Modulus |
| F | Total Torsional Force (in a cylinder of full circumference) |
| $k_S$ | Buckling coefficient |
| L | Axial length of cylinder |
| m | Number of axial half buckling waves |
| n | Number of circumferential full buckling waves |
| $N_X$,$N_Y$ | Inplane direct stress resultants |
| $N_{XY}$ | Inplane shear stress resultant |
| p | External pressure |
| $P_Y$ | Yield Stress |
| R | Cylinder Radius |
| t | Cylinder thickness |
| w | Lateral Displacement |
| x | Circumferencial cylindrical co-ordinate |
| y | Axial cylindrical co-ordinate |
| Z | Curvature parameter |
| $\nu$ | Poisson's ratio |
| $\tau_{CR}$ | Critical shear stress |

# 1 Introduction

## 1.1 General

The emphasis of this work is on Finite Element analysis of orthogonally stiffened steel cylinder structures that would typically be used as column and pontoon components on floating drilling offshore platforms. Floating drilling platforms have been used for world wide operation and will become even more important as offshore operations move to deeper waters world wide.

Orthogonally stiffened cylinders for offshore applications are heavily fabricated structures, typically incorporating flanges on the frame components. While structural strength for a given structural weight can be enhanced by incorporating a cylindrical grillage on the cylinder, welding the components together creates geometric distortion and locked in stress, which in turn affects structural integrity.

Two design cases of orthogonally stiffened cylinders are considered for investigation by Elasto-plastic, non-linear Finite Element analyses of shape imperfect models with the Finite Element program ABAQUS. For the first case, model 1(ortho), the geometric parameters of a typical tension leg platform orthogonally stiffened cylinder design are used. In this case the five ring - six bay design is modified to a five bay four ring design, to allow axial symmetry at the central circumferential hoop in the Finite Element analysis. The cylinder in second model, model 2(ortho), has the same cylinder radius, 5.3 M, and the same axial height, 8 M, and the same weight as model 1(ortho). The principal differences between the models are the smaller and thinner rings, smaller, thinner and more widely spaced stringer frames and thicker cylinder shell of model 2(ortho).

An overall radial shape imperfection is introduced to the cylinder at the mesh generation stage. Residual stress arising from cold forming the cylindrical shell and residual stress and shape imperfection arising from welding frame components are implicitly considered in the Finite Element analysis with thermal expansion and contraction steps. Static axial loading and active uniform surface pressure are considered in large displacement buckling analysis.

Boundary conditions for torsional buckling of Finite Element cylinder sector models of half axial height are formulated and tested in the final chapter.

## 1.2 Aims and scope

The work presented in this thesis aims to:

- further develop the type of work established by Bushnell [14] and Guggenberger [15] by exploiting the improved capabilities of high performance computational facilities with the finite element program ABAQUS;
- give greater certainty to the design factors in design codes that consider fabrication procedures [27,28,29], by implicitly introducing cold forming and welding steps in finite element analysis of orthogonally stiffened cylinders.

## 1.3 Finite Element analysis

### 1.3.1 Eigenvalue analysis

In the non-linear elasto plastic shape imperfect Finite Element analysis of Chapter 3, circumferential and axial symmetry is used to keep the number of elements in the Finite Element models to a minimum. While the case of axial symmetry is straight forward, the model is cut in half at mid height and axial symmetry imposed, for the case of circumferential symmetry a critical sector angle must be established.

It was attempted initially to find this critical angle by eigenvalue buckling analyses of shape perfect orthogonally stiffened cylinders. However it was found because of the arch locking effect of the perfectly circular circumferential components, high surface pressures that created large membrane forces were necessary to cause buckling, and when buckling occurred it was local buckling of the cylindrical shell between frames. It was possible to create overall buckling modes by increasing the thickness of the cylinder shell, however the shell thickness had to be multiplied several times and this would greatly affect the stiffness of the cylinder.

The approach taken in Chapter 3, 'Eigenvalue analysis', is to simulate the elastic stiffness of the orthogonally stiffened cylinder in an un stiffened cylinder by using the formulae in API Bulletin 2U Sections 4.4 and 4.4.2 to calculate elastic stiffness coefficients and implementing them directly in ABAQUS in the analysis of a 180° un stiffened cylinder with the same radius and axial height as the orthogonally stiffened cylinder.

### 1.3.2 Non-linear Elasto-plastic shape imperfect analysis

It is attempted in this chapter to include in the Finite Element analysis the aspects that in real tests of orthogonally stiffened cylinders would greatly affect structural strength. The critical sector angle established in the previous chapter is used and an overall shape imperfection of amplitude 0.5% of the radius is introduced at the mesh generation stage.

The first two Finite Element analysis steps are circumferential thermal expansion and thermal contraction steps that simulate the cylinder shell cold forming process and produce plastic straining and residual stress in the cylinder shell, while the frame components remain largely unaffected. The next analysis step alters the boundary conditions to those of axial and circumferential cylindrical symmetry. This is followed by a step that alters the coefficient of thermal expansion to an isotropic state, which is necessary for thermal expansion and contraction in the following two welding analysis steps.

A static axial load is applied to the model after the welding steps. The axial load produces a compressive axial stress of approximately 100 N/mm$^2$, while this stress is large enough to affect buckling behaviour in following steps, it is not expected to produce buckling on it's own, or even to produce large displacement. This is evident as the axial load is applied in a non-linear step which could be completed over a number of increments with the automatic incrementation facility in ABAQUS, but is completed in one increment.

The final step is the buckling step which utilises the modified Rik's limit point algorithm to produce non-linear static elasto-plastic buckling in the orthogonally

stiffened cylinder. With the static axial load from the previous step held constant, a uniform external surface pressure is applied to the cylinder elements. Local buckling of the cylinder shell between frames typically occurs initially followed by large displacement overall buckling. The analysis is always carried out to the point where an post buckling limit point has been reached and well beyond this. The post buckling limit point was reached at a maximum radial displacement of between 7 and 35 mm, depending on the particular analysis.

### 1.3.3 Torsional buckling analysis

Chapter 5, 'Torsional buckling', can be considered separately to chapters 3 and 4. The contents of the chapter is taken from [13] which describes work carried out in formulating boundary conditions for cyclic cylindrical torsional symmetry in Finite Element analysis, to allow the type of half axial cylindrical sector described in Chapter 4 to be buckled under torsional load.

Eigenvalue torsional buckling tests are carried out on un-stiffened elastic cylinder models as a comparison with classical elastic torsional stability theory. Stringer stiffened and orthogonally stiffened cylinders are then tested in non-linear elasto-plastic tests under combinations of torsional, axial and surface pressure loads.

# 2. Literature Review

## 2.1 Research papers

In [1] the problem is defined by two main aspects, firstly the likely nature and severity of initial locked in stresses and distortions and secondly their effect in reducing the strength and stiffness of the supposed perfect structure. Cold forming operations and weld shrinkage actions are considered.

It is pointed out that while residual stresses arising from hot rolling structural sections and cold rolling plate usually do not affect the strength of fabricated structures, the effects of residual stress from cold bending ring frame stiffeners is usually significant.

Where fillet welds at 'T' configurations are being considered, the concept of the tension block is introduced to investigate the effects of weld shrinkage actions. This is the area of steel close to a weld which is in tension after the welding process. The across the weld length of the tension block is described in relation to the plate thickness with the parameter $\eta$, the across the weld length is equal to $\eta t$ where t is the plate thickness. Typical values for $\eta$ of between 3 and 6 are suggested for ships, while smaller values would typically be applied to civil structures. It is established that the tensile stress at the tension block is balanced by a compressive stress in the same thickness of plate, at the reverse side of the weld or at the mid thickness of plate, and by a compressive membrane stress at regions of the plate away from the welds. It is also suggested that welding temperatures are about twelve times greater than the range to cause yield in resisted thermal expansion of structural steels. The 'hungry horse' type of shape imperfections in the shell of stiffened panels caused by welding procedures and the magnitudes of displacements are discussed.

Compression strength of grillages is considered in relation to plate failure, column failure, frame tripping and grillage instability. The design of long ring-stiffened cylinders under external pressure is considered for shell buckling and ring frame buckling modes.

The work in [17] contains detailed examinations of theoretical design formulae for the buckling strength of flat plates based on the critical stress, maximum stress and effective width methods. These formulae are compared with results of physical tests on box, cruciform and clamped web welded structures.

The tension block width parameter $\eta$ is discussed and it is suggested that values of $\eta$ of between 2 and 4 are appropriate for steel thicknesses between approximately 5 and 15 mm. It is not suggested however that the tensile residual stress close to the weld is balanced by a compressive stress through the thickness as in 1. above, rather that the tensile stress in the tension block is balanced by a compressive membrane stress in the shell away from the weld.

In [14] the finite element program BOSOR5 is used in this work to analyse ring stiffened cylinders of infinite length, by considering a single ring section with a half bay on both sides, with axial symmetry at the edges. Bifurcation buckling tests are carried out under uniform surface pressure on the cylinder.

The effects of shell cold forming are simulated in the cylinder elements by manipulating gradients of total strain through the thickness of the shell with an orthogonal co-efficient of thermal expansion in a thermal loading cycle. Material

shrinkage at fillet weld locations is also simulated, however there is no variation of applied thermal strain through the thickness of the shell.

Comparison is made between finite element tests and physical tests. The conclusions indicate that irregularities in the shell thickness and in welding procedures, and geometric shape imperfections need to be taken into account in the finite element analysis for a better match with physical tests.

Shape imperfections and cold forming residual stresses in cylindrical silo structures and their effects on buckling resistance under axial loading are investigated in this [15] using the finite element program ABAQUS. Cold forming residual stresses are introduced in the unstiffened cylinders by bending the plate and allowing it to spring back, circumferential and axial boundary conditions are then introduced and a buckling analysis is carried out. Radial dents are imposed on the cylinder in some cases. A general conclusion is stated in this work that, 'If initial stresses are taken into account in buckling computations they should be linked to a physical process which is responsible for their creation'.

[10] gives guidance on the design of Ring Frames in orthoganally stiffened cylinders affected by axial loading and hydrostatic pressure. Finite Element Analysis of a tension leg platform column, using the eigenvalue and Riks limit point methods in the Finite Element program ABAQUS, give results for bay instability and general collapse. It is shown by a second design that the first model analysed could be redesigned with smaller ring frames, producing a considerable saving in cost and weight.

The study by Morandi Et.Al. in [23] examines the methods of structural design for externally pressurised ring and flange stiffened vessels using the Finite Element analysis program ABAQUS for linear analysis of models of infinite axial length. The results of tests with different geometries and boundary conditions, and taking into account modal interaction effects, are discussed with reference to the partial safety factors applied to the reliability analysis and design of stiffened pressure vessels.

The Finite Element program LUSAS is used to carry out several finite element analyses of ring stiffened cylinders that would typically be found on steel offshore structures in [19], under external pressure. The semi-loof shell element is used and shape imperfections are included in the finite element mesh. Localised torsional ring tripping failures are simulated using a single half bay and symmetrical boundary conditions that simulate a compartment of infinite axial length. A review of current design formulae is included in and comparison is made between these formulae and the results obtained from the finite element analyses. Emphasis is placed on the reduction of buckling resistance under external pressure caused by out of circularity of the cylindrical shell and shape imperfection in both flat bar and tee type ring stiffeners.

Physical model tests of Ring Stiffened compartments are outlined and compared with Finite Element tests of similar models in [23]. There is an emphasis in this paper on the negative effects that out of circularity of the cylindrical form imposes on the resistance to buckling of Submarine structures, with secondary structural deck components. The Finite Element program ADINA was used in with shape imperfections introduced in the Finite Element mesh, while in the physical model the shape imperfection is intentionally induced. There is a good correlation between physical test results and finite element results and the importance of considering the effects of shape imperfections in this type of design is highlighted.

The magnitudes and distribution of shape imperfections on stringer stiffened and un-stiffened composite ply cylinders are measured and outlined in [25]. These shape imperfections are then introduced in Finite Element meshes. An elastic buckling

analysis is carried out on the composite cylinder and an elastic-plastic buckling analysis is carried out on the stringer stiffened cylinder, both under axial compression. It is shown that probabilistic modelling of shape imperfections allows more accurate partial safety factors to be predicted for use in design of axially loaded cylindrical structures.

## 2. Codes of practice

Elasto-plastic material properties for steel used in this work were largely taken from [26]. Further discussion is given in Section 4.1.2.

The [27] British Standard published document and the associated paper is directed towards design for fatigue, sections 1 and 2 give approximate methods for assessing the through thickness residual stress distribution at fillet and butt type welds. Exact information about the energy input in the welding process is necessary to produce information about the magnitudes of residual stress after welding.

[28] was particularly useful to this work in providing a set of orthotropic stiffness coefficients to allow the stiffness of the orthogonally stiffened cylinders to be represented as unstiffened cylinders, to establish the critical number of circumferential buckling waves in eigenvalue buckling tests in chapter 3.

The effects of residual stress on buckling resistance is accounted for by a general plasticity reduction factor which is to be multiplied by the design buckling pressure calculated from empirical formulae, the value of which depends on the calculated stress levels in the steel at the point of buckling.

In [29] Section 4, 'Stiffened circular cylindrical shells', formulae are given for the calculation of critical buckling stresses under axial force, bending moments, torsional moments, shear force and lateral pressure. It is stated in Section 4.1.4 of this code that 'The methods are to be considered semi-empirical. The reason for basing the design on semi-empirical methods is that the agreement between theoretical and experimental buckling loads for some cases has been found to be non-existent. This discrepancy is due to the effect of geometric imperfections and residual stresses in fabricated structures. Actual geometric imperfections and residual stresses do in general not appear as explicit parameters in the expressions for buckling resistance'.

Section 4.1.5 states that 'The recommended methods for buckling analyses may be substituted by more refined analyses or model tests taking into account the real boundary conditions , pre-buckling edge disturbances, the actual geometric imperfections, the non-linear material behaviour and the residual welding stresses'.

# 3 Eigenvalue Analysis

The purpose of the eigenvalue buckling tests is to estimate the characteristic overall buckling modes with regard to overall compartment buckling, and in particular to estimate the number of circumferential buckling waves, n, of the orthogonally stiffened, elasto-plastic, shape imperfect cylinder models in the following chapter, so that the half circumferential wave sector angle that gives the estimated lowest buckling resistance can be modelled.

In this chapter elastic eigenvalue buckling tests are carried out on shape perfect un stiffened cylinders, models 1(eig) and 2(eig), which have similar orthotropic stiffness properties to the orthogonally stiffened, elasto-plastic, shape imperfect cylinder models, models 1(ortho) and 2(ortho) in the following chapter. Model 1(ortho) and model 2(ortho) have very similar material volumes with different geometric parameters.

## 3.1 Material Properties

Elastic orthotropic material properties are used to represent the combined shell and stiffener stiffness in a cylindrical shell with no stiffeners, models 1(eig) and 2(eig). Elastic stiffness coefficients are calculated from the formulae given in API Bulletin 2U [28] sections 4.4 and 4.4.2. The formulae and calculations that are used are given in the Mathcad spreadsheets in Appendix 1. The geometric parameters of models 1(ortho) and 2(ortho) are outlined in Table 1.

| **Dimensions (mm)** | **model 1 (ortho)** | **model 2 (ortho)** |
|---|---|---|
| Cylinder Radius | 5300 | 5300 |
| Stringer Spacing | 6° | 9° |
| Ring Spacing | 1600 | 1600 |
| Cylinder Thickness | 13 | 18 |
| Top Ring Depth | 200 | 150 |
| Top Ring Thickness | 50 | 50 |
| Stringer Web Depth | 200 | 150 |
| Stringer Web Thickness | 12 | 10 |
| Stringer Flange Depth | 150 | 150 |
| Stringer Flange Thickness | 12 | 10 |
| Ring Web Depth | 600 | 300 |
| Ring Web Thickness | 11 | 10 |
| Ring Flange Depth | 150 | 150 |
| Ring flange Thickness | 13 | 10 |
| Circumferential sector angle modelled | 36° | 27° |

*Table 1.1, Geometric Parameters of Orthogonally Stiffened Cylinders*

### 3.2 The Finite Element models

#### 3.2.1 Geometry and Boundary Conditions

Models 1(eig) and 2(eig) refer to the cylindrical model without stiffeners or bulkheads, which are used as a representation of the stiffened cylinders. Both models 1(eig) and model 2(eig) have identical geometric parameters (ie. only the cylindrical component), only the orthotropic material properties are different.

The models are 4 M in height, with axial symmetry at the bottom edge (edge 3), giving an effective length of 8 M. The radii of both models is 5.3 M. Both models are 180° sector angles, with circumferential symmetry at the vertical edges (edges 2 and 4). As circumferential waves in multiples of a half can result with this type of circumferential symmetry, the 180° sector angle is wide enough to allow for any number of waves around a full circumference greater than one, allowing for the response of the elements when small wave lengths are considered. The case of the number of waves, n, equal to one, would result from a displacement of the central vertical axis towards the centre, which is associated with overall bending, and as the cylinders are buckled under axisymmetric loading, the n=1 case is not considered.

It was also attempted to use circumferential anti-symmetry at the edges of 90° sector angle models, as this should allow buckling waves in multiples of a quarter to occur, simulating a full circumferential model. However there were convergence problems and all analyses in this section were carried out on 180° sector angles.

The top of the cylinder (edge 1) is free to move in the axial direction only, allowing an axial load to produce displacements vertically downwards only.

#### 3.2.2 Elements and mesh

Thick shell elements with eight nodes are used in all cases of shell elements in models 1(eig) and 2(eig). In the Finite Element models, 50 elements are used in the circumferential direction and 8 are used in the axial direction.

#### 3.2.3 Loading

Axial load is applied as a series of nodal forces, a type of knife edge loading, on the top edge of the cylinder. This stage of loading is applied in an initial static step, before any surface pressure is introduced.

Surface pressure is a uniformly distributed load normal to the surface of the elements in the cylindrical shell. The second step in each analysis is an eigenvalue buckling step, with the eigenvalue associated with surface pressure only.

### 3.3 Eigenvalue Buckling analysis

#### 3.2.1 Model 1(eig)

Model 1(ortho) is heavily reinforced with frames and has a thin shell. The large rings in model 1(ortho) give a large elastic circumferencial stiffness coefficient to model 1(eig), and this produces relatively large circumferential buckling waves. With no

axial loading and an active surface pressure Model 1 buckles in two and a half full circumferential waves at the centre of the cylinder (at the bottom of the Finite Element model). The eigenmode is illustrated in figure 3.1, the cylinder buckled at a surface pressure of 3.53N/mm$^2$. Two and a half circumferential waves in 180° is equivalent to five waves in a full 360° circumference, n=5. A full wave extends over 72°, and as it required to model a half buckling wave in section 4., a 36° sector angle will be necessary.

In another analysis an axial load was applied to the top edge of the cylinder as described in 3.1.4, the magnitude of the force was that to cause an axial stress of 100N/mm$^2$ if it is evenly distributed across the shell-stringer web-stringer flange cross sectional area in model 1(ortho) in section 4. The result remained n=5 with no apparent change in the eigenmode and a small decrease in buckling pressure to 3.42N/mm$^2$.

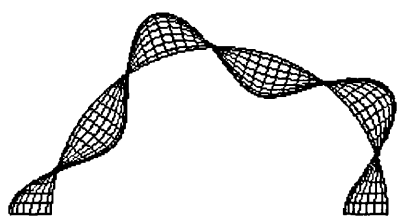

*Fig. 3.1, Model 1(eig) eigenmode.*

### 3.2.2 Model 2(eig)

The stiffening components of model 2(ortho) are smaller and thinner and the shell component is thicker than the corresponding components of model 1(ortho). Under active surface pressure with no axial loading, the model buckled into three and a half waves (figure 3.2), with a buckling pressure of 1.23N/mm$^2$. The higher number of circumferential buckling waves and the lower buckling pressure in model 2(eig) in comparison to model 1(eig) can be attributed to the smaller elastic stiffness coefficients in model 2(eig) and the smaller frames in model 2(ortho).

When an axial load was introduced of the same magnitude as model 1(eig) above and the model was buckled under an additional active surface pressure, there was no change in the number of circumferential buckling waves and a small decrease in buckling pressure to 1.15N/mm$^2$.

In this case n=7, a full buckling wave extends around 51.43° of the central circumference and a half wave 25.71° model is required for the detailed analysis of model 2(ortho) in section 4. As stringers are spaced at 9° in model 2(ortho) a 27° sector angle will be analysed.

There is a large difference in buckling pressures for the shape perfect elastic models 1(eig) and 2(eig), this is caused by the difference in elastic stiffness coefficients. In section 4 the effects of the shape imperfection, non-linear deformation, elasto-plastic material behaviour and ring frame tripping are considered, resulting in a reduction of, and a smaller difference between, the buckling pressures of models 1(ortho) and 2(ortho).

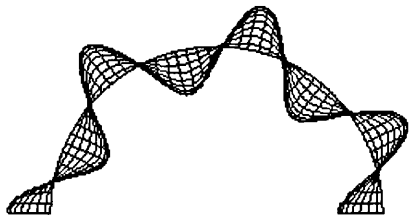

*Fig. 3.2, Model 2(eig) eigenmode.*

150

**Note :** Fig. A2.3.1.1, page 151 of Appendix 2, shows the elasto-plastic limit point load displacement paths for model 2(ortho), an orthogonally stiffened cylinder, for the 27° and 36° sector angles. The 36° sector angle appears to have an 'artificially' high elastic response to surface pressure when compared to the 27° sector angle and shows un stable behaviour immediately after the elastic limit of response when the surface pressure is suddenly reduced.

# 4 Elasto-plastic limit point analysis

## 4.1 Material properties

The type of material being modelled is grade 55 steel. A material hardening slope is introduced for strains in the plastic range because plastic straining occurs in the cold forming and welding processes.

### 4.1.1 Elasticity

A Young's modulus of 205 MPa at zero temperature is used for all components. The variation of Young's modulus with temperature is discussed in 4.3.1, Young's Modulus remains constant during the cold forming process.

### 4.1.2 Plasticity

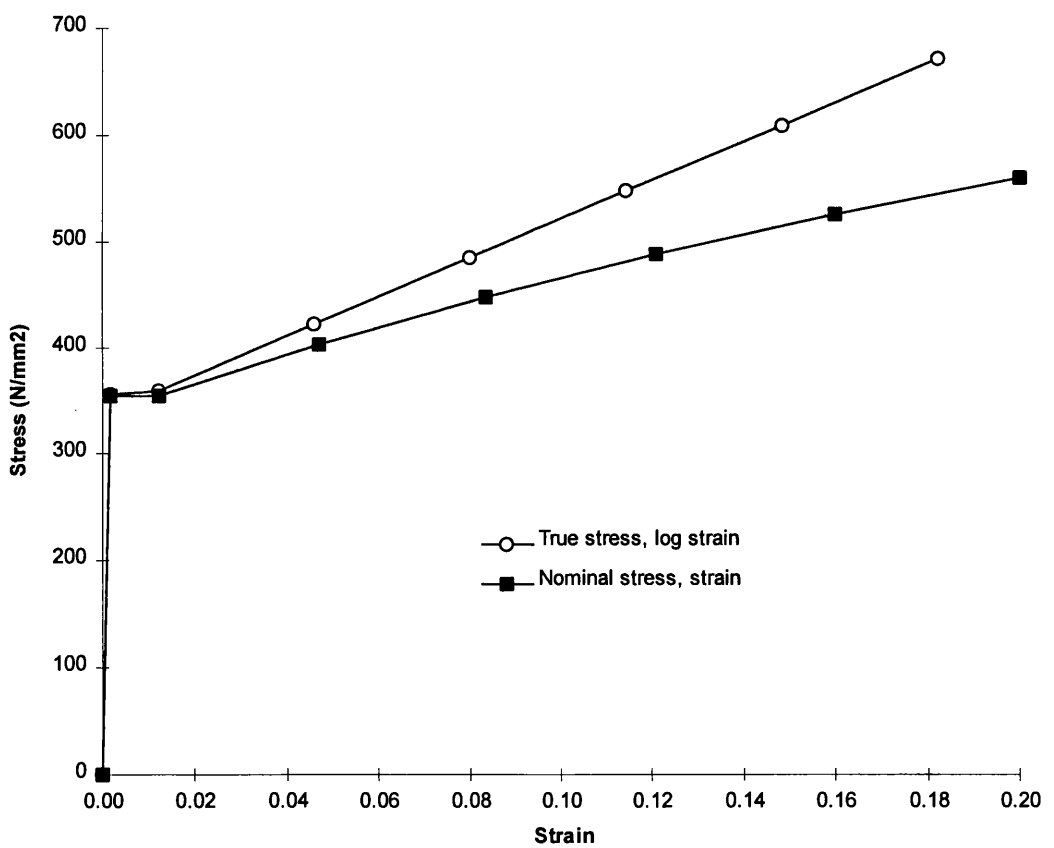


*Fig. 4.1 Material stress strain curve.*

From European Standard EN 10025 [23], a yield stress of 355 N/mm$^2$ is used for steel thickness less than 16mm, and 345 N/mm$^2$ for thickness greater than or equal to 16mm. BS 5950 indicates that a plateau of perfect plasticity at first yield of seven times the value of elastic strain at first yield should be used for steel calculations involving material hardening. European Standard EN 10025, Table 5 gives a value of

20% minimum elongation at between 490 and 630 N/mm$^2$ for grade 55 steel; a maximum hardening stress of 560 N/mm$^2$ at 20% strain is used (Figure 4.1). Perfect plasticity is assumed at nominal strains greater than 20%. The nominal stress and strain parameters are converted to true stress and log strain for material definition in ABAQUS.

## 4.2 The finite element models

### 4.2.1 Mesh

Eight noded thick shell elements are use for all components of the finite element models. The geometric parameters of model 1(ortho) and model 2(ortho) are outlined in table 1.1, Section 1. An inside view of the mesh used for model 1(ortho) is illustrated in figure 4.2 and an outside view of the mesh used for model 2(ortho) is illustrated in figure 4.20. Model input files are generated using the FORTRAN 77 code 'ORCYL.f77'. The 'ORCYL.f77' code was developed from the 'ABAINP.f77' code which was written by Dr. Morandi at the Department of Naval Architecture and Ocean Engineering at the University of Glasgow in 1995.

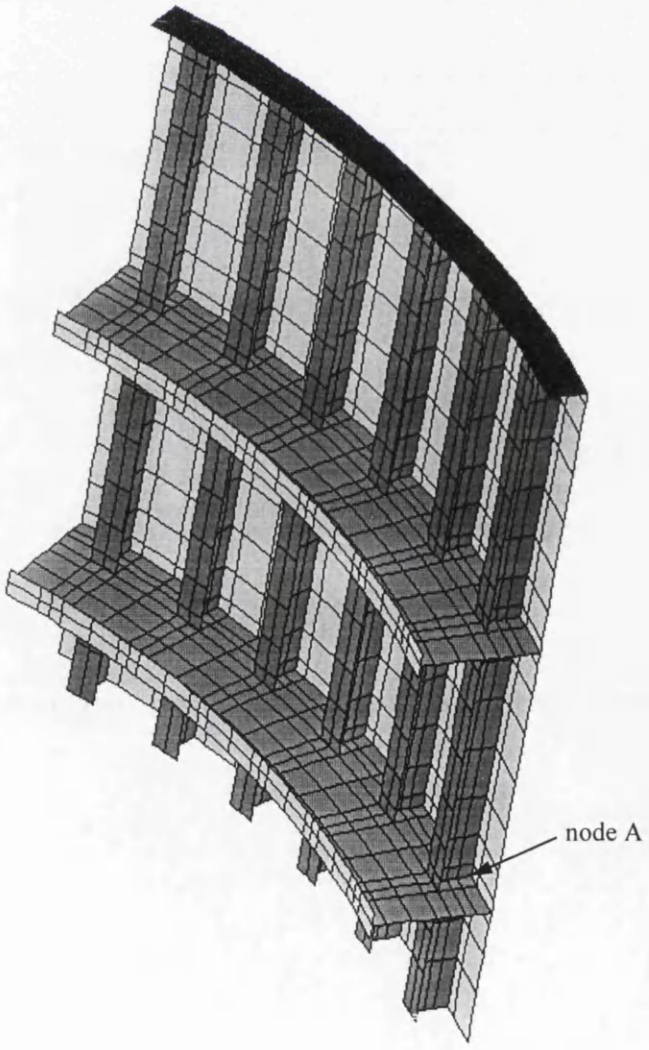


*Fig. 4.2, Model 1(ortho) mesh.*

### 4.2.2 Loading

Axial load is applied before the Rik's limit point buckling step in a non-linear static step, the axial loading is applied on the surface of the elements of the 'top ring' or bulkhead component, creating an axial compressive stress of 100 N/mm$^2$ over the cylinder-stringer web-stringer flange cross sectional area in model 1(ortho). This requires a total force of 636.961 kN if it is applied over a full 360° circumference. This magnitude of axial load is also applied to model 2(ortho). The axial load remains constant during the buckling step. ABAQUS POST axial stress contour plots of model 1(ortho) and model 2(ortho) under this axial load are illustrated in figures A2.1.7.10 and A2.2.7.10 respectively.

All surface pressure buckling steps are preceded by an axial loading step. The active force in the Rik's limit point buckling step is an external surface pressure on the cylinder elements only.

### 4.2.3 Shape imperfection

An overall radial shape imperfection is introduced in model 1(ortho) and model 2(ortho) in a half cosine wave in the circumferential direction as illustrated in an un stiffened cylinder in figure 4.3 and in a half cosine wave also in the axial direction as illustrated in figure 4.4. The maximum amplitude of the shape imperfection is 26.5 mm inward, 0.5% of the cylinder radius. The frame components are displaced to the same circumferential magnitudes as the cylinder, the shape imperfection is introduced at the mesh definition stage and so dose not cause any residual stress or strain from components being bent or twisted.

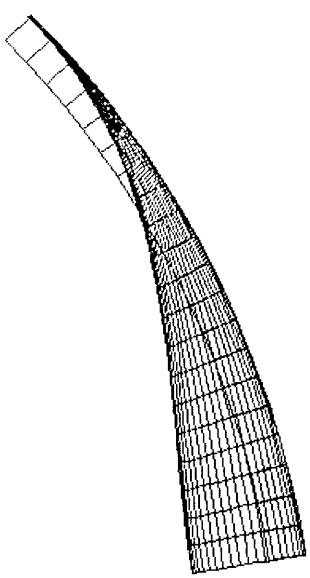

*Fig. 4.3, Exaggerated overall radial shape imperfection, circumferential variation.*

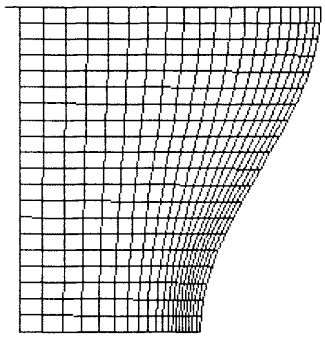

*Fig. 4.4, Exaggerated overall radial shape imperfection, axial variation.*

The load displacement behaviour of the models was greatly affected by the variation and amplitude of overall shape imperfection. A smaller shape imperfection amplitude created a higher limit to elastic response and a sudden load factor reduction once this point of loading had been passed. Fully inward shape imperfection as illustrated in figures 4.3 and 4.4 and fully outward shape imperfection gave less resistance to initial buckling than a central shape imperfection, where the imperfection magnitude is at a maximum at the ends of the circumferential arc sector and zero at the centre. This appeared to be caused by a geometric locking effect at the point of overall buckling.

An axial shape imperfection in a half cosine wave was introduced in the large rings of model 1(ortho), increasing to a maximum amplitude of 5 mm at the ring web to ring flange intersection at the circumferential ends of the finite element sector. This greatly affected the post buckling behaviour of model 1(ortho) where initially without the ring shape imperfection, the load factor was increasing immediately after the elastic range of response as the rings were being forced to buckle suddenly. A similar axial shape variation was introduced in the smaller rings of model 2(ortho), in proportion to the shape imperfection in the rings of model 1(ortho). There was no apparent change in load displacement behaviour, this was probably due to the smaller magnitudes of shape imperfection variation and the different buckling characteristics of the two models which is discussed further in Section 4.5.

### 4.2.4 Boundary Conditions

Each finite element model contains four edges, the top or end (edge1) of the cylinder where a bulkhead would typically be found, two vertical edges (edges 2 & 4) which provide circumferential cylindrical symmetry, and the bottom edge (edge 3) of the finite element model, the central hoop of the cylinder, which is restrained with axial symmetry.

The top ring is effectively free to translate, but is restrained against buckling under the high surface pressure applied in the axial loading step. This is achieved by equating all nodes in a radial line (figure 4.6) to translate in the axial direction together.

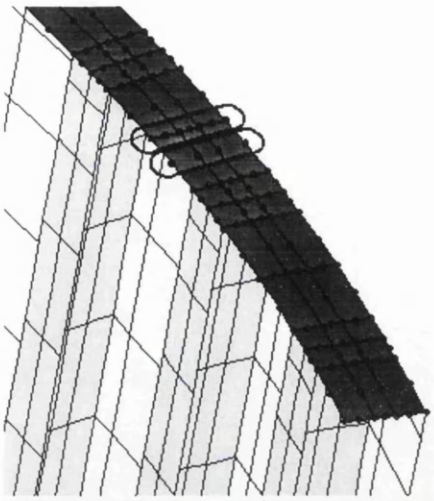

*Fig. 4.6, Nodes in the top ring along radial lines are equated to translate together in the axial direction.*

A shell thickness of 50 mm is used in the top ring to provide relatively less flexibility here compared to the other frame components. It was found that if the top ring was made rigid or if all nodes in the top ring were constrained to move in the axial direction together, the buckling behaviour of the cylinder, for overall buckling modes in particular, was greatly affected and convergence problems were encountered, the analysis would typically end at the elastic limit of response. A small degree of circumferential flexibility in the top ring allows large inward radial displacement of the cylinder in overall buckling modes. One side of the sector, the side with the inward shape imperfection, will buckle inward in the radial direction, causing a small downward displacement of the top ring above, while the other side, and the top ring above it, remains relatively unaffected.

## 4.3 Cold forming analysis

### 4.3.1 Shell element cold forming

It is assumed that during manufacture the cylindrical shell plates are initially flat and are formed by forcing them through a three wheel mechanism, so that curvature is introduced gradually along the plate in the circumferential direction (figure 4.7). It is also assumed that the process illustrated in figure 4.8, where curvature is produced by passing the plate between two drums of different radii and laterally compressing the plate with an out of balance distribution of stress and strain through the thickness, is not used.

A series of Finite Element tests were carried out beginning with a flat plate, which is restrained into a prescribed radius of curvature by prescribed displacements, to the point where plastic straining and material hardening occurs at the outer layers of the shell (figures 4.11 and 4.12). The prescribed displacements are then released and the shell is allowed to spring back to a lesser curvature (figures 4.14 and 4.15). The curvature is measured, the released radius calculated and the process repeated until the required released radius of the cylinder is obtained, in an iterative process (figure 4.10). Where a different thickness is to be used or a different cylinder radius is to be obtained the process is repeated.

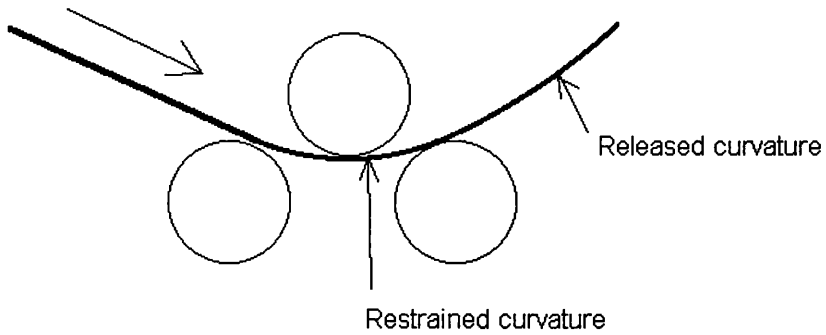


*Fig. 4.7, Three wheel mechanism, cold forming type 1.*

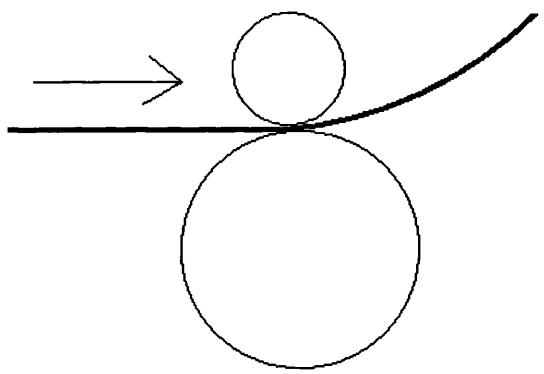

*Fig. 4.8, Cold forming type 2.*

A series of tests were also carried out where the number of layers at the integration points, which are used for plasticity calculations, were varied to establish the minimum number of layers necessary for accurate representation of stress and strain through the thickness of the shell (figure 4.9). It was found that thirteen layers were adequate, the default number for shell elements in ABAQUS is five.

A FORTRAN 77 code 'FORM.f77' has been written to produce an ABAQUS input file, that will define a flat plate of eight noded shell elements with the material properties described in section 4.1, restrain the plate into a specified radius of curvature in several non-linear increments, and release the plate to the equilibrium curvature in a second step of several non-linear increments.

The program asks the user to input the root file name, the number of elements in the two principal directions of the flat plate, the real dimensions of the plate, the real thickness of the plate, the number of plasticity calculation points through the thickness of the plate and the radius of curvature the plate is to be restrained into before the plate is released to spring back. An ABAQUS job is then processed with this root file name and the released curvature is calculated from the rotational displacement of a node at the centre of the plate. The FORTRAN 77 computer code 'FORM.f77' was developed from the FORTRAN 77 code 'ORCYL.f77'.

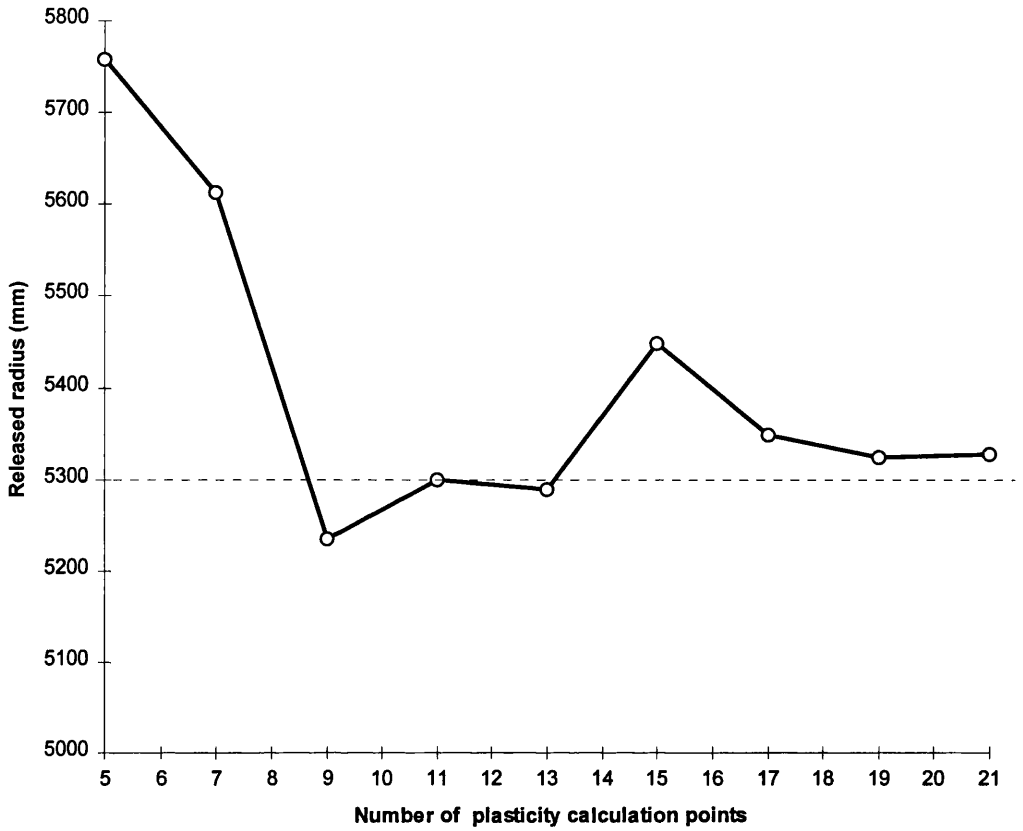


*Fig. 4.9, Number of plasticity calculation points - released radius*

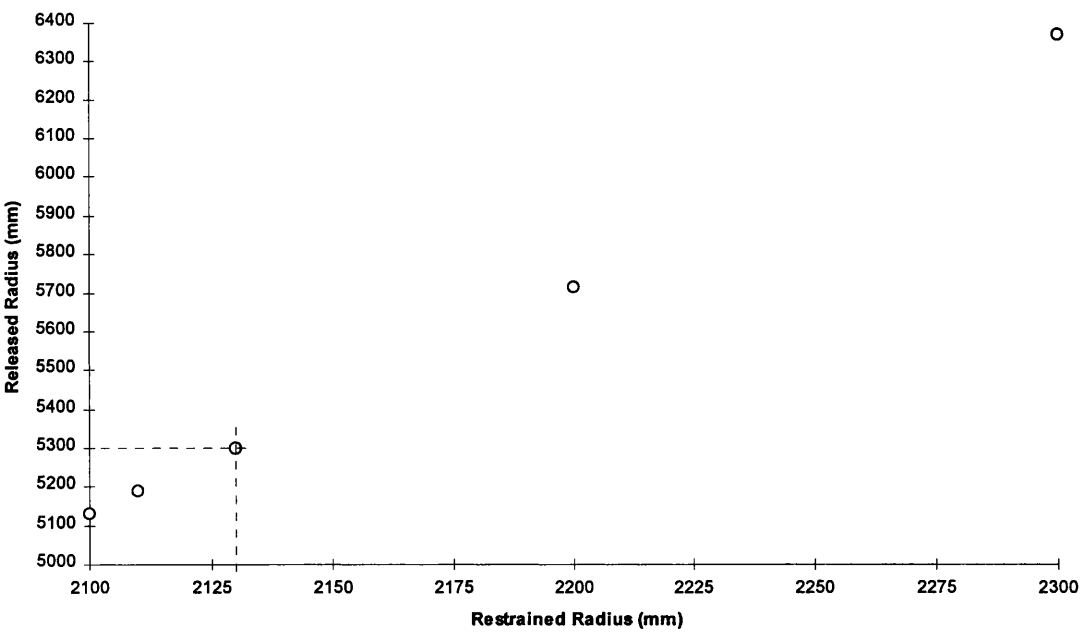


*Fig. 4.10, Prescribed radius - released radius*

During the analysis one straight edge is held fixed, the two curved edges are constrained with axial symmetry and the fourth straight edge is prescribed a rotational value consistent with the curvature of the shell (figures 4.11 and 4.14).

### 4.3.2 Cold forming stress and strain distribution

Figures 4.12, 4.13, 4.15 and 4.16 show the distribution of circumferential stress and circumferential strain respectively through the thickness of the shell during the two phases of the cold forming process. The right hand side of the graphs shows the face of the plate closest to the centre of curvature. As the elastic strain limit of the material is reached at the outer calculation points (figure 4.12), with further curvature plastic straining begins, moving inwards (the analysis is completed over several increments) towards the mid-thickness. Stress is greatest at the outer layers (figure 4.13), most of the material that yields hardens and reaches a circumferential stress of approximately 400 N/mm$^2$, the yield stress in this case is 355 N/mm$^2$.

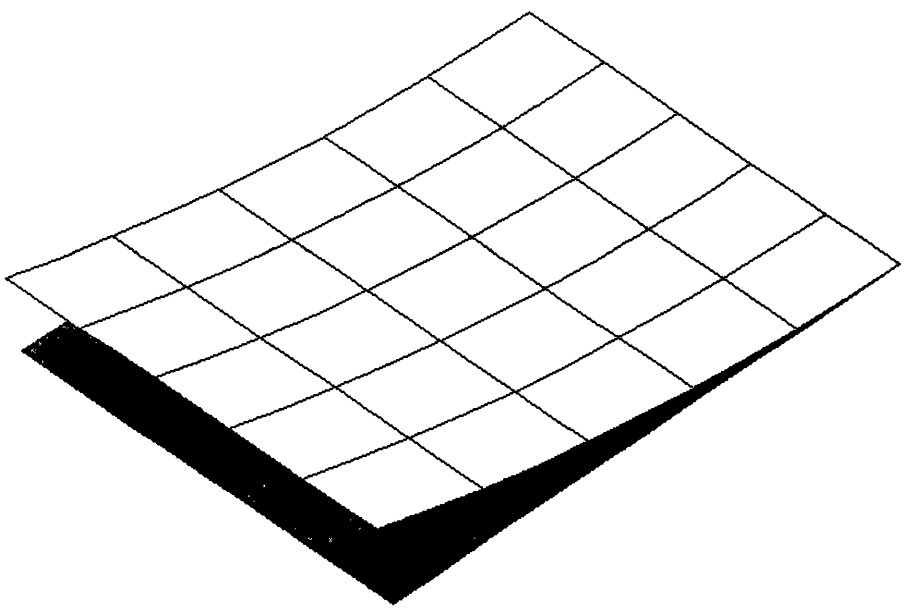

*Fig. 4.11, Bending the plate back.*

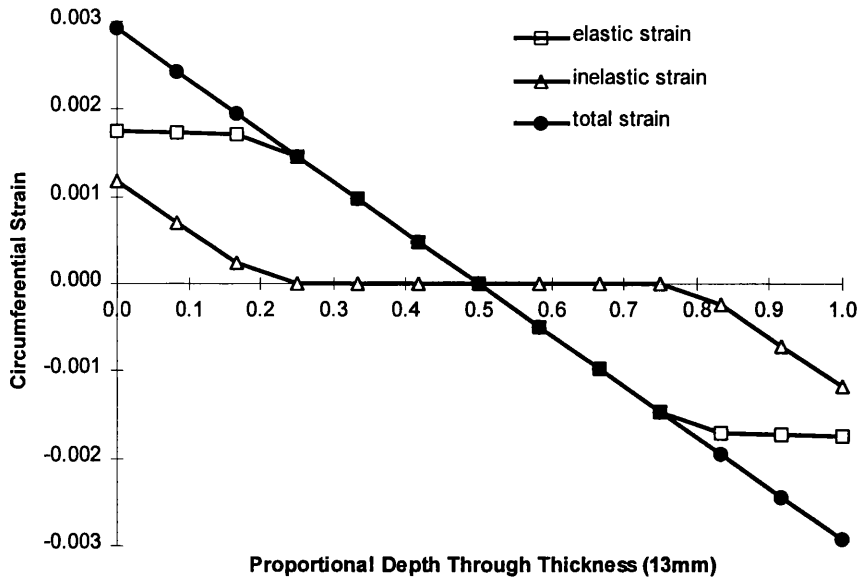


*Fig. 4.12, Circumferential strain - bending the plate back.*

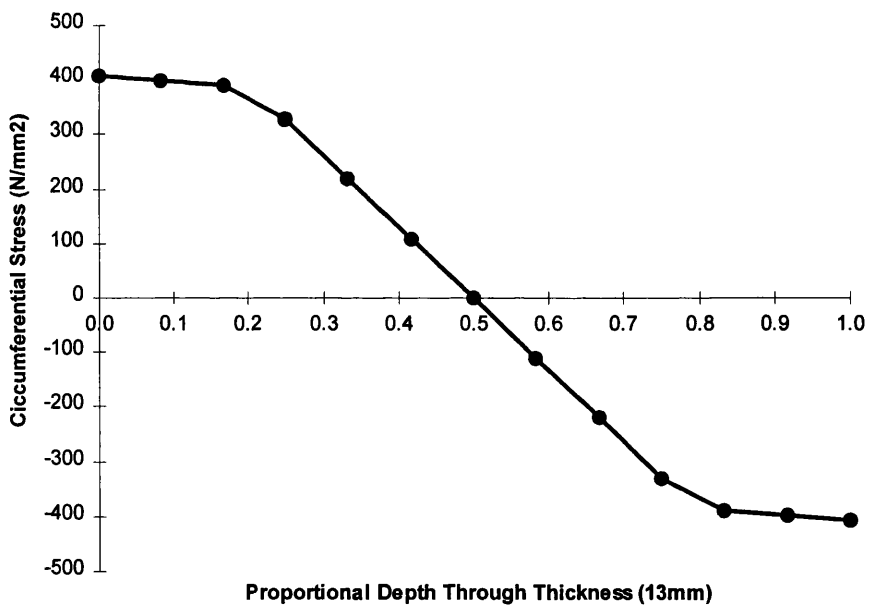


*Fig. 4.13, Circumferential stress - bending the plate back.*

When the prescribed displacements are released and the shell is free to spring back to its equilibrium position, the plastic strains remain and the elastic strains balance the difference between the plastic strain and the total strain, which must be linear through the thickness of the shell (figure 4.15). The resulting residual circumferential stress forms an 'S' or 'Z' pattern through the thickness of the shell (figure 4.16), of different magnitudes depending on thickness and required curvature (see figure A2.1.1.4 page 4 and figure A2.2.1.4, page 78 in Appendix 2), tensile at the outer layer nearest the centre of curvature, compressive between this and the mid-thickness, approximately zero at the mid-thickness, tensile between mid-thickness and the outer face and

compressive at the outer face. Corresponding magnitudes of axial residual stress are of smaller amplitude, approximately 20 N/mm$^2$ in this case, and have a slightly different pattern. The 'S' shape is approximately zero at the outer layers and mid-thickness and maximum at quarter thickness (figure A2.1.1.8, page 8 and A2.2.1.8, page 82 in Appendix 2). Magnitudes of shear stress are very small, less than 1 N/mm$^2$.

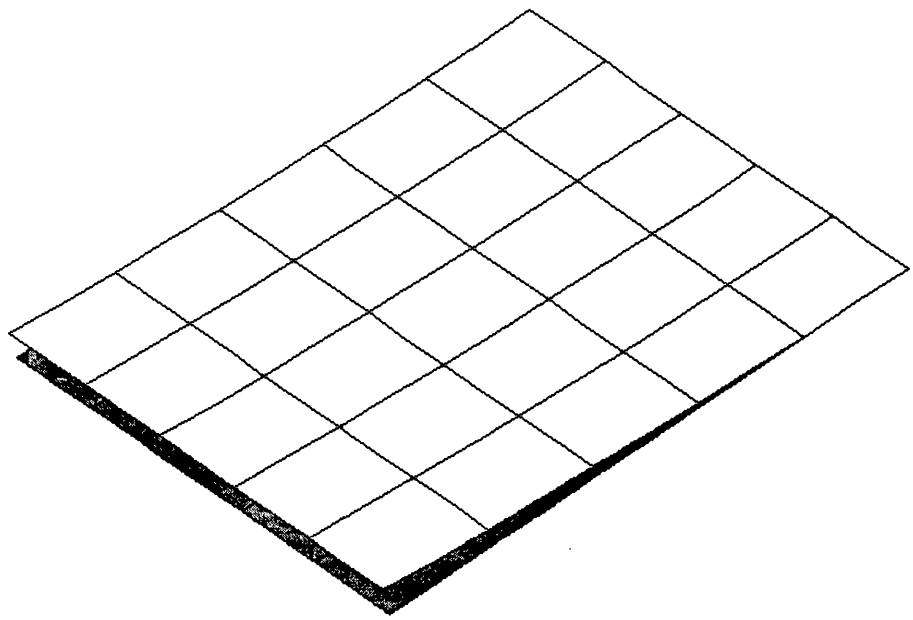

*Fig. 4.14, Releasing the plate to spring back.*

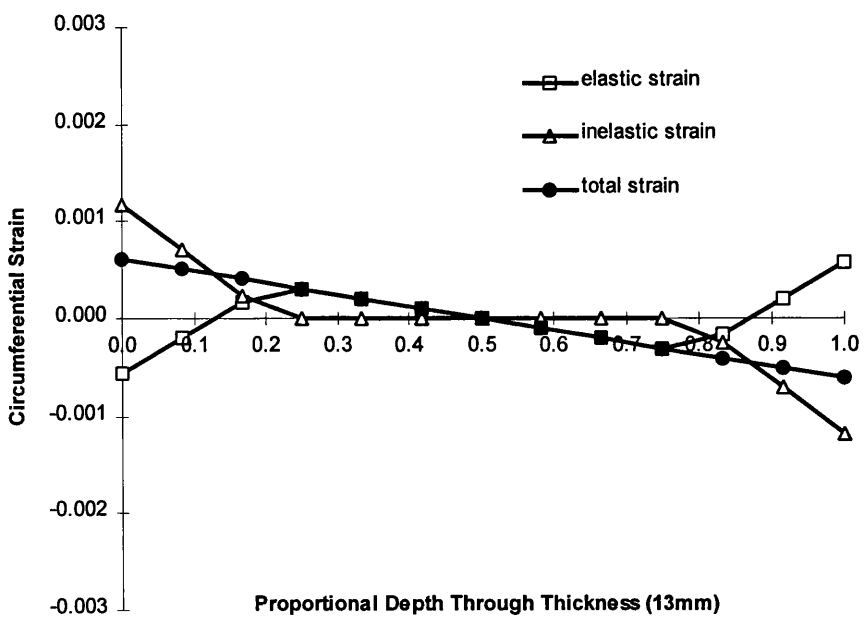


*Fig. 4.15, Circumferential strain after spring back.*

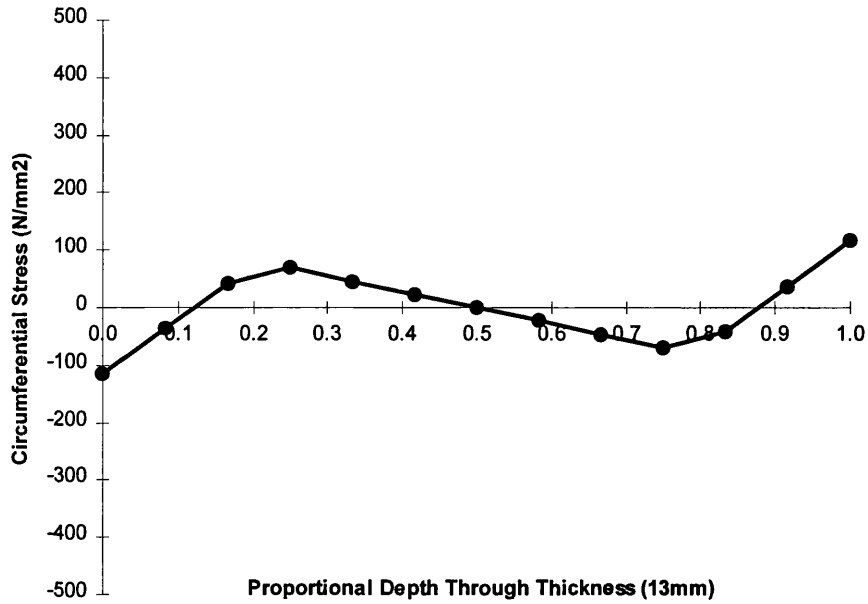


*Fig. 4.16, Circumferential stress after spring back.*

### 4.3.3 In-situ shell cold forming

In the stiffened structure it is required to introduce the plastic strains and residual stresses described above in the cylindrical shell without bending the frames. In order to achieve this the model is developed with all components of the model defined with an individual set of node points. The various components are then tied together, all rotational and translational degrees of freedom at nodes to be joined are equated (figure 4.20). This allows manipulation of material of separate components which meet by assigning a coefficient of thermal expansion to the material and applying temperatures to the node points of that separate component.

All nodes in the shell are restrained in all degrees of freedom for the cold forming simulation and an orthogonal coefficient of thermal expansion is assigned to the shell with the circumferential component given a value of 10E-6/° and the axial component given a zero value. Throughout the analysis of the cold forming process the coefficient of thermal expansion is used as a means of manipulating states of strain in the material with temperature variation through the thickness of the shell.

The values of total strain through the thickness of the shell described in the test plate model are applied to the cylinder in two steps by temperature values at each node in the cylinder and at thirteen points through the thickness of the cylinder. In the first step a linear gradient of total strain to cause plastic strain at the outer layers to the magnitudes previously established, of the shell being curved back (figure 4.12) are applied, in the second step total strains through the thickness are reduced to those of the released curvature (figure 4.15). The resulting distributions of elastic and plastic strain and residual stress in the axial and circumferential directions in the cylinder are almost identical to those of the restrained and released plate described earlier.

Initial temperature gradient conditions are introduced in the shell, before expansion is applied, to ensure that the model is at zero temperature at the end of the cold

forming analysis, when the co-efficient of thermal expansion is altered to an isotropic state for the following welding analysis.

The degrees of freedom in the cylinder which were restrained during this step are released and boundary conditions of cylindrical symmetry are applied before any further steps are taken. This change of boundary conditions has no apparent effect on the cylinder and frames at all areas except at the top 'free' curved edge, adjacent to the top ring, where there is a slightly uneven stress pattern, following the edges of the frames. This stress pattern is small in magnitude, less than 1 $N/mm^2$ in tension and compression, and is assumed not to affect the analysis significantly.

## 4.4 Welding analysis

### 4.4.1 Welding shell elements

#### 4.4.1.1 Variation of Young's modulus with temperature

The variation of Young's modulus with temperature in the welding analysis is plotted in figure 4.17. This variation is intended to take account of material softening at very high temperatures and will significantly affect material through the thickness of the shell between the weld-shell surface and approximately 2 mm below this. The cold forming process is not affected by this variation because the applied temperatures are below 7E7°, where Young's modulus remains constant.

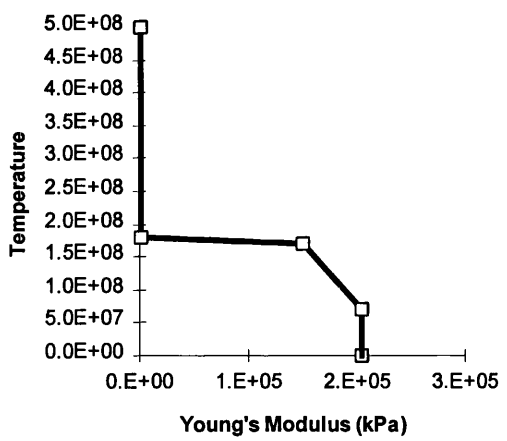


*Fig. 4.17, Variation of Young's Modulus with temperature.*

#### 4.4.1.2 Distribution of welding thermal strains in model 1(ortho) and model 2(ortho)

Before any welding thermal strains are introduced the coefficient of thermal expansion is altered from an orthotropic state with a 10E-6/° circumferential component and a zero axial component in the cold forming steps to an orthotropic state with a 10E-6/° circumferential component and a axial 10E-6/° component, by means of a field variable in the input file.

In the welding analysis of model 1(ortho) and model 2(ortho), in the cylinder or a frame flange, total 'thermal' strains at the shell-weld surface (at depth through thickness = 0 in figure 4.18) of 2% are introduced [1], with an approximate 'S' shape

variation of 'thermal' strain below this reducing to zero at 8 mm below the shell-weld surface. This distribution is maintained for different thicknesses of plates in model 1(ortho) and model 2(ortho).

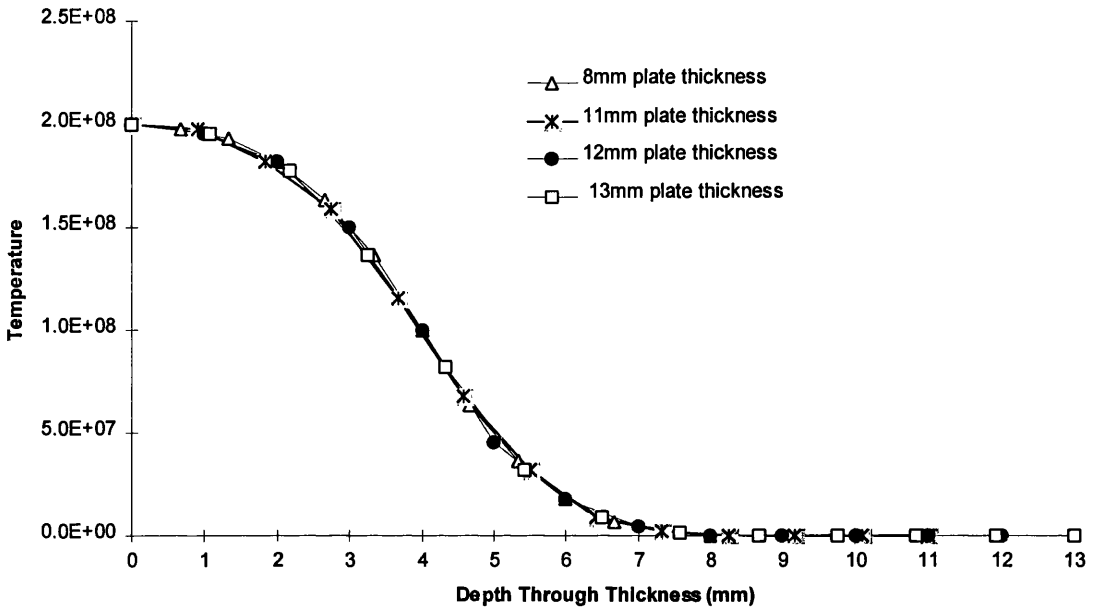


*Fig. 4.18, Distribution of total 'thermal strains' through the thickness of the cylinder and frame flanges of model 1(ortho) at weld locations (see Fig. 20, Detail B, Node 1).*

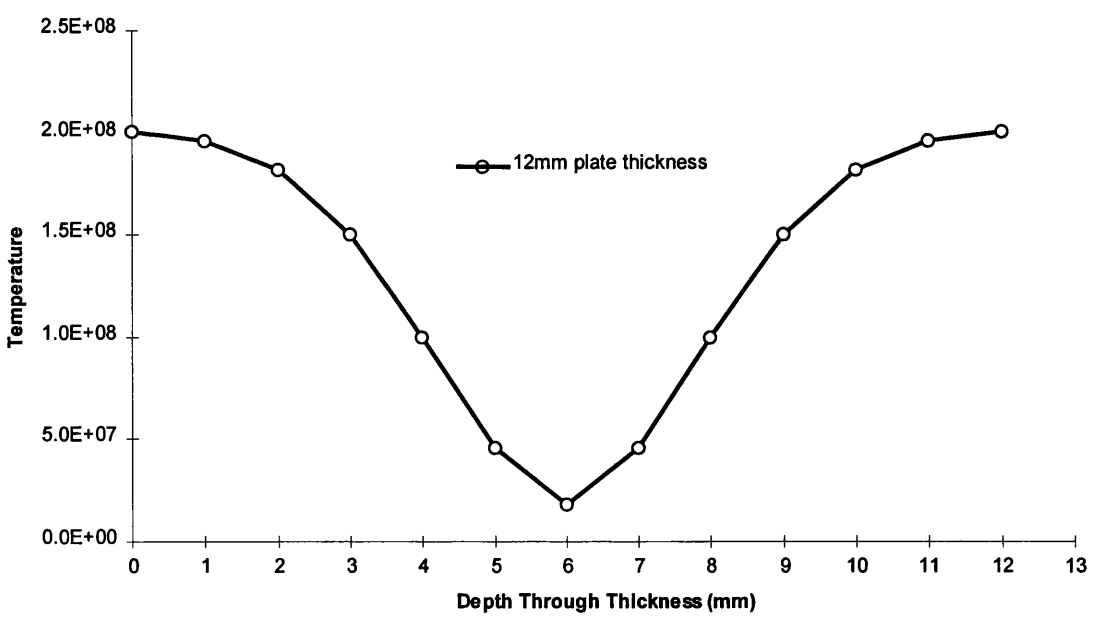


*Fig. 4.19, Distribution of total 'thermal strains' through the thickness of the stringer frame webs of model 1(ortho) at weld locations (see Fig. 20, Detail B, Node 2).*

At frame web weld locations, such as the frame web component in the frame-cylinder intersection of figure 4.20, Detail A, where there is a weld on both sides of the plate, the 'S' shape distributions described above are applied from the shell-weld

surface to where they overlap (figure 4.19). It is necessary to tie two separate nodes (Figure 4.20, Detail B, Node 1 and Node 2) which are at the same point in space, to define different variations of thermal strain at the same nodal position (Figure 4.20, Detail C, Position A).

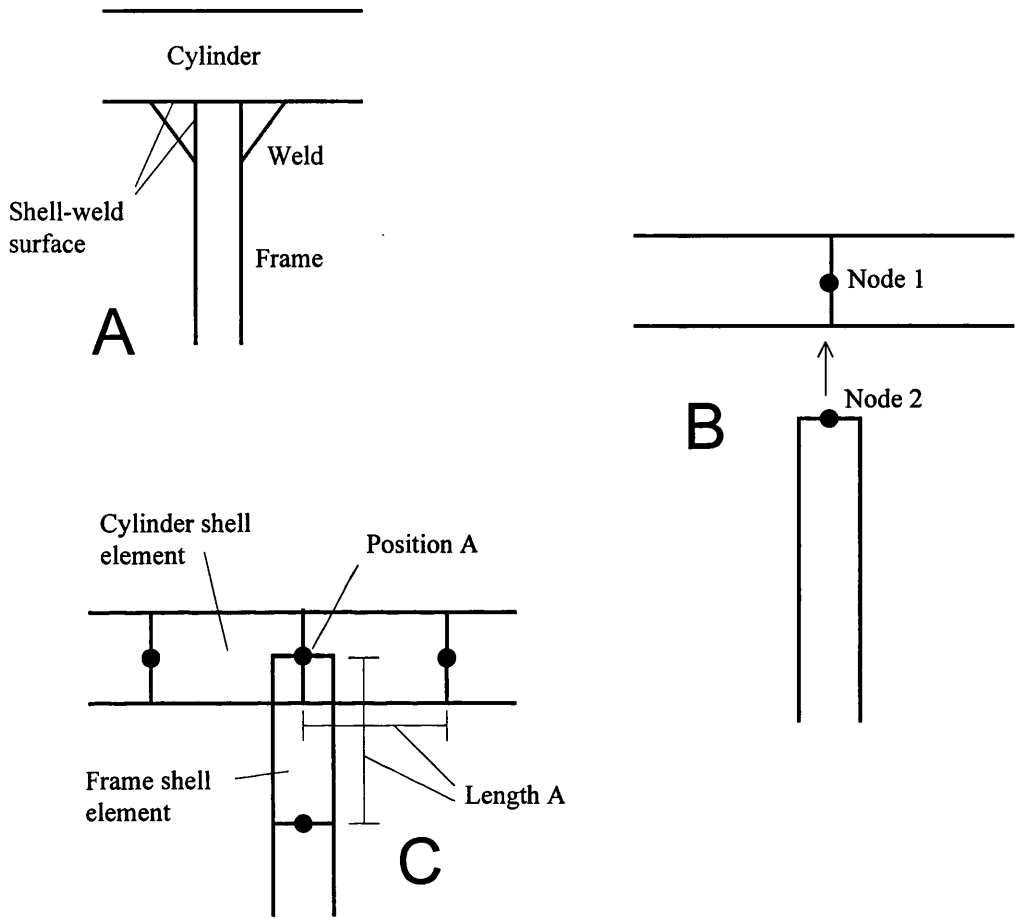


*Fig. 4.20, Finite Element welding configuration.*

All element lengths adjacent to a weld in the Finite Element models are 75 mm in length (Length A in Figure 4.20, Detail C). Approximately half the element surface on plan, i.e. the two integration points out of four closest to the nodes on the line of the weld, are affected significantly by the thermal expansion specified along this line of nodes. This gives a value for $\eta$ [1 and 17] of 75 divided by twice the thickness, between 3.75 for a 10 mm plate and 2.08 for an 18 mm plate, the range of thicknesses in models 1(ortho) and 2(ortho).

Total 'thermal' strains are applied in a single non-linear step of approximately eight increments. These strains are reversed when the model is returned to zero temperature at all nodes in the following non-linear step, also of approximately eight increments, before the model is loaded and buckled in the following non-linear steps.

#### 4.4.1.3 The effect of other variations of welding thermal strain on buckling resistance

In developing the method of applying through thickness total strains to simulate welding procedures in the stiffened cylinders, different distributions of through thickness thermal strains to those used in the refined analyses of model 1(ortho) and model 2(ortho) were used, although the magnitude of thermal strain at the shell-weld surface integration points was always 2%. Figure A2.3.2.1, page 152 of Appendix 2, illustrates two 'S' type variations of through thickness thermal strain in the cylinder at a fillet weld location. This variation is applied to a model with similar geometric parameters to model 1(ortho) but with a 30° sector angle rather than the 36° sector angle. The application of these distributions of thermal strain through the plate thicknesses was based on a proportional depth through thickness basis rather than on real depth of penetration, i.e. a 13 mm plate thickness has a deeper real depth of welding thermal strain penetration compared to an 11 mm thick plate.

Figure A2.3.2.2, page 153 of Appendix 2, illustrates the load displacement paths of buckling tests carried out on the 30° sector angle after cold forming, welding and axial loading steps with reference to the welding thermal strain distributions in figure A2.3.2.1. While there is some difference in buckling characteristics between the residual stress models, it is a small difference when compared to the difference between these two tests and the test with no residual stress.

### 4.4.2 Residual stress distribution

#### 4.4.2.1 Residual stress distribution at weld locations

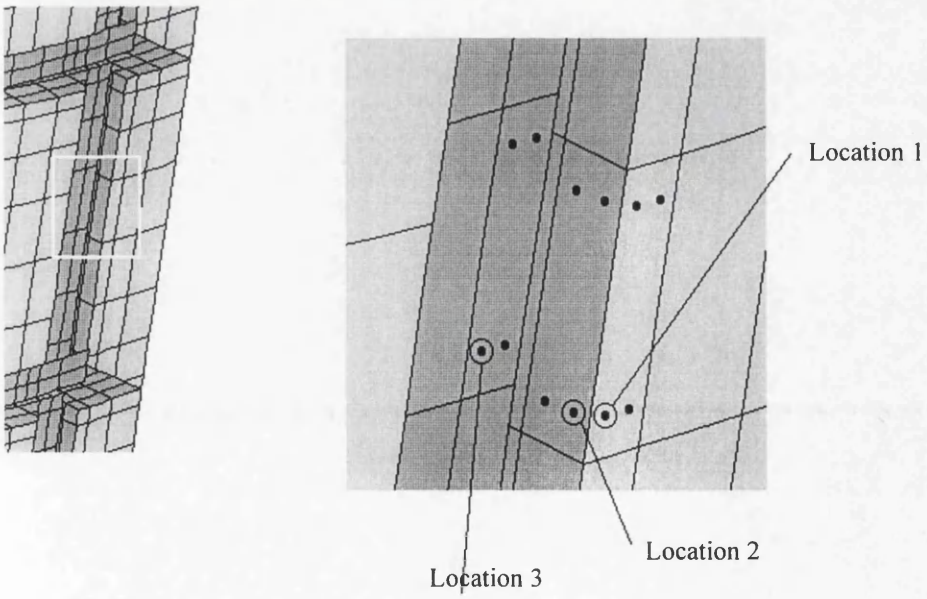


*Fig. 4.21, Through thickness residual stress locations for graphs in Appendix 2.*

Figures A2.1.2.1 and A2.1.2.2, pages 9 and 10 of Appendix 2, show the distribution of circumferential strain and stress respectively at thirteen points through the thickness of the cylinder shell (location 1 in figure 4.21) in the 'thermal' expansion step for the

case of model 1(ortho). The light lines in figures A2.1.2.2 and A2.1.2.4 are the magnitudes of strain and stress in the increments leading up to the final increment. The thick black line represents the final increment at the end of the step. It can be seen that the magnitudes of circumferential stress at points close to where the weld heat is applied (at proportional depth through the thickness = 1.0) in figure A2.1.2.2 reduce to very small values at high temperatures in the final increments of the step, when the Young's modulus is affected. Figures A2.1.2.3 and A2.1.2.4 show the distribution of circumferential strain and stress in the 'heat removal' step, when the 'thermal' expansion has been reversed.

The thick black line in Figure A2.1.2.4 shows the effect of the welding steps on circumferential residual stress at the weld location. In this case, at a stringer to shell weld, the circumferential direction is the across the weld direction. At points close to where the weld heat had been applied there is a tensile stress of approximately 300 $N/mm^2$. This is balanced by a compressive stress of approximately 400 $N/mm^2$ in the mid-thickness of the plate, gradually returning to 300 $N/mm^2$ in tension at the reverse side of the plate.

Figures A2.1.2.5-8, pages 13 to 16 of Appendix 2, illustrate values of axial strain and axial stress in the welding steps. The axial 'along the weld' stress at points close to where the weld heat is applied is approximately 400 $N/mm^2$ in tension. This is due to the greater stiffness of the shell in the direction of the stringer frame and the tendency for the material at these points to produce smaller total strains in response to the applied thermal strains along the weld in comparison to across the weld.

At weld locations in the cylindrical shell, the welding procedure is being applied 'on top' of locations affected by the previous cold forming step. The welding 'thermal' strains have the effect of cancelling cold forming stresses at the weld locations. This can be expected, as the largest total strains applied in the cold forming steps are approximately 3.5 times the values of strain to cause yield in the material, while in the welding steps total 'thermal' strains applied are approximately 11.5 times the values of strain to cause yield.

Figures A2.1.3.1-8, pages 17 to 24 of Appendix 2, illustrate values of strain and stress in the stringer web of model 1(ortho) in the welding steps at location 2 in figure 4.21, adjacent to the point in the cylinder shell discussed above. Total strain is always constant across the plate thickness due to the balanced distribution of thermal strain (figure 4.19), membrane stretching and relaxing is caused rather than the combination of stretching and bending caused by the welding procedures.

Figures A2.1.4.1-8, pages 25 to 32 of Appendix 2, illustrate values of strain and stress in the stringer flange of model 1(ortho) in the welding steps at location 3 in figure 4.21, at a weld location. This point is of particular interest as there is little circumferential restraint as there is for point 1, in the cylinder shell.

Values of stress and strain in model 2(ortho) over the cold forming and welding steps at similar locations to those described above are illustrated in figures A2.2.1.1-8, A2.2.2.1-8, A2.2.3.1-8, A2.2.4.1-8.

#### 4.4.2.1 Residual stress distribution in the cylinder away from weld locations

In the case of model 1(ortho), with a 13 mm thick cylindrical shell, the distribution of circumferential residual stress along a circumferential distance between two stringer frames, and midway between rings (figure 4.22), is illustrated for the thirteen plasticity calculation points (figure 4.23) in figures A2.1.5.1-13, pages 33 to 45 of Appendix 2. The corresponding magnitudes of axial residual stress are plotted in figures A2.1.6.1-13, pages 46 to 58 of Appendix 2.

Circumferential residual stress in the case of model 2(ortho), with an 18 mm thick cylindrical shell are plotted in figures A2.2.5.1-13, pages 107 to 119 of Appendix 2, corresponding magnitudes of axial stress in model 2(ortho) are plotted in figures A2.2.6.1-13, pages 120 to 132 of Appendix 2.

Generally from these plots it can be seen that the finite element welding thermal expansion and contraction steps produce bending in the plate away from the welds, this is shown by the high compressive (negative) stress at layer 1 (figure A2.1.5.1) and high tensile stress at layer 13 (figure A2.1.5.13). Stress values at mid-thickness i.e. at layer 7 of 13 (figure A2.1.5.7), away from the welds can be considered to be the membrane stress values as there is no unbalanced direct through thickness thermal straining in the central area. Considering that welding thermal strain distribution is similar in terms of real depth of penetration for model 1(ortho) and model 2(ortho), model 1(ortho), 13 mm thickness, produces a circumferential residual membrane stress of approximately 23 $N/mm^2$ in compression and model 2(ortho), 18 mm thickness, produces a circumferential residual membrane stress of approximately 17 $N/mm^2$ in compression.

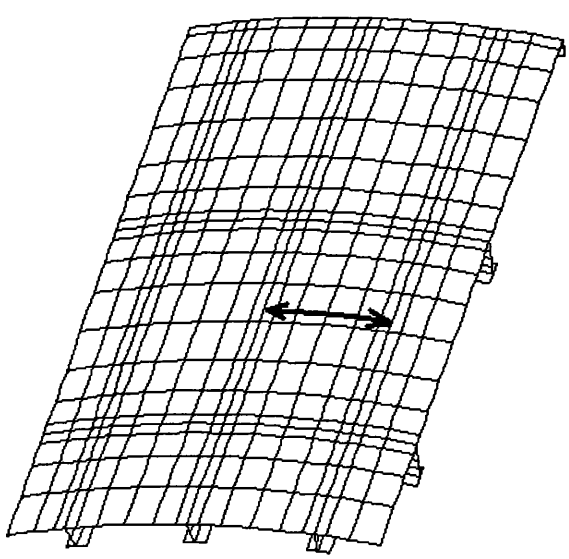

*Fig. 4.22, Arc length considered in Fig.s A2.1.3.1-13 and Fig.s A2.2.3.1-13, Appendix 2.*

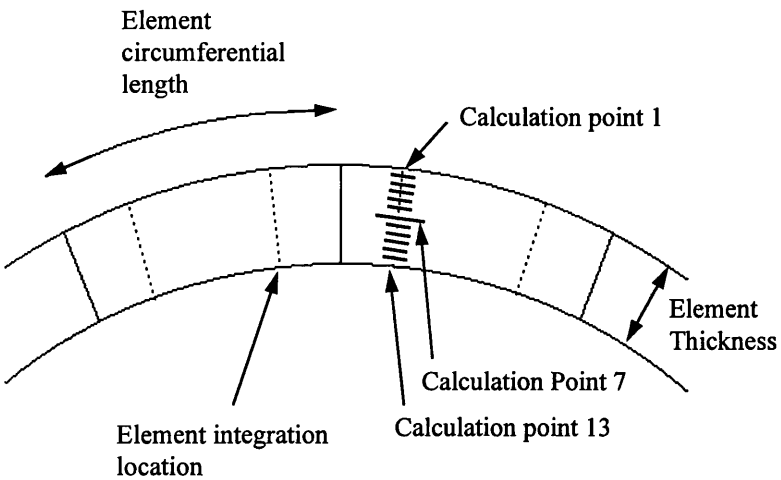


*Fig. 4.23, Element plasticity calculation point locations with reference to Fig.s A2.1.5.1-13, A2.1.6.1-13, A2.2.5.1-13 and A2.2.6.1-13 of Appendix 2.*

ABAQUS POST contour plots of circumferential, axial and Von Mises equivalent stress at extreme fibres and mid thickness after cold forming and welding steps for model 1(ortho) and model 2(ortho) are illustrated in figures A2.1.7.1-9 and A2.2.7.1-9, pages 59 to 67 and 133 to 141 of Appendix 2 respectively. It should be noted that there is a process of interpolation to produce the contours in these plots and stress output is not always represented accurately. For example the material hardening data in Section 4.1.2 defines perfect plasticity at a true stress of 672 N/mm$^2$, while some direct stresses are plotted at close to 900 N/mm2 in the contour plots. A cut off stress of 355 N/mm2 is used in some cases to illustrate where the yield value has been reached, these are the red regions for the case of the Von Mises equivalent stress plots.

### 4.4.3 Welding displacement pattern

Figure 4.23 illustrates the hungry horse displacement pattern that occurs after the welding steps, with a displacement magnification of 20. The maximum shell displacement, $\delta_p$ at the centre of the cylinder shell between frames is 2.15 mm for the 13 mm thick shell of model 1(ortho) with 555 mm circumferential arc length between frames and 2.11 mm for the 18 mm thick shell of model 2(ortho) with 833 mm circumferential arc length between frames.

A flat grillage analysis was carried out with similar geometric characteristics to the stiffened cylindrical shell of model 1(ortho), with a plate thickness of 13 mm. The displacement $\delta_p$ in this case was 1.87 mm which shows that the arch effect of the curvature of the shell provides more flexibility for this type of displacement compared to the straight shell, where circumferential membrane stretching occurs.

Applied welding strains in the frame webs were symmetrically distributed across the thickness of the plates (figure 4.19), and there was no circumferential bending of

the stringer frames or axial bending of the ring frames arising directly from this. However the half circumferential wave of axial shape imperfection introduced in the large ring frames of model 1(ortho) was slightly exaggerated by the circumferential straining of the frame webs and flanges in the welding steps.

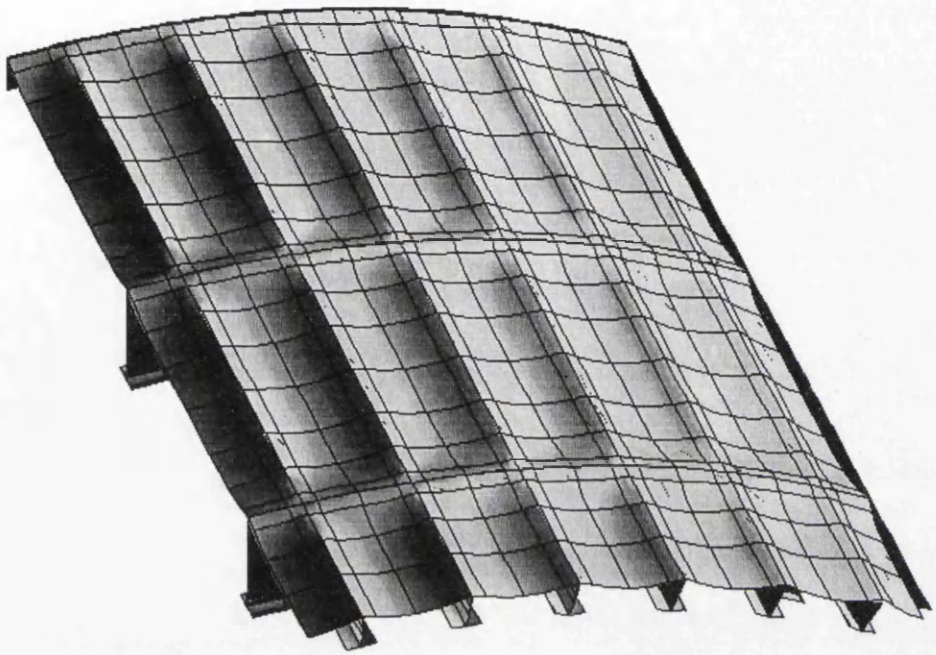


*Fig. 4.23, 'Hungry horse' displacement pattern.*

### 4.5 Buckling analysis

After the residual stress and axial loading steps, model 1(ortho) and model 2(ortho) are tested to collapse using the modified Rik's algorithm which is available in ABAQUS, for a non-linear elasto-plastic limit point analysis. Further tests are carried out on models 1(ortho) and 2(ortho) without the residual stress steps as a comparison to estimate the effects of residual stress.

Figures A2.1.8.1 and A2.2.8.1, pages 71 and 145 of Appendix 2, show load displacement paths for model 1(ortho) and model 2(ortho) during the buckling steps. The displacement variable on the x-axis is typically inward radial displacement of a node common to the cylinder, a ring web and a stringer web, closest to the largest magnitude of overall shape imperfection, node A in figure 4.2. The load variable on the y-axis is the active surface pressure on the cylinder elements only.

#### 4.5.1 Model 1(ortho)

Figure A2.1.8.1 shows the load displacement path for model 1(ortho), for the cases with and without residual stress. At the beginning of the buckling step when surface pressure is zero, there is an initial circumferential expansion from axial loading in the previous step. This expansion is largely cancelled by tensile hoop strains in the welding steps for the case with residual stress.

In figure A2.1.8.1 there is a linear elastic response to surface pressure until the cylinder shell buckles between frames, at a surface pressure of approximately 0.56 $N/mm^2$ for the case without residual stress, and 0.43 $N/mm^2$ for the case with cold forming and welding residual stress, a reduction of 23%. A contour plot of Von Mises equivalent stress at the outer fibre nearest to the inside of the cylinder at the end of the linear response to surface pressure (point A in figure A2.1.8.1) is illustrated in figure A2.1.7.11, page 69 of Appendix 2. Surface pressure increases until the large ring frames have buckled. A contour plot of Von Mises equivalent stress at mid thickness at large displacement buckling is illustrated in figure A2.1.7.12, page 70 of Appendix 2.

In figure A2.1.8.2, page 72 of Appendix 2, the load displacement path is illustrated for a buckling analysis of model 1(ortho) after the cold forming residual stress steps, without the welding steps. The case with no residual stress steps is included for comparison. It can be seen that with the relatively thin shell (13 mm) of model 1(ortho), cold forming residual stress has little effect on buckling behaviour.

The displaced shape of model 1(ortho) for the case without residual stress is illustrated in figure A2.1.9.1, page 73 of Appendix 2, the displaced shape of the case with cold forming and welding residual stress is illustrated in figure A2.1.9.2. The analysis becomes unrealistic at very large displacements due to steel fracture and element contact criteria not being considered.

**Note :** The effects of different combinations of types of residual stress on the buckling resistance of a similar model to model 1(ortho), including the effects of welding without cold forming, are illustrated in figure A2.3.3.1, page 154 of Appendix 2.

### 4.5.2 Model 2(ortho)

The end of elastic response to surface pressure for model 2(ortho) is caused by overall compartment buckling rather than local cylinder buckling. This occurs at approximately 0.655 $N/mm^2$ for the case without residual stress and 0.475 $N/mm^2$ for the case with residual stress, a reduction of 27.5% (figure A2.2.8.1, page 145 of Appendix 2). A contour plot of Von Mises equivalent stress at the outer fibre nearest to the inside of the cylinder at the end of the linear response to surface pressure (point B in figure A2.2.8.1) is illustrated in figure A2.2.7.11, page 143 of Appendix 2.

Although welding residual stress will have a lesser effect on the cylinder shell strength in model 2(ortho) due to the greater shell thickness of 18 mm, compared to 13 mm in model 1(ortho), the thinner and smaller frame components of model 2(ortho) are greatly affected by residual stress, affecting overall stiffness and causing a large reduction in resistance to overall compartment buckling.

The irregular load displacement path in figure A2.2.8.1 for the case without residual stress, is caused by unstable behaviour in the rings as they buckle, this is illustrated with surface pressure against ring vertical displacement graphs in figures A2.2.8.3 and A2.2.8.4, pages 147 and 148 of Appendix 2, with reference to points illustrated on the displaced shape plot A2.2.9.1, page 149 of Appendix 2.

When model 2(ortho) was tested with cold forming residual stress without welding residual stress, there was a sudden bifurcation of the cylindrical shell between frames at a surface pressure of approximately 0.65 $N/mm^2$ (figure A2.2.8.2, page 146 of Appendix 2). The load factor is suddenly reduced and increased again, from which

point there is a smooth load displacement relationship. A surface pressure limit load of approximately 0.65 $N/mm^2$ is reached. This behaviour is caused by the thicker shell of 18 mm in model 2(ortho) and the different cold forming characteristics needed to curve the shell, causing greater plastic straining in the extreme fibres and more severe cold forming residual stress. When cold forming and welding residual stress are considered together cold forming residual stresses at weld locations are superseded by welding residual stress and the buckling behaviour has greater regularity. The displaced shape for the case with cold forming and welding residual stress is illustrated in figure A2.2.9.2, page 150 of Appendix 2.

# 5 Torsional buckling

The investigation of torsional stability of cylinders has previously largely been through physical verification, where laboratory tests of cylinders under torsion and combined torsional loads have produced widely varying buckling modes, and through theoretical investigation, as an extension of methods applied to stability under axial and surface pressure loading.

The method for applying torsional boundary conditions to cylindrical finite element models in this study was developed as a result of observations of photographs of cylinders buckled in torsion, such as those in [30] and [31]. There is clearly a pattern of repetition in the circumferential direction and also an anti-symmetry across the central hoop, at full buckle wave intervals.

The cylindrical form provides good resistance to elastic buckling under torsion, as all torsional applied loads initially create shear stress, distributed through the material in the cylinder. This state of stress provides relative stability when compared to the state of membrane compression produced by axial and surface pressure load combinations.

Design codes for offshore cylindrical structures often overlook torsional stability and focus on designing for axial force and surface pressure. In reality a large cylindrical component will be subject to some magnitude of torsional force, arising form its own inertia or irregular applied loading, in addition to uniform axial and surface pressures, in terms of both serviceability and collapse criteria.

It is demonstrated in the following sections that the resistance to torsional buckling can be significantly reduced under combinations of surface pressure and axial force, and that although stiffeners have no significant effect on initial plastic torsional failure, the post-buckling behaviour is greatly affected by the arrangement of stiffeners.

## 5.1 Classical elastic torsional buckling theory

### 5.1.1 The Donnell equation

Among the simplest of linear differential equations to describe the deformation of a shell, in terms of lateral displacement, w, is the Donnell equation (1).

$$D\nabla^8 w + \frac{Et}{R^2}\frac{\partial^4 w}{\partial x^4} + \nabla^4\left[N_X\frac{\partial^2 w}{\partial x^2} + 2N_{XY}\frac{\partial^2 w}{\partial x \partial y} + N_Y\frac{\partial^2 w}{\partial y^2}\right] = 0 \quad \ldots(1)$$

Under torsional loading, the circumferential and axial stress resultants, $N_X$ and $N_Y$ are zero and the shear stress resultant, $N_{XY} = \tau t$ . The Donnell equation (1) reduces to

$$D\nabla^8 w + \left[\left[\frac{Et}{R^2}\frac{\partial^4 w}{\partial x^4}\right] + \left[2\tau\, t\, \nabla^4 \frac{\partial^2 w}{\partial x \partial y}\right]\right] = 0 \quad \ldots(2)$$

Using the solution for lateral displacement in equation (3) for a cylinder under torsion, with a boundary condition at the ends of the cylinder that provides elastic restraint at some value between clamped and pinned,

$$w=w_{mn}\left[\sin\left[\frac{m\pi x}{L}+\frac{ny}{R}\right]-\sin\left[\frac{(m+2)\pi x}{L}+\frac{ny}{R}\right]\right] \qquad \ldots(3)$$

equation (2) was derived by Donnell [34], and again by Batdorf et al. [35], to give the relationship between the critical shear stress, $\tau_{CR}$ and the buckling coefficient, $k_S$ as,

$$\tau_{CR} = \frac{\pi^2 k_S E}{12(1-\nu^2)}\left[\frac{t}{L}\right]^2 \qquad \ldots(4)$$

The relationship between the buckling coefficient, $k_S$ and the curvature parameter, Z, for moderate length cylinders is illustrated in Figure 5.2 and given in [33] as

$$k_S = 0.85\, Z^{3/4} \qquad \ldots(5)$$

where Z = Curvature Parameter

$$= \frac{L^2(1-\nu^2)}{Rt}$$

### 5.1.2 Verification of the Finite Element boundary conditions with classical elastic buckling theory

Two un-stiffened cylinder geometries, Model A and Model B (Table 1), with varying thicknesses and a range of sector arc angles are subjected to Torsional Eigenvalue Buckling tests with the Finite Element program ABAQUS, incorporating the methods for torsional loading and boundary conditions described in following sections. The ends of the cylinders are pinned to a thick top ring. The material behaves elastically.

| | MODEL A | MODEL B |
|---|---|---|
| *Cylinder Radius, R (mm)* | 4000 | 4000 |
| *Overall Cylinder Height, L (mm)* | 1300 | 8000 |
| *Top Ring Depth (mm)* | 212 | 212 |
| *Top Ring Thickness (mm)* | 50 | 50 |

*Table 1. Model A and B geometries*

The lowest value of critical shear stress for a given model with different sector arc angles is used for comparison with classical elastic stability theory (Figure 5.1). Larger arc angles produce smaller numbers of circumferential buckling waves, which use greater amounts of membrane stretching energy in buckling, smaller arc angles produce larger numbers of circumferential buckling waves, which use greater amounts of bending energy in buckling.

Critical shear stress values are obtained from Finite Element analyses (Figure 5.1), the buckling coefficient $k_s$ is calculated with equation (4), and $k_s$ is plotted against Z as a comparison to equation (5) in Figure 5.2. The Finite Element data is slightly conservative when compared to the corresponding theoretical data, this could be attributed to the shear flexibility of the Finite Elements.

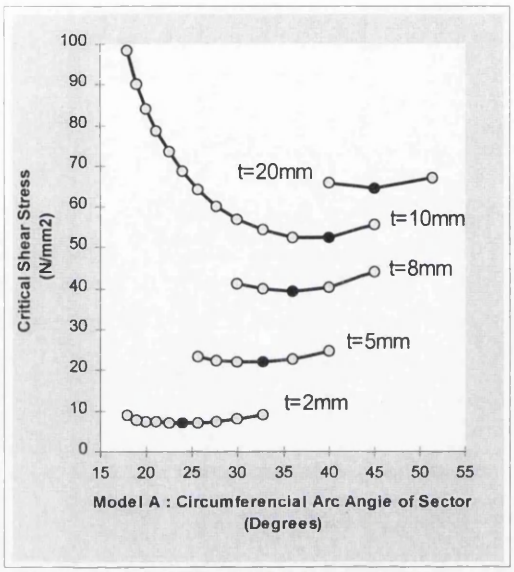


*Fig. 5.1, Model A, Critical shear stress with varying thickness.*

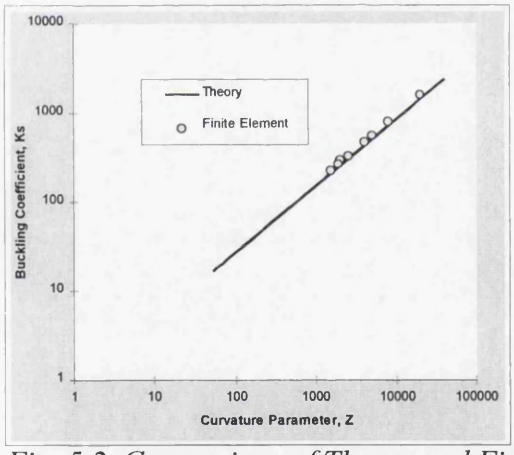


*Fig. 5.2, Comparison of Theory and Finite Element data.*

## 5.2 The Elasto-Plastic Finite Element Models

Two stringer stiffened models and one ring and stringer stiffened cylinder model were analysed, with varying sector arc angles. The geometric parameters of the three basic models are outlined in Table 3.

Element type S8R are used in all components, these are 'thick' shell elements which take account of shear flexibility about the principal axes of the elements. The ends of the stringer webs and flanges are fixed to the top ring, and in the case of the ring stiffened cylinder, the stringer flanges are fixed to the ring webs where they meet (Figure 5.3).

### 5.2.1 Material Properties

Structural steel with a yield stress of 355 N/mm$^2$ and a hardening value of 560 N/mm$^2$ at a nominal strain of 20% is used in all models, with a Young's Modulus of 205 MPa. A plateau of perfect plasticity of 0.9% strain is included at first yield. These values are converted to true stress and log strain for input in ABAQUS. The material is assumed to be perfectly plastic at strains greater than 20%. A Poisson's ratio of 0.3 is used.

### 5.2.2 Limit Point Loading

Surface pressure is applied as an evenly distributed load on the surface of elements that make up the cylinder only. Axial loading is applied as a surface pressure on the top ring, acting in the axial direction, the top ring bears on the cylindrical shell and on the ends of the stringer webs and the ends of the stringer flanges where these components meet, allowing a realistic distribution of axial force through the top of the stiffened cylinder. A constraint is imposed on the top ring to prevent it from buckling under this concentrated surface pressure.

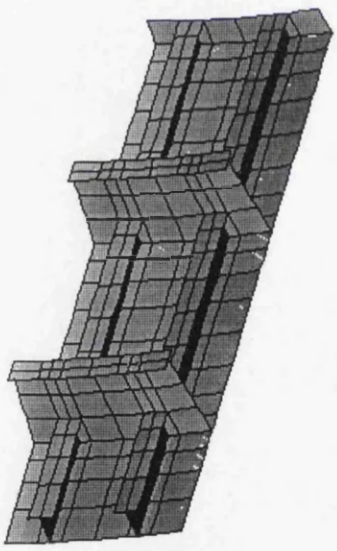

*Fig. 5.3, Model 1, 12° Section.*

Torsional load is applied as a circumferential force in the top ring, producing a circular turning action in the top ring, and a twisting action in the cylinder.

Where surface pressure, axial loading and torsional loading are described together, the surface pressure and axial components of loading are applied simultaneously in an initial non-linear step of one or more increments. The torsional load is then applied in a second non-linear step by the modified Rik's limit point method which is available in ABAQUS. The load is applied by a factor which will increase until a limit point is reached, where no further increase in load is required for further displacement or

buckling at that point in the loading history. This is the point of collapse which could occur at forces greater than forces to cause local bifurcations.

### 5.2.3 Shape Imperfection

Where a shape imperfection is introduced in a model, in the axial direction a half cosine wave is imposed, beginning at zero at the top ring, increasing to the shape imperfection amplitude at the intersection of the central circumferential plane and the bottom of the half sector. In the circumferential direction a full cosine wave is introduced as illustrated in figure 5.5 and figure 5.6.

## 5.3 Boundary Conditions

### 5.3.1 Boundary Conditions for Buckling under Torsion

The half sector of stiffened cylinder has continuity in the circumferential direction by equating all degrees of freedom at nodes on one vertical side of the half sector to the corresponding nodes on the other vertical side of the half sector (Relationship 1 in Figure 5.4). Nodes on each vertical side of the half sector have identical radial and axial cylindrical co-ordinates and all degrees of freedom at these edges are transformed into the cylindrical system. These nodes also have zero initial rotation relative to the central vertical axis of the cylinder. Nodes at the bottom corners of the cylinder in Figure 5.4 are included in this relationship.

The resulting effect is of circular repetition, the number of repetitions of geometry, stress and displacement patterns depending on the arc angle of the section chosen. Hence this arc angle should divide into of 360°, and must be divisible by the stringer spacing.

Axial anti-symmetry is introduced in the central circumferential plane by a similar method of equating degrees of freedom at nodes in this plane equidistant from the sector circumferencial centre (Relationship 2 in Figure 5.4). Two degrees of freedom are equated to be equal and the remaining four are equated to be equal and opposite. This relationship between degrees of freedom is summarised in Table 2, column 3. The point in the central circumferential plane that is common to the central axial plane (Point A in Figure 5.4) is a point of contraflexure in the plane of the cylinder, this node is free to translate in the radial direction and to rotate about the radial axis, all other degrees of freedom are restrained. These four restraints, which are applied at point A only are all of the restrained degrees of freedom in the Finite Element model during this phase.

Figure A3.4 shows the displaced shape of a Finite Element half sector with the boundary conditions described above, under torsional loading. Four view angles of the same model have been superimposed to illustrate the effect of circumferential continuity and axial anti-symmetry on the buckled shape.

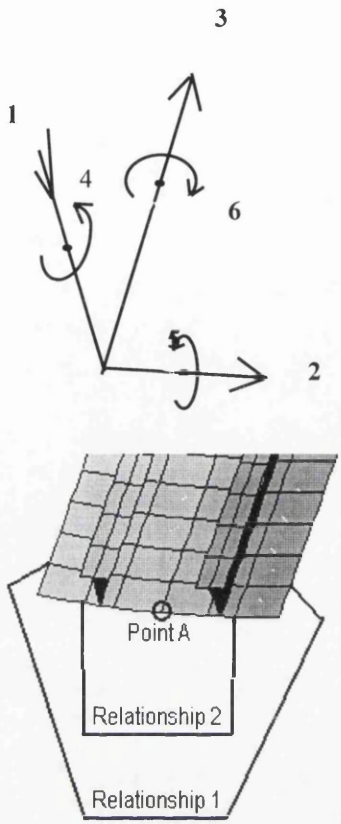


*Fig. 5.4, Associated nodal points and numbered degrees of freedom.*

| DEGREE OF FREEDOM NUMBER | AXISYMMETRIC BUCKLING | TORSIONAL BUCKLING |
|---|---|---|
| *Relationship 1* | | |
| 1 | = | = |
| 2 | restrained | = |
| 3 | = | = |
| 4 | restrained | = |
| 5 | = | = |
| 6 | restrained | = |
| *Relationship 2* | | |
| 1 | = | = |
| 2 | = - | = - |
| 3 | restrained | = - |
| 4 | restrained | = |
| 5 | restrained | = - |
| 6 | = - | = - |
| *Point A* | | |
| 1 | free | free |
| 2 | restrained | restrained |
| 3 | restrained | restrained |
| 4 | restrained | free |
| 5 | restrained | restrained |
| 6 | restrained | restrained |

*Table 2, Boundary conditions*

### 5.3.2 Boundary Conditions for Axisymmetric Loading

Where analysis is to be carried out to investigate the effects of axial loading and external pressure on torsional buckling resistance, two steps of loading are implemented, with different boundary conditions for each step. For the first step boundary conditions of cylindrical symmetry are introduced and external pressure and axial loading are applied simultaneously.

It was found that when using the Finite Element program ABAQUS, while boundary restraints could be introduced or released from step to step, equations between degrees of freedom could not be changed in this way. The following method allows boundary conditions of cylindrical symmetry to be established in the first step and modified to produce boundary conditions for cylindrical torsion in a following step.

In the first step the nodal equations and boundary conditions described in 5.5.1 are initialised, with additional restraints. Considering the vertical edges which have been equated in all degrees of freedom, translation in the circumferential direction, rotation about the radial axis and rotation about the vertical axis are restrained. These are degrees of freedom 2,4 and 6, (Table 2, column 2). In addition to the equations applied to the nodes in the central circumferential plane (the bottom plane of the half sector in Figure 5.4), restraints are applied to translation in the axial direction, rotation about the radial axis and rotation about the circumferential axis, degrees of freedom 3,4 and 5. The point in the central circumferential plane that is common to the central axial plane (Point A in Figure 5.4) is restrained in all degrees of freedom other than in radial translation. This is one restraint more than those applied torsional buckling at this node.

## 5.4 Torsional buckling Analysis

For all cases of torsional loading alone, with or without stiffeners, the Elastic Limit of response corresponds approximately to Von Mises Yield criterion under applied shear stress,

$$\tau = \frac{F}{\pi R t} = \frac{P_Y}{\sqrt{3}}$$

In the following sections the post buckling behaviour and limit loading are investigated.

| | MODEL 1 | MODEL 2 | MODEL 3 |
|---|---|---|---|
| *Cylinder Radius (mm)* | 5300 | 5300 | 4000 |
| *Stringer Spacing (Degrees)* | 6° | 9° | 9° |
| *Ring Spacing (mm)* | 1600 | 1600 | 1600 |
| *Cylinder Thickness (mm)* | 13 | 13 | 12 |
| *Top Ring Depth (mm)* | 212 | 212 | 212 |
| *Top Ring Thickness (mm)* | 50 | 50 | 50 |
| *Stringer Web Depth (mm)* | 212 | 212 | 212 |
| *Stringer Web Thickness (mm)* | 12 | 12 | 12 |
| *Stringer Flange Depth (mm)* | 150 | 150 | 150 |
| *Stringer Flange Thickness (mm)* | 12 | 12 | 12 |
| *Ring Web Depth (mm)* | 613 | - | - |
| *Ring Web Thickness (mm)* | 11 | - | - |
| *Ring Flange Depth (mm)* | 150 | - | - |
| *Ring Web Thickness (mm)* | 13 | - | - |

*Table 3, Geometric Parameters*

### 5.6.1 Orthoganally Stiffened Cylinder, Model 1

Three sector arc angles, 6°, 12° and 18°, of a similar model with circumferential rings and ring flanges and longitudinal stringers and stringer flanges (Table 3.), were tested under torsional loading. Stringers in these cases are spaced at six degrees.

Radial geometric imperfection is introduced in the meshes of amplitudes four, eight and twelve mm, in proportion to the arc angle of the sector (d in Figure 5.5).

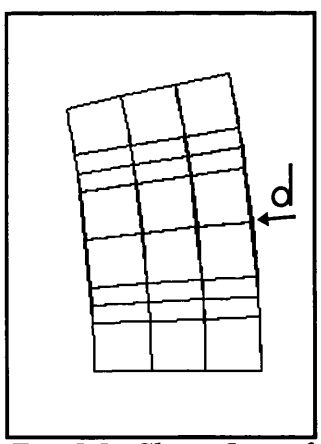


*Fig. 5.5, Shape Imperfection, Model 1, Ring and Stringer Stiffened Cylinder, Central Circumferential Section.*

In all cases the elastic limit of torsional loading was almost equal, and the limit point and load displacement path were also almost equal (Figure A3.1). Local shell buckling between the frames occurred in all cases (Figure A3.2), the arc angle of the sector chosen or the magnitude of shape imperfection introduced did not significantly affect the buckling resistance or the buckling mode.

### 5.6.2 Stringer Stiffened Cylinder under Torsional Loading, 6 Degree Stringer Spacing, Model 2

The rings described in section 5.6.1 are removed to investigate the effects of torsional loading on stringer stiffened cylinders. The elastic limit of torsional loading is similar for all cases of sector angle analysed, there is also a similarity between the elastic limit of torsional loading in these stringer stiffened models and the corresponding value for orthoganally stiffened cylinders in section 5.6.1.

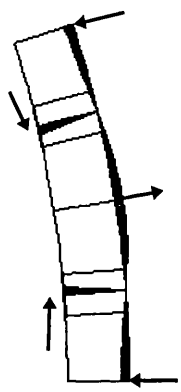

*Fig. 5.6, Exaggerated Shape Imperfection, Model 3, Stringer Stiffened Cylinder, Central Circumferential Section.*

The post-buckling behaviour of different sector arc angles varies in these stringer stiffened models, as the buckling wave occurs over the over the entire section. Load displacement graphs for varying sector arc angles are illustrated in Figure A3.3. Torsional load can be described as the circular force that would be applied in a full 360° cylinder through the top ring. Circumferential displacement in angular degrees of the top ring is calculated from values of circumferential displacement, in length, of a node in the top ring. The 18° sector arc angle produced the lowest torsional limit load. The different buckling modes are further investigated in a similar analysis in the following section.

### 5.6.3 Stringer Stiffened Cylinder under Torsional Loading, 9 Degree Stringer Spacing, Model 3

Stringers are spaced at 9° to allow larger circumferential angles to be investigated with computational efficiency. The thickness of all section components is made constant at 12mm and the average radius of the cylindrical shell is reduced to 4 meters to encourage a more slender circumferential buckling pattern. Load displacement graphs for sector arc angles of 9°, 18° and 36° are shown in Figure A3.5. Corresponding buckled shapes are illustrated in Figure A3.6. The 27° sector arc angle is omitted as it dose not divide evenly in 360°, it is possible however that the critical section angle would be 27.69°, creating 13 circumferential buckling waves, or 25.71° creating 14 circumferential buckling waves, this is overlooked to allow the type of symmetry described in Section 5.6.1 to be imposed in each analysis with even stringer spacings.

It can be seen in Figure A3.5. that the lowest limit point value for torsional loading occurs in the 18° section.

### 5.6.4 Shape Imperfect Stringer Stiffened Cylinder under combined Axial Load, Surface Pressure and Torsional Loading, Model 3

A radial shape imperfection is introduced in the model described in section 5.5.3 of amplitude 8mm and a circumferential shape imperfection is introduced in the stringer webs in such a way that the stringer webs remain perpendicular to the shape imperfect cylinder shell (Figure 5.6).

An 18° sector arc angle is subjected to 25 combinations of axial and surface pressure loading, which are each then subjected to a limit point phase of torsional loading. The variation of torsional loading limit values following axial and surface pressure loading is illustrated in Figure A3.7. At higher values of surface pressure than those shown in Figure A3.7. the cylinder begins to buckle before torsional loading is introduced. Similarly under higher values of axial loading the shell and stringers squash at values greater than those shown. The effect of axial loading on torsional buckled shape is illustrated in Figure 3.8. Surface pressure dose not have any significant effect on the torsional buckled shape. However the critical sector arc angle under combined surface pressure and torsional loading could be affected by the influence of the critical buckling mode under higher uniform pressures, without torsional load.

# 6 Conclusions

## 6.1 Eigenvalue analysis

Chapter 3, 'Eigenvalue analysis', describes a procedure for establishing the critical circumferential arc angle of a stiffened cylinder when circumferential symmetry is to be used in Finite Element analysis. After other methods were attempted the method of using orthotropic elastic stiffness coefficients was the most successful.

## 6.2 Elasto-plastic limit point analysis

Finite Element methods for simulating cold forming residual stress in the cylindrical shell and welding residual stress and displacement patterns in the cylinder and frames of stiffened cylinders are described in chapter 4, 'Elasto-plastic limit point analysis'. The basis of the methods is that magnitudes total strains are applied through the thickness of components in loading steps to simulate fabrication procedures. Cold forming residual stress patterns and welding residual stress and displacement patterns are investigated and appear to be reasonably close to what is expected from previous research.

The residual stress methods are implemented in two orthogonally stiffened cylinder models, with similar cylinder dimensions and material weights, but with different frame sizes and thicknesses and in particular different cylinder shell thicknesses. Other considerations given to these models are overall shape imperfection and steel hardening behaviour. The top ring is given less flexibility compared to other frame components and is constrained against buckling into the cylinder. The boundary stiffness provided to the top ring in this way allows large radial displacement of the cylinder.

The two models were buckled with a static axial load and an active uniform surface pressure on the cylinder, using the modified Rik's limit point method in non-linear elasto-plastic Finite Element tests using the Finite Element program ABAQUS. The characteristic buckling behaviour of the models was an initial elastic response to surface pressure followed by inter frame shell buckling, which causes a sudden reduction of circumferential stiffness and a begins overall buckling. The end to linear elastic response in all cases is clearly defined.

In the case of the first model, when residual stress steps were introduced to the analysis there was a reduction in resistance to initial inter frame buckling of approximately 23%. The effects of residual stress caused less difference to post buckling behaviour. This could be attributed to areas away from frame and cylinder weld locations being buckled and twisted at larger displacements, compared to the clearly defined areas of stress concentration at frame and cylinder intersections at the initial buckling stage. The cold forming residual stress step without the welding residual stress step had little effect on buckling behaviour.

The second model had a thicker cylinder shell, smaller and thinner rings and smaller, thinner and more widely spaced stringers. The overall shape imperfection was distributed over a smaller arc angle. Cold forming thermal strains were re-calculated for the thicker shell. Welding thermal strains were introduced to the same through thickness real depths in the first model. Without residual stress a higher elastic response was achieved. Although the reduction in initial buckling resistance

caused by the residual stress steps was higher than the reduction for first model at approximately 27.5%, the initial buckling pressure was slightly higher than in the first model. Post buckling surface pressure was slightly reduced by residual stress procedures. When cold forming was considered without welding a higher cold forming residual stress was produced and a sudden 'snap through' type inter frame buckling in the cylindrical shell occurred, followed by smooth post buckling behaviour.

### 6.3 Torsional buckling

Boundary conditions for torsional buckling of cylindrical structures in Finite Element Analysis can be formulated with respect to circumferential continuity and axial anti-symmetry. These boundary conditions can be modified to boundary conditions of cylindrical symmetry by the addition of restraints of translation and rotation at particular nodes.

In the case of cylinders under applied torsional loading, which yield under applied shear stress before elastic buckling occurs, the elastic limit of response is not significantly affected by stiffening frames attached to the cylinder shell. However the post buckling behaviour is greatly affected. The addition of ring frames and stringers induces local shell buckling between frames, and a high torsional collapse load is achieved. In the case of stringer stiffened cylinders, overall compartment buckling can occur which results in a lower torsional collapse load or limit point. The buckling mode will also be dependant on the geometric properties of components and the material properties. Variation of the flexibility of the end boundary conditions in the analysis of moderate length cylinders did not have a significant effect on elastic or elasto-plastic buckling resistance in this work.

The negative effect of varying surface pressure loading on the resistance to collapse under torsion is approximately linear while resistance to collapse under torsion decreases more rapidly under axial stress. A combination of axial force and surface pressure reduces resistance to buckling under torsional forces considerably.

# References :


1. Faulkner, D.: 'Effects of residual stresses on the ductile strength of plane welded grillages and of ring stiffened cylinders', *Journal of Strain Analysis*, Vol.12, No 2, 1977.
2. Faulkner, D. et al: 'Model code for structural design of tension leg platforms (draft)', CONOCO-ABS Rule Case Committee, ABS, New York, 1983.
3. Faulkner, D.: 'Efficient design of orthogonally stiffened cylinders', Seminar on Tensioned Buoyant Platforms, London, 25-26 May 1993.
4. API 'Bulletin on stability design of cylindrical shells', API Bul 2U first Ed., May 1987.
5. Das, P.K., Faulkner, D., Zimmer, R.A.: 'Selection of robust strength models for efficient design of ring and stringer stiffened cylinders under combined loads', OMAE-92, Calgary, June 1992.
6. Das, P.K., Faulkner, D., Zimmer, R.A.: 'Efficient reliability based design of ring stiffened cylinders under combined loads', BOSS-92, London, July 1992.
7. Das. P.K.: 'The reliability analysis of stiffened cylinders using deterministic and stochastic methods', The Royal Institution of Naval Architects, 1986.
8. Morandi, A.C., Das, P.K., Faulkner, D.: 'Frame tripping in ring stiffened externally pressurised cylinders', Marine Structures, 1995.
9. Morandi, A.C., Das, P.K., Faulkner, D.: 'Reliability based design of externally pressurised vessels', OMAE-95, Copenhagen, June 1995.
10. Morandi, A.C., Das, P.K., Faulkner, D.: 'Ring Frame Design in orthogonally stiffened cylindrical structures', OTC-95, Houston, April 1995.
11. Morandi, A.C., Das, P.K., Faulkner, D.: 'finite element analysis and reliability based design of externally pressurised ring stiffened cylinders', The Royal Institution of Naval Architects, 1996.
12. Morandi, A.C.: 'Computer aided reliability based design of ring-stiffened cylindrical shells under external pressure', PhD Thesis, Dept. Naval Arch. & Ocean Engineering, University of Glasgow.
13. Lennon, R.F., Das, P.K.: 'Torsional buckling behaviour of stiffened cylinders under combied loading', Submitted to the Journal of Ocean Engineering, Dec.1996.
14. Bushnell, D.: 'Effect of Cold Bending and Welding on Buckling of Ring-Stiffened Cylinders', Computers and Structures, Vol. 12, pp.291-307, 1980.
15. Guggenberger, W.: 'Effect of geometric imperfections taking into account the fabrication process and consistent residual stress fields of cylinders under local axial loads', Institute for Steel, Timber & Shell Structures, Technical University Graz, Austria, April 1996.
16. Smith.C.S., Kirkwood W.: 'Influence of initial deformations and residual stresses on inelastic flexural buckling of stiffened plates and shells', Steel Plated Structures, Eds. P.J.Dowling, J.E.Harding, P.A.Frieze, *Crosby Lockwood Staples*, London, 1977.
17. Dwight, J.B., Moxham, K.E.: 'Welded steel plates in compression', *The Structural Engineer*, Vol.47, No 2, 1969.
18. Frieze, P.A. : 'The experimental response of flat-bar stiffeners in cylinders under external pressure', Charles Smith Memorial Conference, DRA, Dunfermline, July 1992.

19. Louca, L.A., Harding, J.E. : 'Torsional buckling of ring stiffeners in cylindrical shells subjected to external pressure', Proc.Instn Civ.Engrs Structs & Bldgs, 1994, P.P. 219-30.
20. Shama, M.A. : 'Cold forming residual stress and their effect on the accuracy of post-forming operations', European Shipbuilding, No.2, 1970.
21. Ellinas. C.P., Croll, J.G.A.: 'Experimental and theoretical correlations for elastic buckling of axially compressed stringer stiffened cylinders', J.Strain analysis, 18(1) pp. 41-68, 1983.
22. Ellinas. C.P., Croll, J.G.A.: 'Experimental and theoretical correlations for elastic buckling of axially compressed stringer stiffened cylinders', J.Strain analysis, 18(2) pp. 41-68, 1983.
23. Morandi A.C., Das, P.K. and Faulkner, D., 'An outline of the application of reliability based techniques to structural design and assessment of submarines and other externally pressurised cylindrical structures' Department of Naval Architecture and Ocean Engineering, The University of Glasgow, 1994.
24. Pegg N.G. and Bosman T.N., 'Experimental and numerical determination of the effect of secondary structure on the overall collapse of imperfect pressure hull compartments', The Royal Institution of Naval Architects, 1996.
25. Chryssanthopoulos, M.K., Poggi C., 'Stochastic imperfection modelling in shell buckling studies', Department of Civil Engineering, Imperial College, London, U.K. Department of Structural Engineering, Politecnico di Milano, Italy, 1995.
26. European Standard EN 10025, 'Hot rolled products of non-alloy structural steels - technical delivery conditions', March 1995.
27. British Standard Published Document BS PD 6493 : 1991, Sections 1& 2, 'Guidance on methods for assessing the acceptability of flaws in fusion welded structures',
*and*
Crack tip opening displacement (CTOD) methods for fracture mechanics assessments: proposals for revisions to PD 6493.
28. API, Bulletin on Stability Design of Cylindrical Shells', API Bul 2U, First Ed., May 1987.
29. DNV Classification Notes No.30.1, 'Buckling Strength Analysis', Det Norske Veritas Classification As., July 1995.

# Appendix 1 : Calculation of elastic orthotropic stiffness coefficients.

# Model 1(ortho), calculation of inertia and cross sectional area.

$b_1 := 150 \cdot mm$

## Circumferential Direction - 1 Ring

$d_1 := 13 \cdot mm$

$b_2 := 11 \cdot mm$

$d_2 := 600 \cdot mm$

$b_3 := 1 \cdot mm$

$d_3 := 0 \cdot mm$ frame only

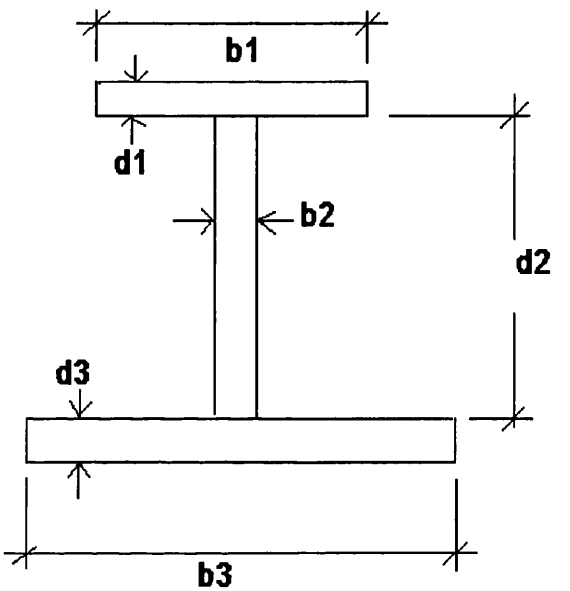


$depth := d_1 + d_2 + d_3$

$depth = 613 \cdot mm$

$a_1 := b_1 \cdot d_1$

$a_1 = 1.95 \cdot 10^3 \cdot mm^2$

$a_2 := b_2 \cdot d_2$

$a_2 = 6.6 \cdot 10^3 \cdot mm^2$

$a_3 := b_3 \cdot d_3$

$a_3 = 0 \cdot mm^2$

$csa := a_1 + a_2 + a_3$ =Ar

$csa = 8.55 \cdot 10^3 \cdot mm^2$

$$ybar := \frac{\left(\frac{d_1}{2} + d_2 + d_3\right) \cdot a_1 + \left(\frac{d_2}{2} + d_3\right) \cdot a_2 + \left(\frac{d_3}{2}\right) \cdot a_3}{csa}$$

ybar = 369.904 •mm =Zr

$$y_1 := \text{depth} - \text{ybar} - \left(\frac{d_1}{2}\right)$$

$y_1 = 236.596 \cdot \text{mm}$

$$y_2 := \frac{d_2}{2} + d_3 - \text{ybar}$$

$y_2 = -69.904 \cdot \text{mm}$

$$y_3 := \text{ybar} - \left(\frac{d_3}{2}\right)$$

$y_3 = 369.904 \cdot \text{mm}$

$$I := a_1 \cdot y_1^2 + a_2 \cdot y_2^2 + a_3 \cdot y_3^2$$

$I = 1.414 \cdot 10^8 \cdot \text{mm}^4$ =Ir

# Model 1(ortho), calculation of inertia and cross sectional area.

$b_1 := 150 \cdot mm$

$d_1 := 12 \cdot mm$

$b_2 := 12 \cdot mm$

$d_2 := 200 \cdot mm$

$b_3 := 1 \cdot mm$

$d_3 := 0 \cdot mm$

$depth := d_1 + d_2 + d_3$

$depth = 212 \cdot mm$

$a_1 := b_1 \cdot d_1$

$a_1 = 1.8 \cdot 10^3 \cdot mm^2$

$a_2 := b_2 \cdot d_2$

$a_2 = 2.4 \cdot 10^3 \cdot mm^2$

$a_3 := b_3 \cdot d_3$

$a_3 = 0 \cdot mm^2$

$csa := a_1 + a_2 + a_3$ =As

$csa = 4.2 \cdot 10^3 \cdot mm^2$

Axial Direction - 1 Stringer

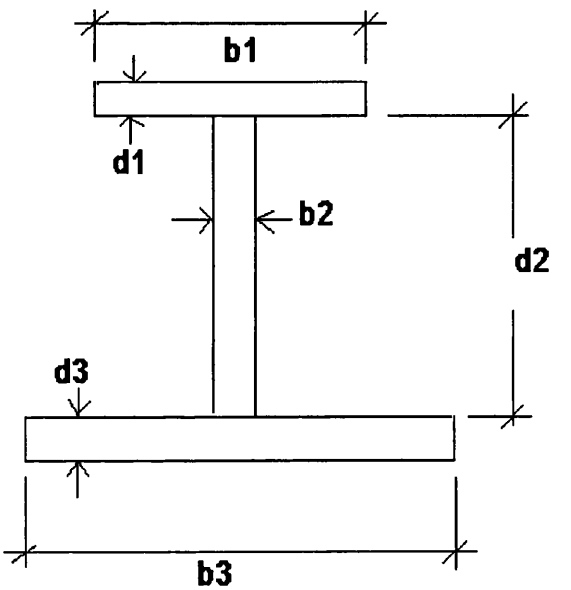

$$ybar := \frac{\left(\frac{d_1}{2} + d_2 + d_3\right)\cdot a_1 + \left(\frac{d_2}{2} + d_3\right)\cdot a_2 + \left(\frac{d_3}{2}\right)\cdot a_3}{csa}$$

$ybar = 145.429 \cdot mm$ **=Zs**

$$y_1 := depth - ybar - \left(\frac{d_1}{2}\right)$$

$y_1 = 60.571 \cdot mm$

$$y_2 := \frac{d_2}{2} + d_3 - ybar$$

$y_2 = -45.429 \cdot mm$

$$y_3 := ybar - \left(\frac{d_3}{2}\right)$$

$y_3 = 145.429 \cdot mm$

$I := a_1 \cdot y_1^2 + a_2 \cdot y_2^2 + a_3 \cdot y_3^2$ **=Is**

$I = 1.156 \cdot 10^7 \cdot mm^4$

# Calculation of orthotropic elastic stiffness coefficients for model 1(eig) from model 1(ortho)

| | |
|---|---|
| $t := 13$ | shell thickness |
| $R := 5300$ | shell radius |
| $E := 205000$ | modulus of elasticity |

general insbility :

| | |
|---|---|
| $L_r := 1600$ | axial length between rings |
| $L_e := 1.56 \cdot (R \cdot t)^{\frac{1}{2}}$ | effective axial length for general insbility |
| $L_e = 409.481$ | |
| $v := 0.0$ | Le<=Lr, v=0 |
| $I_s := 1.156 \cdot 10^7$ | stiffner inertia |
| $I_r := 1.414 \cdot 10^8$ | ring inertia |
| $b := 555$ | arc length between stiffeners |
| $b_e := 555$ | effective arc length between stiffeners (b=b for general instability) |
| $A_s := 4.2 \cdot 10^3$ | stringer cross section area |
| $A_r := 8.55 \cdot 10^3$ | ring cross section area |
| $Z_s := 145.249 + 6.5$ | strinnger eccentricity from shell |

$Z_s = 151.749$

$Z_r := 369.904 + 6.5$ ring eccentricity from shell

$Z_r = 376.404$

$G := \frac{E}{2 \cdot (1 + v)}$ shear modulus

$G = 1.025 \cdot 10^5$

$h_s := 200$ stringer depth

$h_r := 600$ ring depth

$t_s := 12$ stringer web thickness

$J_s := \frac{h_s \cdot t_s^3}{3}$ stringer torsional constant

$J_s = 1.152 \cdot 10^5$

ring web thickness

$t_r := 13$

$J_r := \frac{h_r \cdot t_r^3}{3}$ ring torsional constant

$J_r = 4.394 \cdot 10^5$

$D_x := \frac{E \cdot t^3}{12 \cdot (1 - v^2)} \cdot \left(\frac{b_e}{b}\right) + \frac{E \cdot I_s}{b} + \frac{E \cdot A_s \cdot Z_s^2}{b}$

$D_x = 4.003 \cdot 10^{10}$

$$D_0 := \frac{E \cdot t^3}{12 \cdot (1 - v^2)} \cdot \left( \frac{L_e}{L_r} \right) + \frac{E \cdot I_r}{L_r} + \frac{E \cdot A_r \cdot Z_r^2}{L_r}$$

$$D_0 = 1.733 \cdot 10^{11}$$

$$D_{x0} := \frac{v \cdot E \cdot t^3}{6 \cdot (1 - v^2)} + \frac{G \cdot t^3}{6} \cdot \left( \frac{L_e}{L_r} + \frac{b_e}{b} \right) + \frac{G \cdot J_s}{b} + \frac{G \cdot J_r}{L_r}$$

$$D_{x0} = 9.656 \cdot 10^7$$

$$G_{x0} := \frac{G \cdot t}{2} \cdot \left( \frac{L_e}{L_r} + \frac{b_e}{b} \right)$$

$$G_{x0} = 8.368 \cdot 10^5$$

$$G_{r0} := \frac{G}{2} \cdot \left( \frac{A_r + L_e \cdot t}{L_r} \right)$$

$$G_{r0} = 4.444 \cdot 10^5$$

$$G_{rx} := \frac{G}{2} \cdot \left( \frac{A_s + b \cdot t}{b} \right)$$

$$G_{rx} = 1.054 \cdot 10^6$$

## ABAQUS INPUT :

$D_{1111} := D_0$

$D_{1111} = 1.733 \cdot 10^{11}$

$D_{2222} := D_x$

$D_{2222} = 4.003 \cdot 10^{10}$

$D_{1122} := D_{x0}$

$D_{1122} = 9.656 \cdot 10^{7}$

$D_{1212} := G_{x0}$

$D_{1212} = 8.368 \cdot 10^{5}$

$D_{1313} := G_{r0}$

$D_{1313} = 4.444 \cdot 10^{5}$

$D_{2323} := G_{rx}$

$D_{2323} = 1.054 \cdot 10^{6}$

# Model 2(ortho), calculation of inertia and cross sectional area.

$b_1 := 150 \cdot mm$

## Circumferential Direction - 1 Ring

$d_1 := 10 \cdot mm$

$b_2 := 10 \cdot mm$

$d_2 := 300 \cdot mm$

$b_3 := 1 \cdot mm$

$d_3 := 0 \cdot mm$ frame only

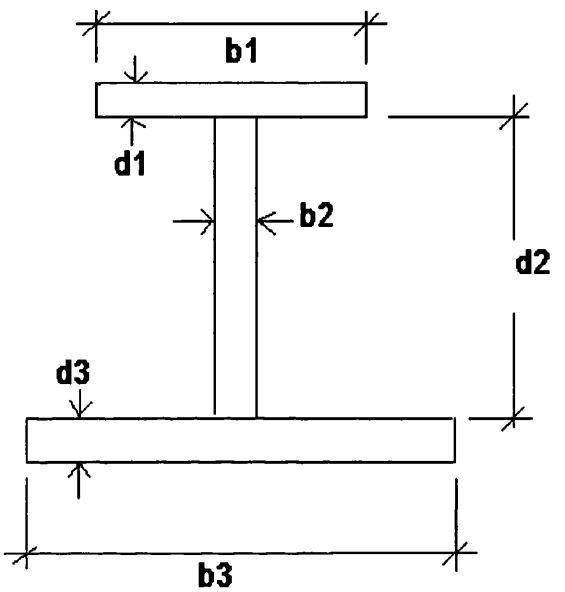


$depth := d_1 + d_2 + d_3$

$depth = 310 \cdot mm$

$a_1 := b_1 \cdot d_1$

$a_1 = 1.5 \cdot 10^3 \cdot mm^2$

$a_2 := b_2 \cdot d_2$

$a_2 = 3 \cdot 10^3 \cdot mm^2$

$a_3 := b_3 \cdot d_3$

$a_3 = 0 \cdot mm^2$

$csa := a_1 + a_2 + a_3$ =Ar

$csa = 4.5 \cdot 10^3 \cdot mm^2$

$$ybar := \frac{\left(\frac{d_1}{2} + d_2 + d_3\right) \cdot a_1 + \left(\frac{d_2}{2} + d_3\right) \cdot a_2 + \left(\frac{d_3}{2}\right) \cdot a_3}{csa}$$

$ybar = 201.667 \cdot mm$ =Zr

$$y_1 := depth - ybar - \left(\frac{d_1}{2}\right)$$

$y_1 = 103.333 \cdot mm$

$$y_2 := \frac{d_2}{2} + d_3 - ybar$$

$y_2 = -51.667 \cdot mm$

$$y_3 := ybar - \left(\frac{d_3}{2}\right)$$

$y_3 = 201.667 \cdot mm$

$$I := a_1 \cdot y_1^2 + a_2 \cdot y_2^2 + a_3 \cdot y_3^2$$

$I = 2.402 \cdot 10^7 \cdot mm^4$ =Ir

# Model 2(ortho), calculation of inertia and cross sectional area.

$b_1 := 150 \cdot mm$

$d_1 := 10 \cdot mm$

$b_2 := 10 \cdot mm$

$d_2 := 150 \cdot mm$

$b_3 := 1 \cdot mm$

$d_3 := 0 \cdot mm$

$depth := d_1 + d_2 + d_3$

$depth = 160 \cdot mm$

$a_1 := b_1 \cdot d_1$

$a_1 = 1.5 \cdot 10^3 \cdot mm^2$

$a_2 := b_2 \cdot d_2$

$a_2 = 1.5 \cdot 10^3 \cdot mm^2$

$a_3 := b_3 \cdot d_3$

$a_3 = 0 \cdot mm^2$

$csa := a_1 + a_2 + a_3$ =As

$csa = 3 \cdot 10^3 \cdot mm^2$

Axial Direction - 1 Stringer

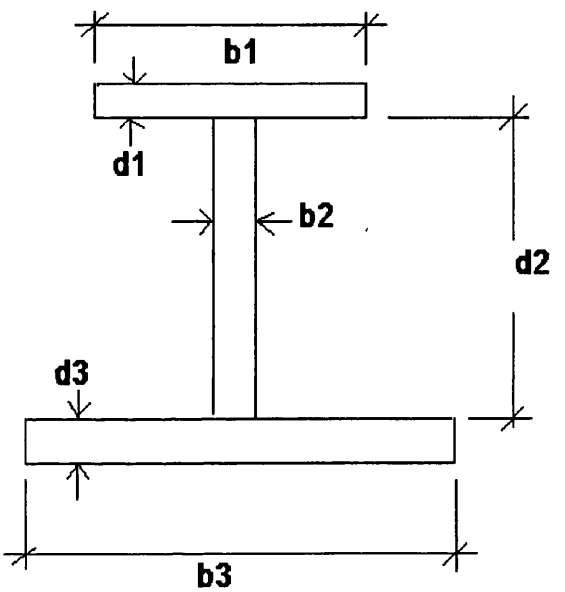

$$ybar := \frac{\left(\frac{d_1}{2} + d_2 + d_3\right)\cdot a_1 + \left(\frac{d_2}{2} + d_3\right)\cdot a_2 + \left(\frac{d_3}{2}\right)\cdot a_3}{csa}$$

$ybar = 115 \cdot mm$ **=Zs**

$$y_1 := depth - ybar - \left(\frac{d_1}{2}\right)$$

$y_1 = 40 \cdot mm$

$$y_2 := \frac{d_2}{2} + d_3 - ybar$$

$y_2 = -40 \cdot mm$

$$y_3 := ybar - \left(\frac{d_3}{2}\right)$$

$y_3 = 115 \cdot mm$

$I := a_1 \cdot y_1^2 + a_2 \cdot y_2^2 + a_3 \cdot y_3^2$ **=Is**

$I = 4.8 \cdot 10^6 \cdot mm^4$

$Z_s = 124$

$Z_r := 201.667 + \frac{t}{2}$ ring eccentricity from shell

$Z_r = 210.667$

$G := \frac{E}{2 \cdot (1 + v)}$ shear modulus

$G = 1.025 \cdot 10^5$

$h_s := 150$ stringer depth

$h_r := 300$ ring depth

$t_s := 10$ stringer web thickness

$J_s := \frac{h_s \cdot t_s^3}{3}$ stringer torsional constant

$J_s = 5 \cdot 10^4$

ring web thickness

$t_r := 10$

$J_r := \frac{h_r \cdot t_r^3}{3}$ ring torsional constant

$J_r = 1 \cdot 10^5$

$$D_x := \frac{E \cdot t^3}{12 \cdot \left(1 - v^2\right)} \cdot \left(\frac{b_e}{b}\right) + \frac{E \cdot I_s}{b} + \frac{E \cdot A_s \cdot Z_s^2}{b}$$

$D_x = 1.264 \cdot 10^{10}$

$$D_0 := \frac{E \cdot t^3}{12 \cdot (1 - v^2)} \cdot \left( \frac{L_e}{L_r} \right) + \frac{E \cdot I_r}{L_r} + \frac{E \cdot A_r \cdot Z_r^2}{L_r}$$

$$D_0 = 2.87 \cdot 10^{10}$$

$$D_{x0} := \frac{v \cdot E \cdot t^3}{6 \cdot (1 - v^2)} + \frac{G \cdot t^3}{6} \cdot \left( \frac{L_e}{L_r} + \frac{b_e}{b} \right) + \frac{G \cdot J_s}{b} + \frac{G \cdot J_r}{L_r}$$

$$D_{x0} = 1.422 \cdot 10^8$$

$$G_{x0} := \frac{G \cdot t}{2} \cdot \left( \frac{L_e}{L_r} + \frac{b_e}{b} \right)$$

$$G_{x0} = 1.2 \cdot 10^6$$

$$G_{r0} := \frac{G}{2} \cdot \left( \frac{A_r + L_e \cdot t}{L_r} \right)$$

$$G_{r0} = 4.219 \cdot 10^5$$

$$G_{rx} := \frac{G}{2} \cdot \left( \frac{A_s + b \cdot t}{b} \right)$$

$$G_{rx} = 1.107 \cdot 10^6$$

## ABAQUS INPUT :

$D_{1111} := D_0$

$D_{1111} = 2.87 \cdot 10^{10}$

$D_{2222} := D_x$

$D_{2222} = 1.264 \cdot 10^{10}$

$D_{1122} := D_{x0}$

$D_{1122} = 1.422 \cdot 10^{8}$

$D_{1212} := G_{x0}$

$D_{1212} = 1.2 \cdot 10^{6}$

$D_{1313} := G_{r0}$

$D_{1313} = 4.219 \cdot 10^{5}$

$D_{2323} := G_{rx}$

$D_{2323} = 1.107 \cdot 10^{6}$

## Appendix 2 : Residual stress plots.

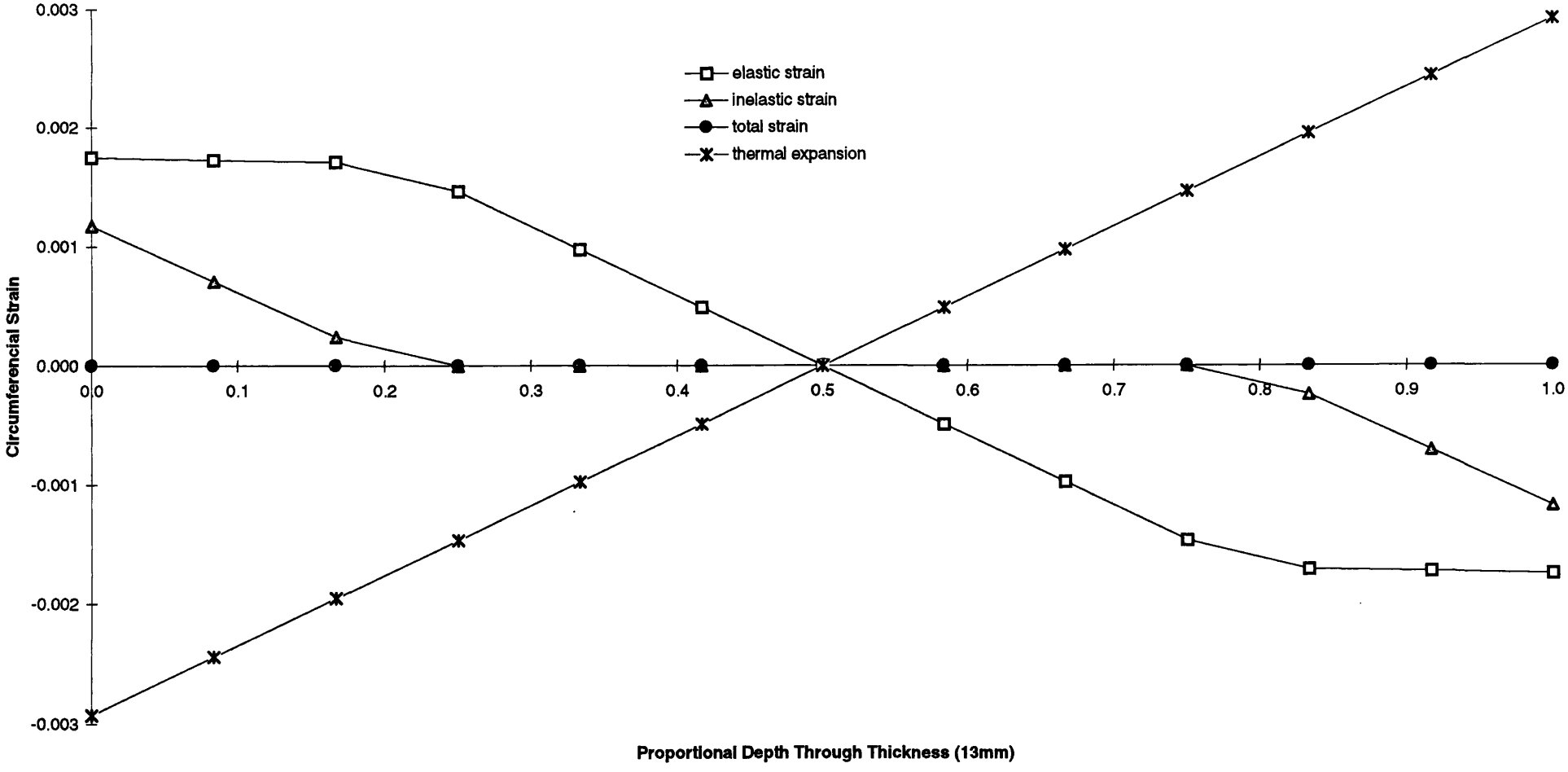


*Fig. A2.1.1.1, Model 1(ortho), bending back in cold forming simulated with thermal expansion, location 1 in Fig.4.21*

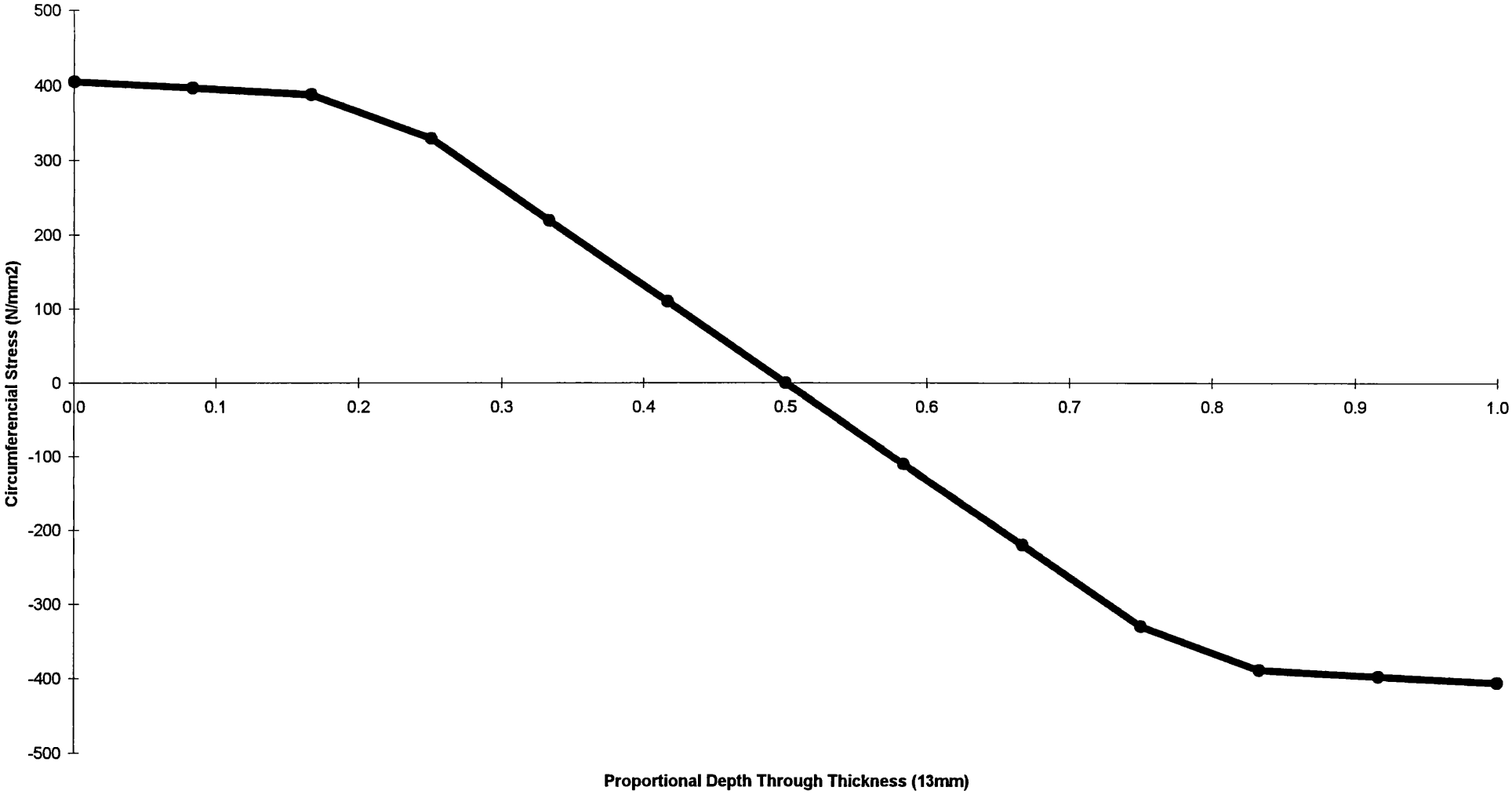


*Fig. A2.1.1.2, Model 1(ortho), bending back in cold forming, location 1 in Fig. 4.21*

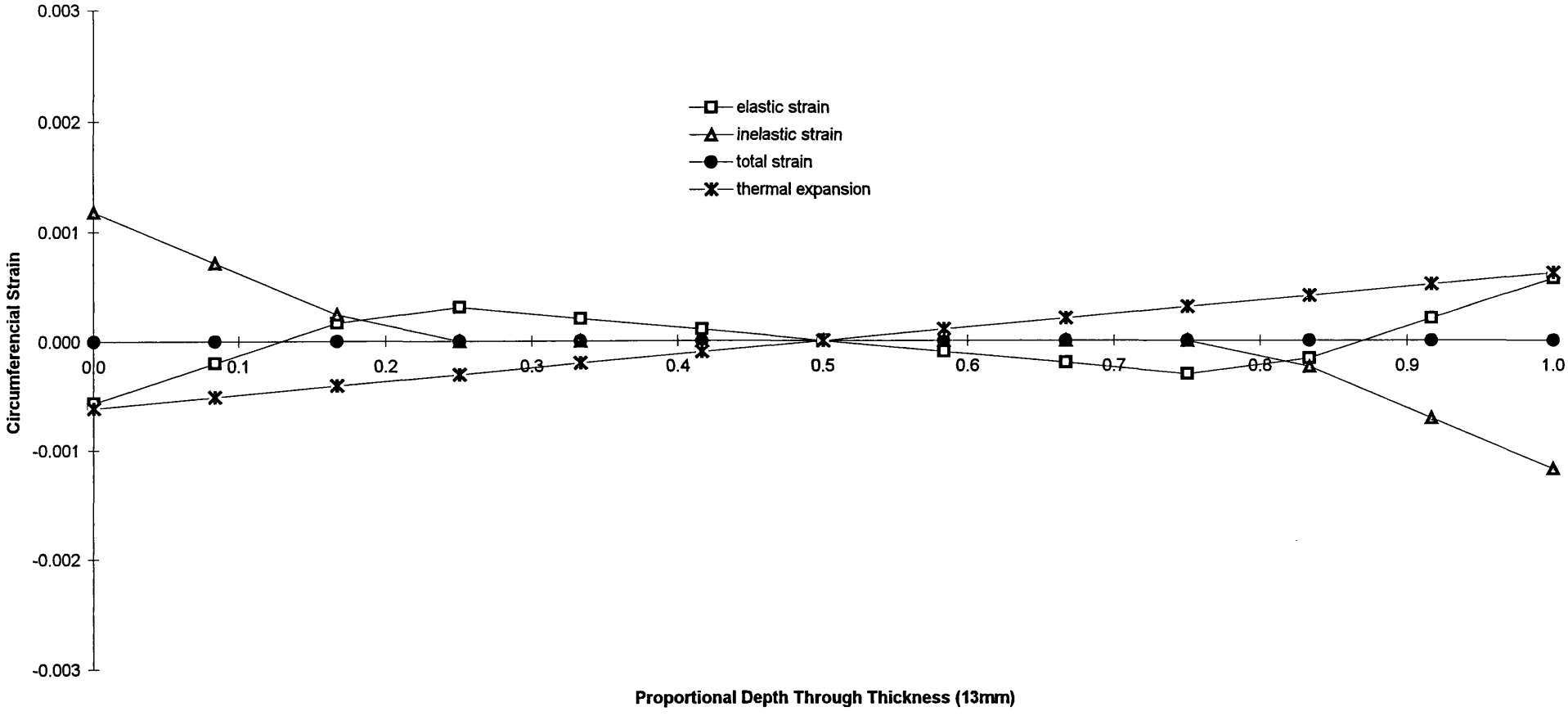


*Fig. A2.1.1.3, Model 1(ortho), spring back in cold forming simulated with thermal expansion, location 1 in Fig. 4.21*

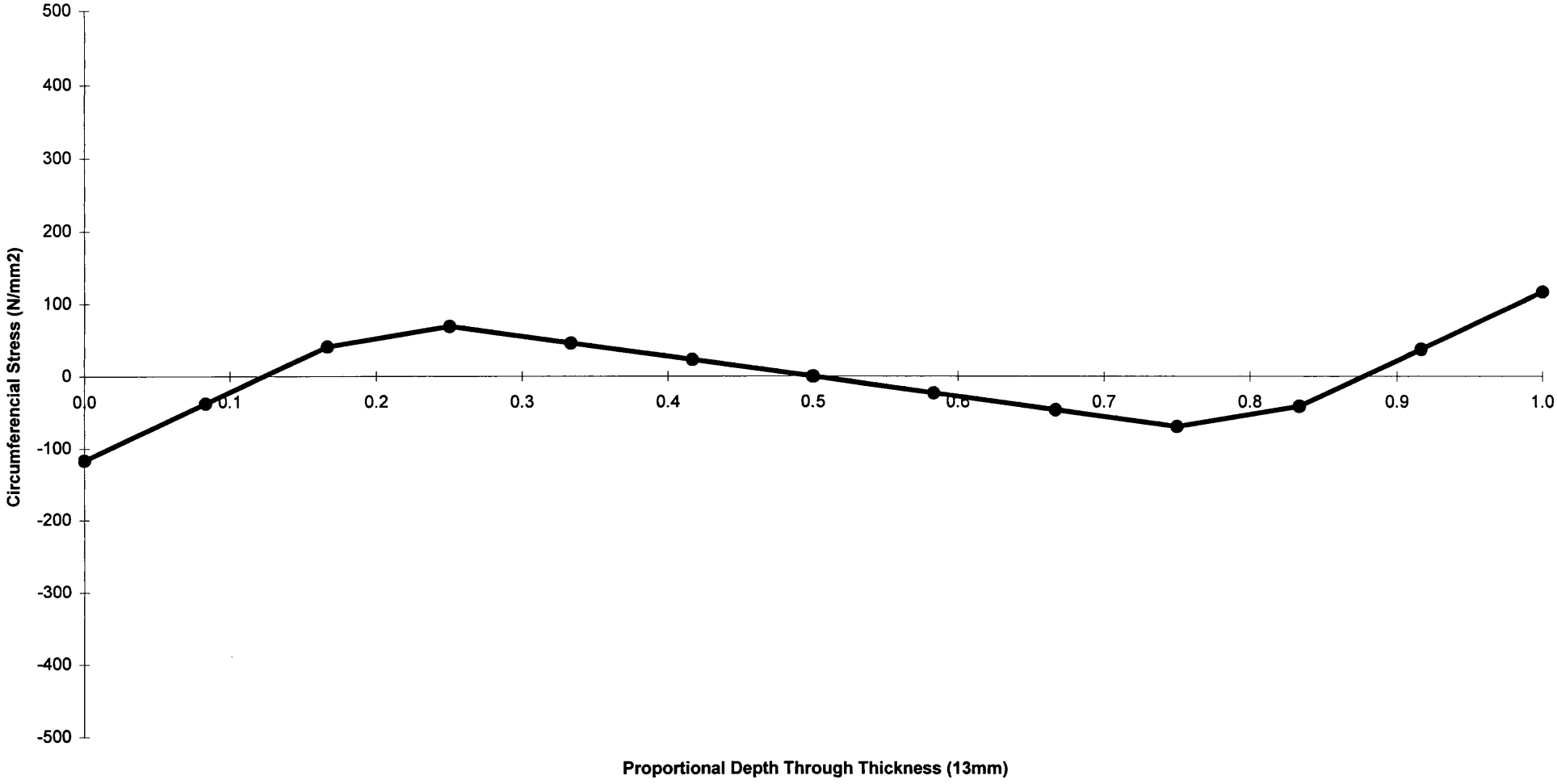


*Fig. A2.1.1.4, Model 1(ortho), spring back in cold forming, location 1 in Fig. 4.21*

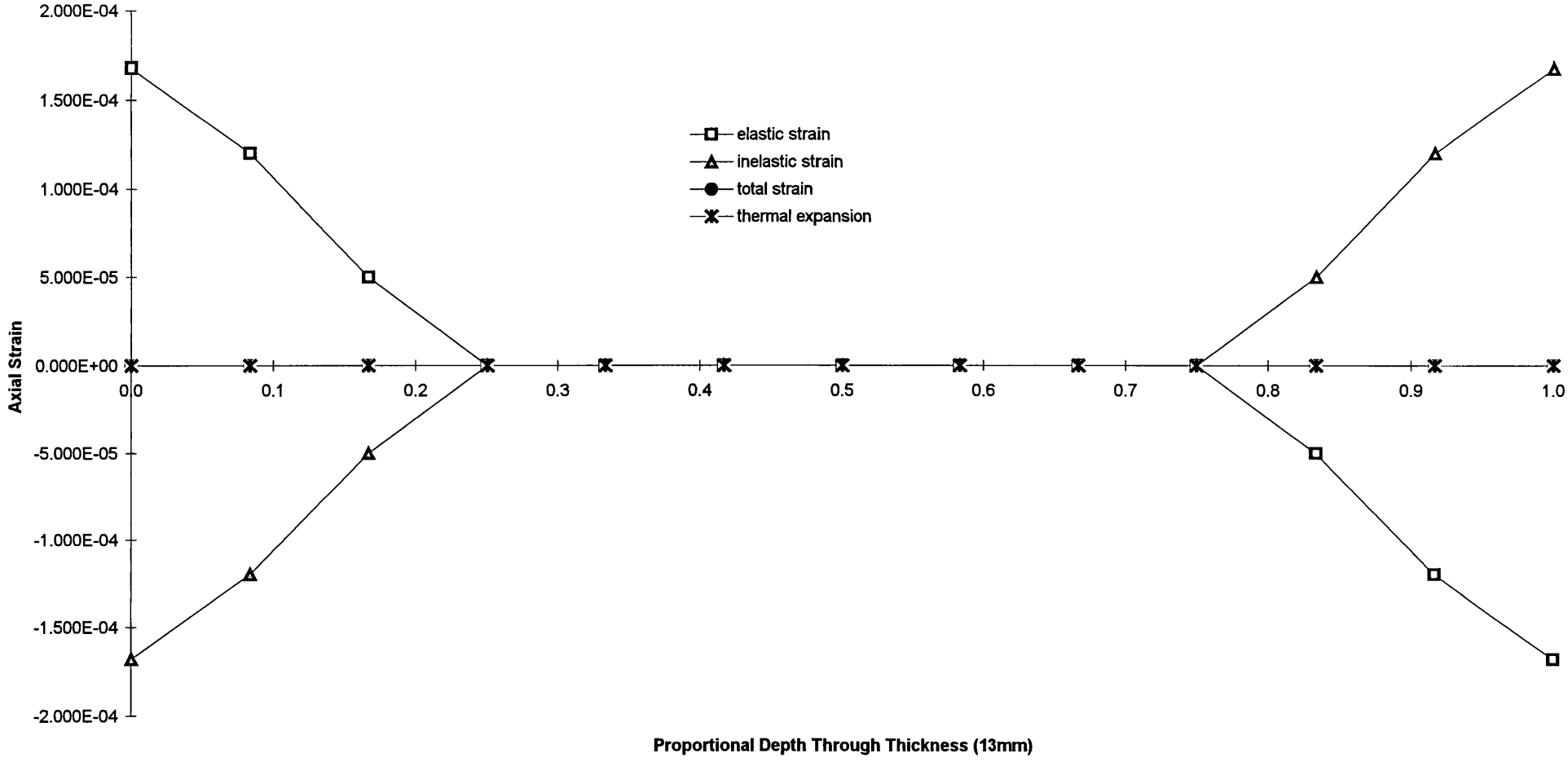


*Fig. A2.1.1.5, Model 1(ortho), bending back during cold forming simulated with thermal exoansion, location 1 in Fig.4.21*

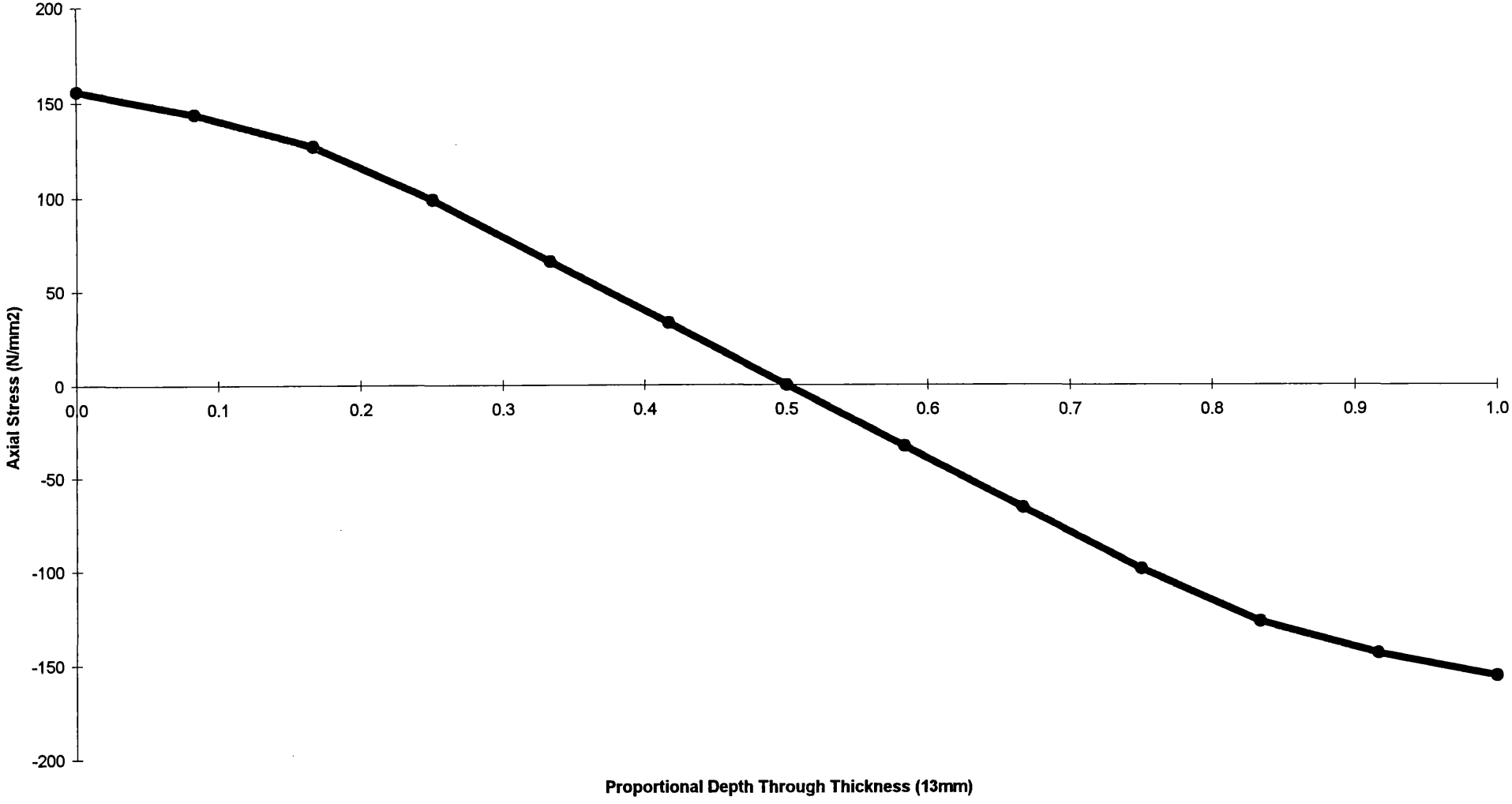


*Fig. A2.1.1.6 , Model 1(ortho), bending back during cold forming , location 1 in Fig. 4.21*

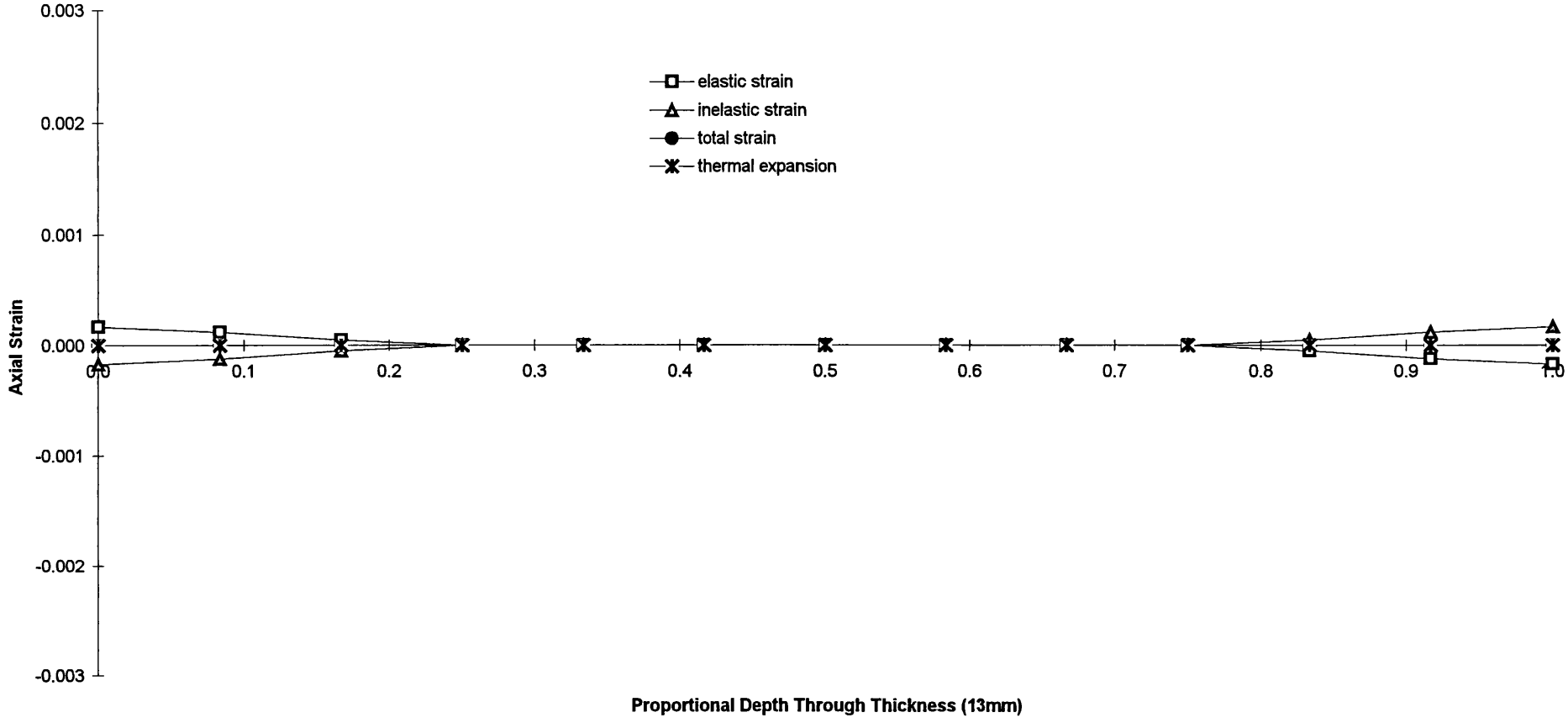


*Fig. A2.1.1.7, Model 1(ortho), spring back in cold forming simulated with thermal expansion, location 1 in Fig. 4.21*

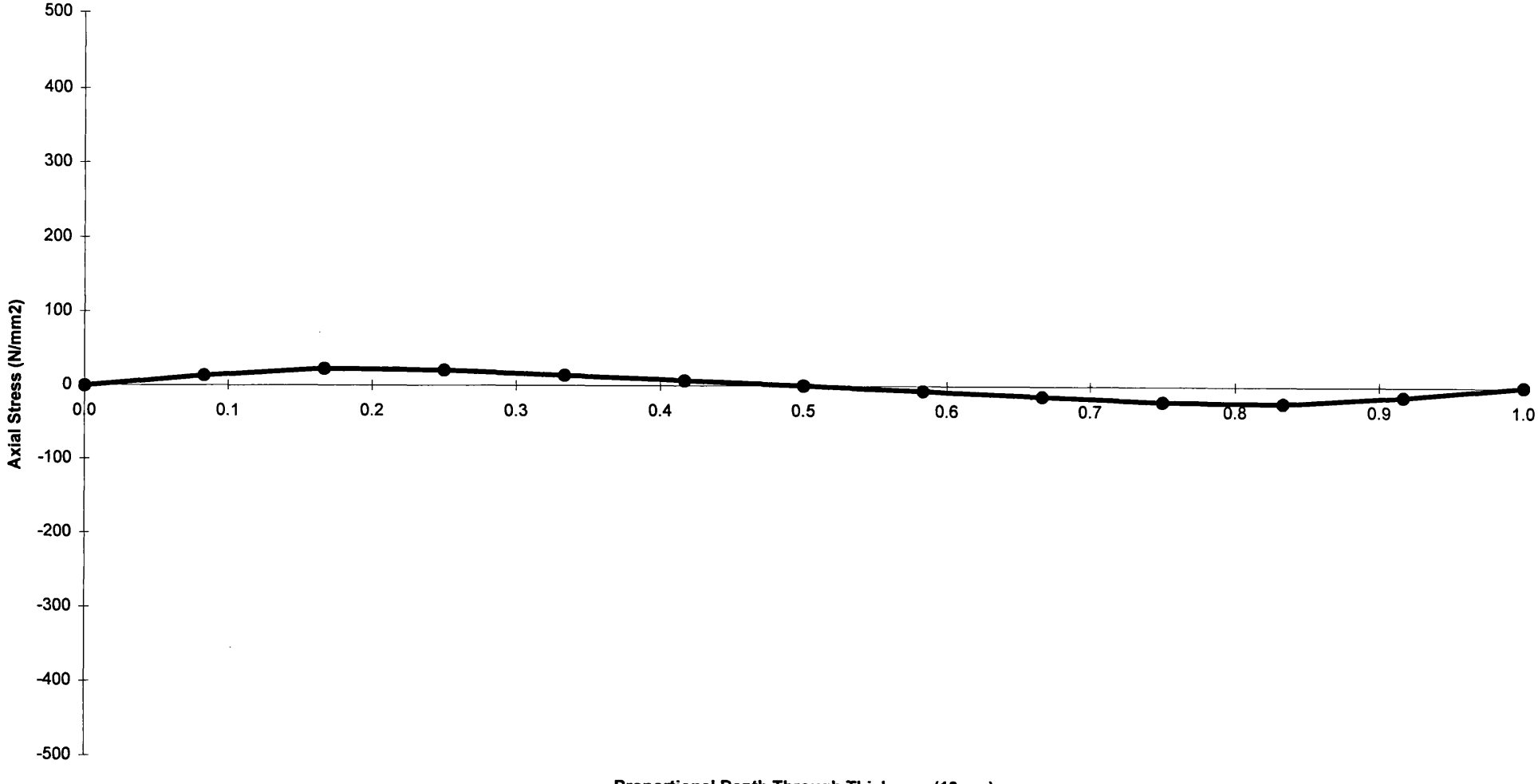


*Fig. A2.1.1.8, Model 1(ortho), spring back in cold forming, location 1 in Fig. 4.21*

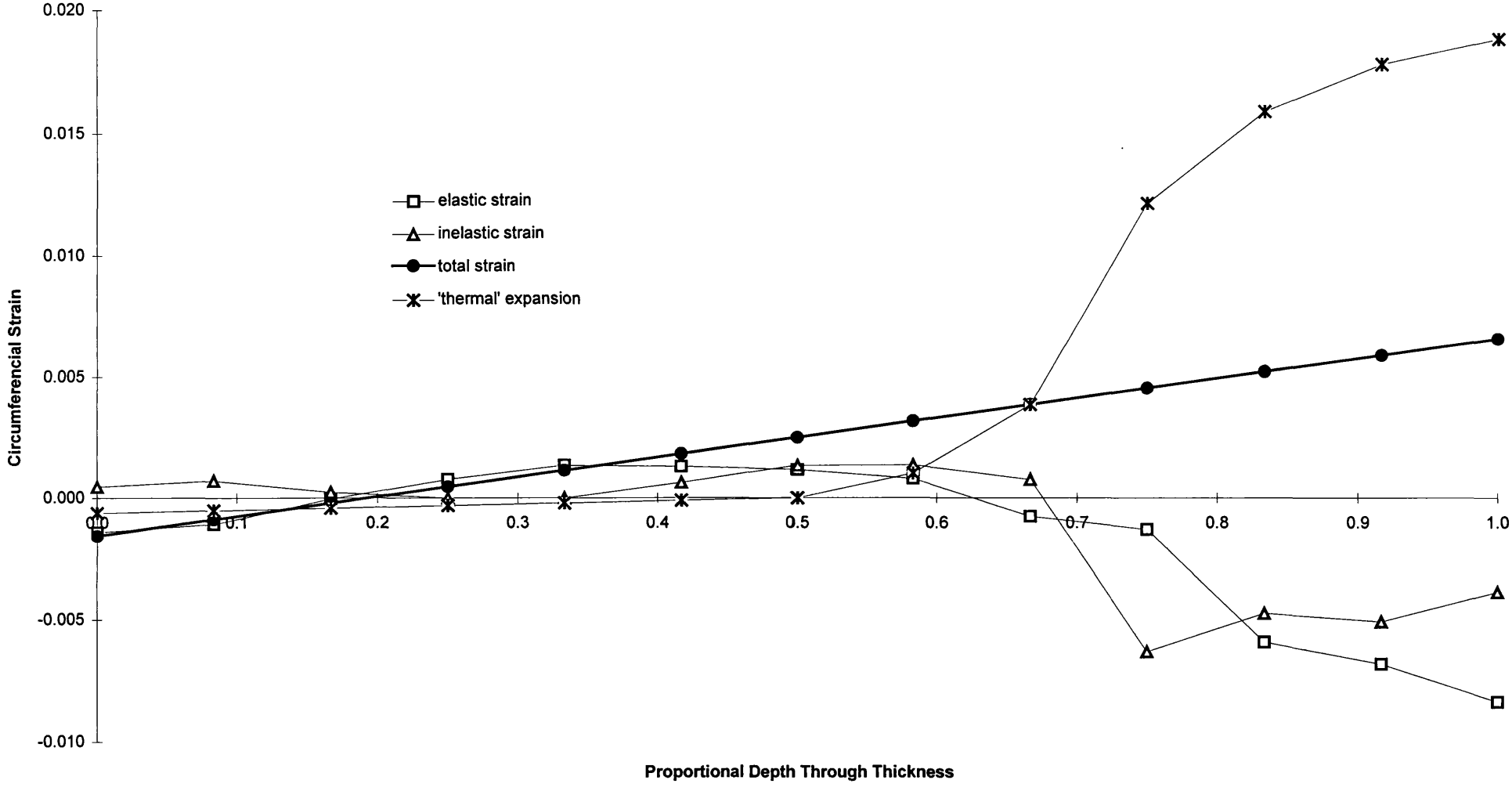


*Fig. A2.1.2.1, Model 1(ortho), thermal expansion in the welding steps, location 1 in Fig.4.21*

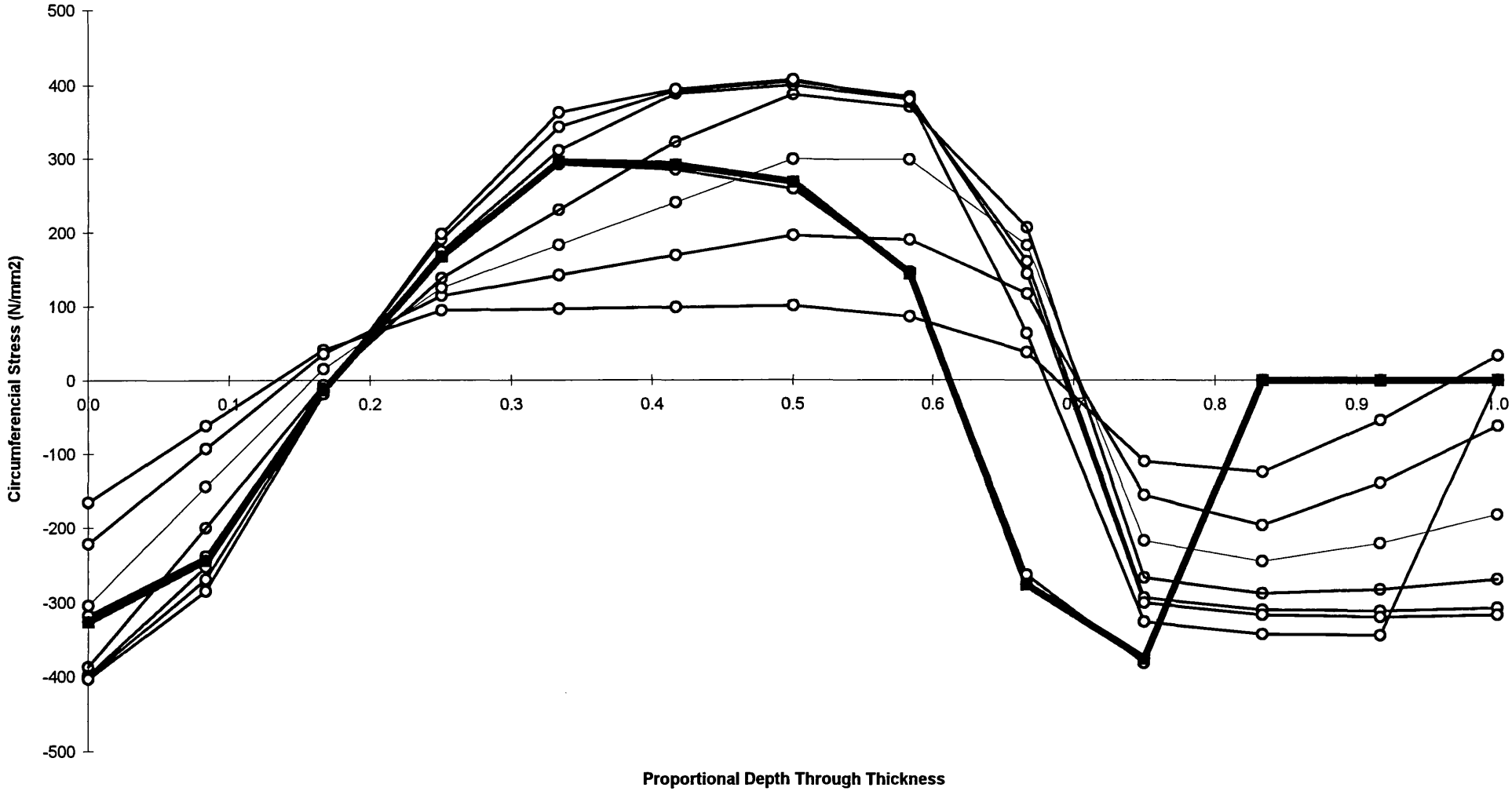


*Fig. A2.1.2.2, Model 1(ortho), thermal expansion in the welding steps, location 1 in Fig. 4.21*

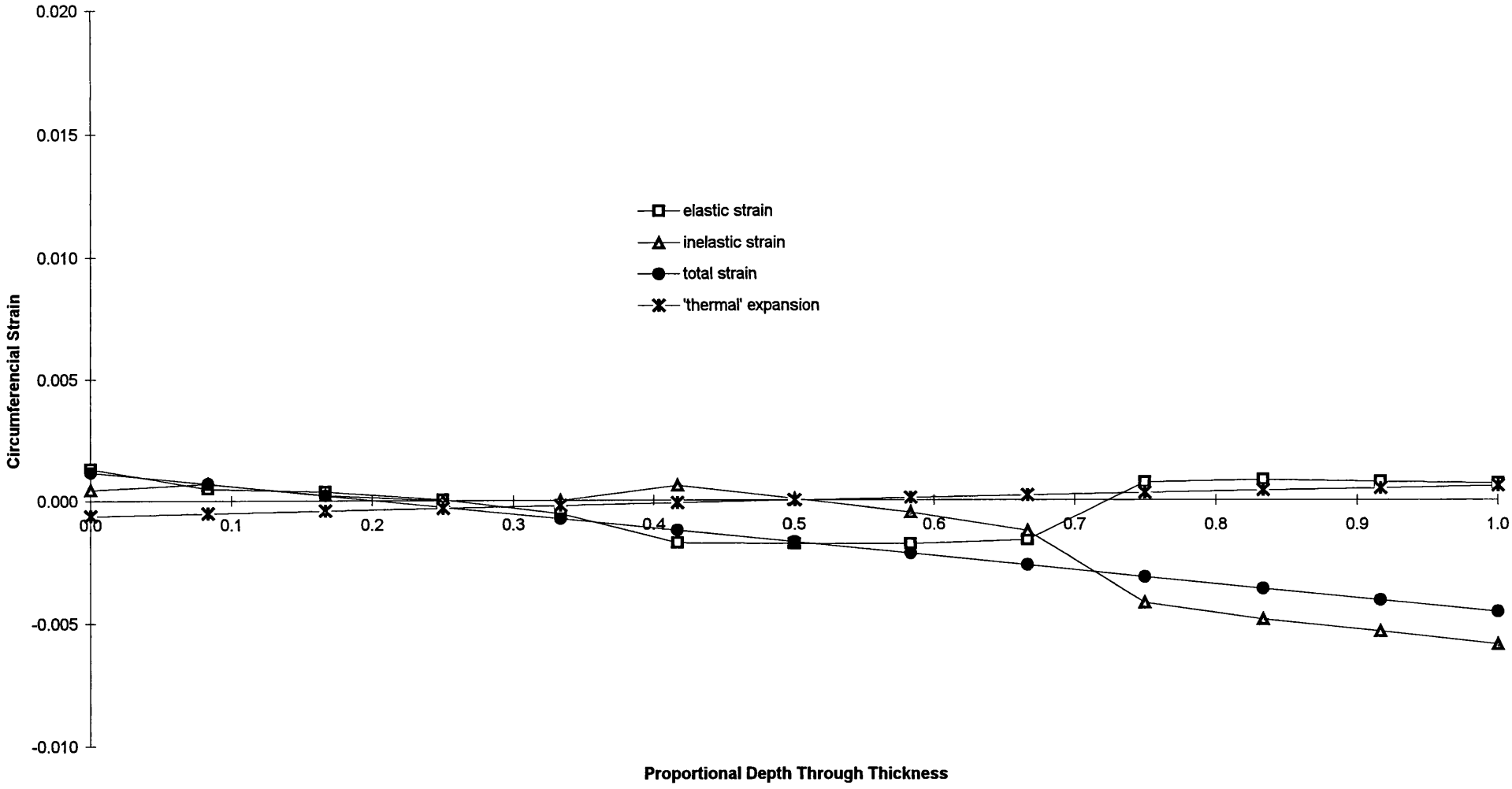


*Fig. A2.1.2.3, Model 1(ortho), thermal contraction in the welding steps, location 1 in Fig. 4.21*

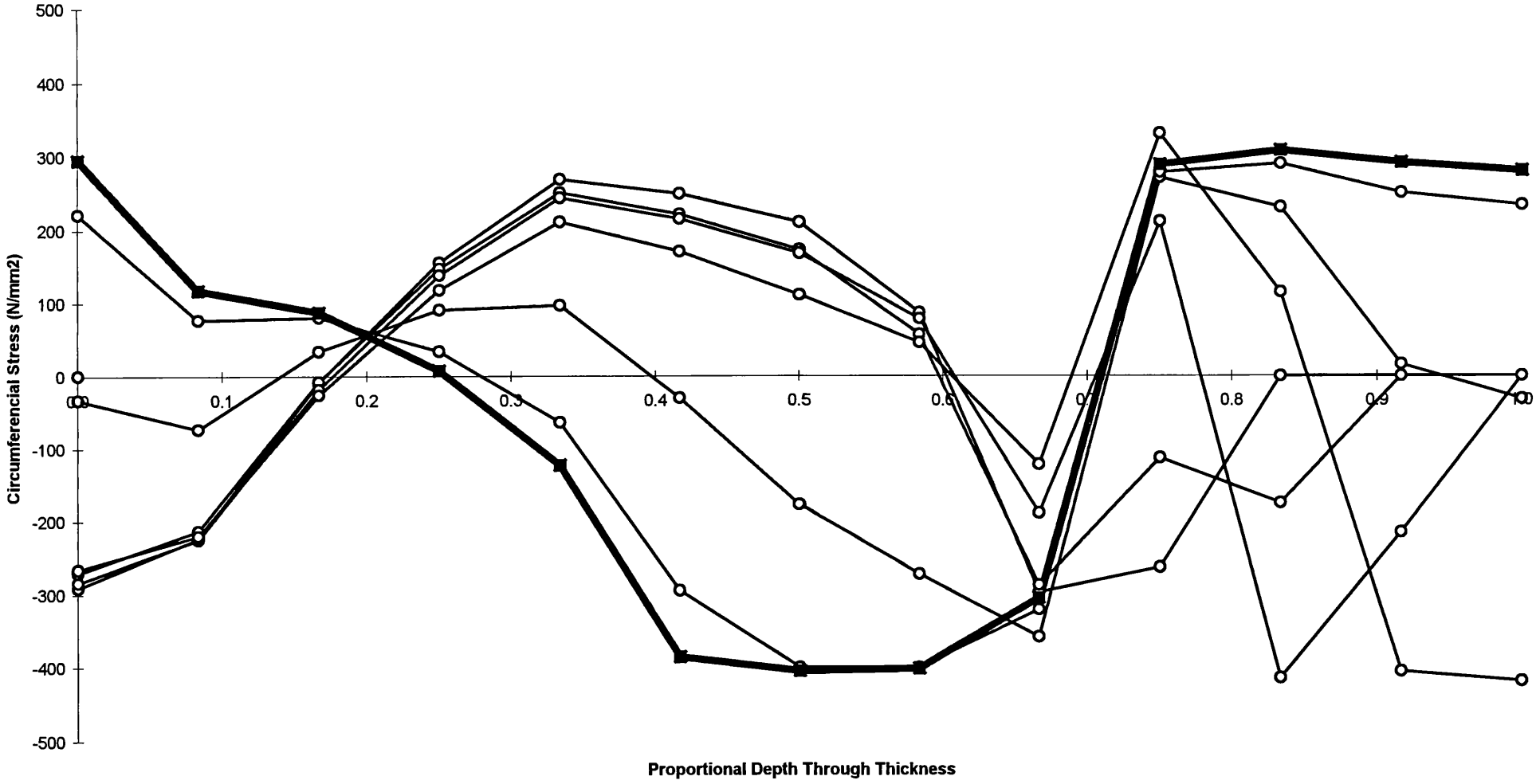


*Fig. A2.1.2.4, Model 1(ortho), thermal contraction in the welding steps, location 1 in Fig. 4.21*

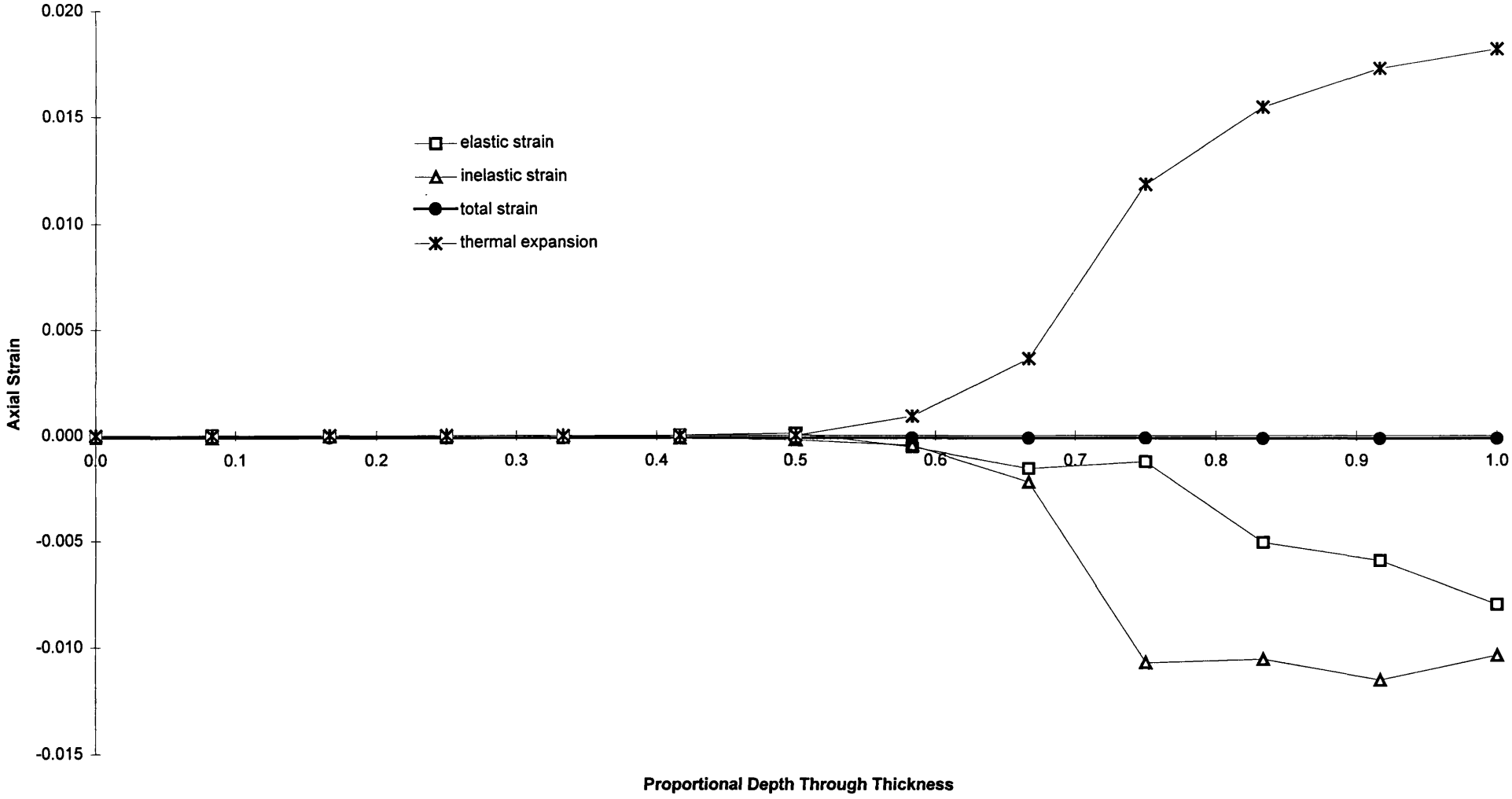


*Fig. A2.1.2.5, Model 1(ortho), thermal expansion in the welding steps, location 1 in Fig.4.21*

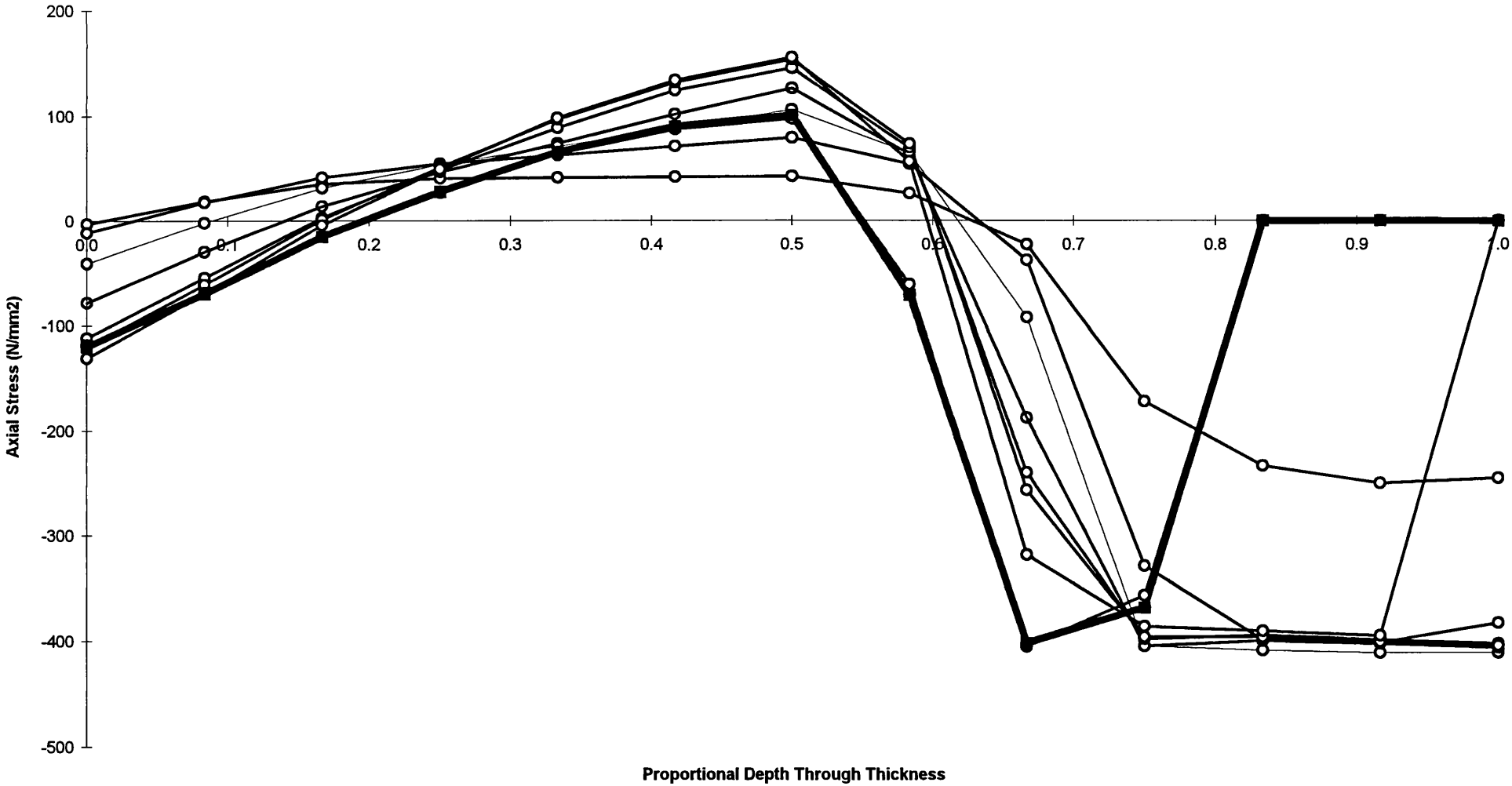


*Fig. A2.1.2.6, Model 1(ortho), thermal expansion in the welding steps, location 1 in Fig. 4.21*

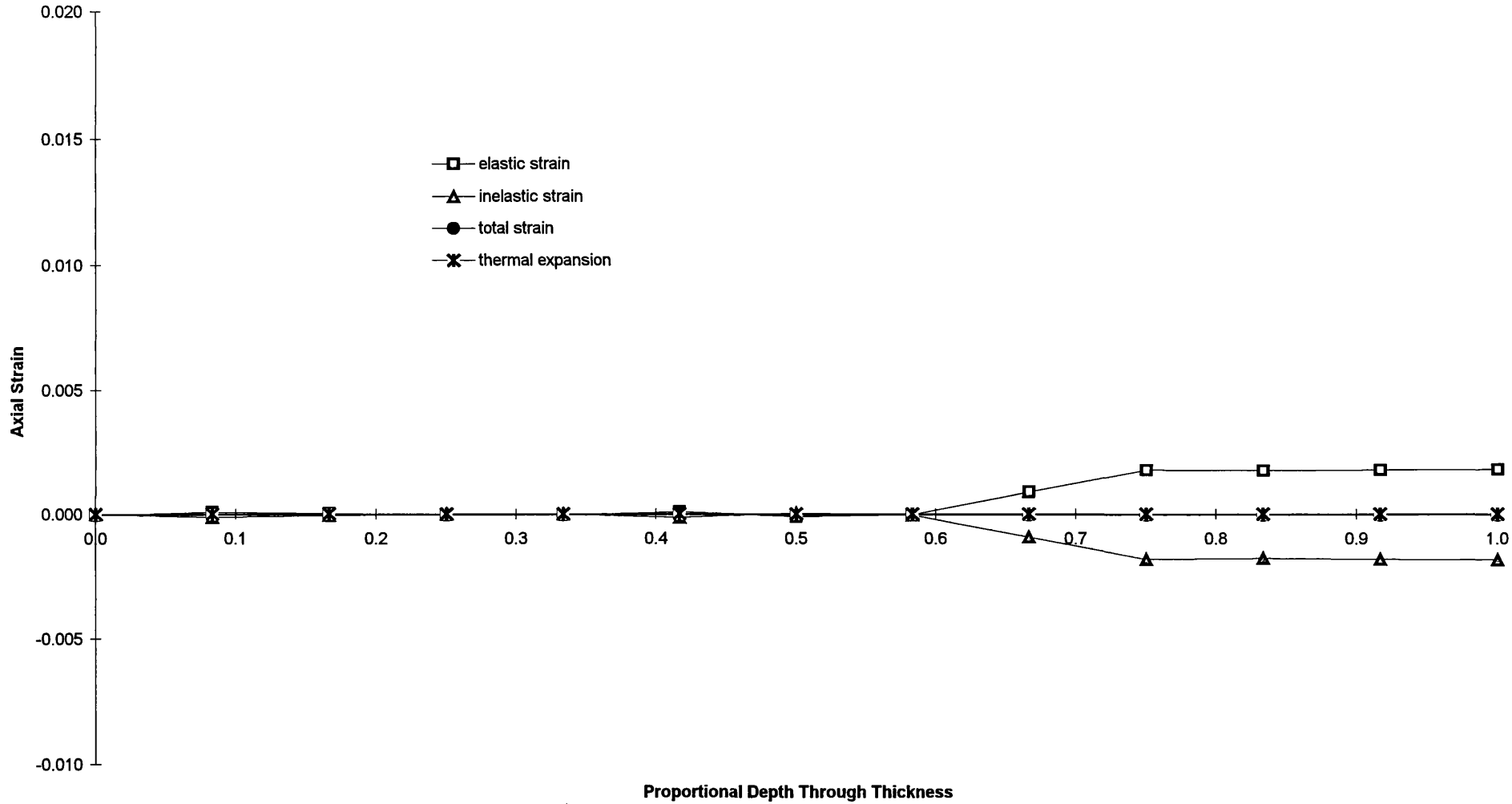


*Fig. A2.1.2.7, Model 1(ortho), thermal contraction in the welding steps, location 1 in Fig. 4.21*

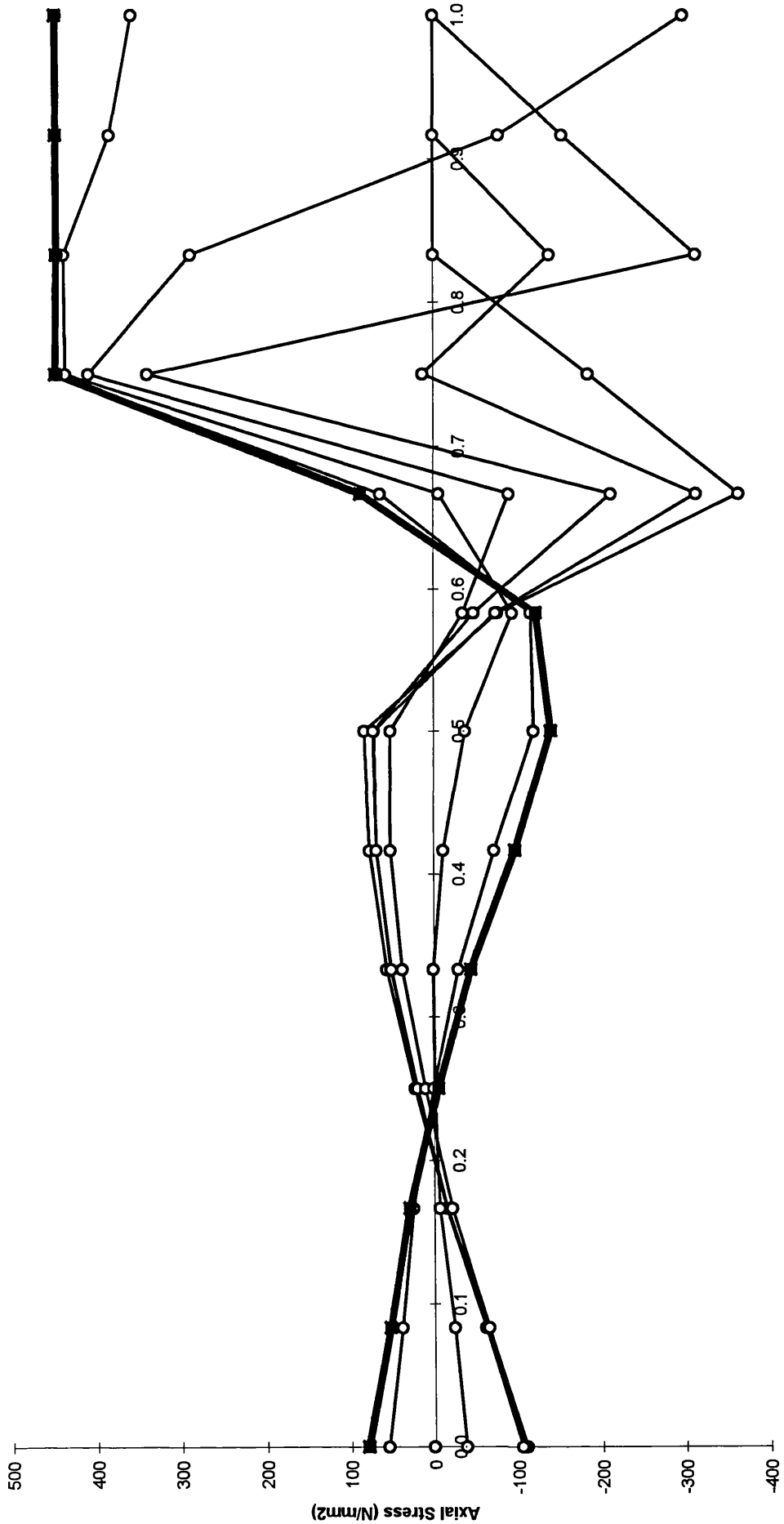


*Fig. A2.1.2.8, Model 1(ortho), thermal contraction in the welding steps, location 1 in Fig. 4.21*

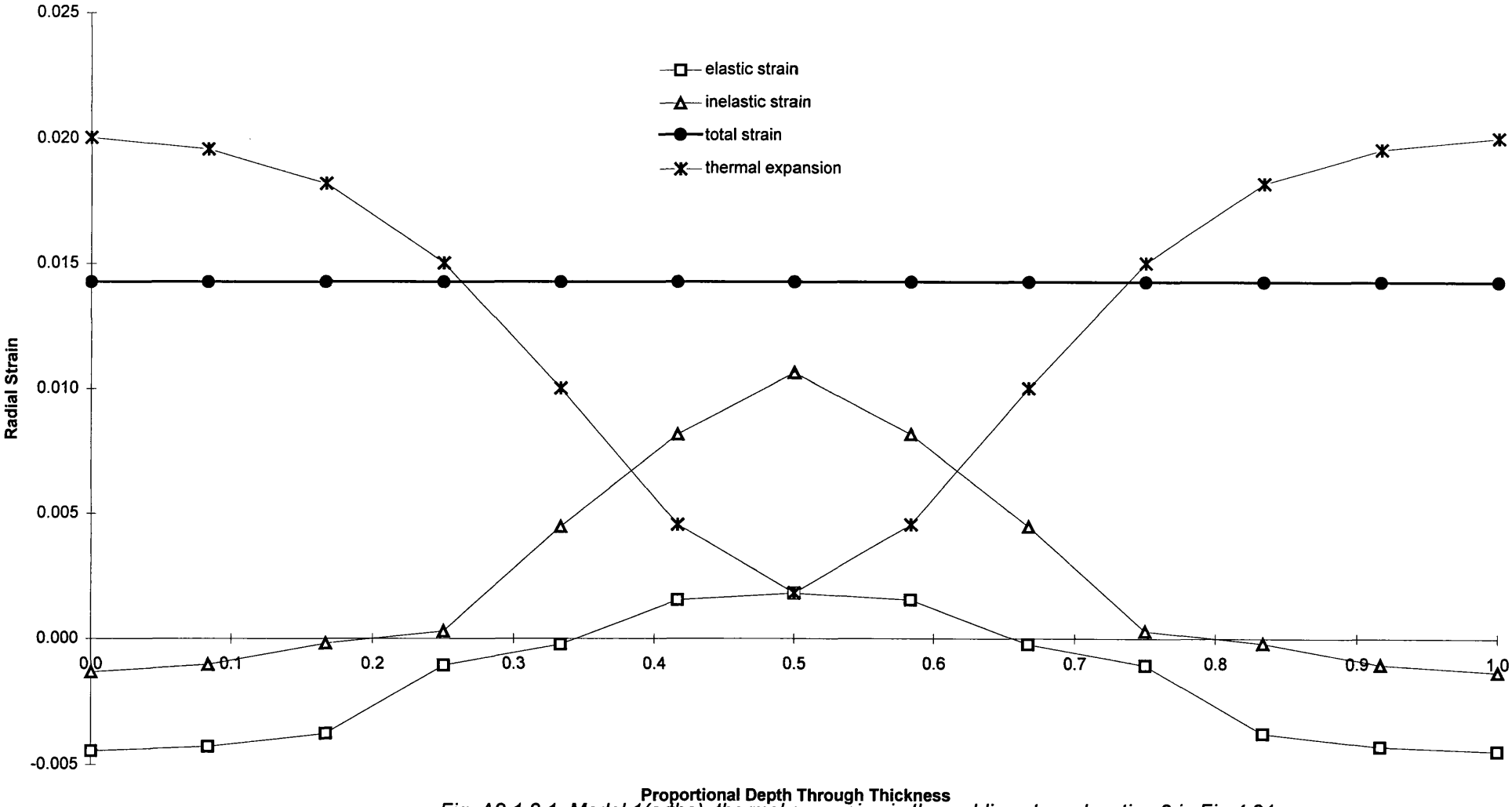


*Fig. A2.1.3.1, Model 1(ortho), thermal expansion in the welding steps, location 2 in Fig.4.21*

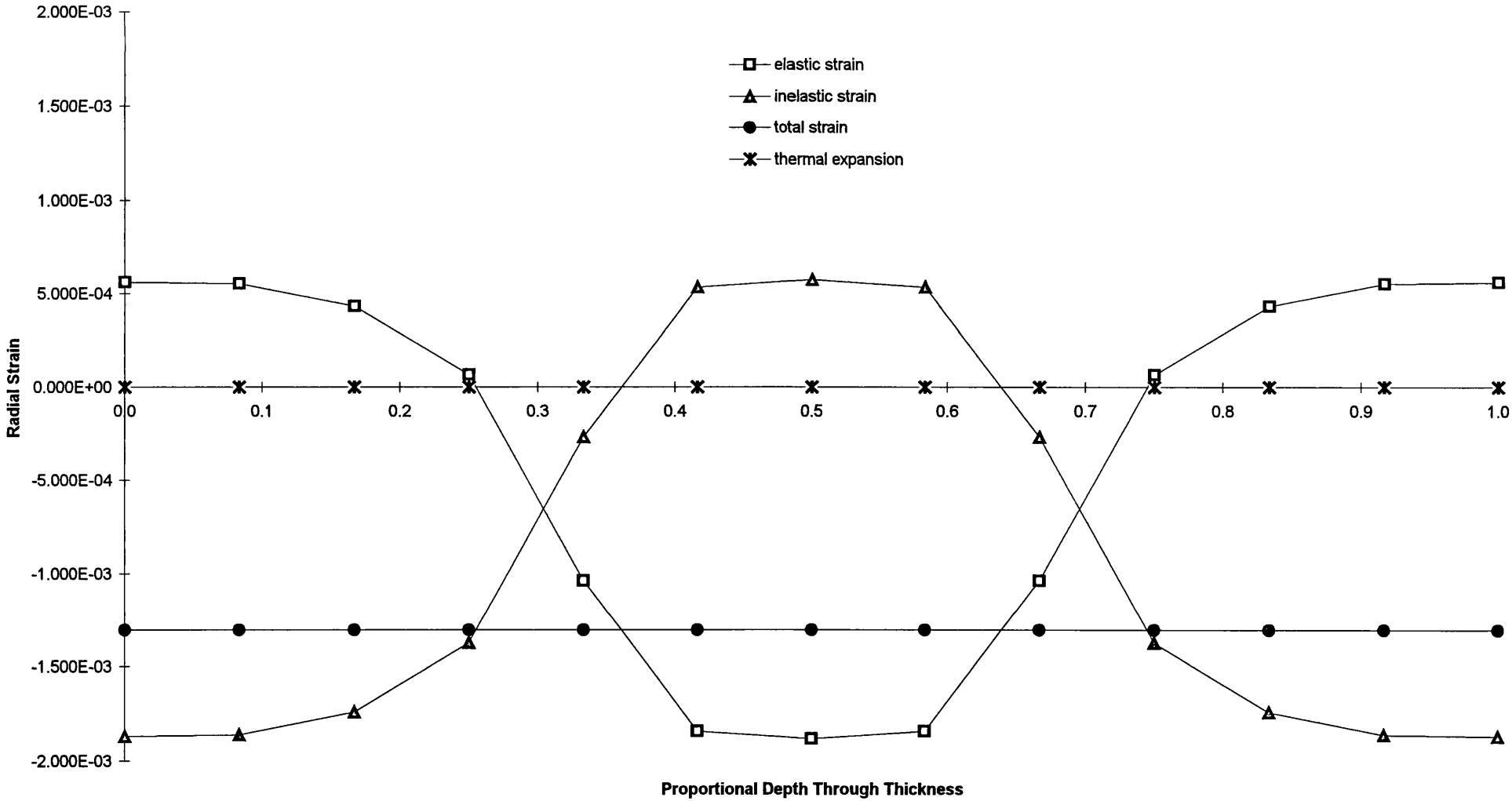


*Fig. A2.1.3.3, Model 1(ortho), thermal contraction in the welding steps, location 2 in Fig. 4.21*

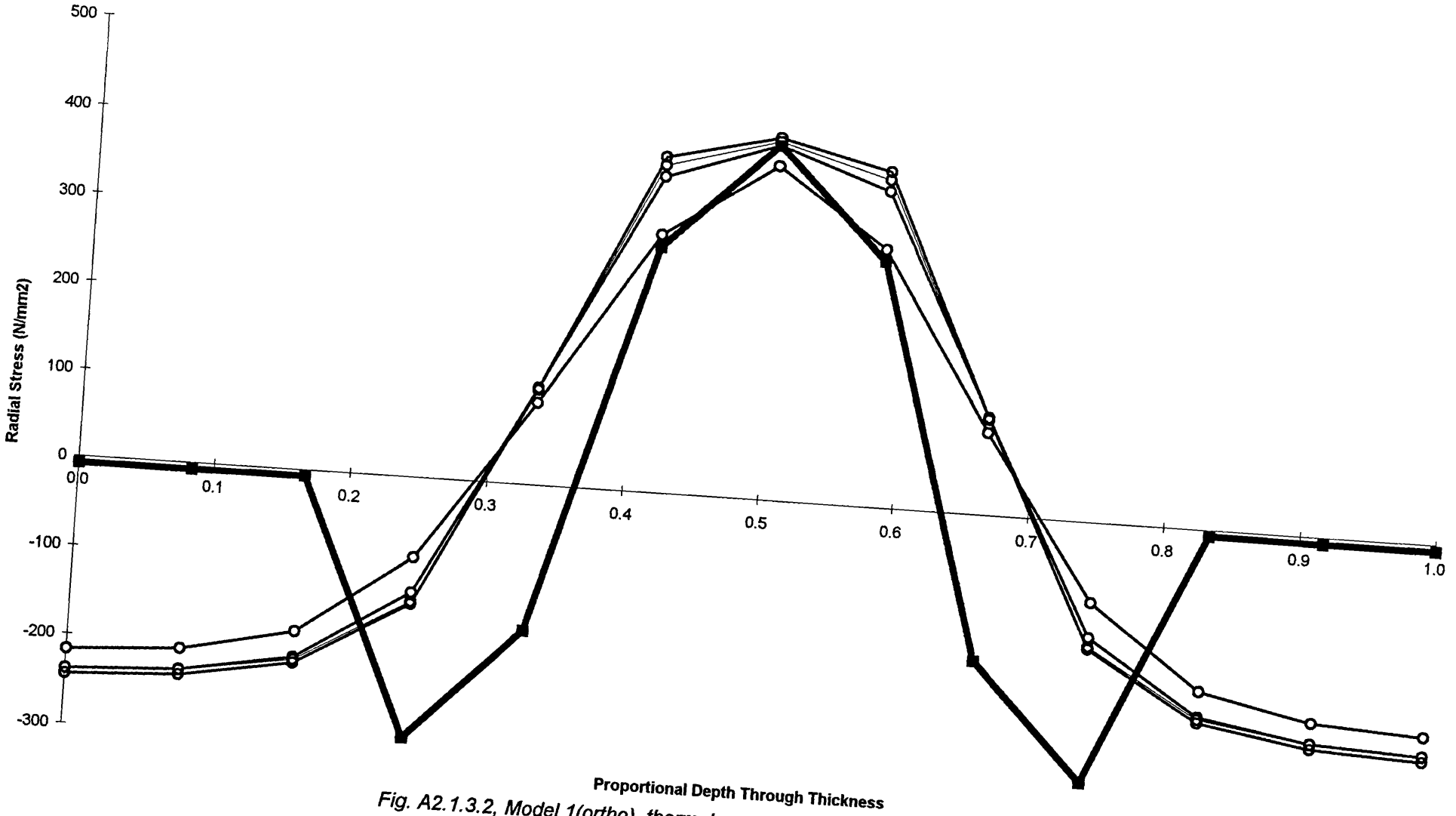


*Fig. A2.1.3.2, Model 1(ortho), thermal expansion in the welding steps, location 2 in Fig. 4.21*

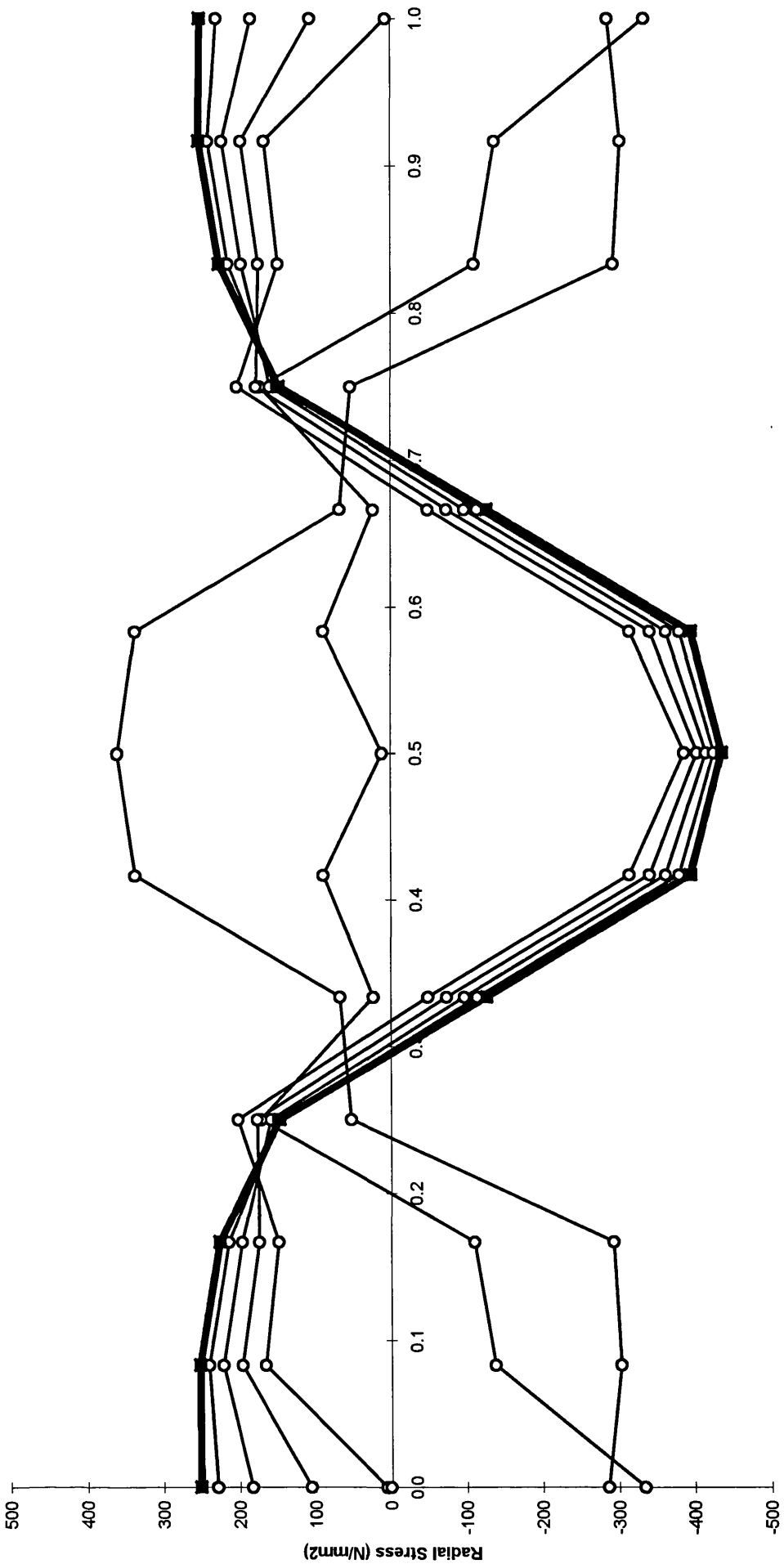


*Fig. A2.1.3.4, Model 1(ortho), thermal contraction in the welding steps, location 2 in Fig. 4.21*

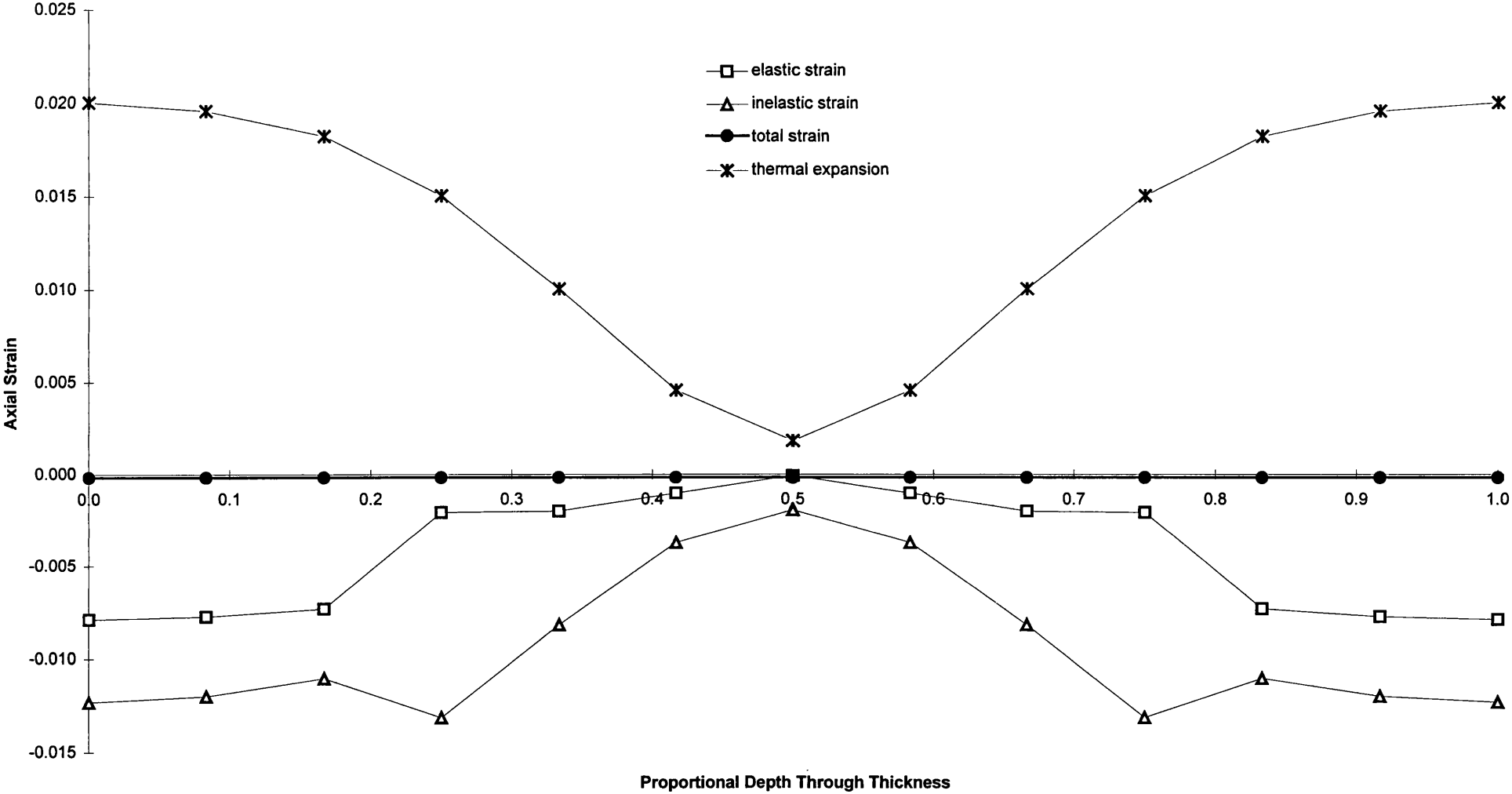


*Fig. A2.1.3.5, Model 1(ortho), thermal expansion in the welding steps, location 2 in Fig.4.21*

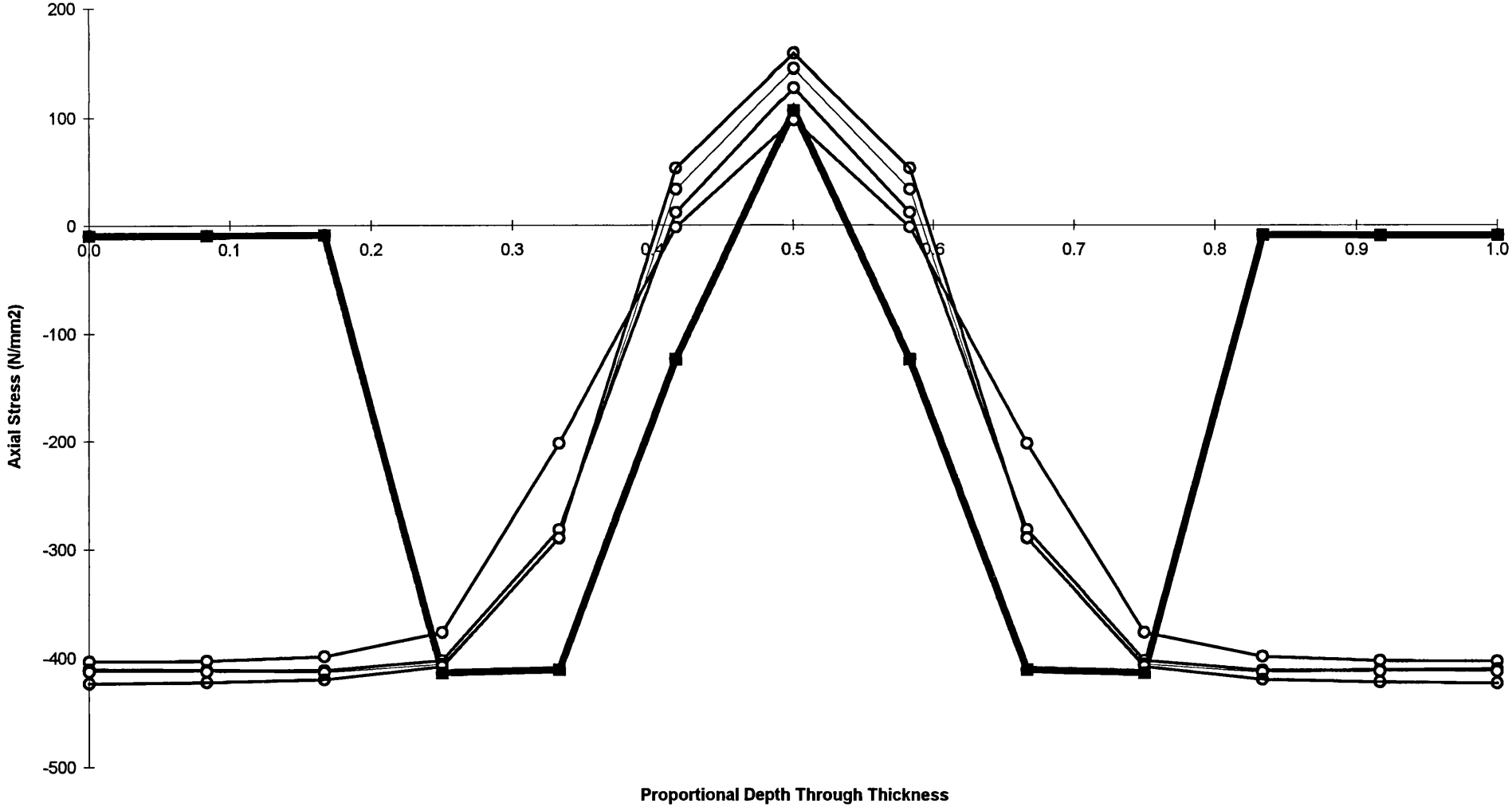


*Fig. A2.1.3.6, Model 1(ortho), thermal expansion in the welding steps, location 2 in Fig. 4.21*

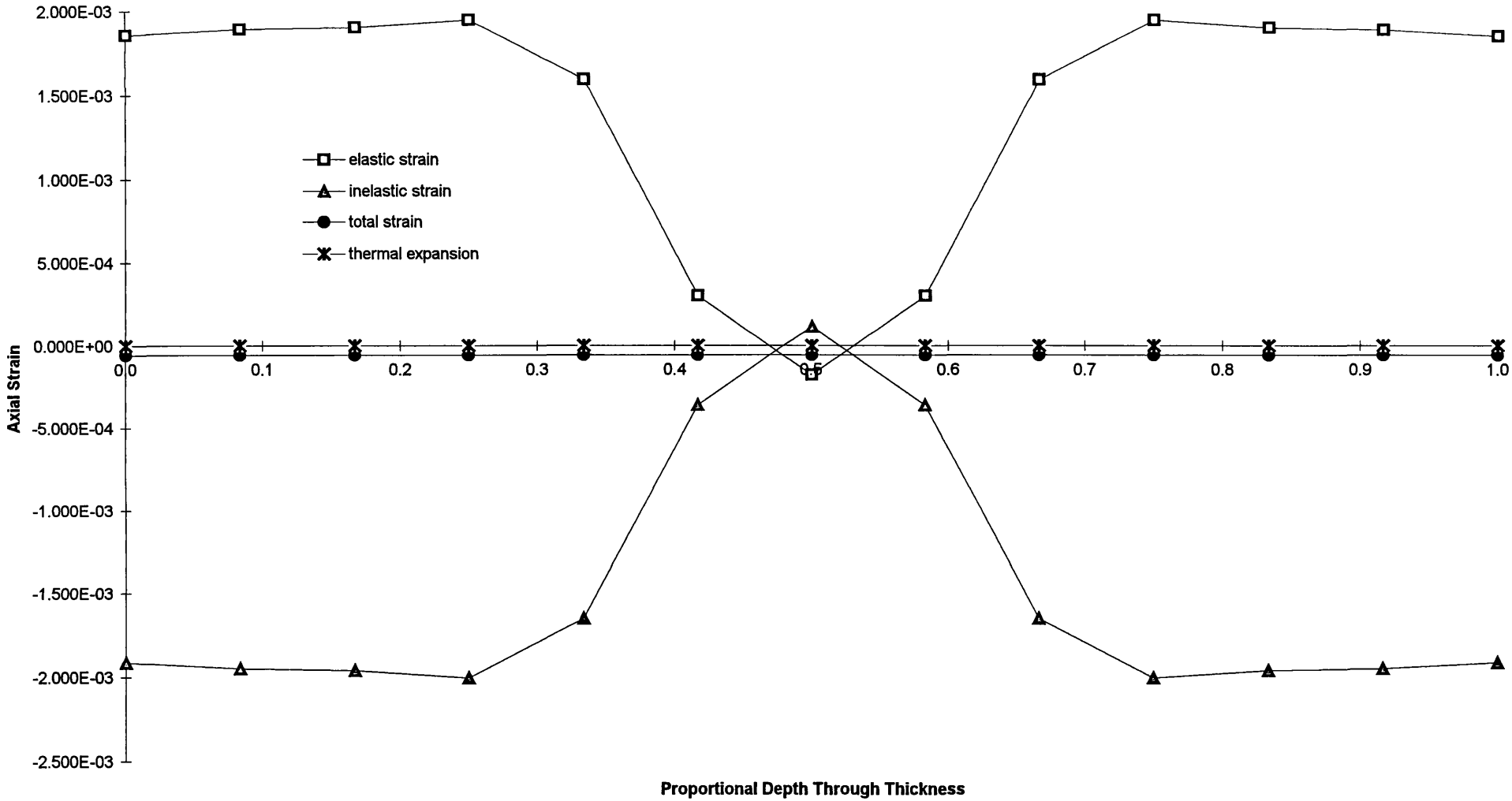


*Fig. A2.1.3.7, Model 1(ortho), thermal contraction in the welding steps, location 2 in Fig. 4.21*

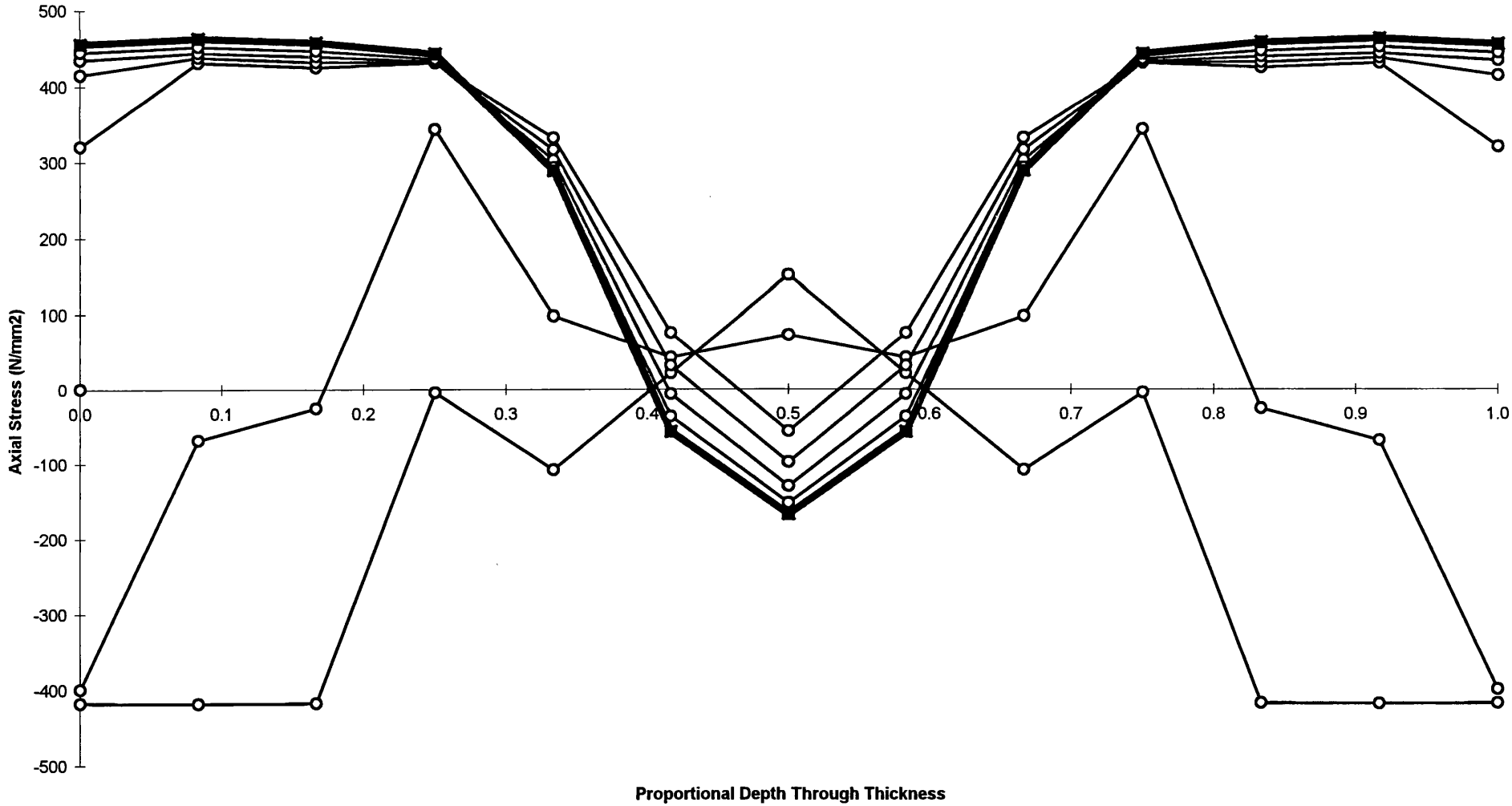


*Fig. A2.1.3.8, Model 1(ortho), thermal contraction in the welding steps, location 2 in Fig. 4.21*

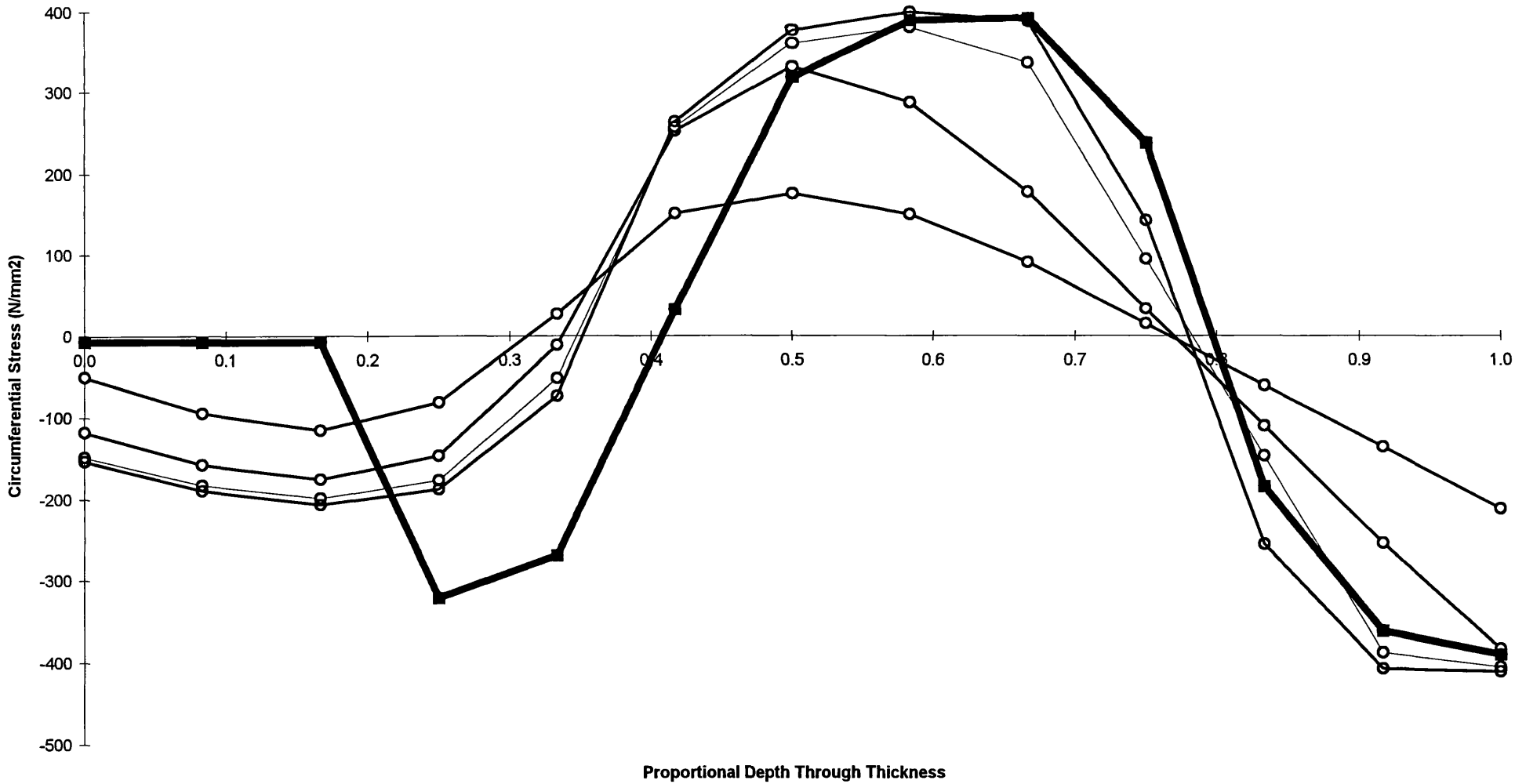


*Fig. A2.1.4.2, Model 1(ortho), thermal expansion in the welding steps, location 3 in Fig. 4.21*

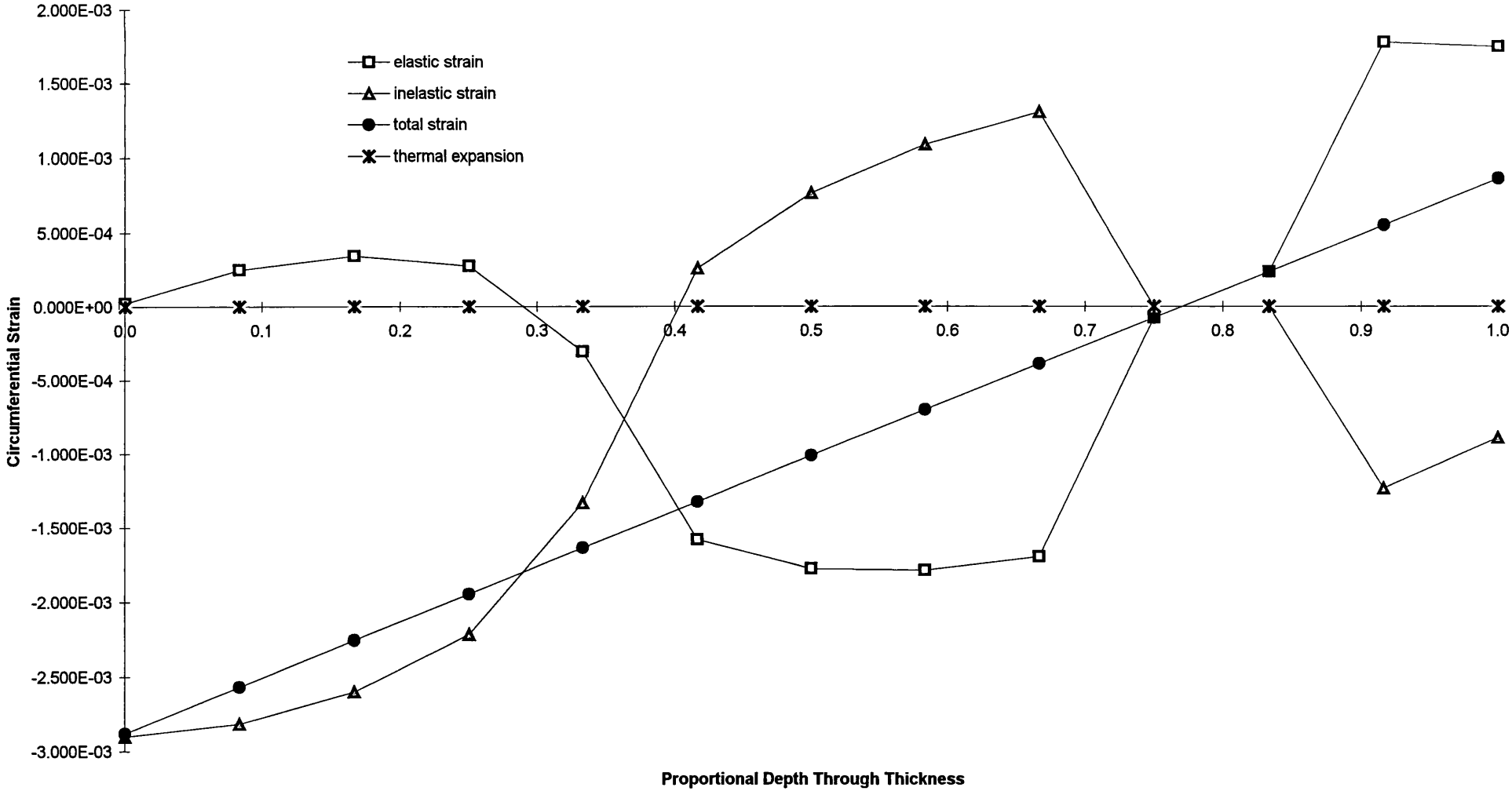


*Fig. A2.1.4.3, Model 1(ortho), thermal contraction in the welding steps, location 3 in Fig. 4.21*

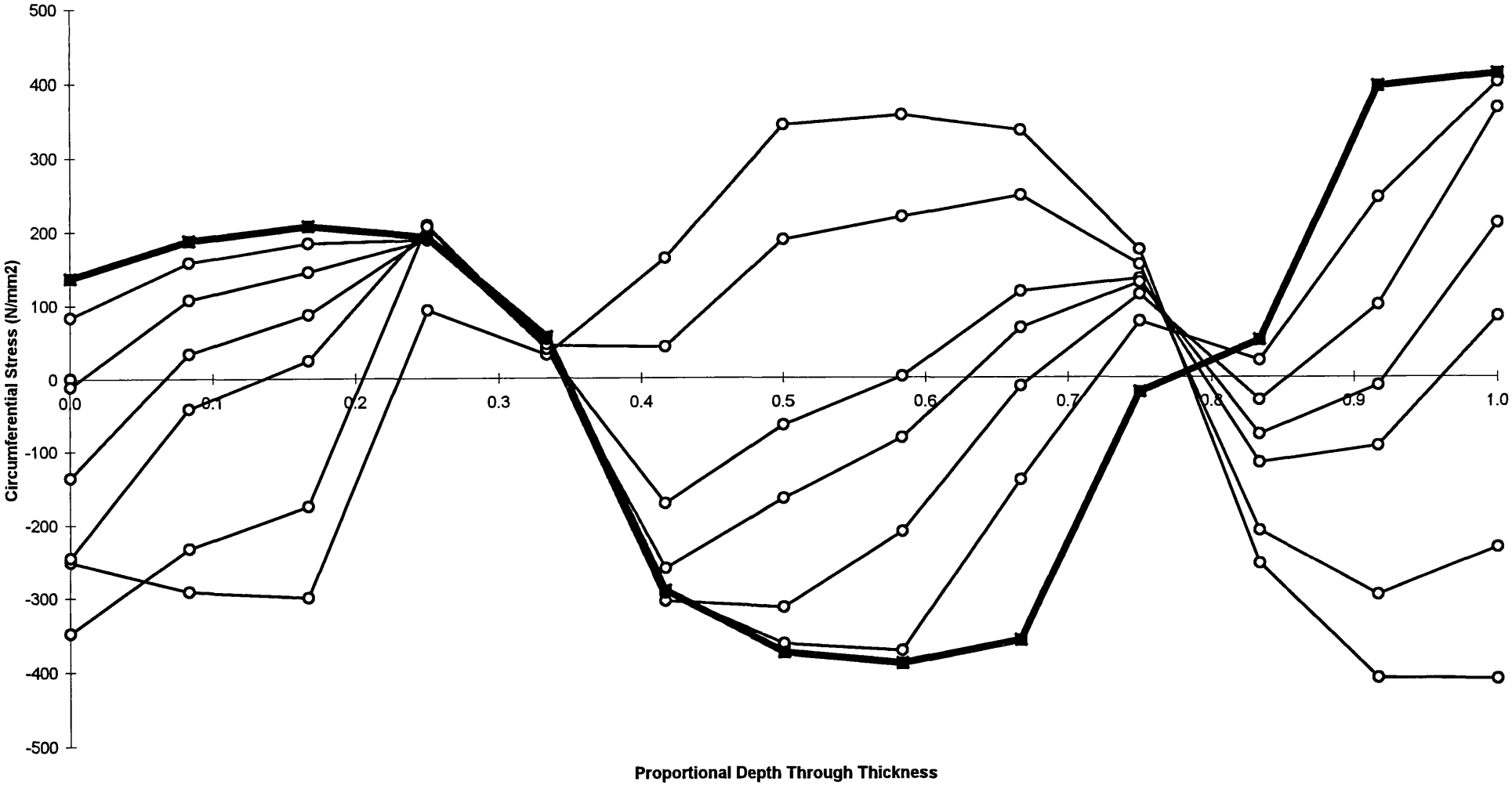


*Fig. A2.1.4.4, Model 1(ortho), thermal contraction in the welding steps, location 3 in Fig. 4.21*

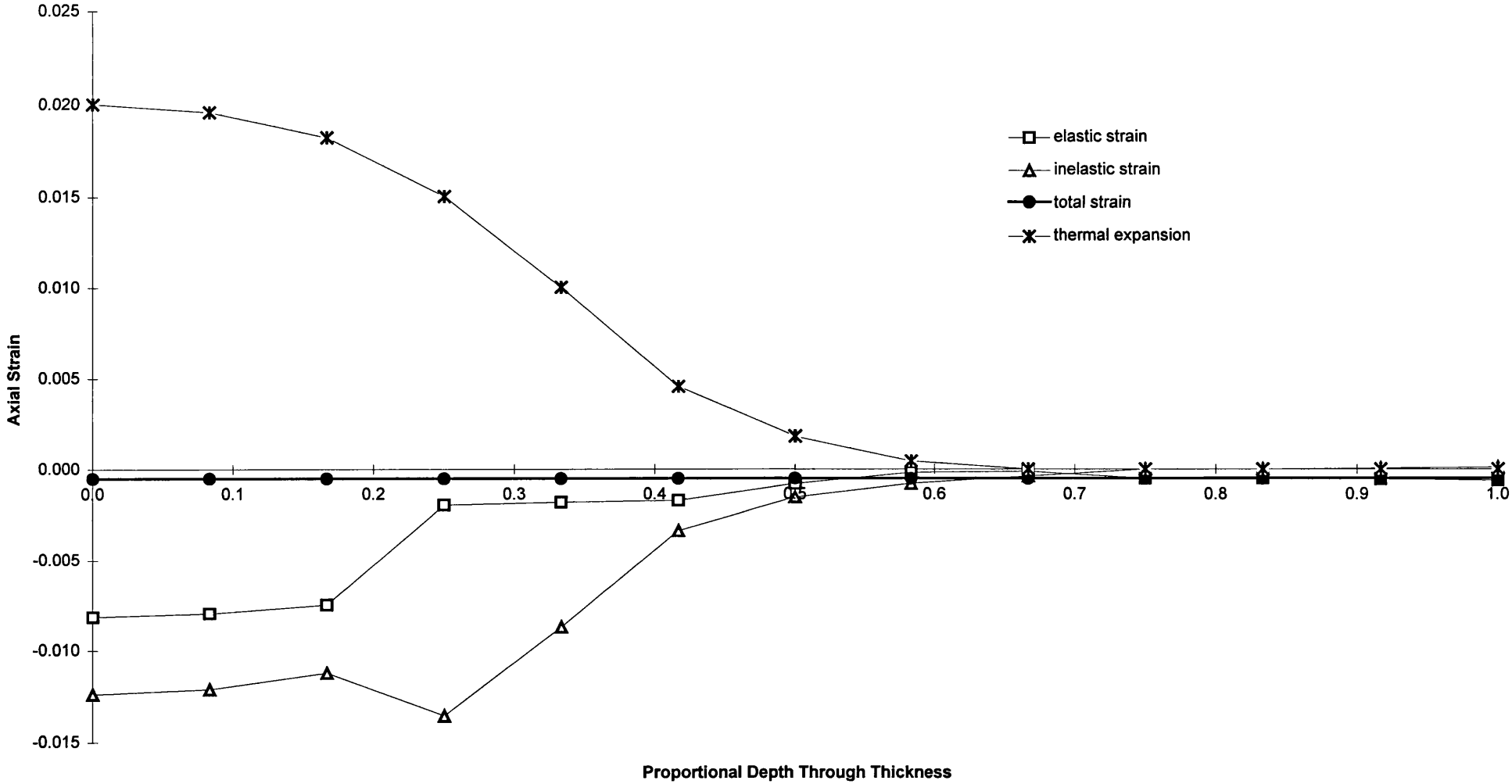


*Fig. A2.1.4.5, Model 1(ortho), thermal expansion in the welding steps, location 3 in Fig.4.21*

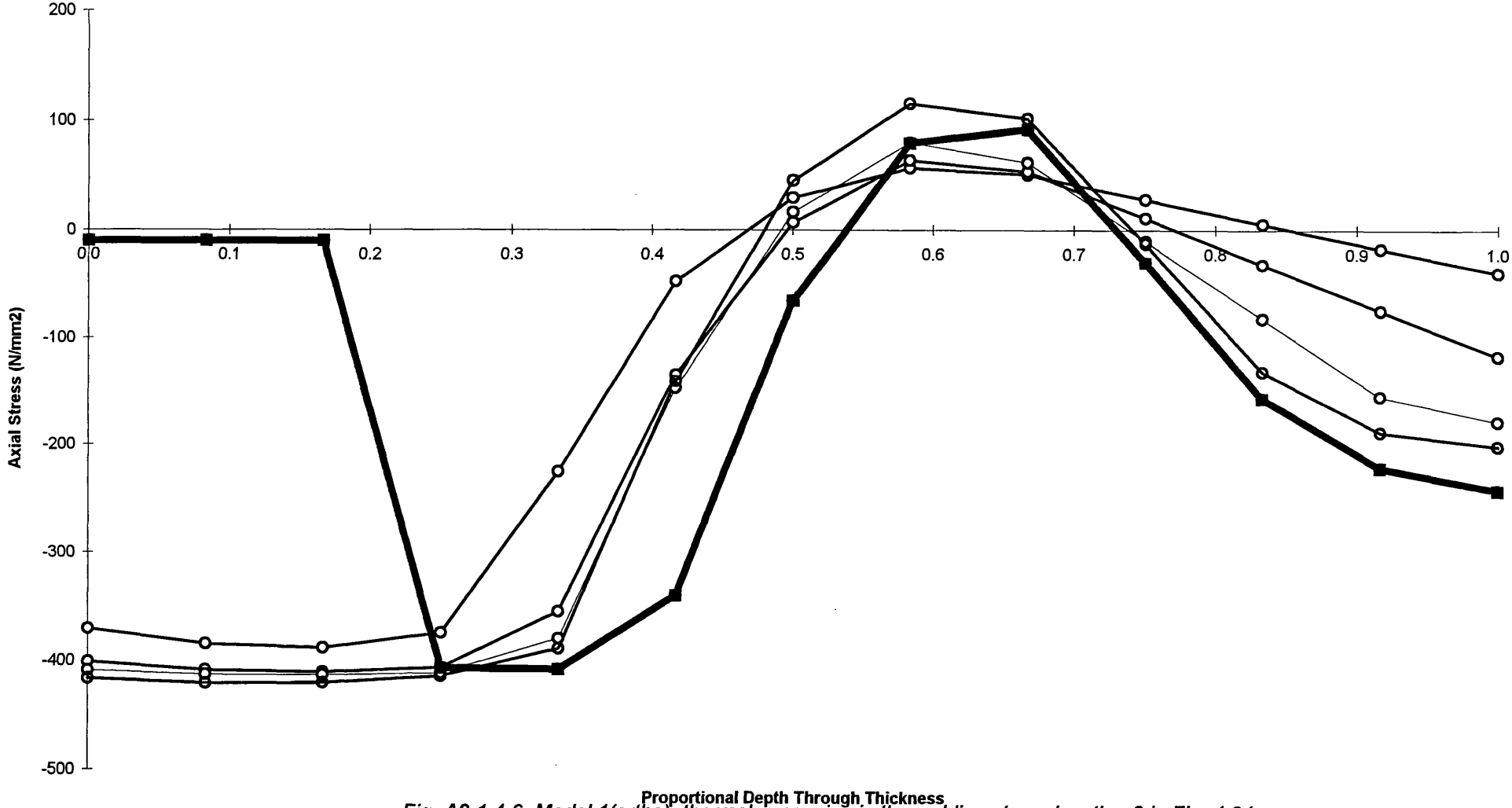


*Fig. A2.1.4.6, Model 1(ortho), thermal expansion in the welding steps, location 3 in Fig. 4.21*

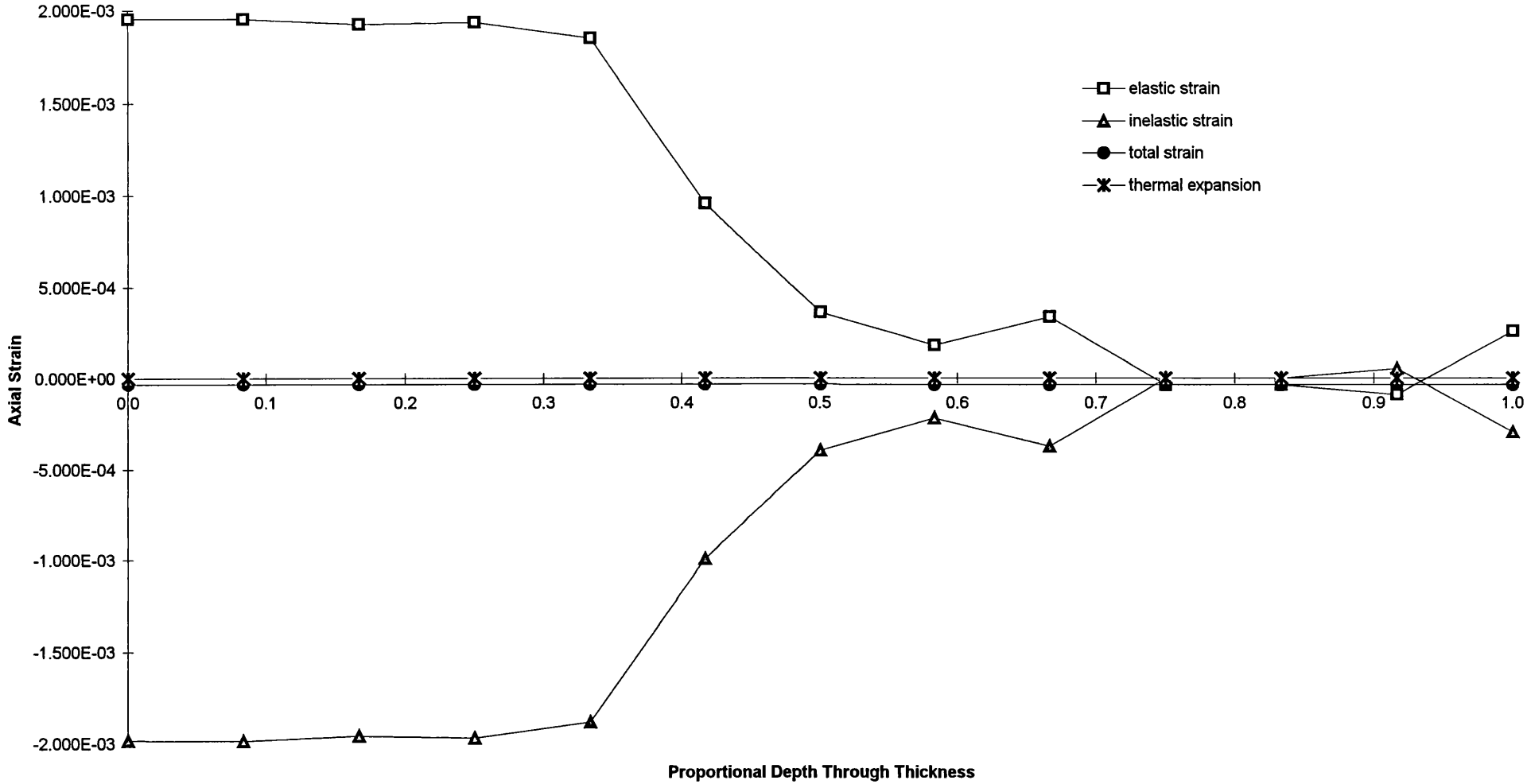


*Fig. A2.1.4.7, Model 1(ortho), thermal contraction in the welding steps, location 3 in Fig. 4.21*

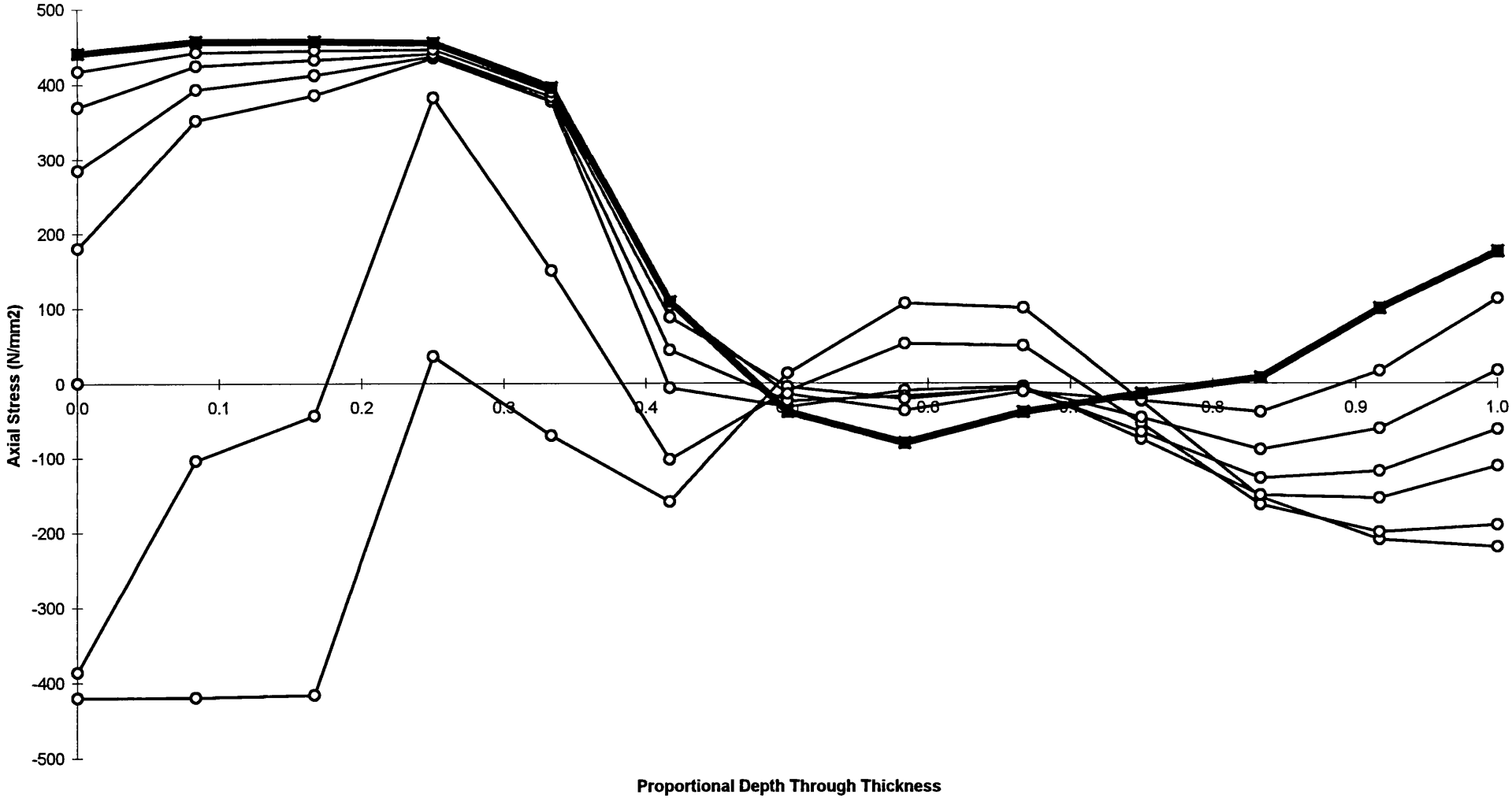


*Fig. A2.1.4.8, Model 1(ortho), thermal contraction in the welding steps, location 3 in Fig. 4.21*

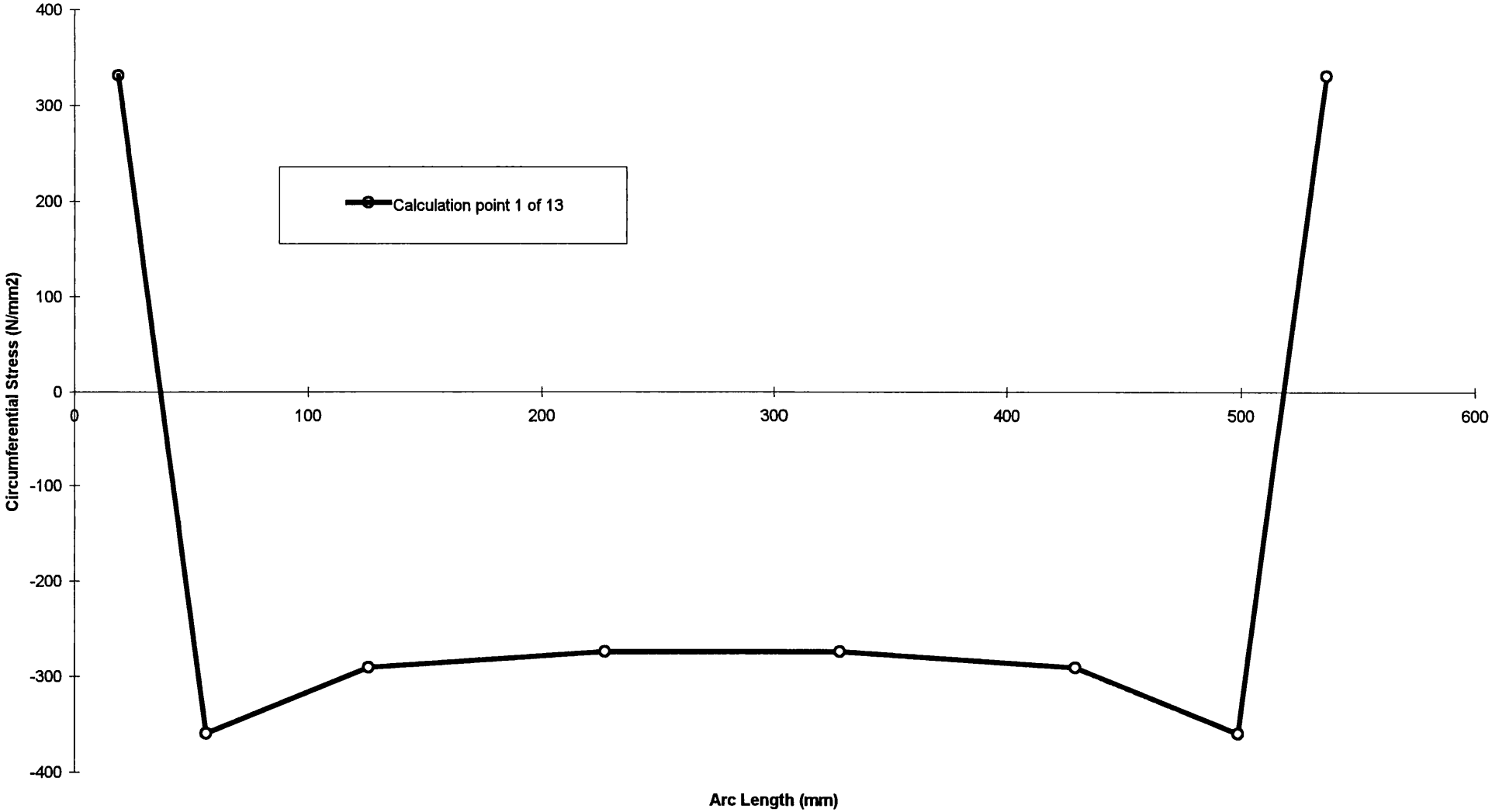


*Fig. A2.1.5.1, Model 1(ortho), Inter frame circumferential residual stress.*

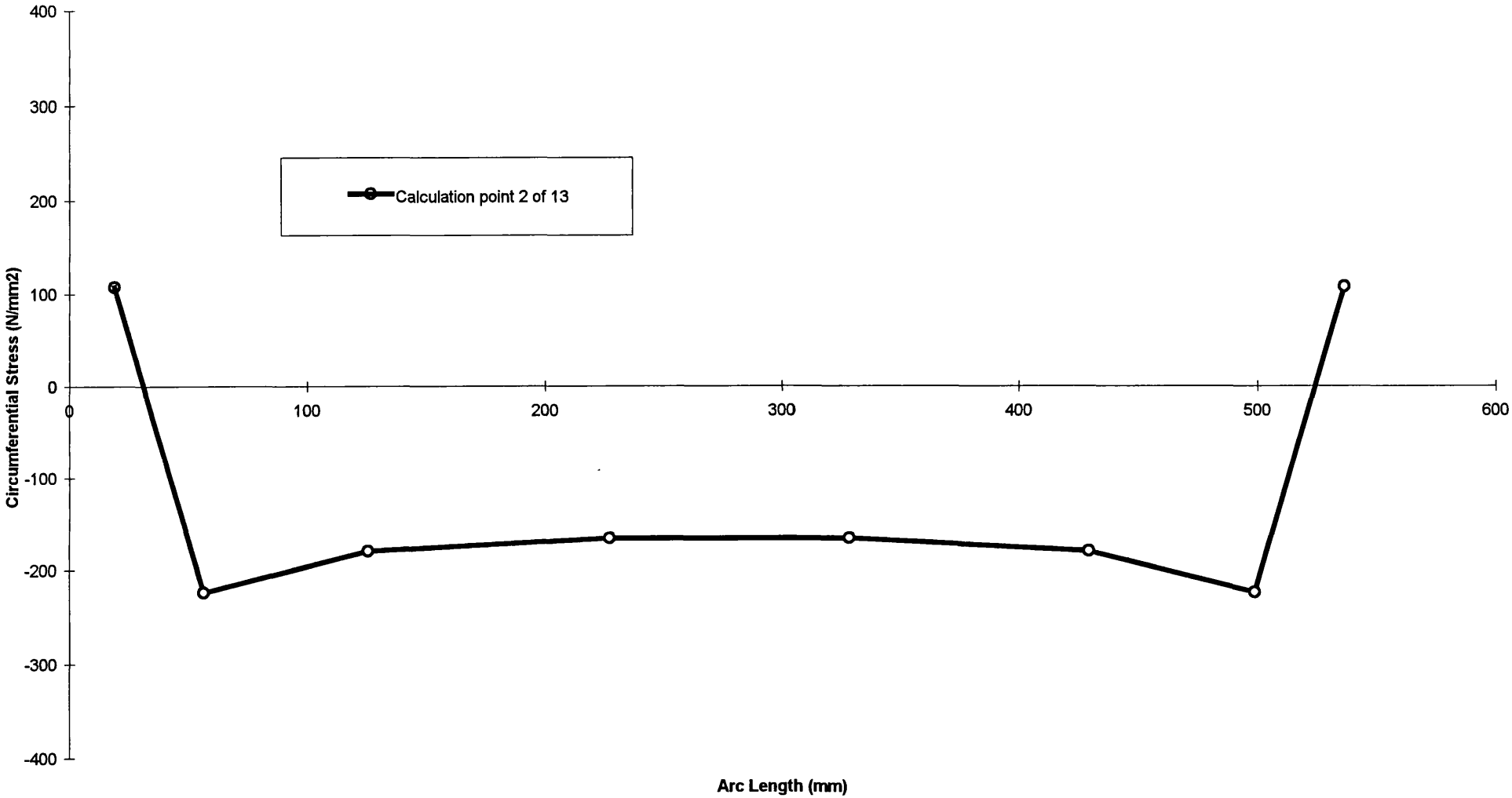


*Fig. A2.1.5.2, Model 1(ortho), inter frame circumferential residual stress.*

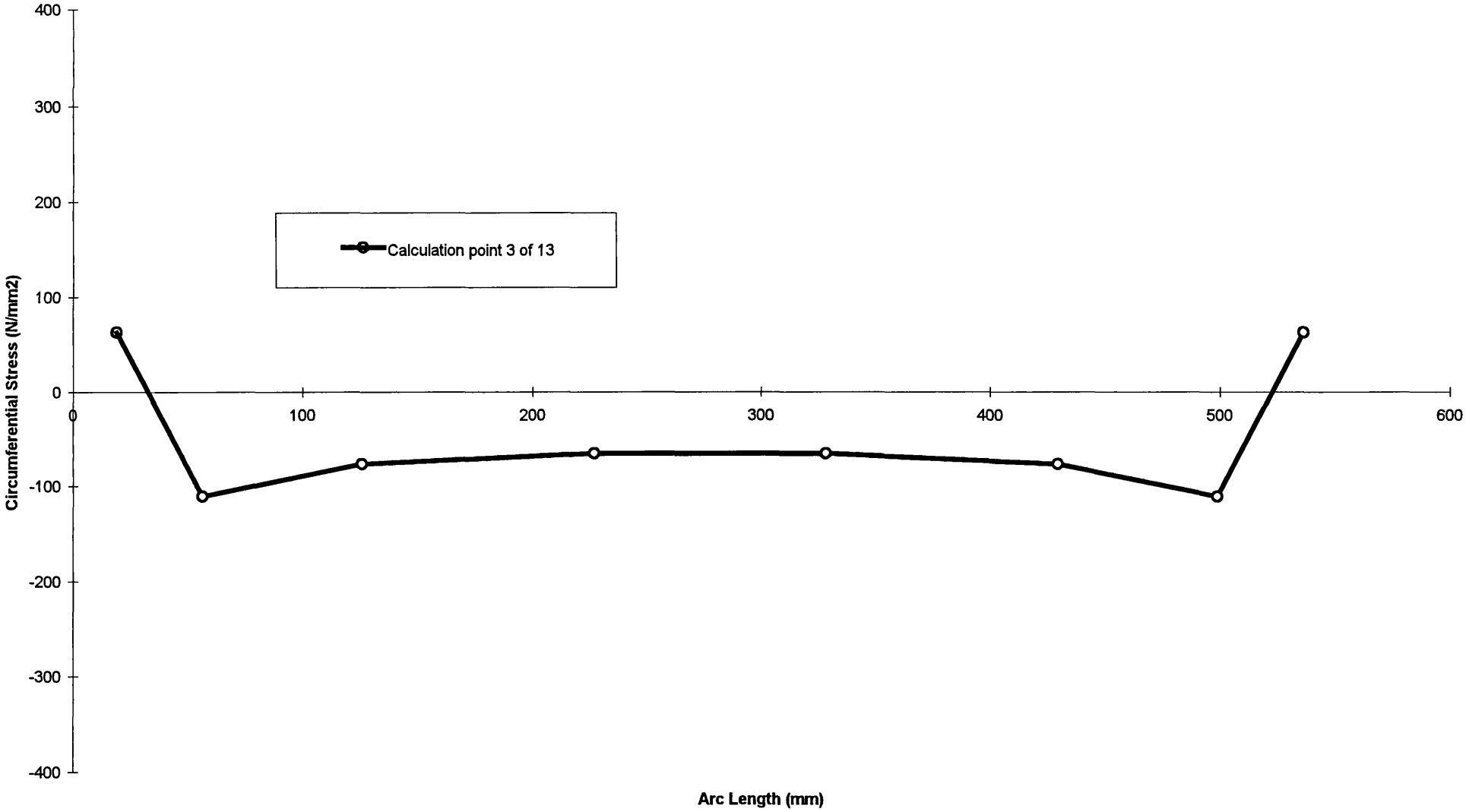


*Fig. A2.1.5.3, Model 1(ortho), inter frame circumferential residual stress.*

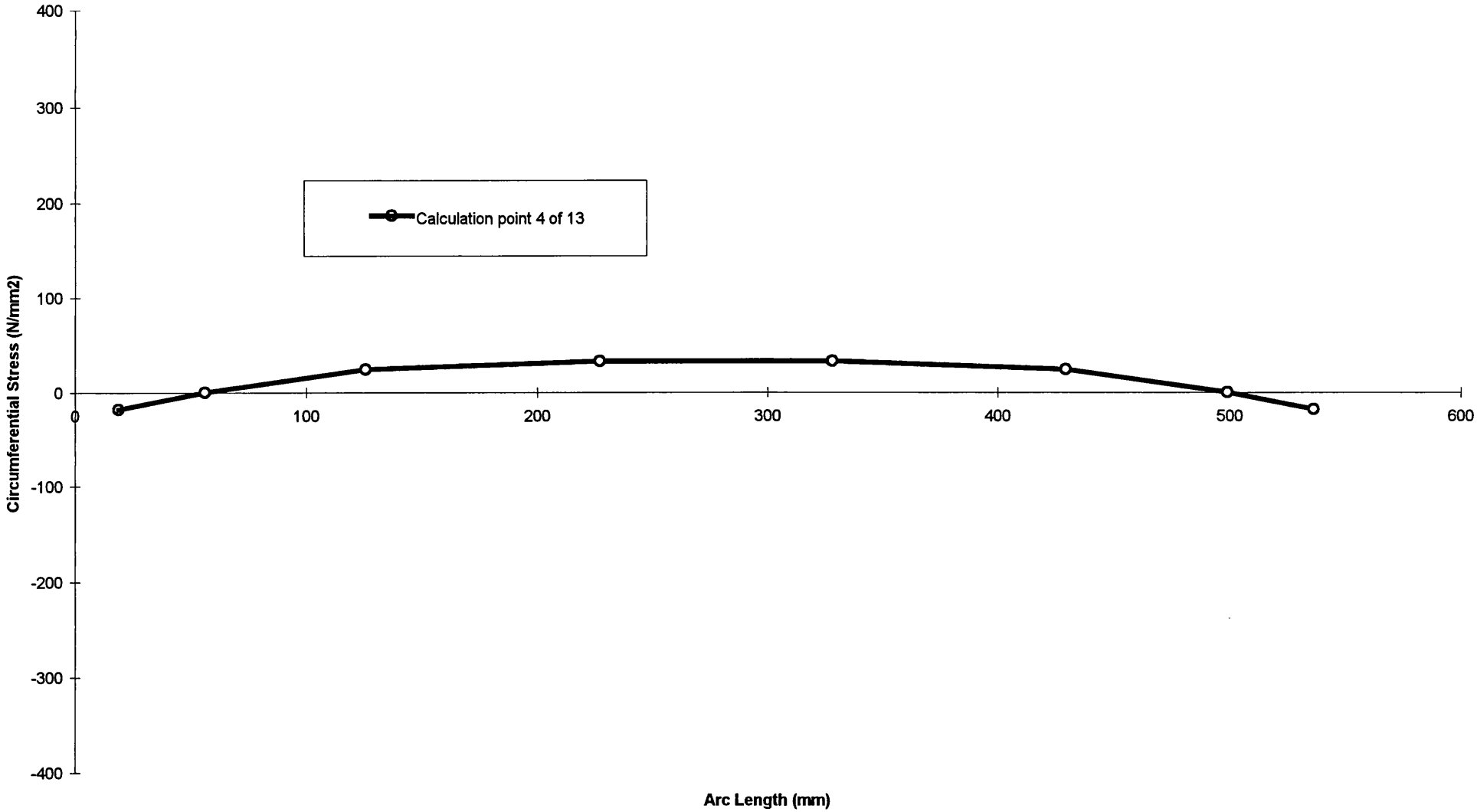


*Fig. A2.1.5.4, Model 1(ortho), inter frame circumferential residual stress.*

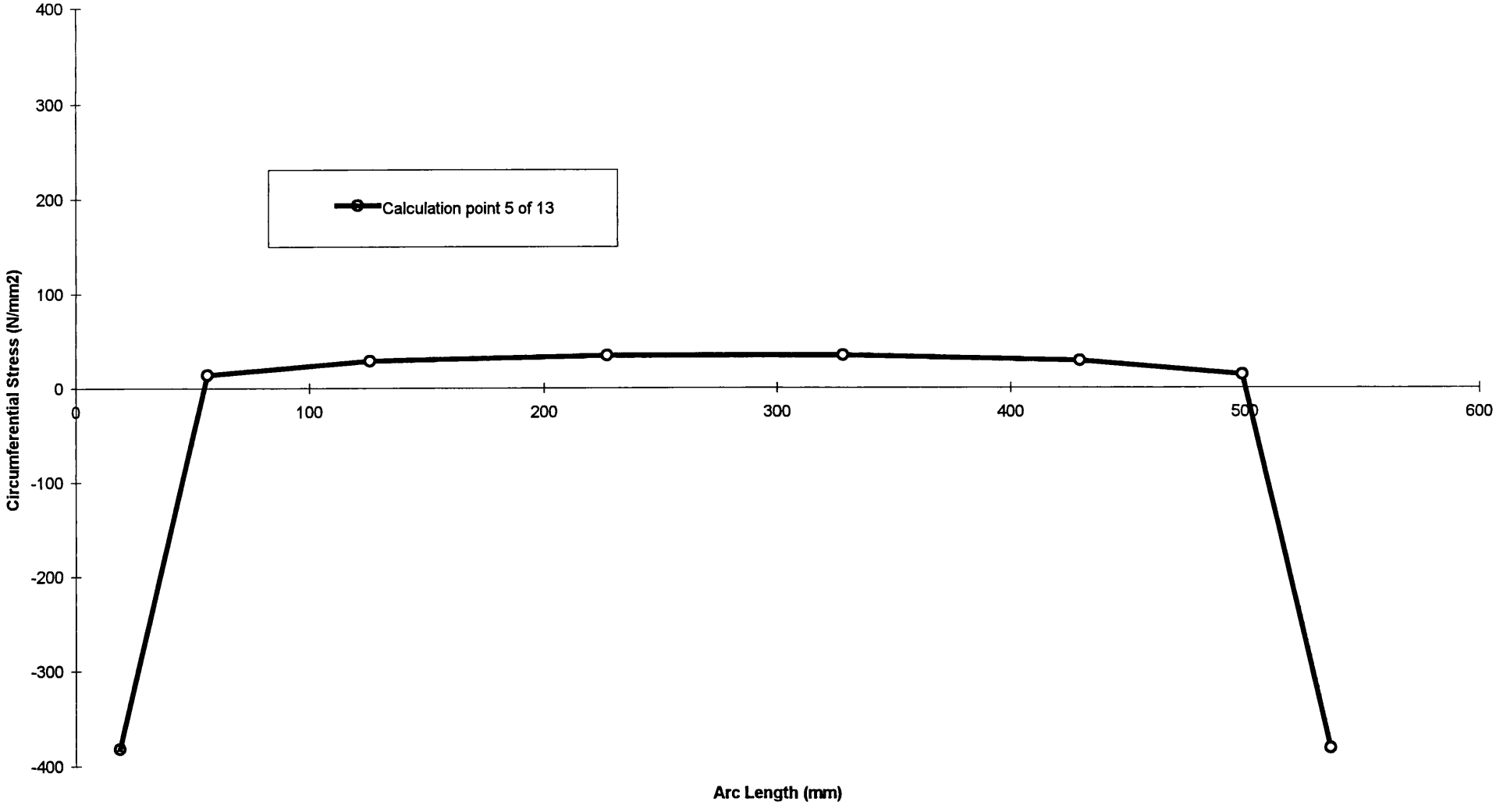


*Fig. A2.1.5.5, Model 1(ortho), inter frame circumferential residual stress.*

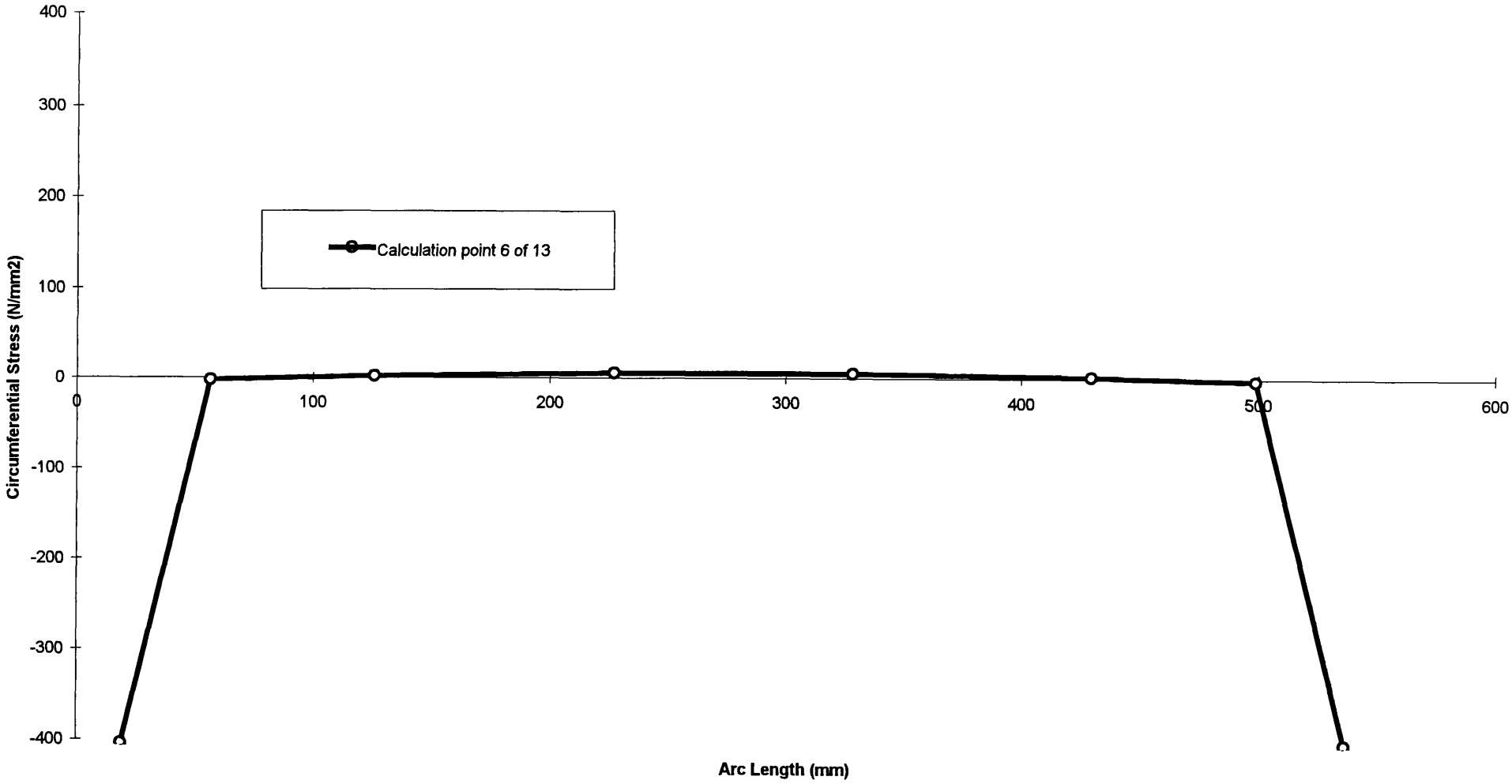


*Fig. A2.1.5.6, Model 1(ortho), inter frame circumferential residual stress.*

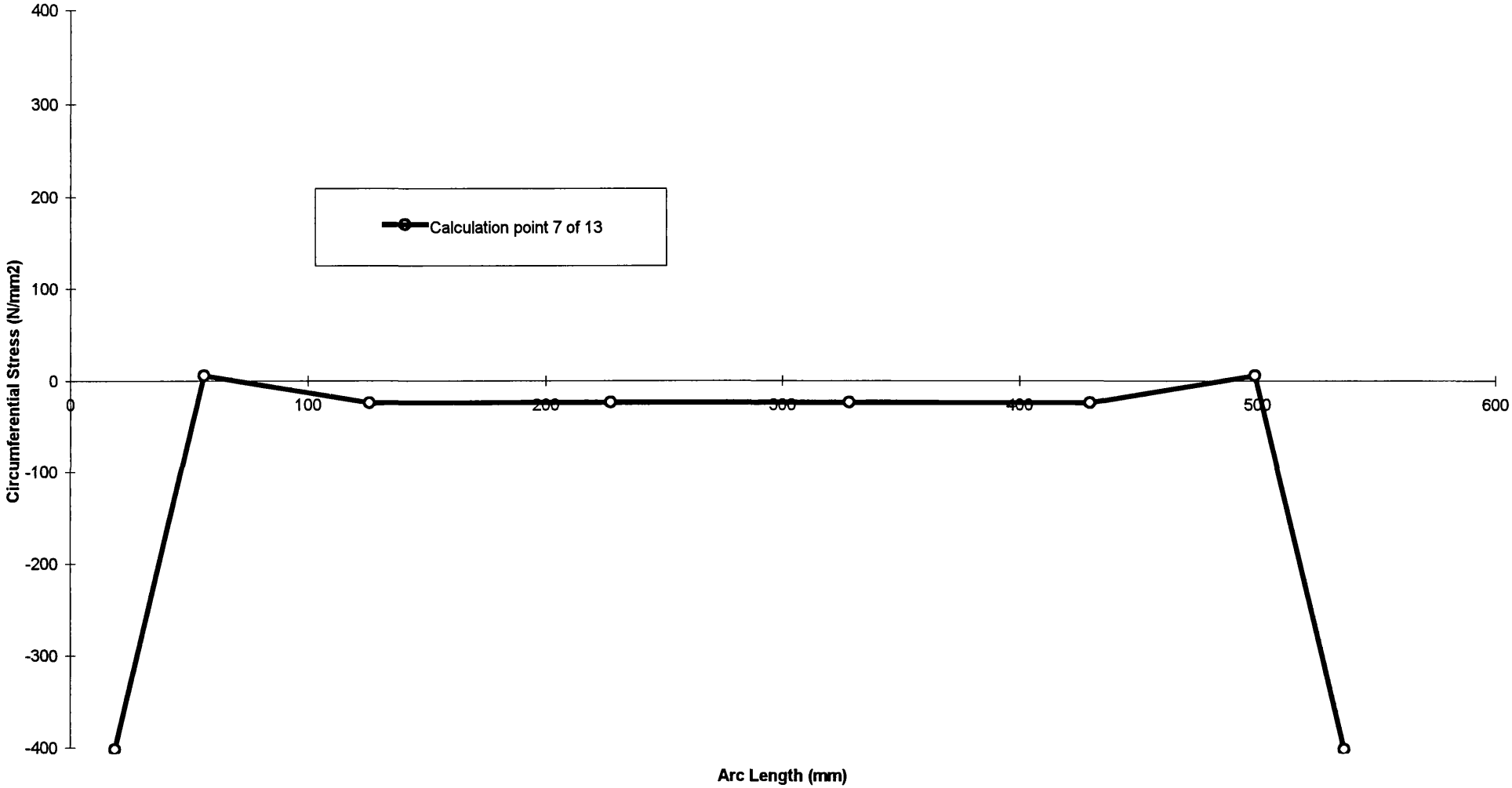


*Fig. A2.1.5.7, Model 1(ortho), inter frame circumferential residual stress.*

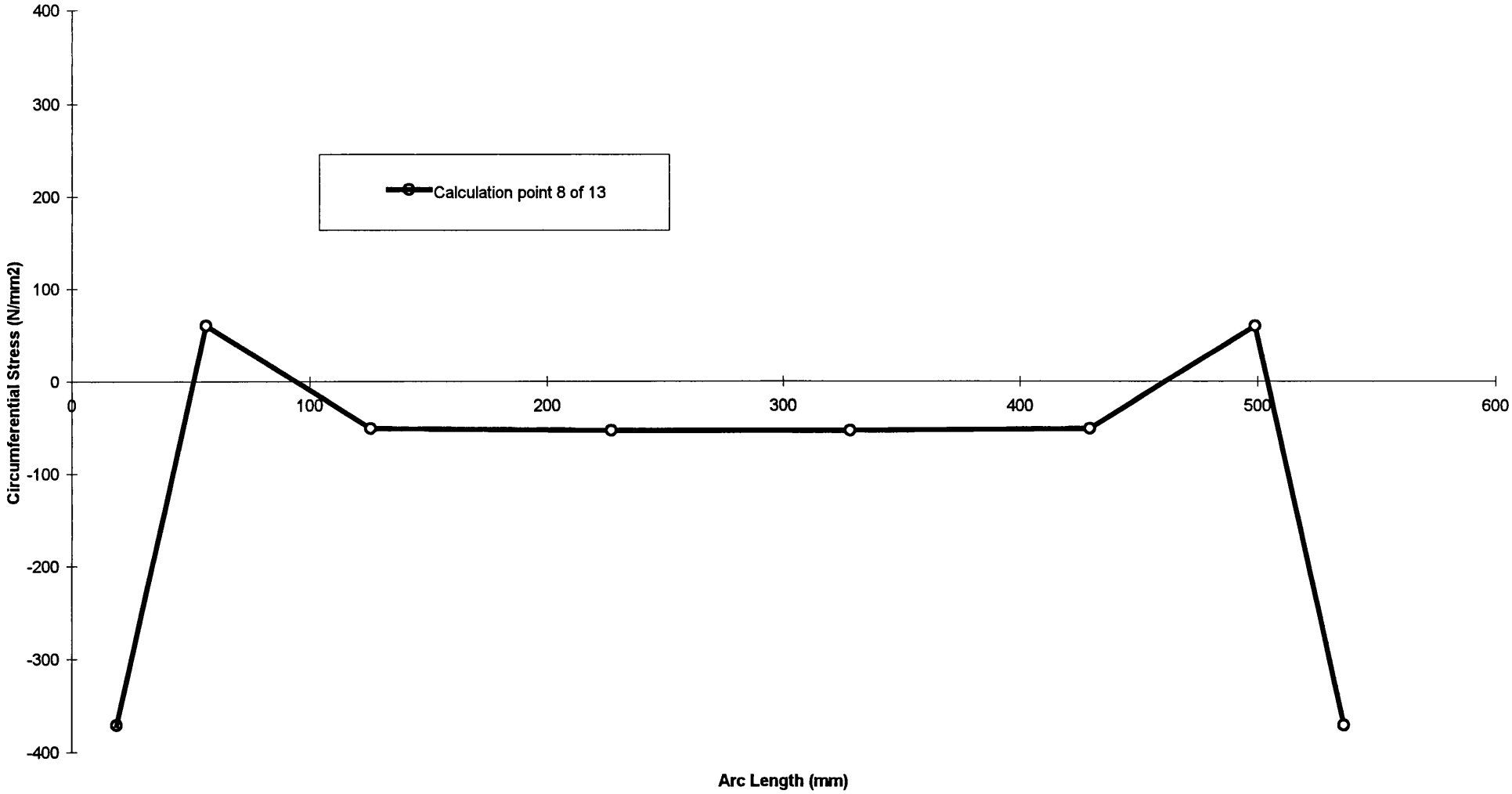


*Fig. A2.1.5.8, Model 1(ortho), inter frame circumferential residual stress.*

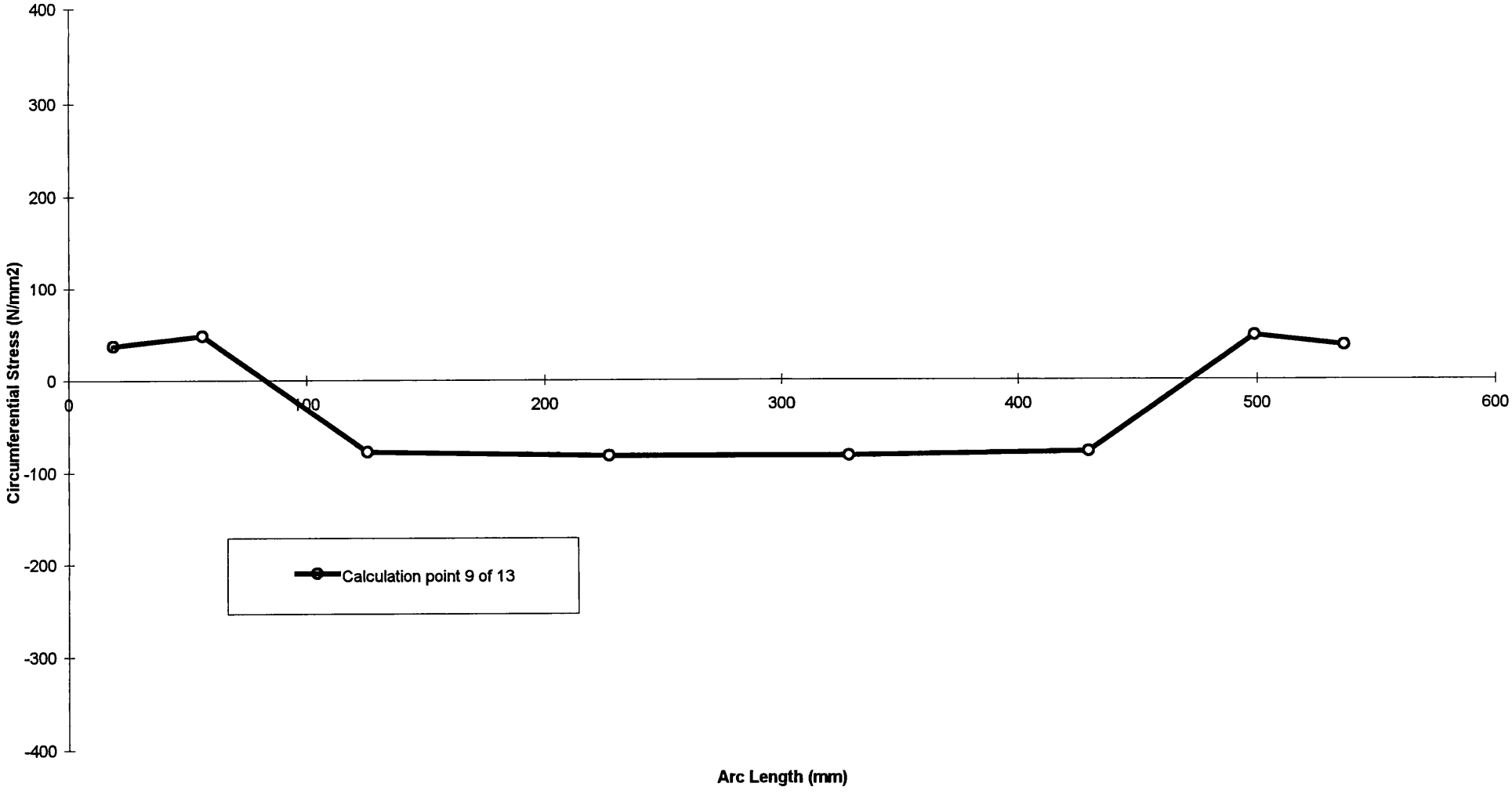


*Fig. A2.1.5.9, Model 1(ortho), interframe circumferential residual stress.*

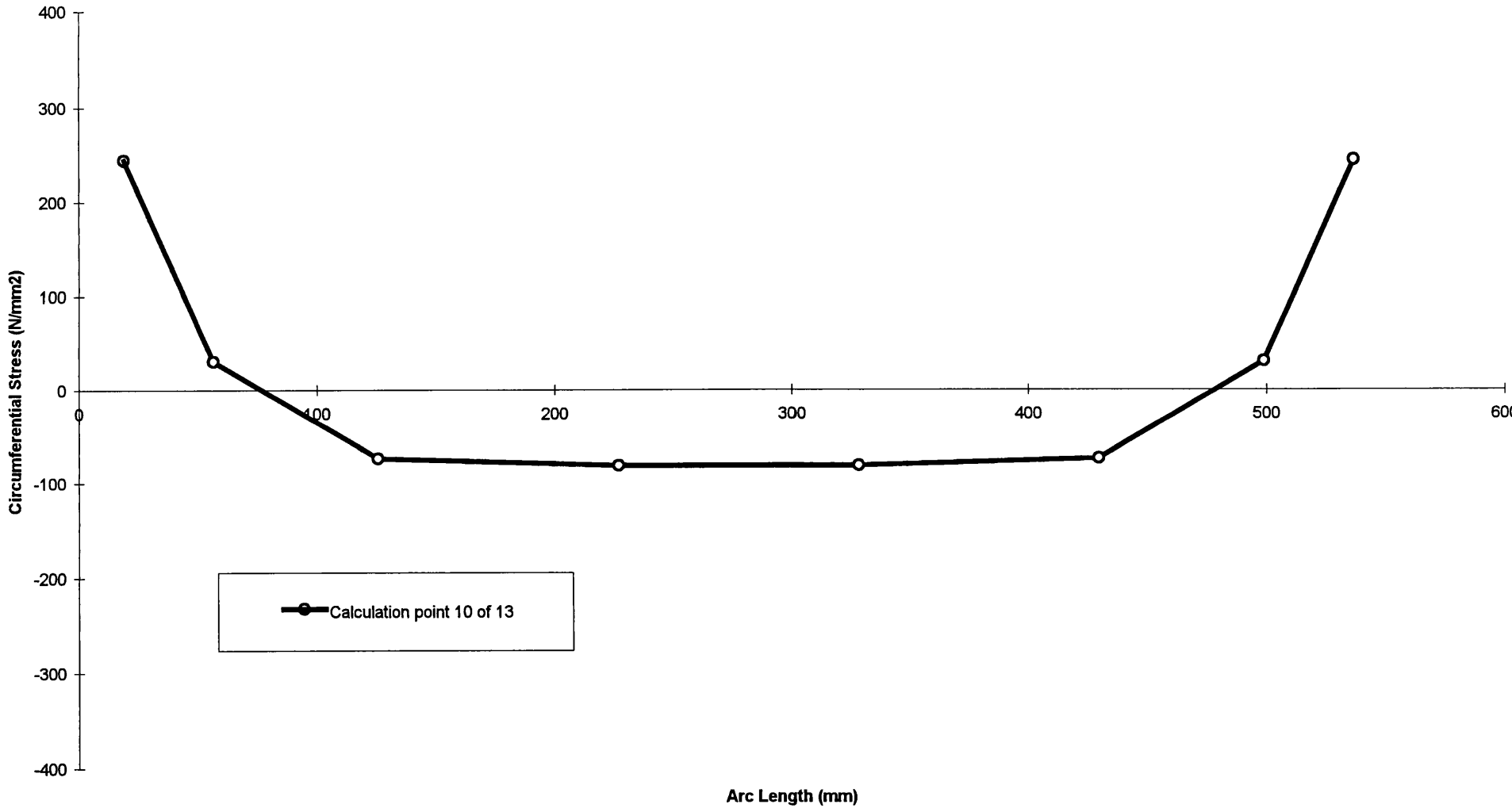


*Fig. A2.1.5.10, Model 1(ortho), inter frame circumferential residual stress.*

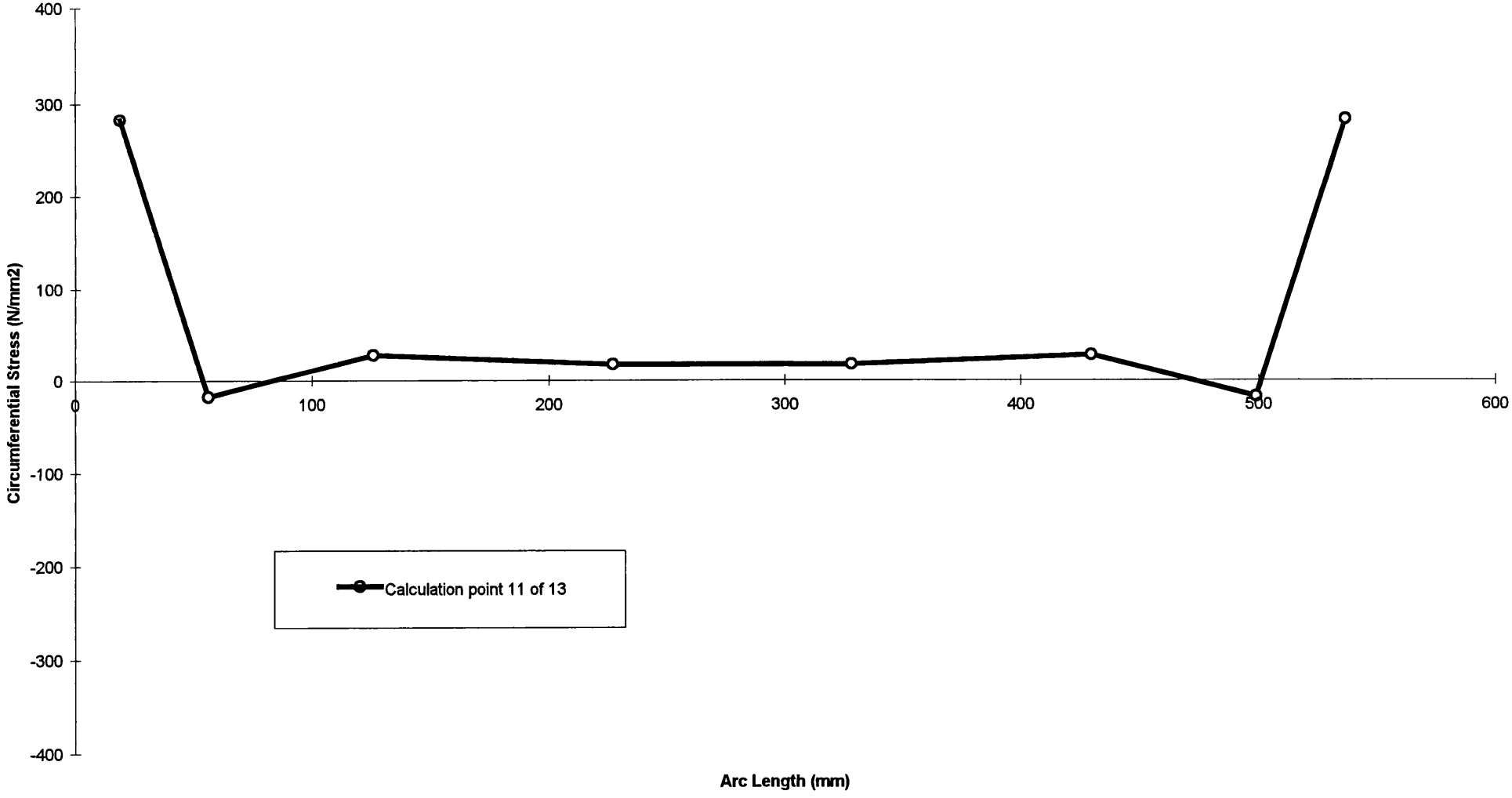


*Fig. A2.1.5.11, Model 1(ortho), inter frame circumferential residual stress.*

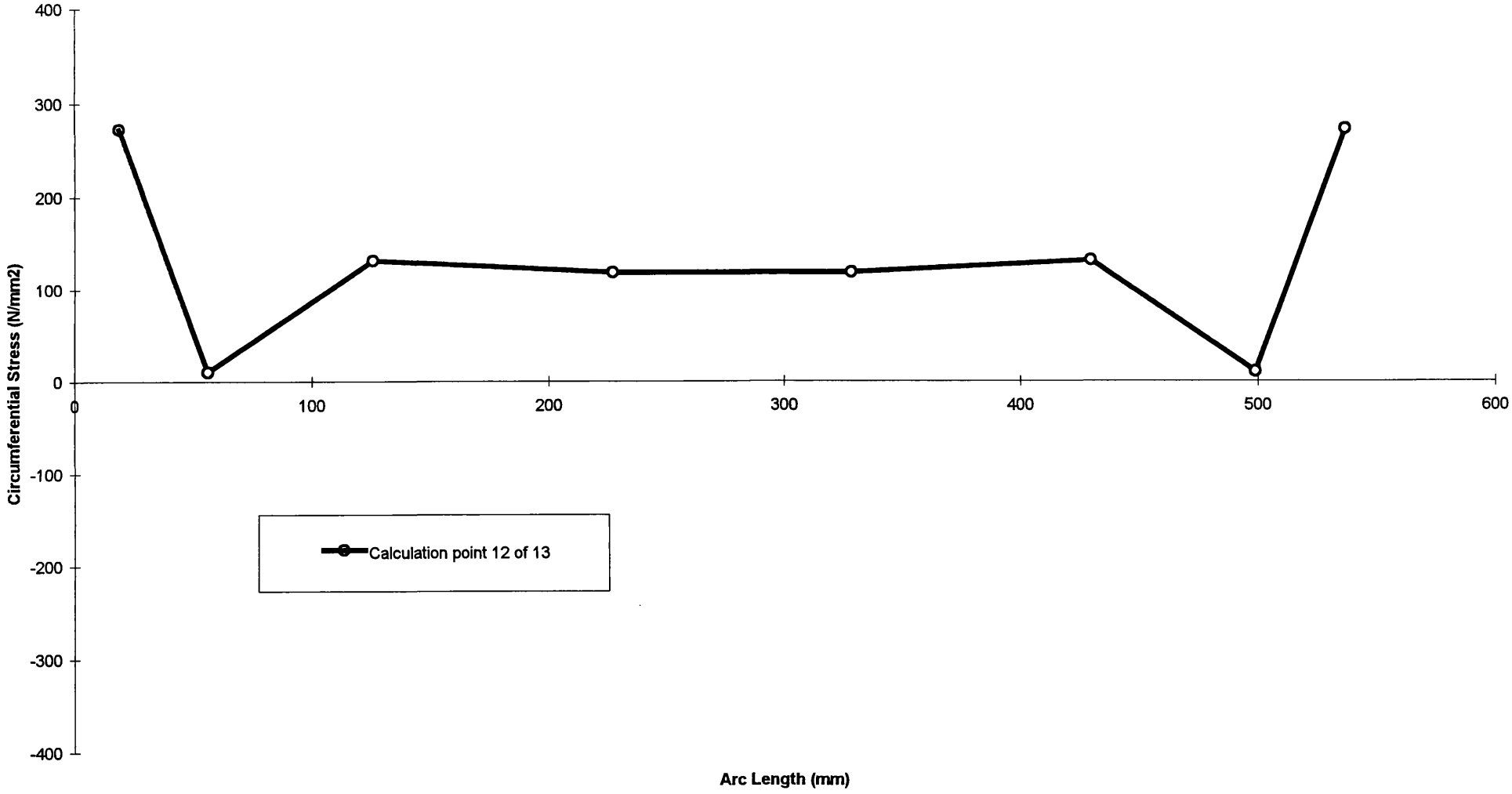


*Fig. A2.1.5.12, Model 1(ortho), inter frame circumferential residual stress.*

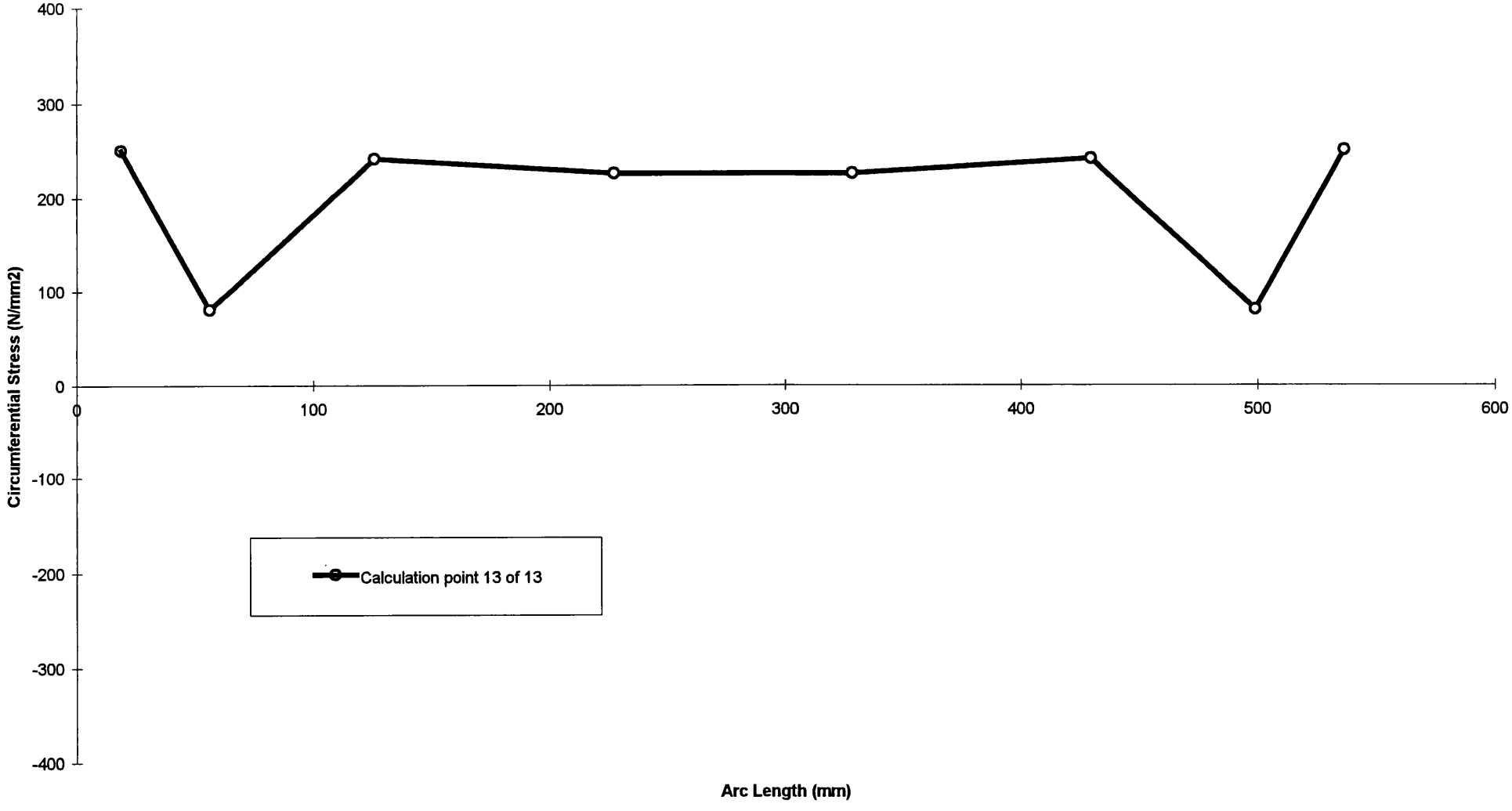


*Fig. A2.1.5.13, Model 1(ortho), inter frame circumferential residual stress.*

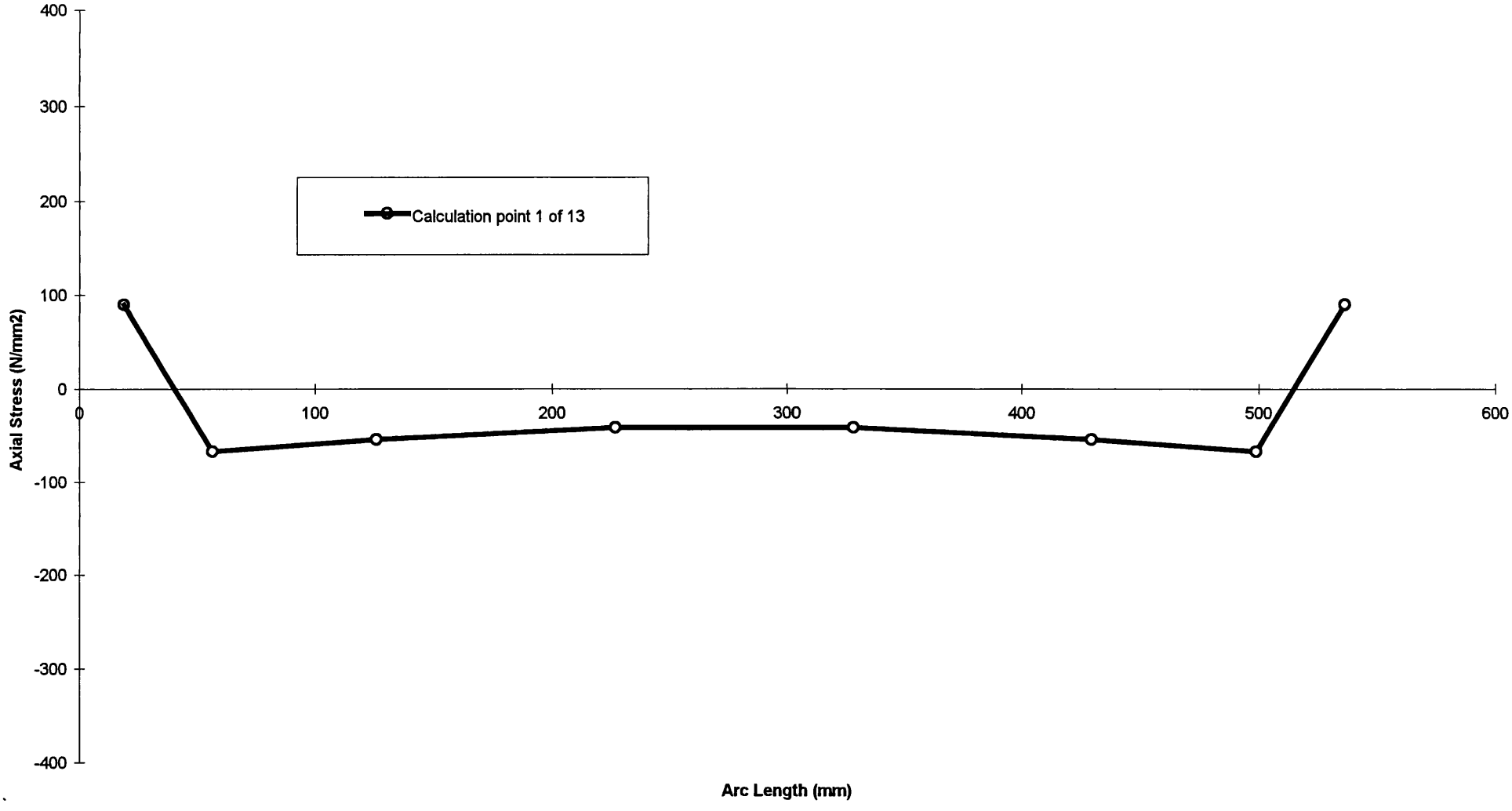


*Fig. A2.1.6.1, Model 1(ortho), Inter frame axial residual stress.*

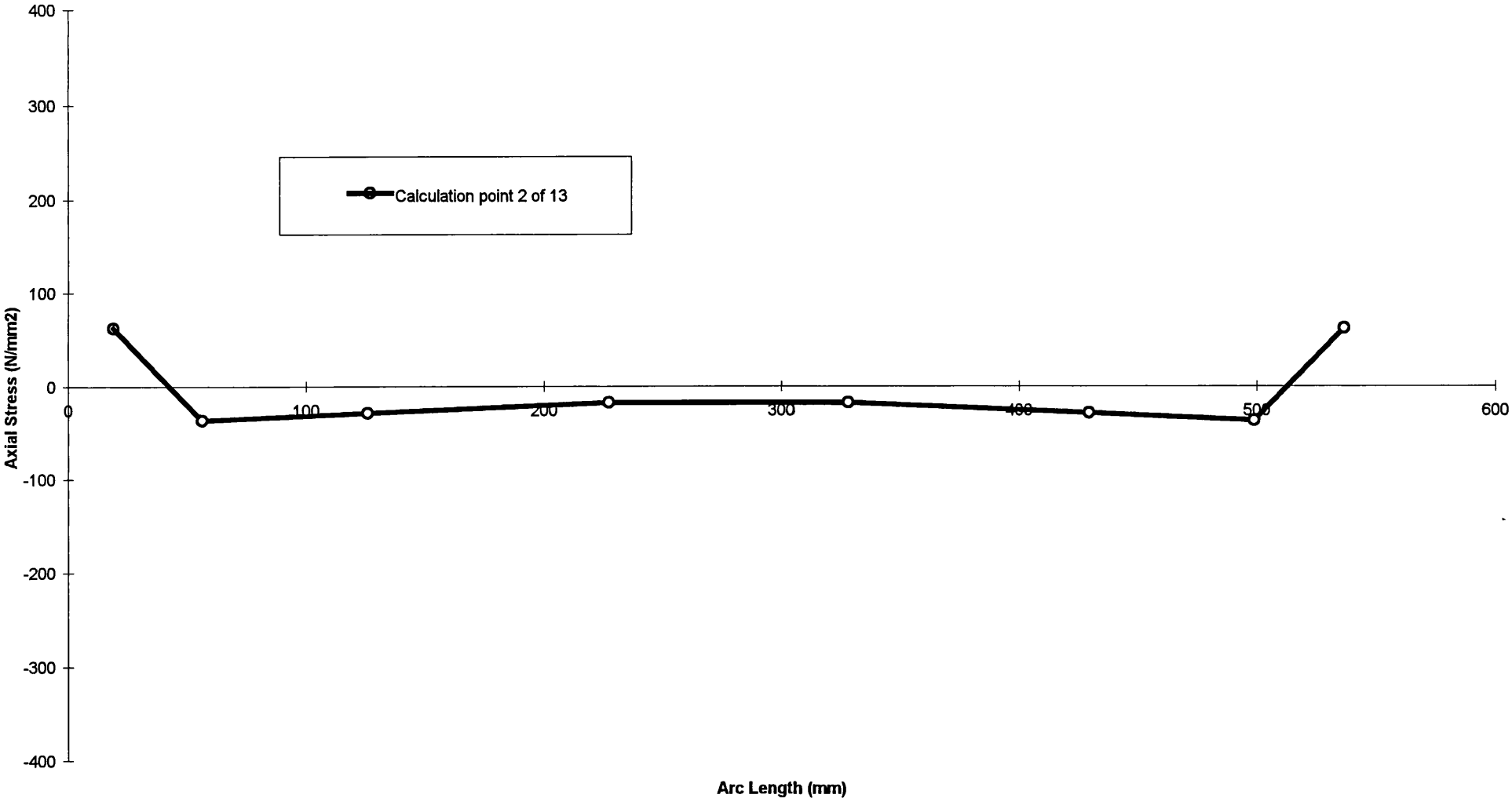


*Fig. A2.1.6.2, Model 1(ortho), inter frame axial residual stress.*

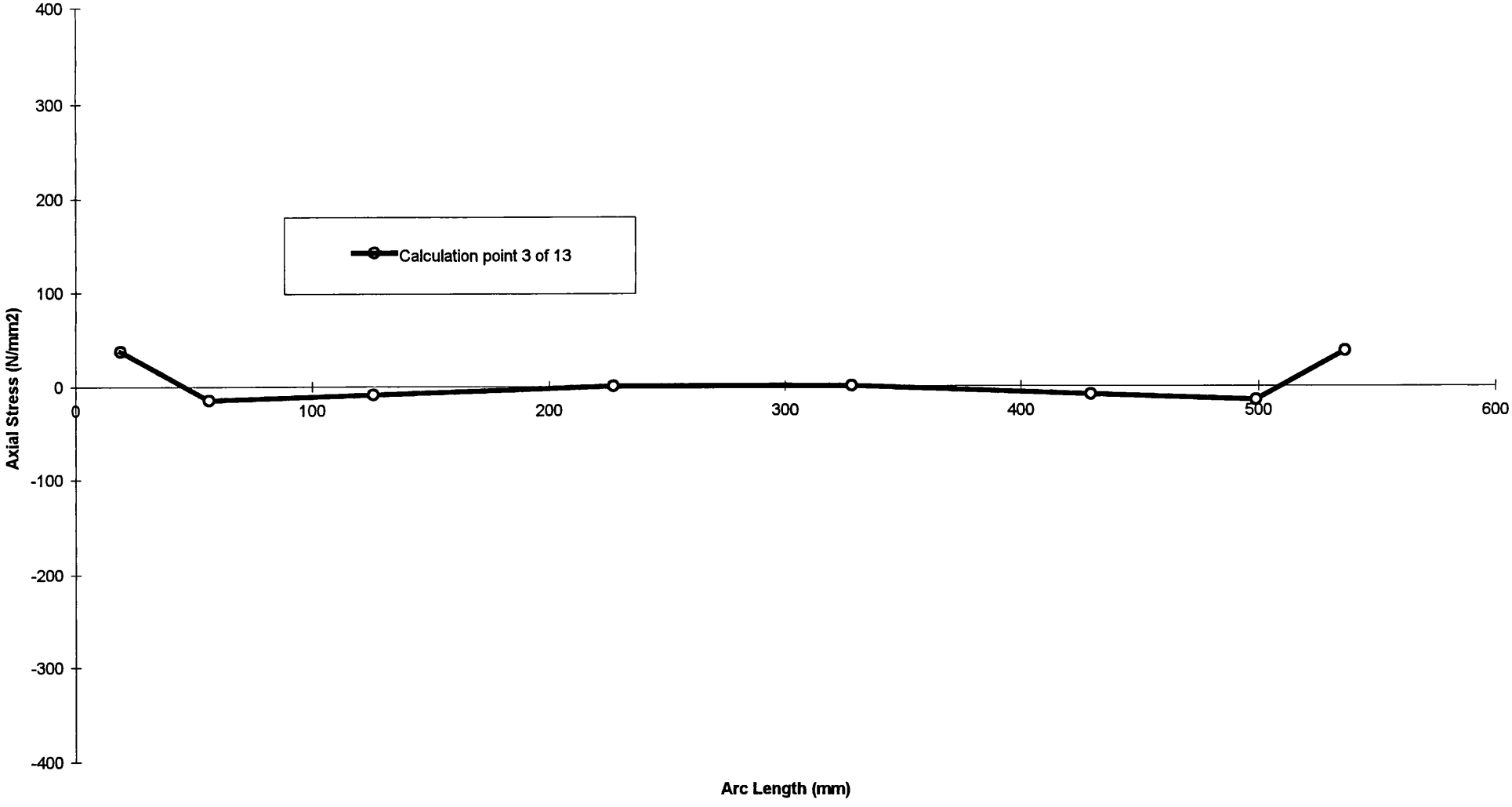


*Fig. A2.1.6.3, Model 1(ortho), inter frame axial residual stress.*

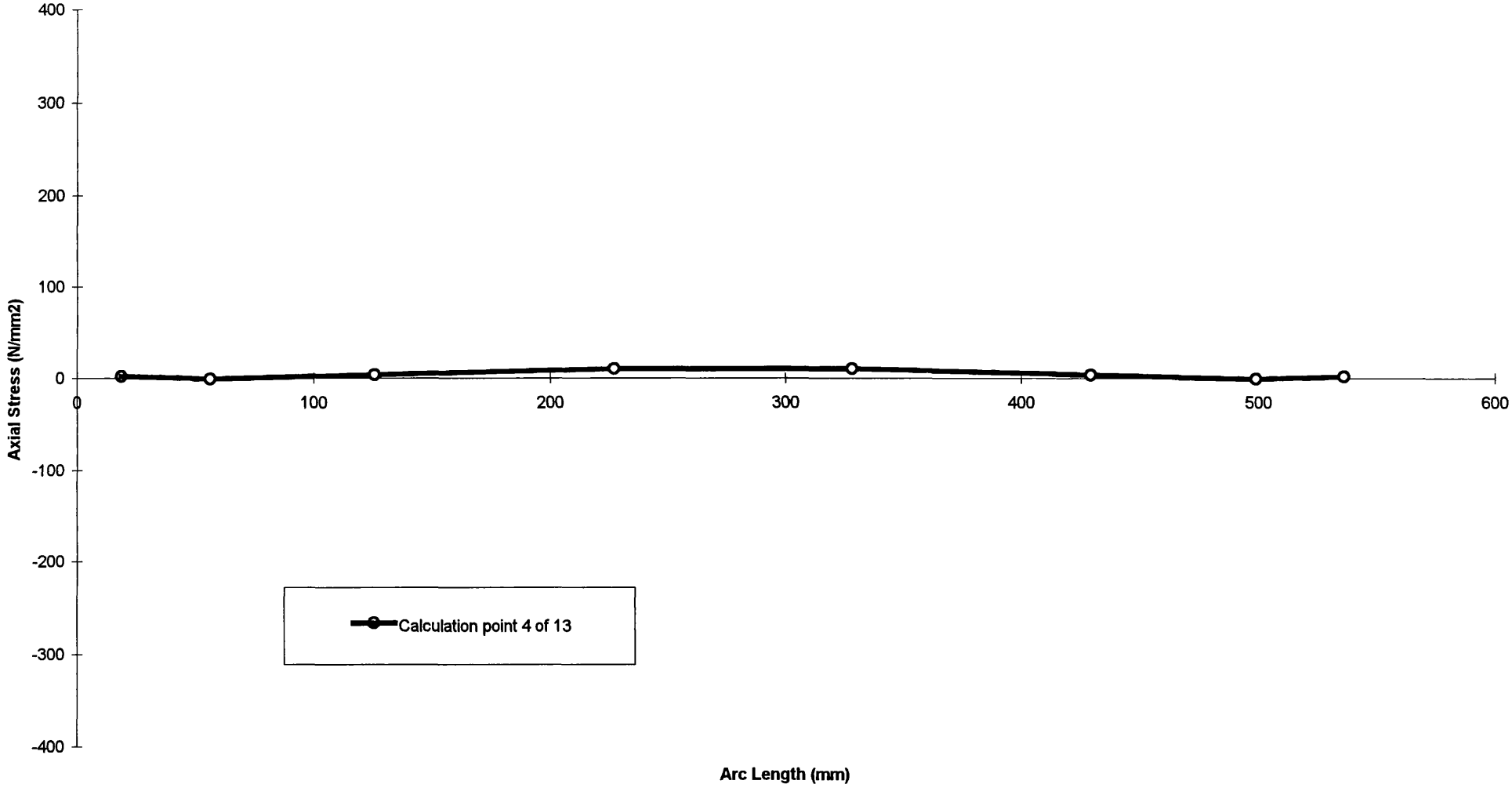


*Fig. A2.1.6.4, Model 1(ortho), inter frame axial residual stress.*

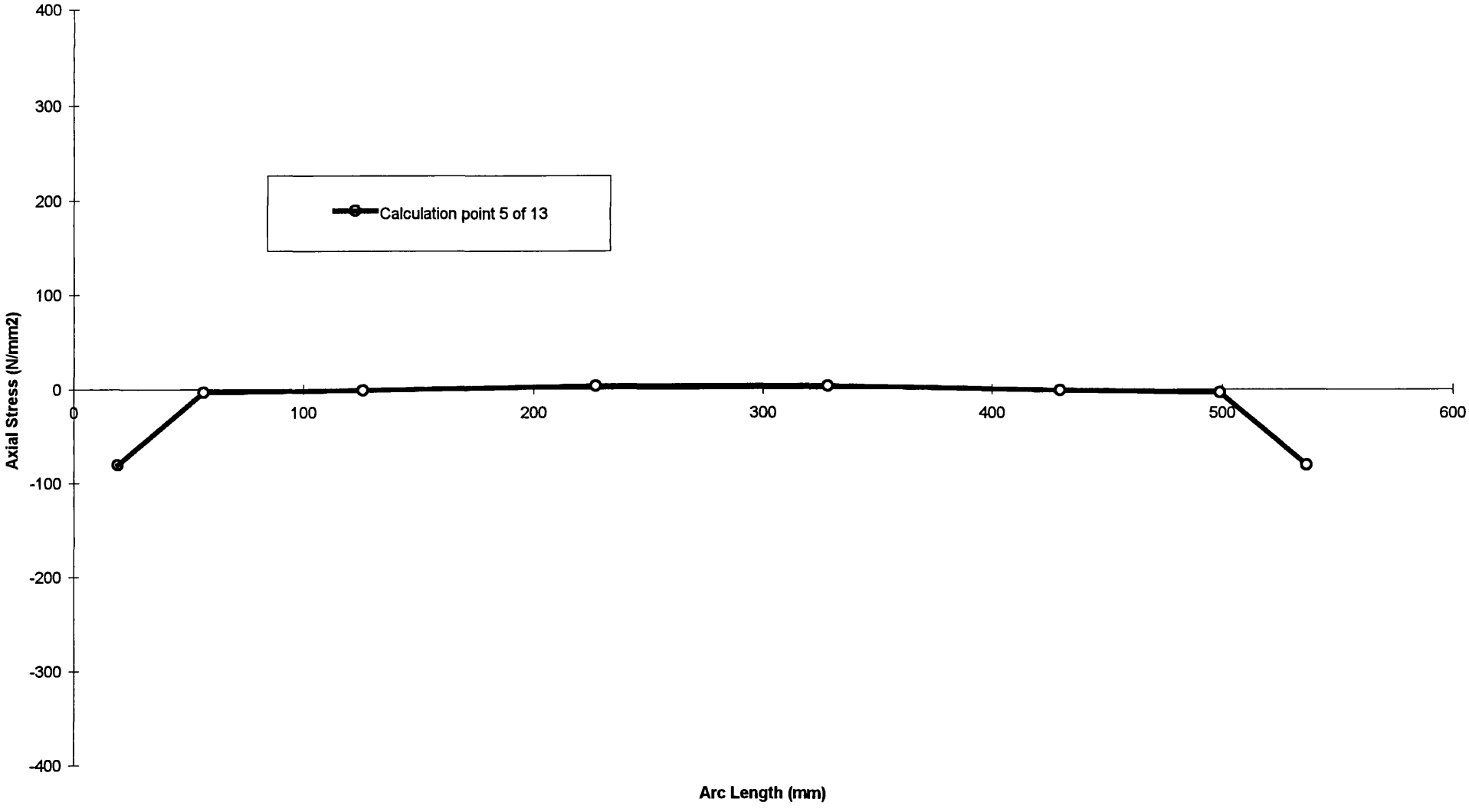


*Fig. A2.1.6.5, Model 1(ortho), inter frame axial residual stress.*

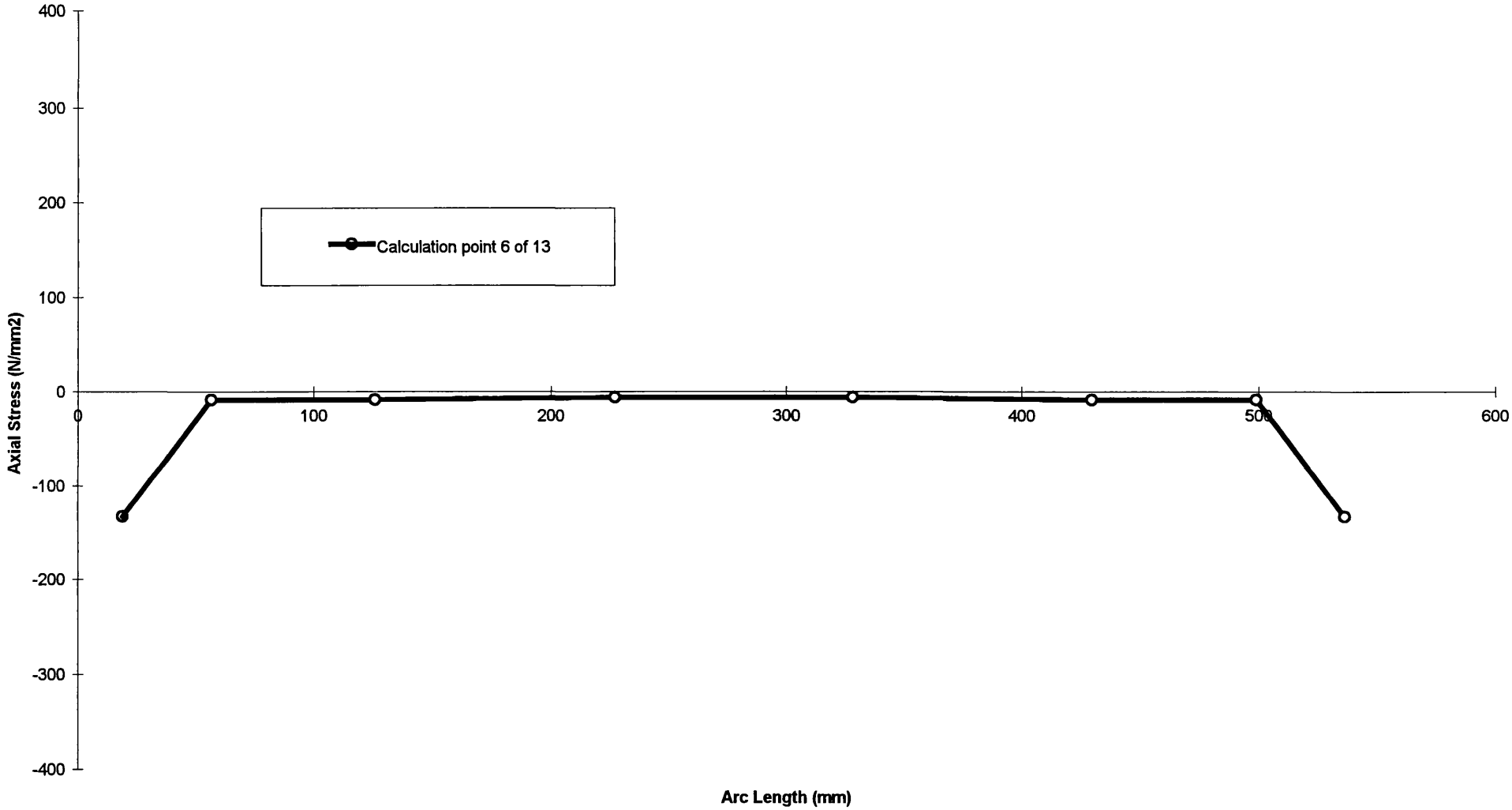


*Fig. A2.1.6.6, Model 1(ortho), inter frame axial residual stress.*

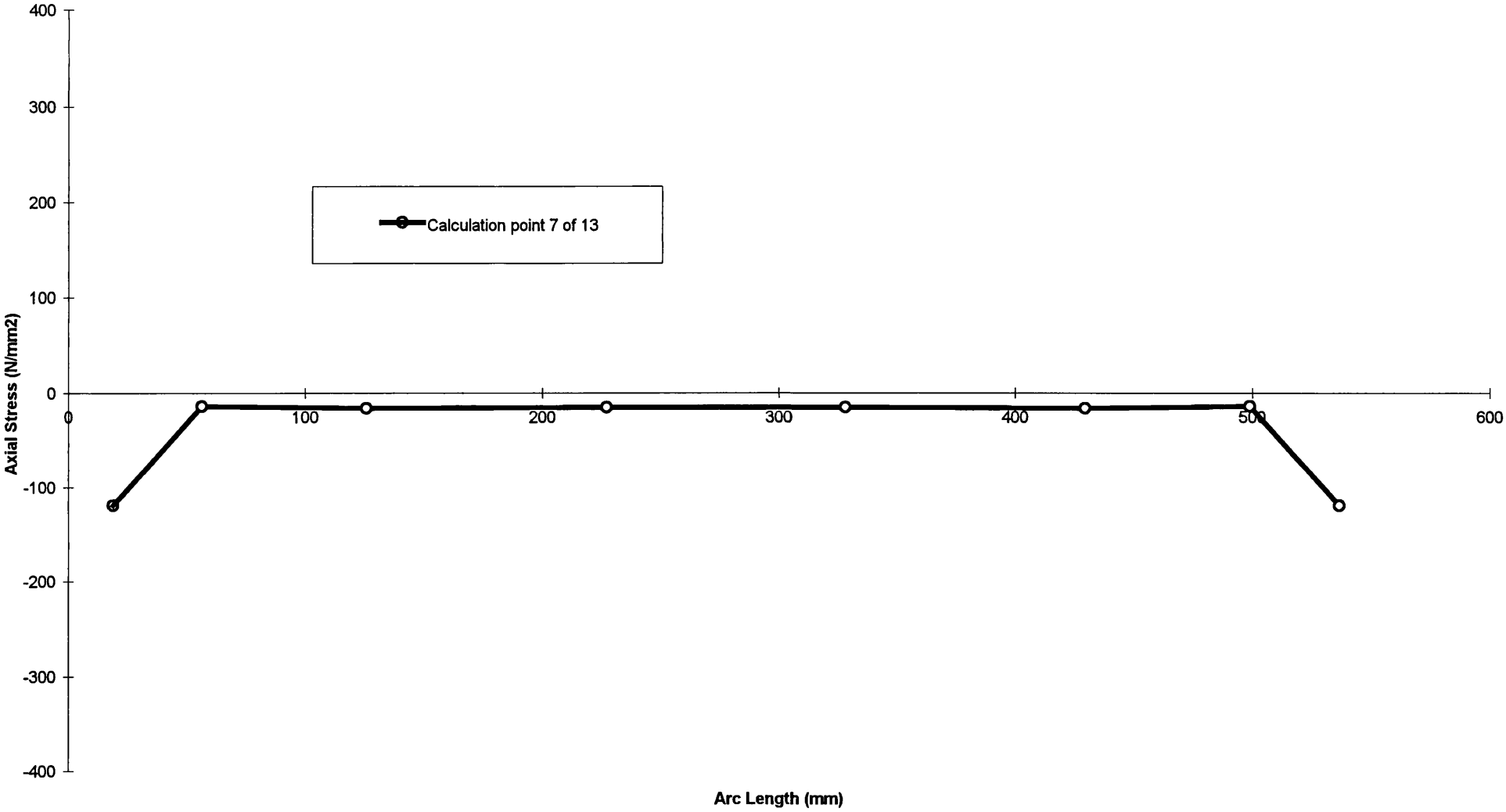


*Fig. A2.1.6.7, Model 1(ortho), inter frame axial residual stress.*

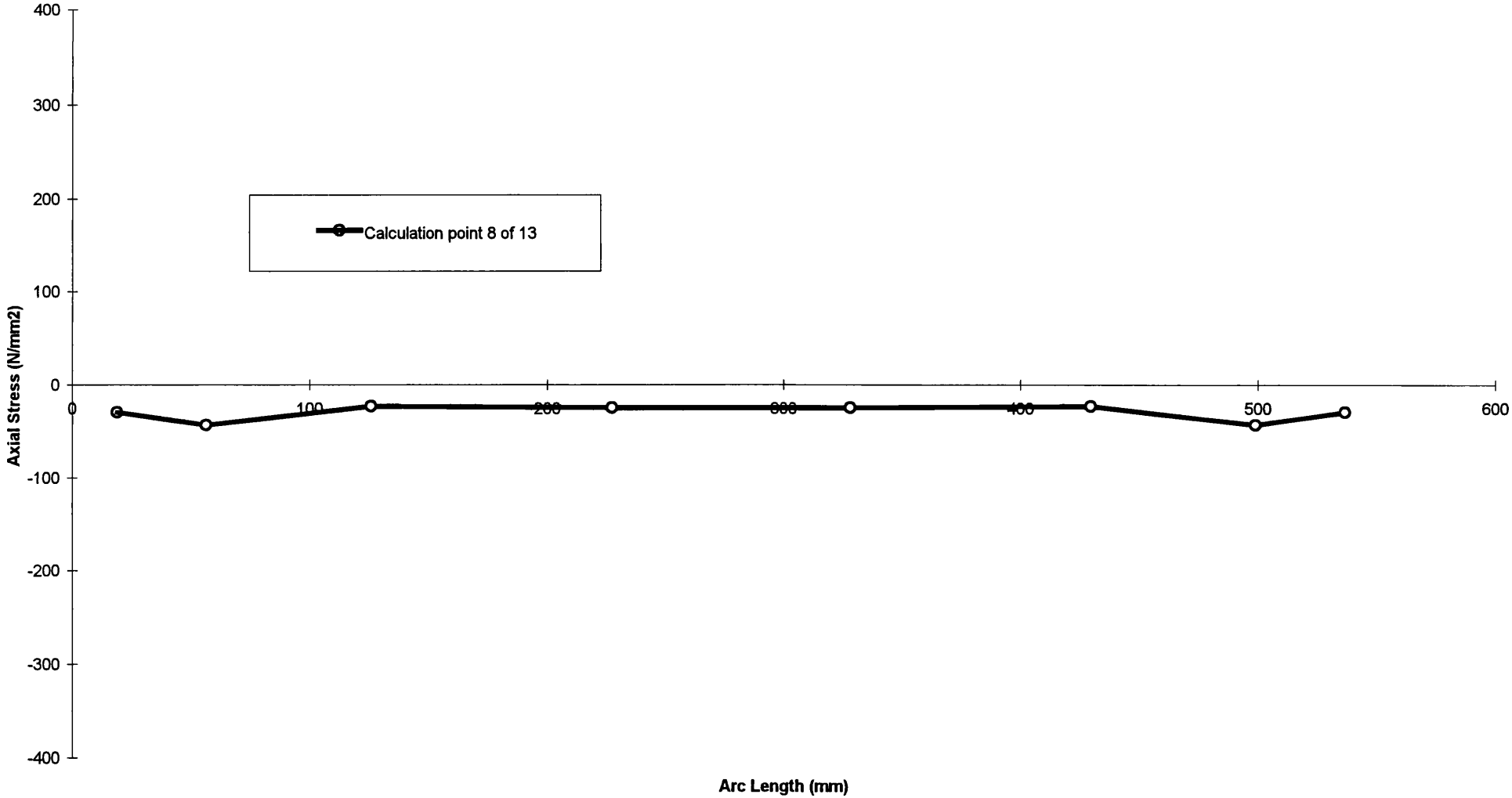


*Fig. A2.1.6.8, Model 1(ortho), inter frame axial residual stress.*

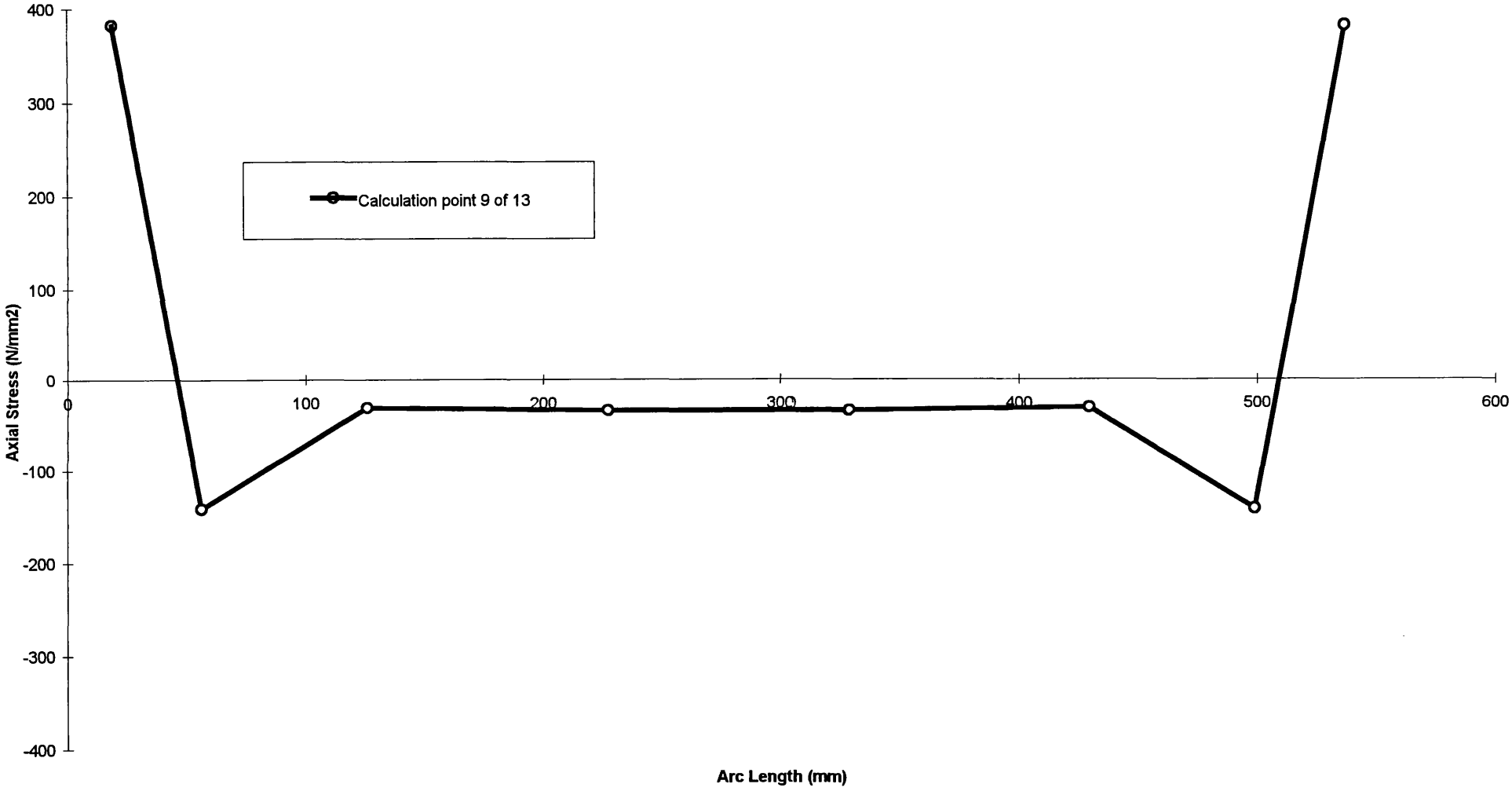


*Fig. A2.1.6.9, Model 1(ortho), interframe axial residual stress.*

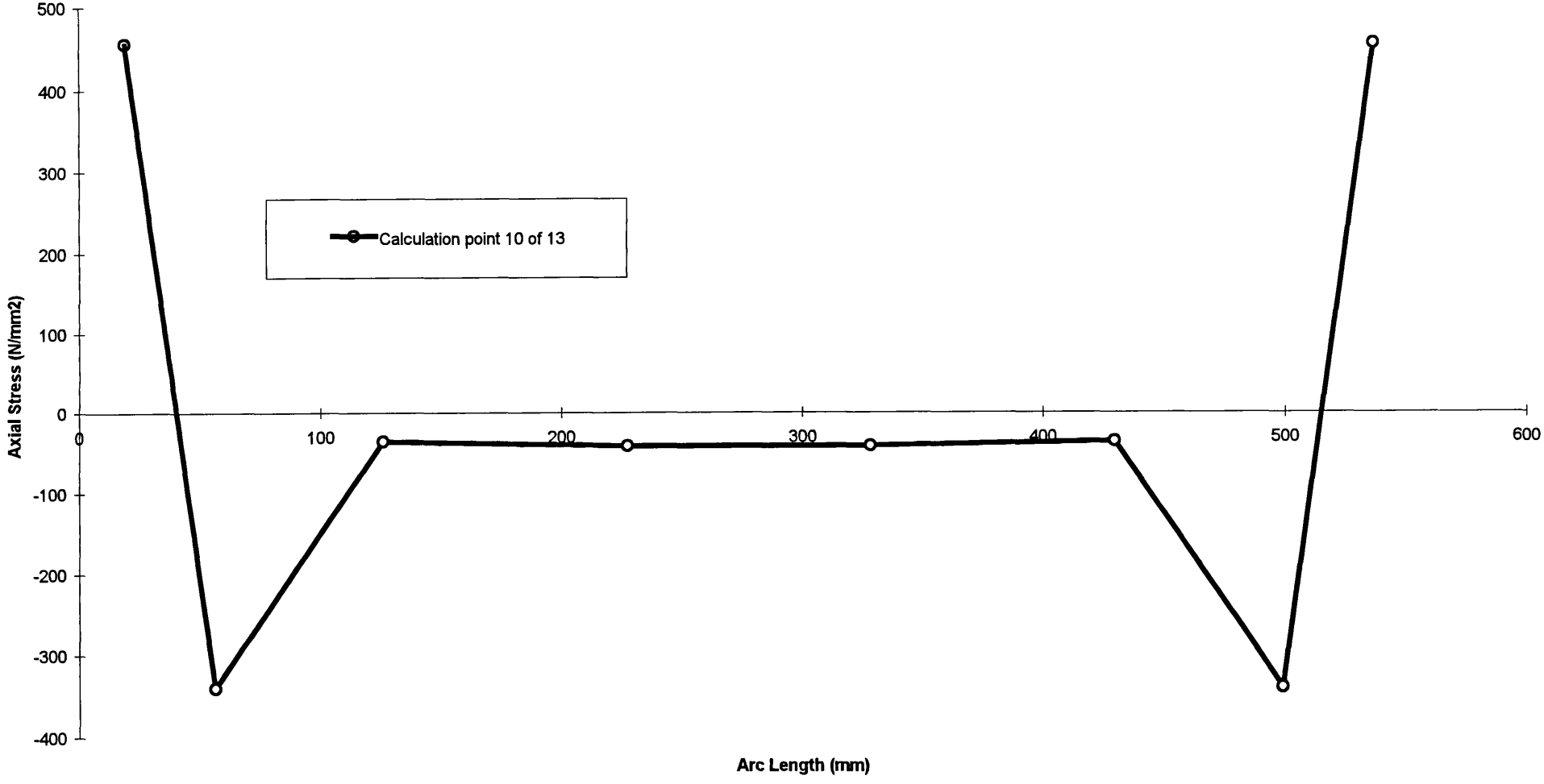


*Fig. A2.1.6.10, Model 1(ortho), inter frame axial residual stress.*

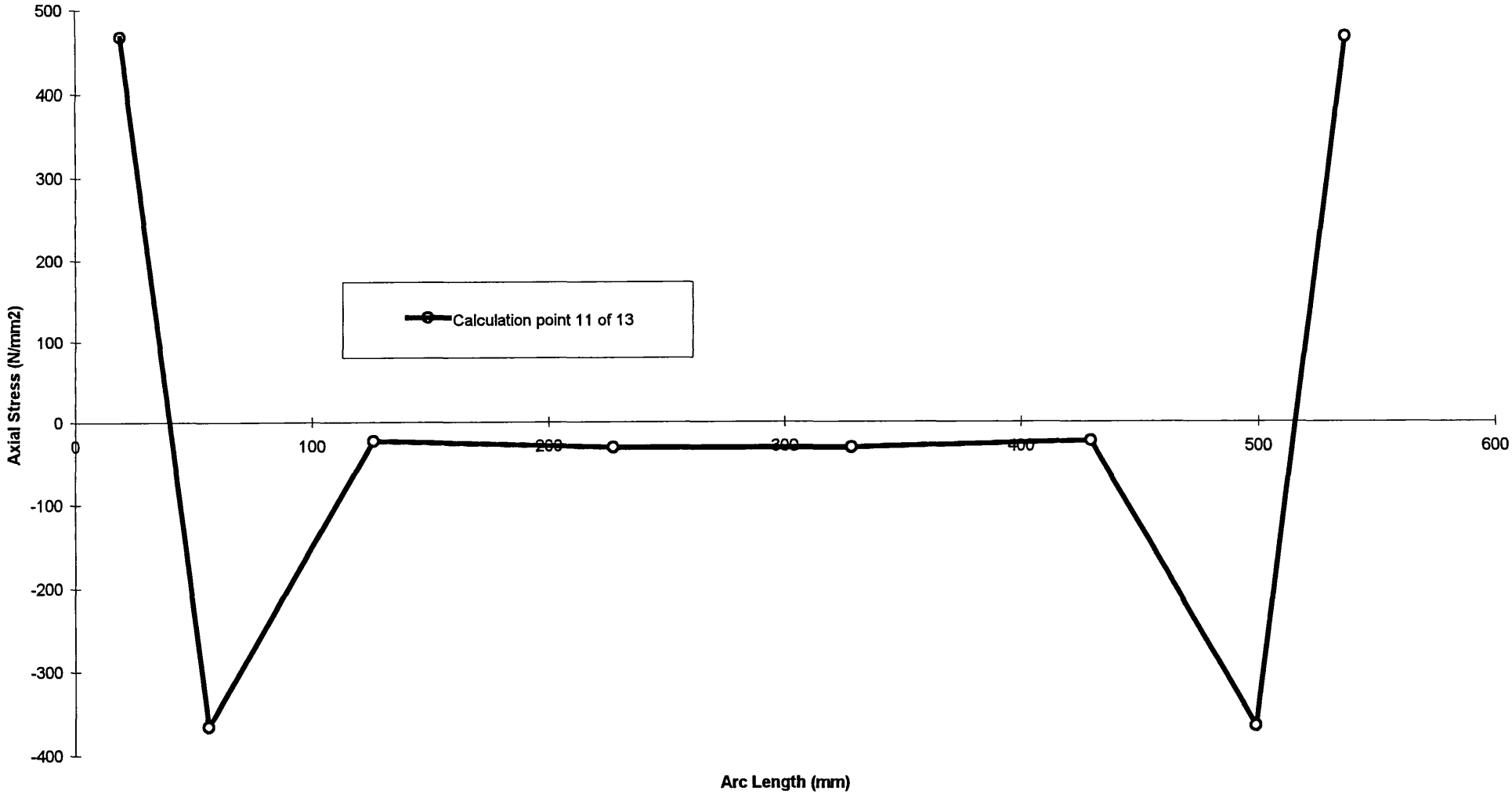


*Fig. A2.1.6.11, Model 1(ortho), inter frame axial residual stress.*

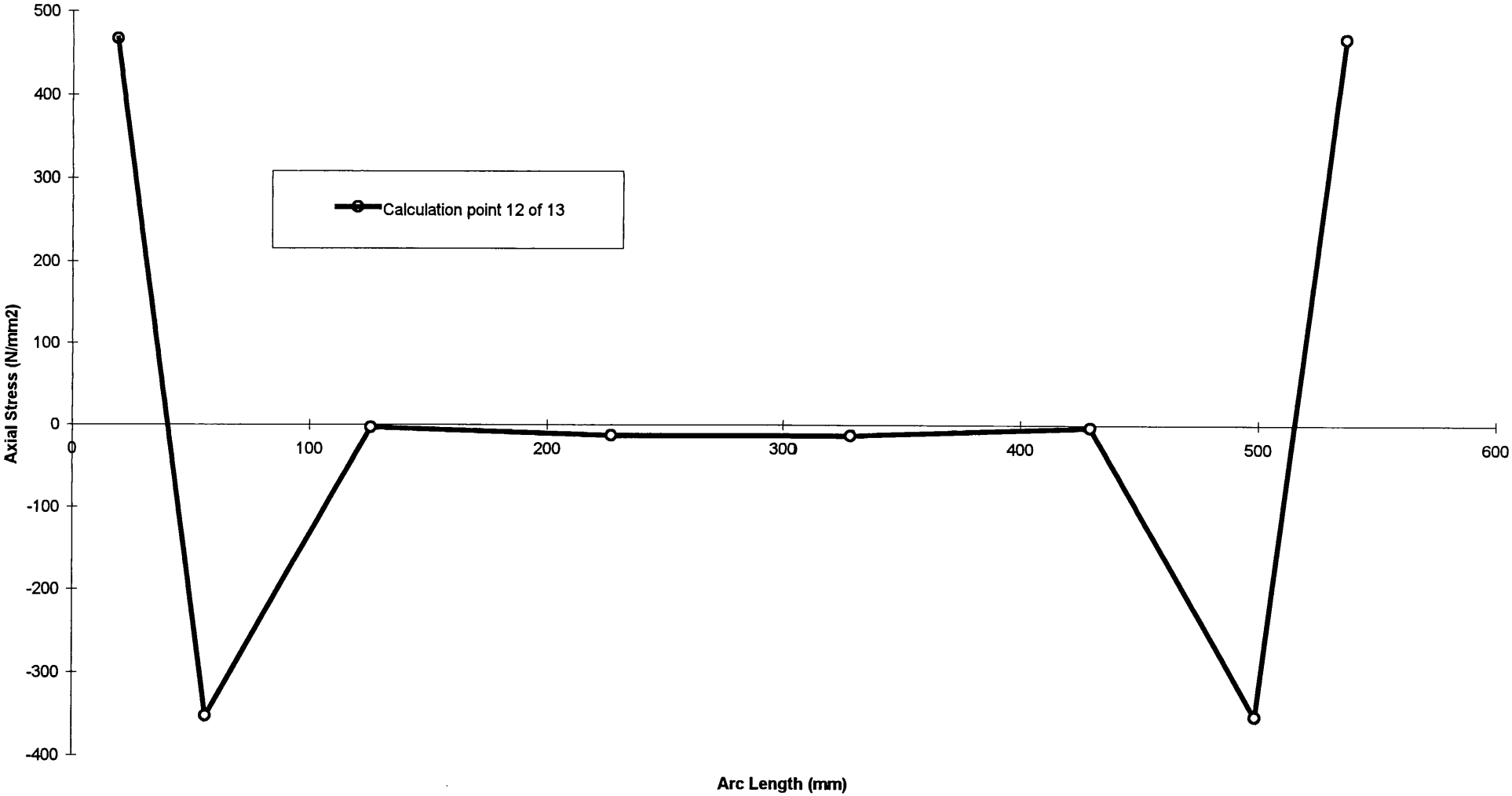


*Fig. A2.1.6.1.12, Model 1(ortho), inter frame axial residual stress.*

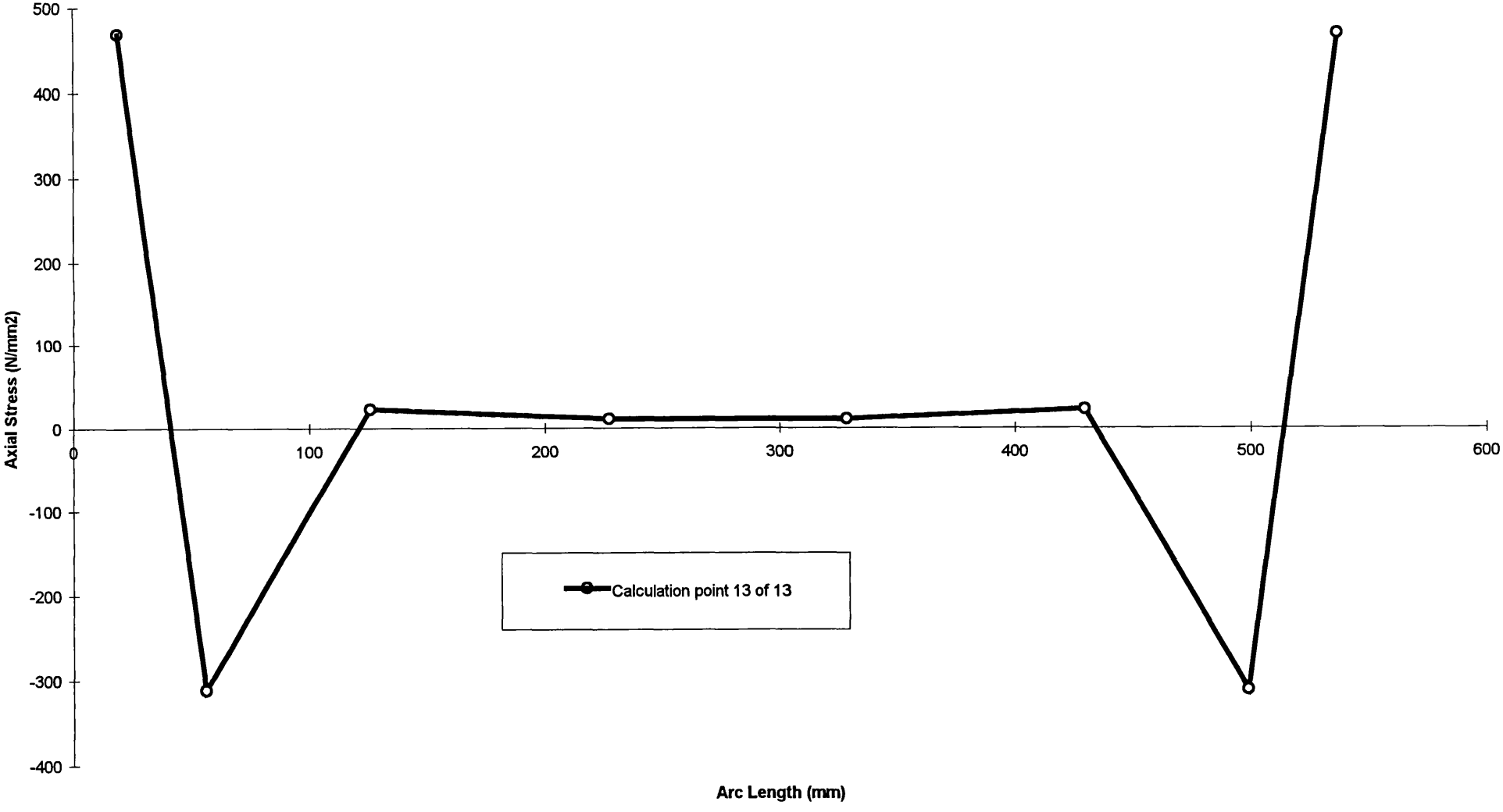


*Fig. A2.1.6.13, Model 1(ortho), inter frame axial residual stress.*

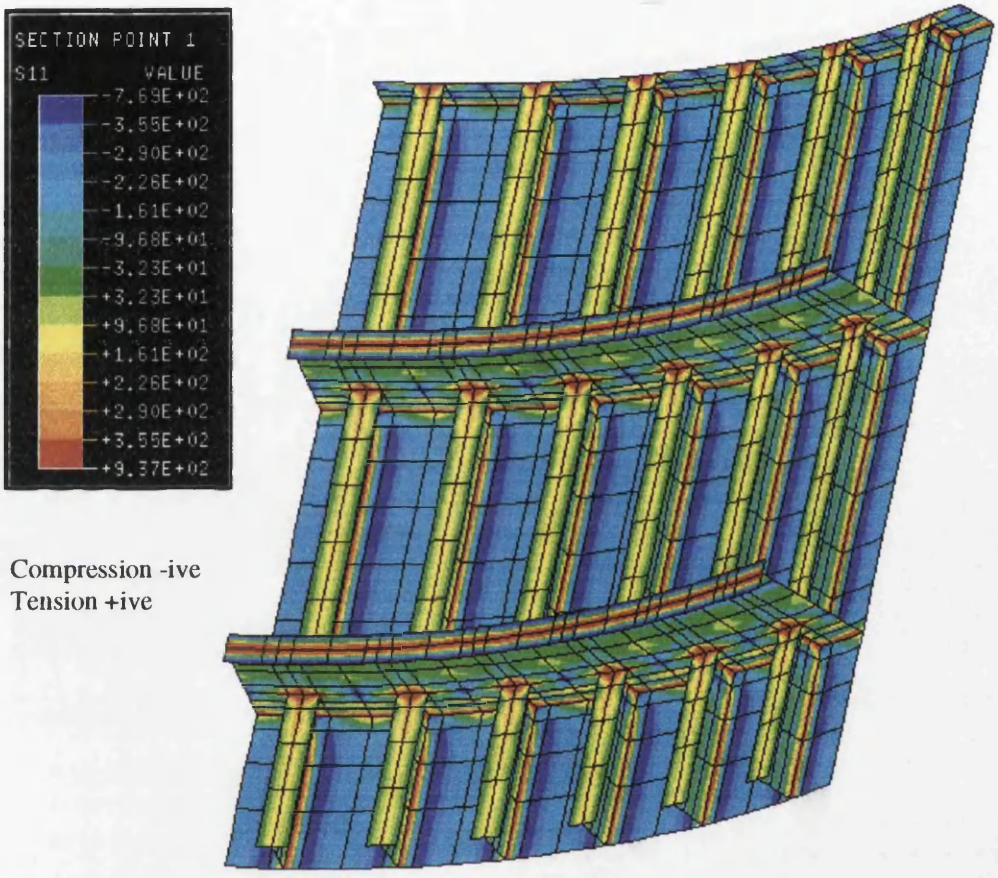


*Fig. A2.1.7.1, Model 1(ortho), circumferential residual stress at layer 1 (the far surface of all elements in the diagram) after the cold forming and welding steps.*

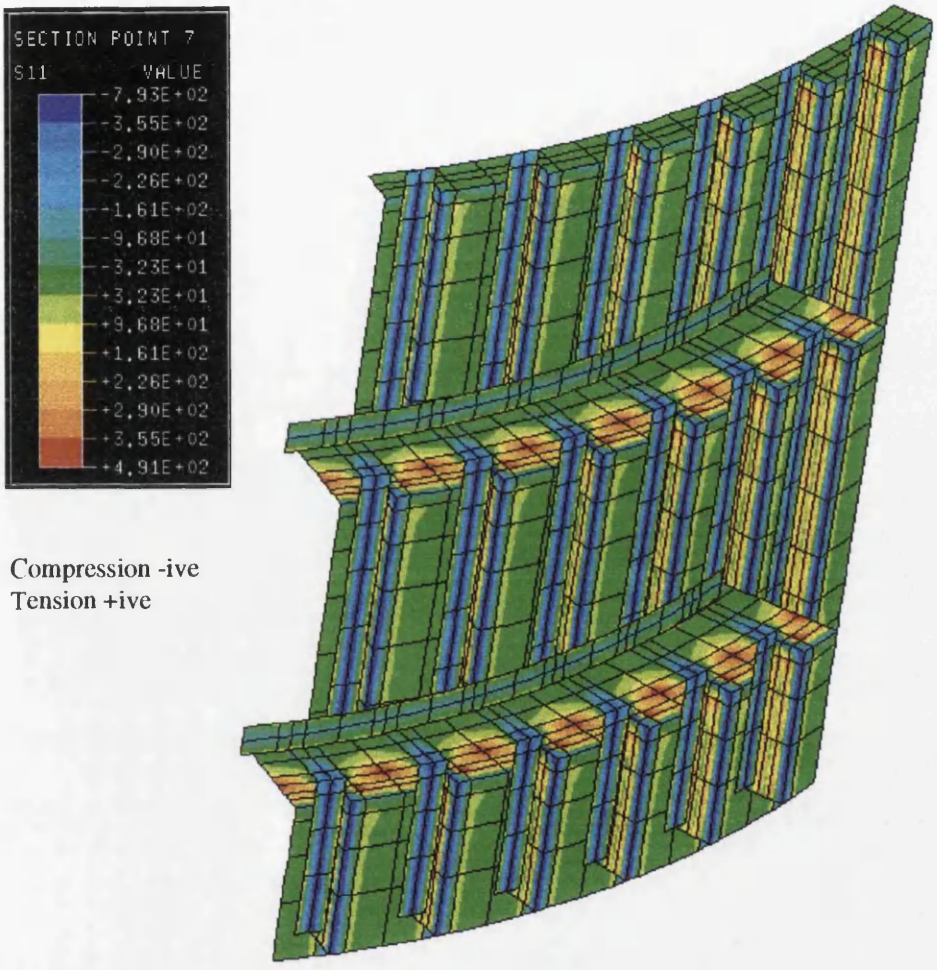


*Fig. A2.1.7.2, Model 1(ortho), circumferential residual stress at mid thickness after the cold forming and welding steps.*

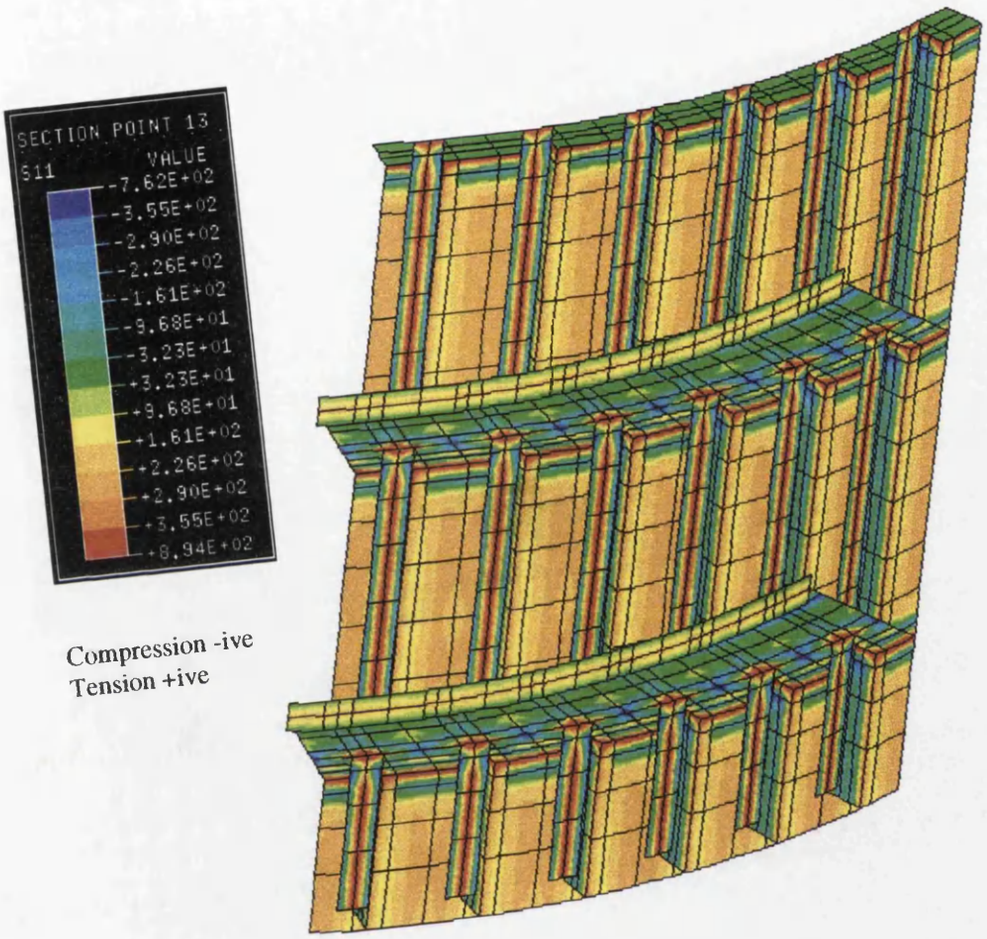


*Fig. A2.1.7.3, Model 1(ortho), circumferential residual stress at layer 13 (the near surface of all elements in the diagram) after the cold forming and welding steps.*

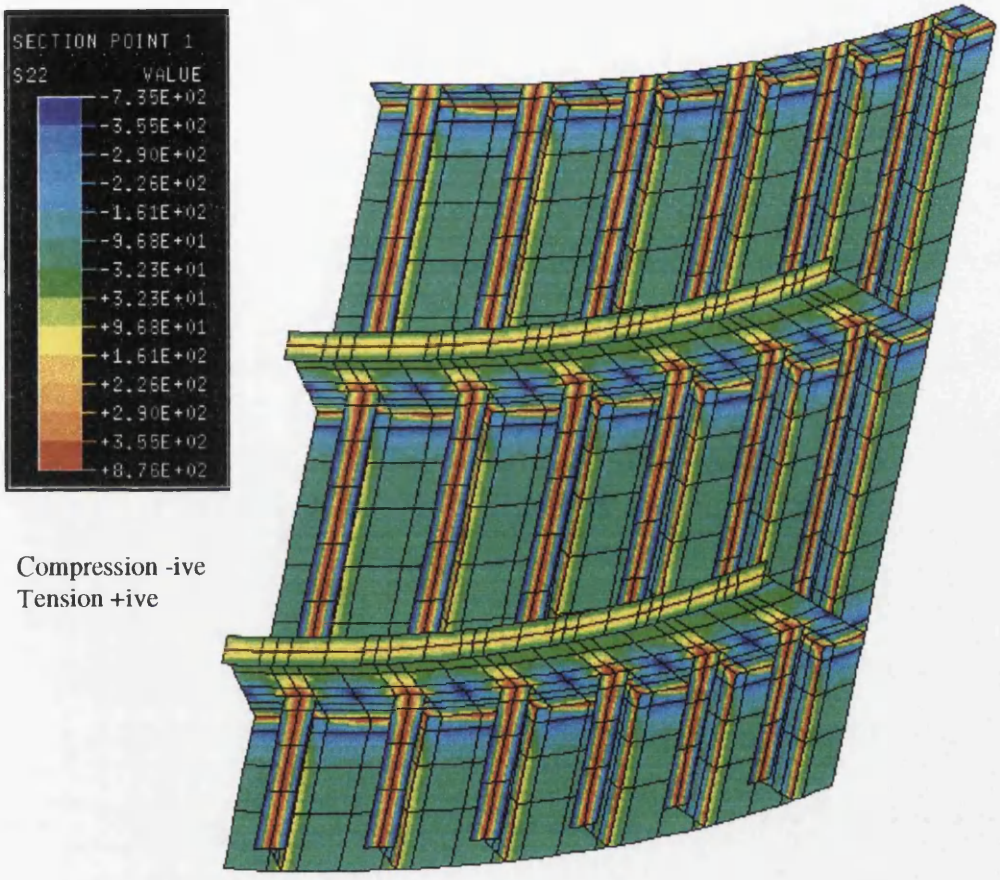


*Fig. A2.1.7.4, Model 1(ortho), axial residual stress at layer 1 (the far surface of all elements in the diagram) after the cold forming and welding steps.*

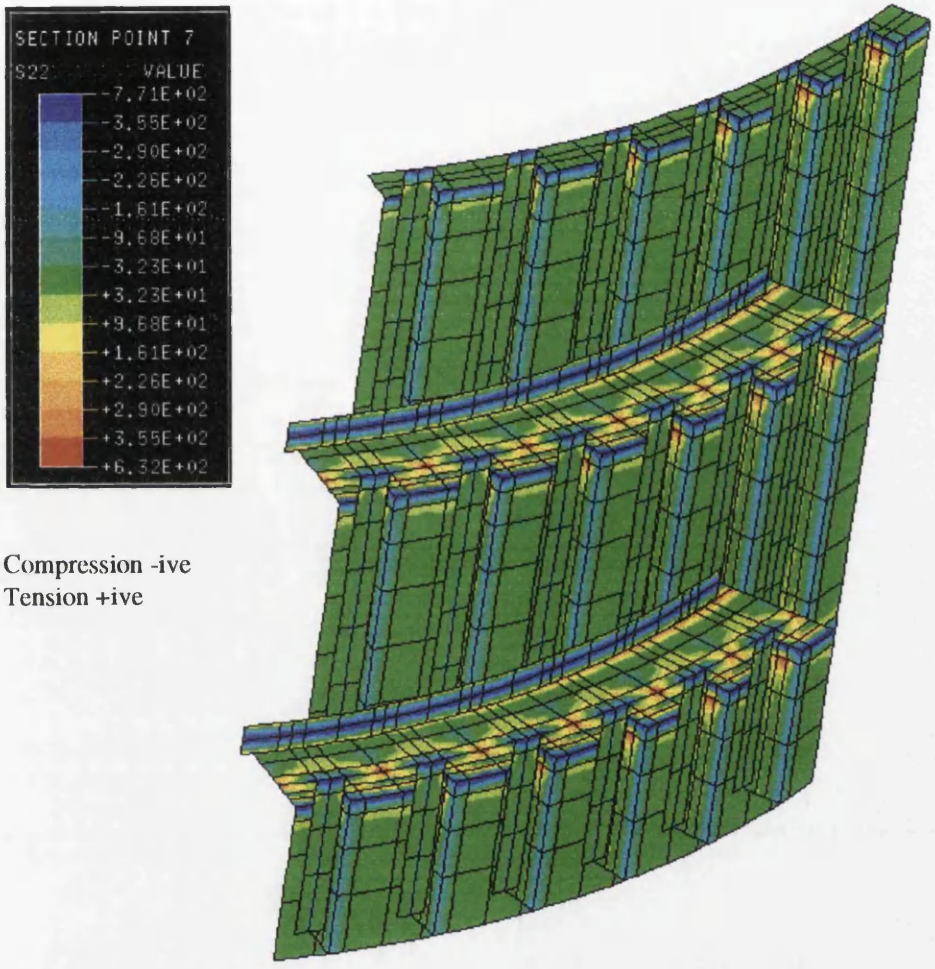


Compression -ive
Tension +ive

*Fig. A2.1.7.5, Model 1(ortho), axial residual stress at mid thickness after the cold forming and welding steps.*

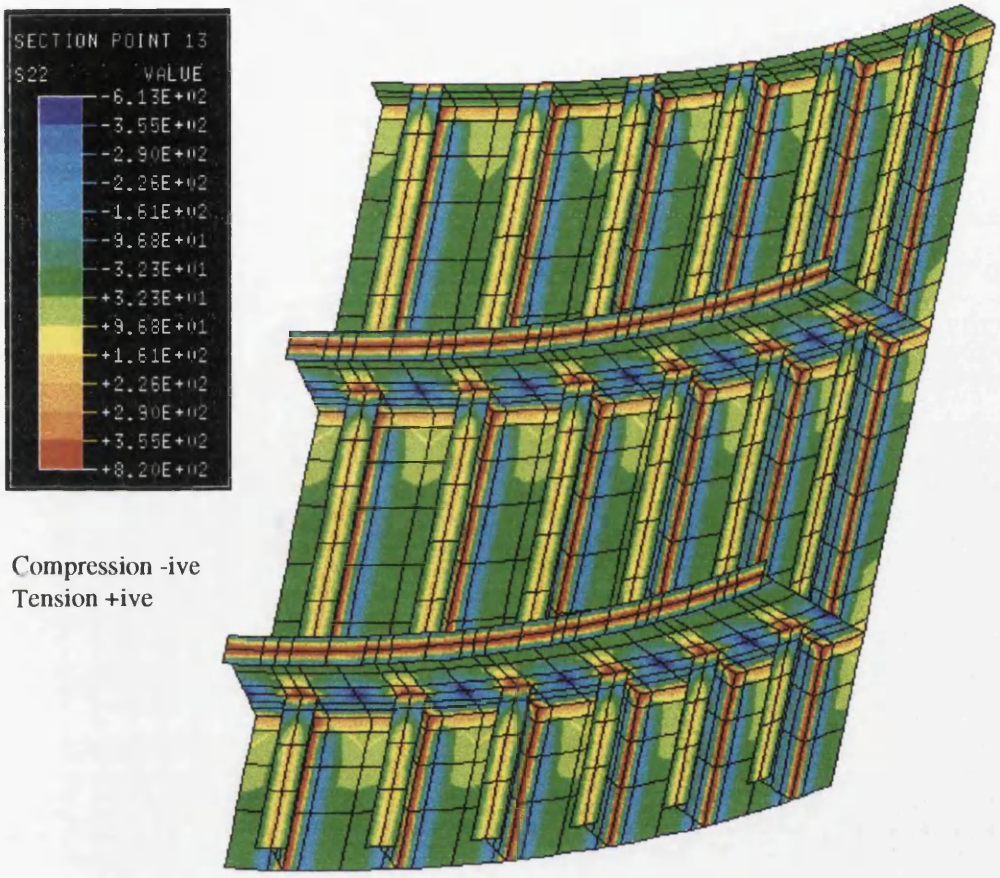


*Fig. A2.1.7.6, Model 1(ortho), axial residual stress at layer 13 (the near surface of all elements in the diagram) after the cold forming and welding steps.*

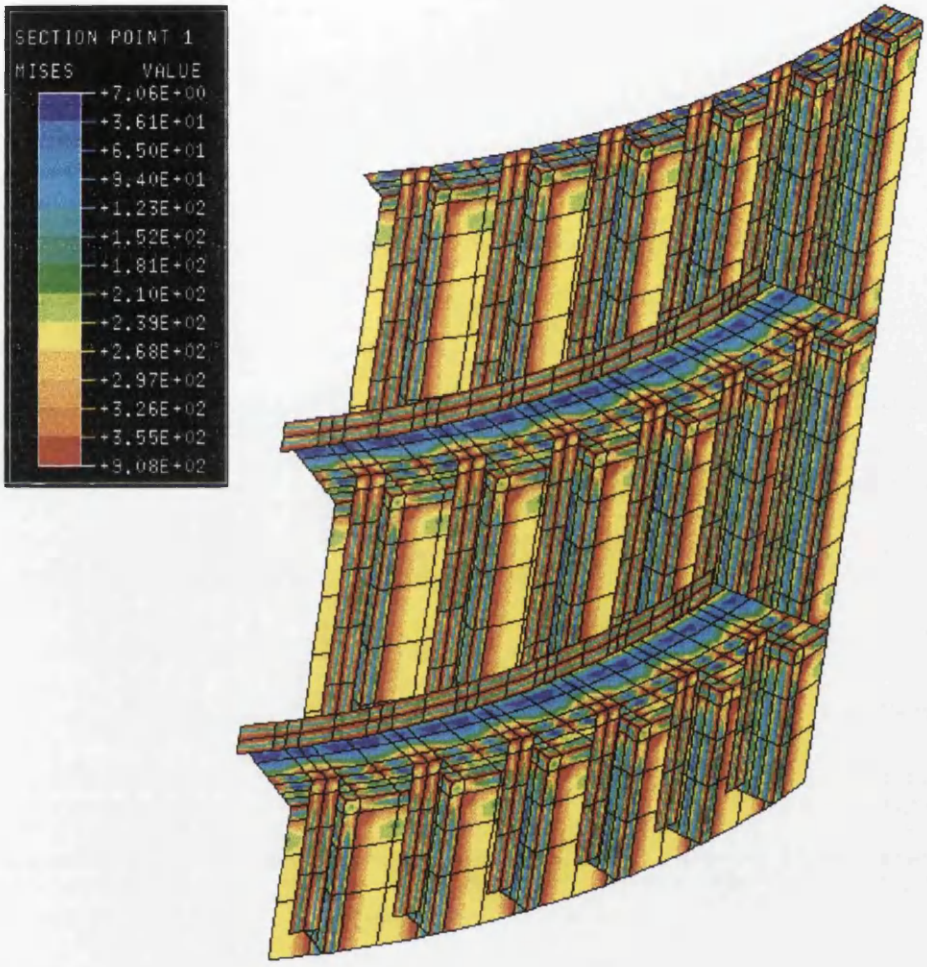


*Fig. A2.1.7.7, Model 1(ortho), Von Mises equivalent stress at layer 1 (the far surface of all elements in the diagram) after the cold forming and welding steps.*

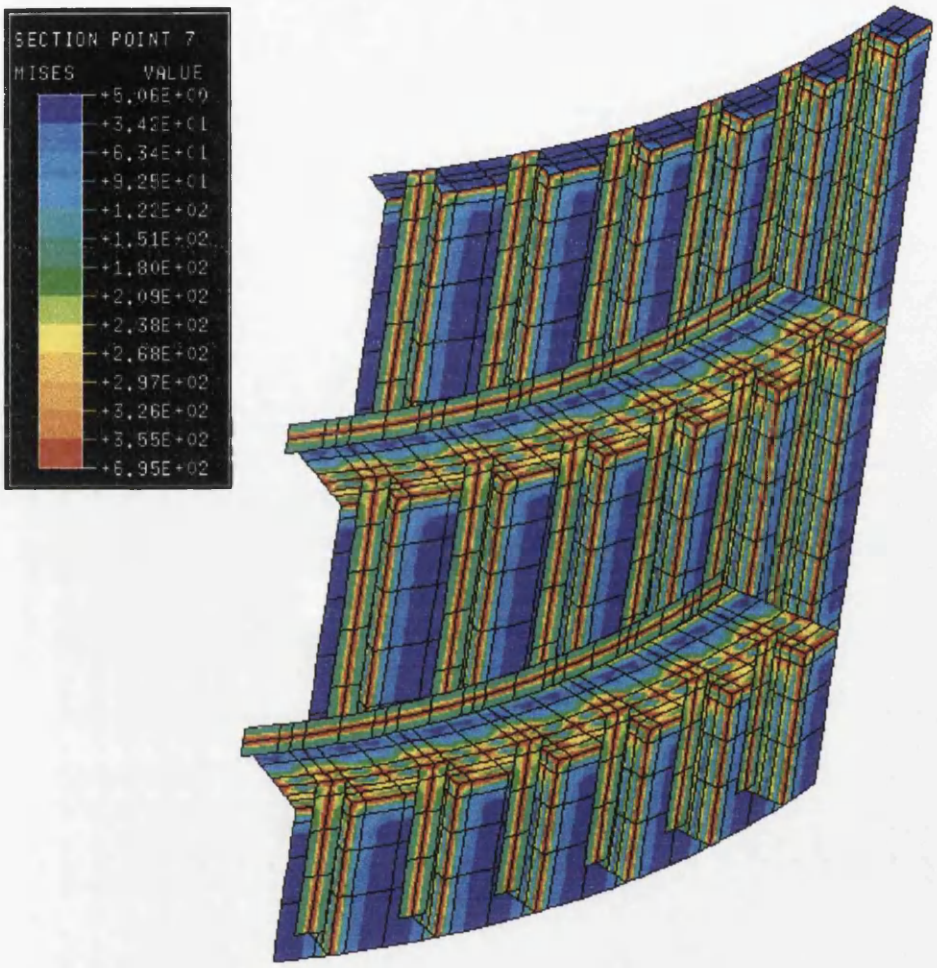


*Fig. A2.1.7.8, Model 1(ortho), Von Mises equivalent stress at mid thickness after the cold forming and welding steps.*

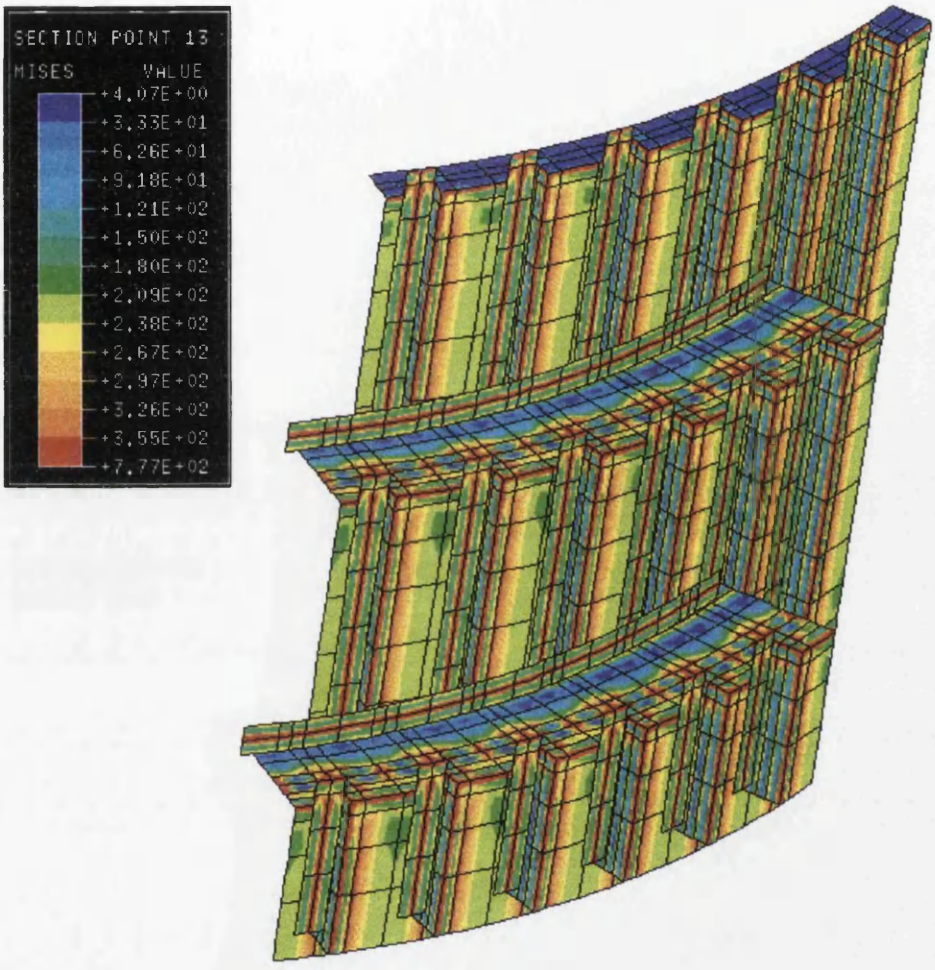


*Fig. A2.1.7.9, Model 1(ortho), mises equivalent stress at layer 13 (the near surface of all elements in the diagram) after the cold forming and welding steps.*

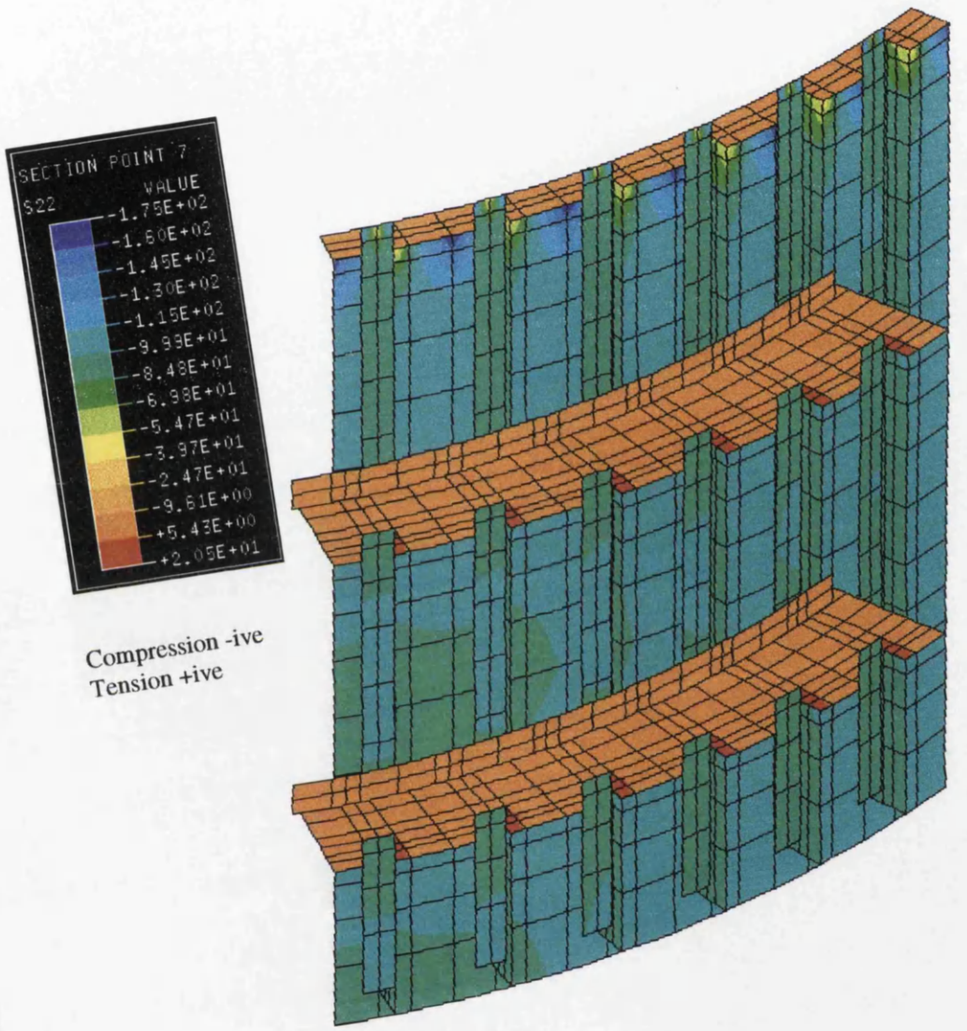


*Fig. A2.1.7.10, Model 1(ortho), Axial stress at mid thickness for the case* ***without*** *residual stress, after the axial loading step.*

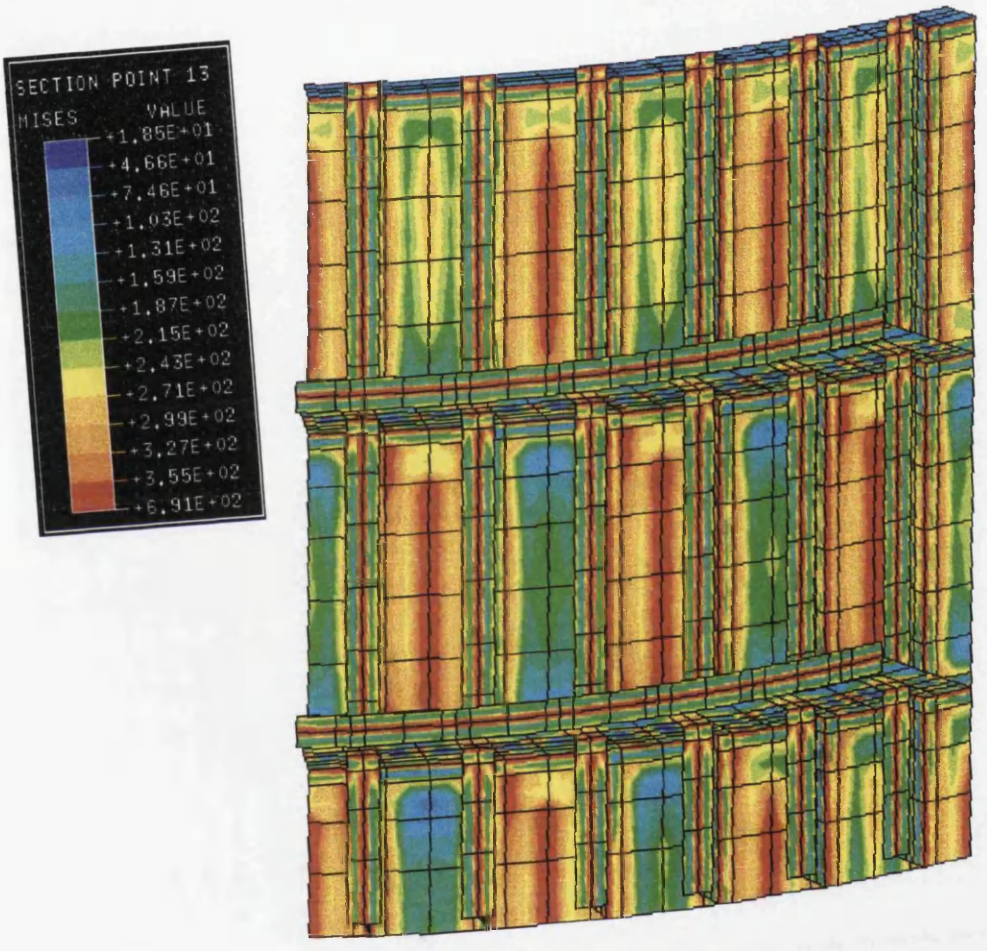


*Fig. A2.1.7.11, Model 1(ortho), Von Mises equivalent stress at layer 13 (the near surface of all elements in the diagram) after cold forming, welding and axial loading steps, in the surface pressure buckling step, at the point of buckling (see point A, Fig. A2.1.8.1)*

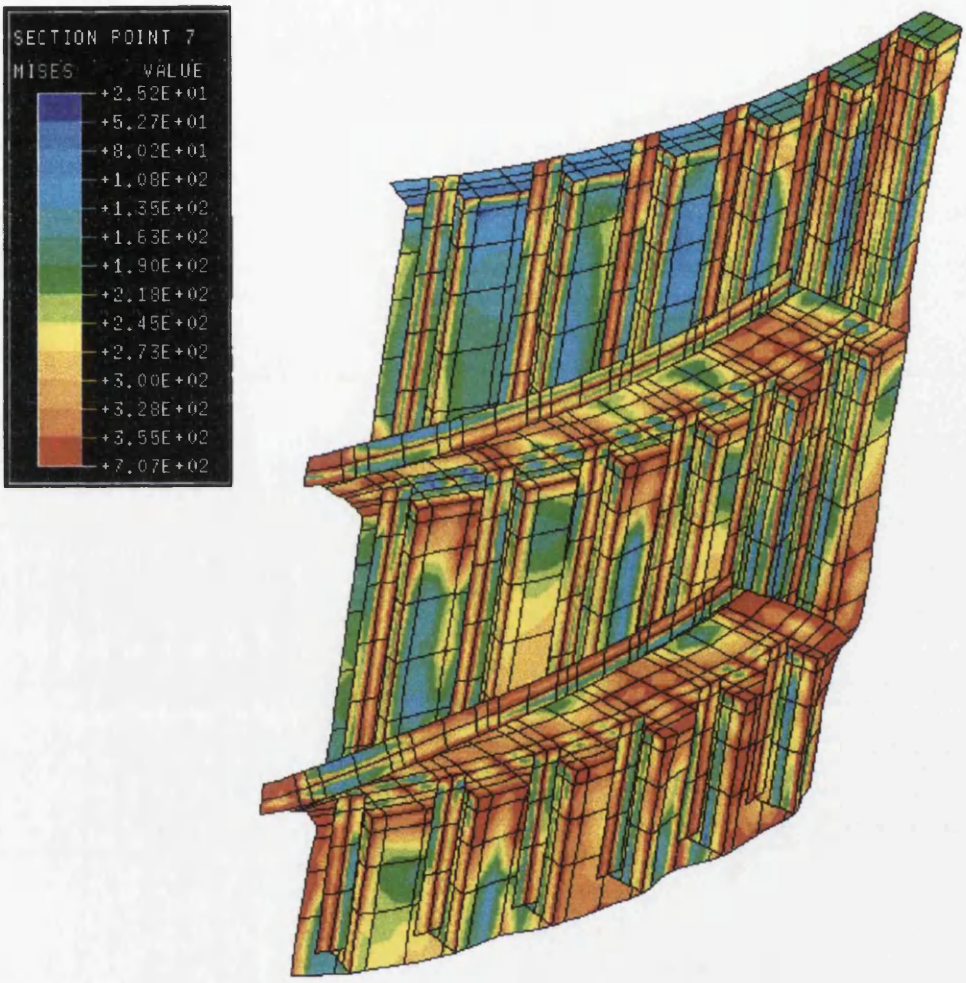


*Fig. A2.1.7.12, Model 1(ortho), Von Mises equivalent stress at mid thickness after cold forming, welding, axial loading and surface pressure buckling steps, at the large displacement buckling stage.*

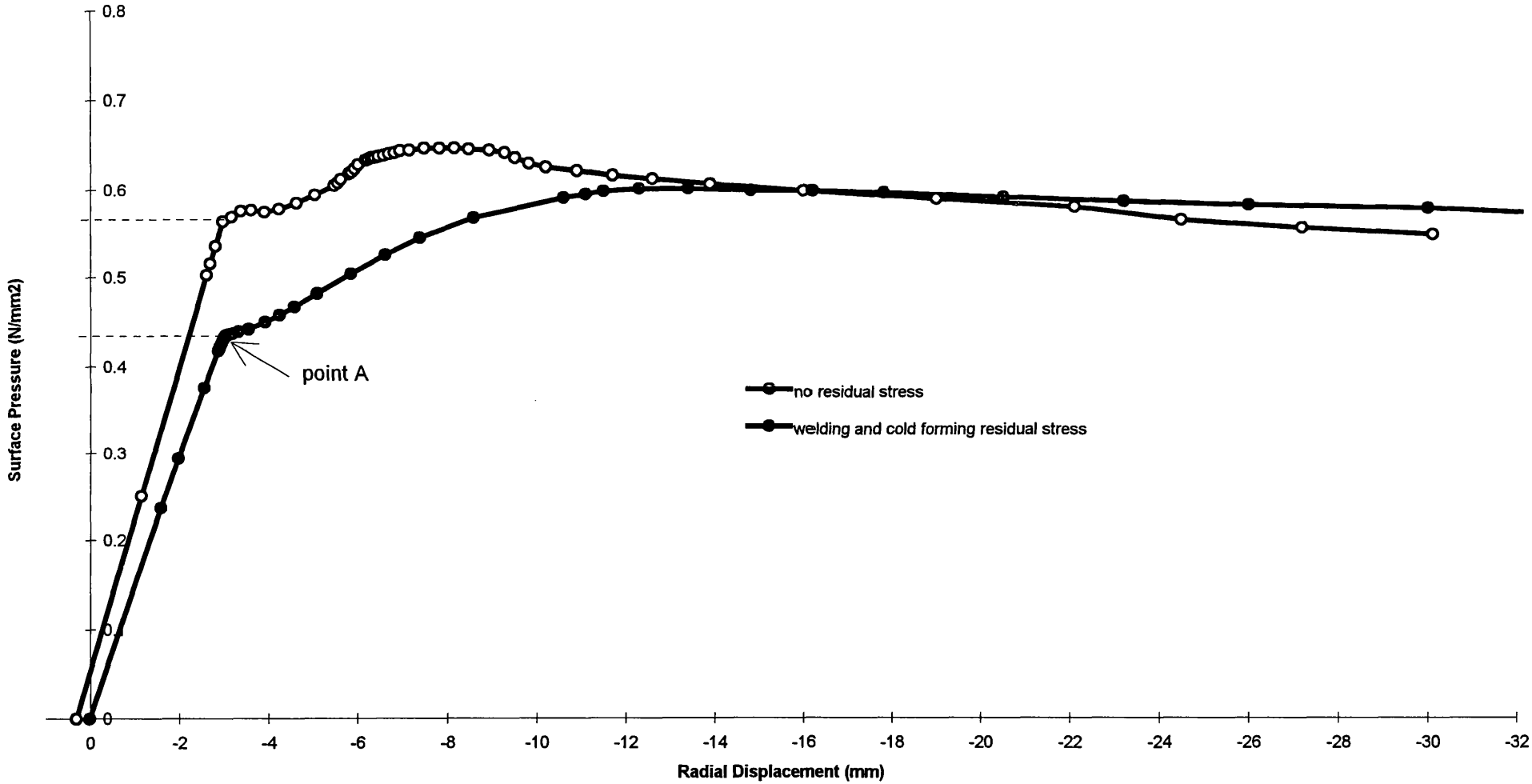


*Fig. A2.1.8.1, Model 1(ortho) load displacement path, Welding and cold forming residual stress*

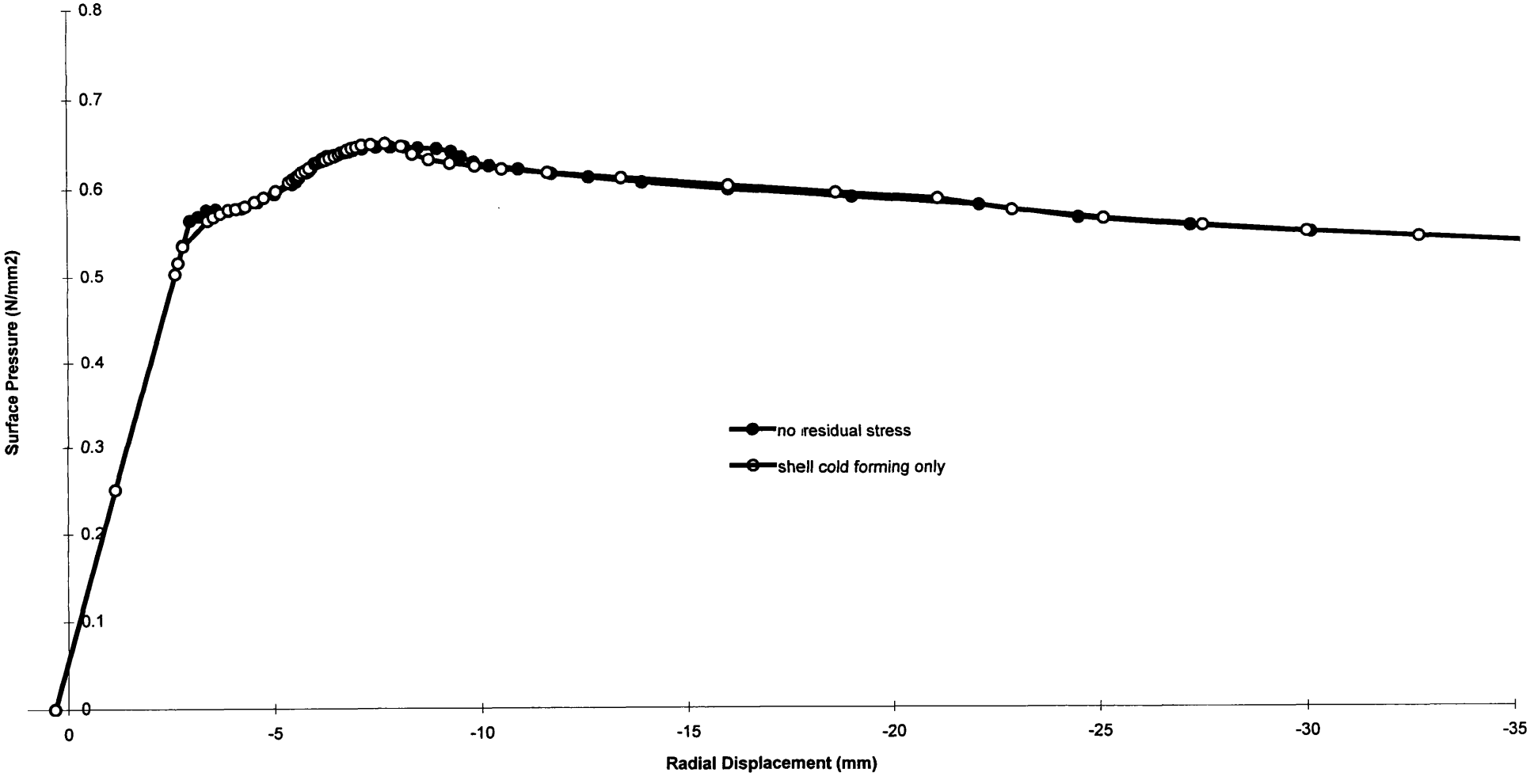


*Fig. A2.1.8.2, Model 1(ortho) load displacement path, cold forming residual stress*

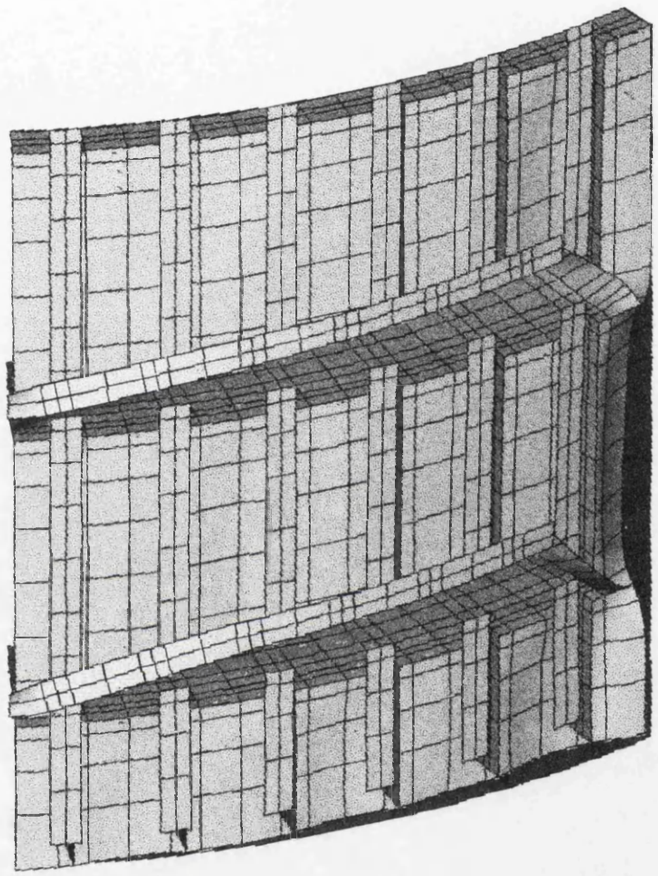

*Fig. A2.1.9.1, Model 1(ortho) without residual stress, with axial loading, displaced shape under active surface pressure at the large displacement buckling stage.*

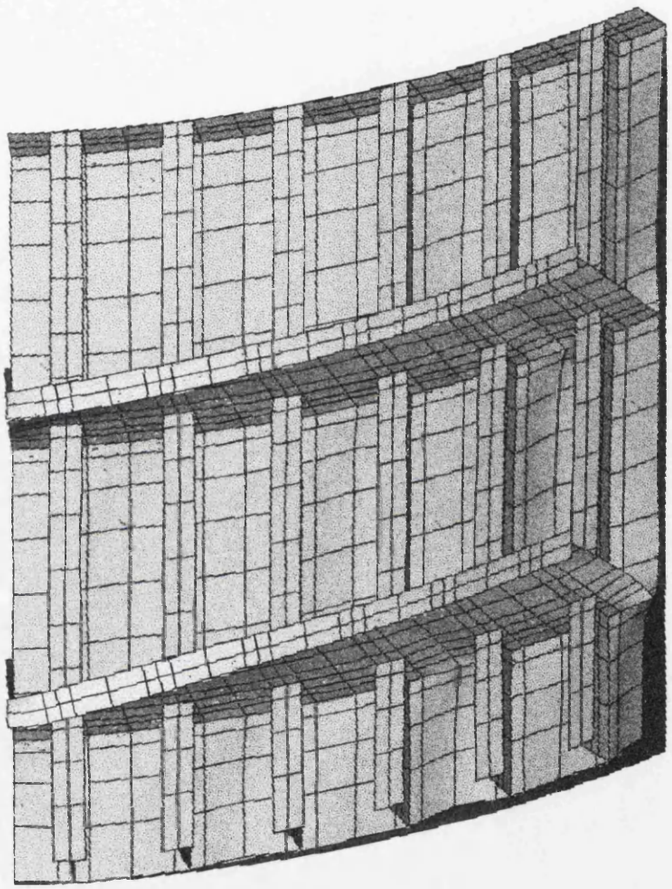

*Fig. A2.1.9.2, Model 1(ortho) with cold forming and welding residual stress and axial loading, displaced shape under active surface pressure at the large displacement buckling stage.*

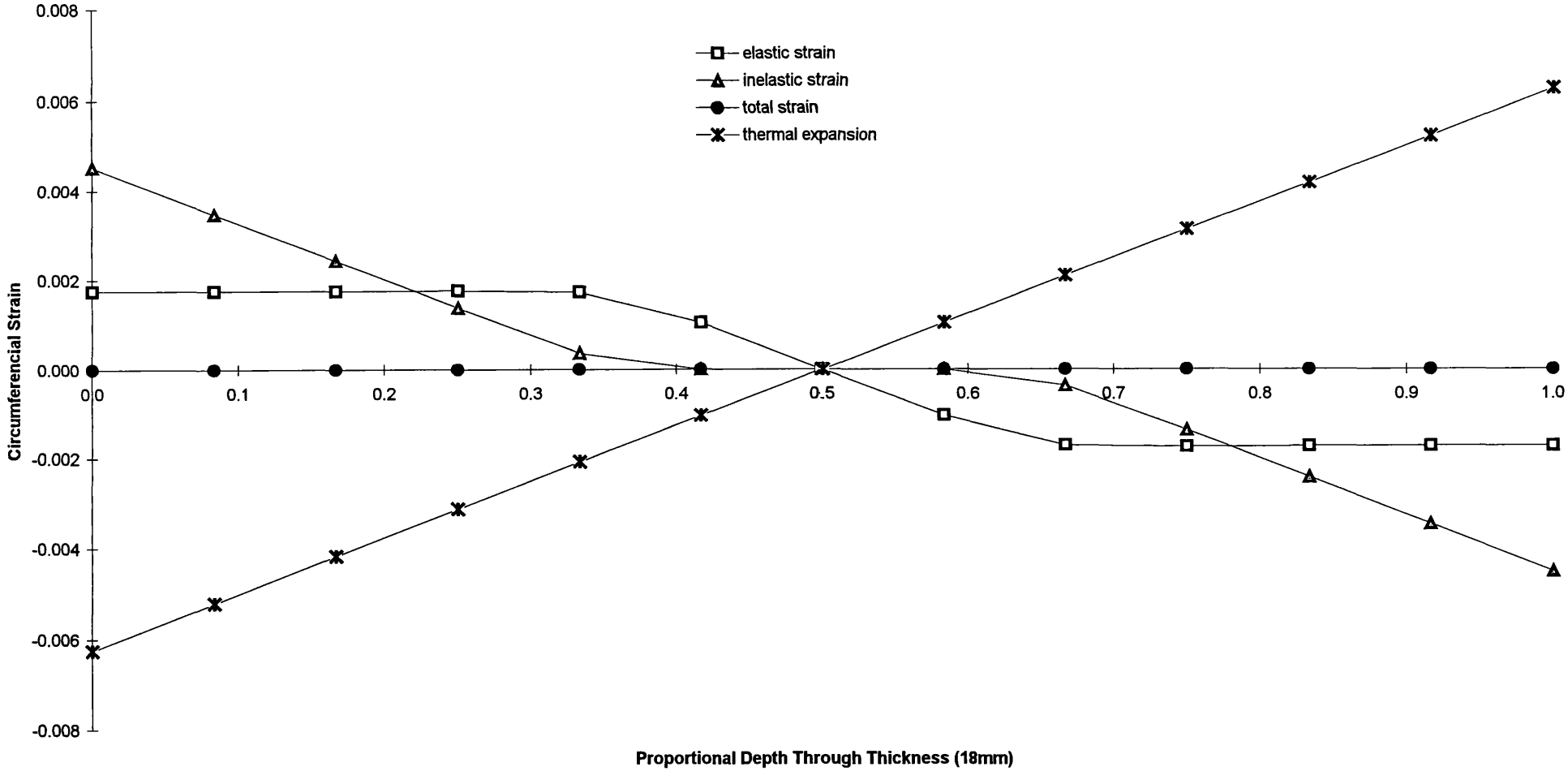


*Fig. A2.2.1.1, Model 2(ortho), bending back during cold forming simulated with thermal exoansion, location 1 in Fig.4.21*

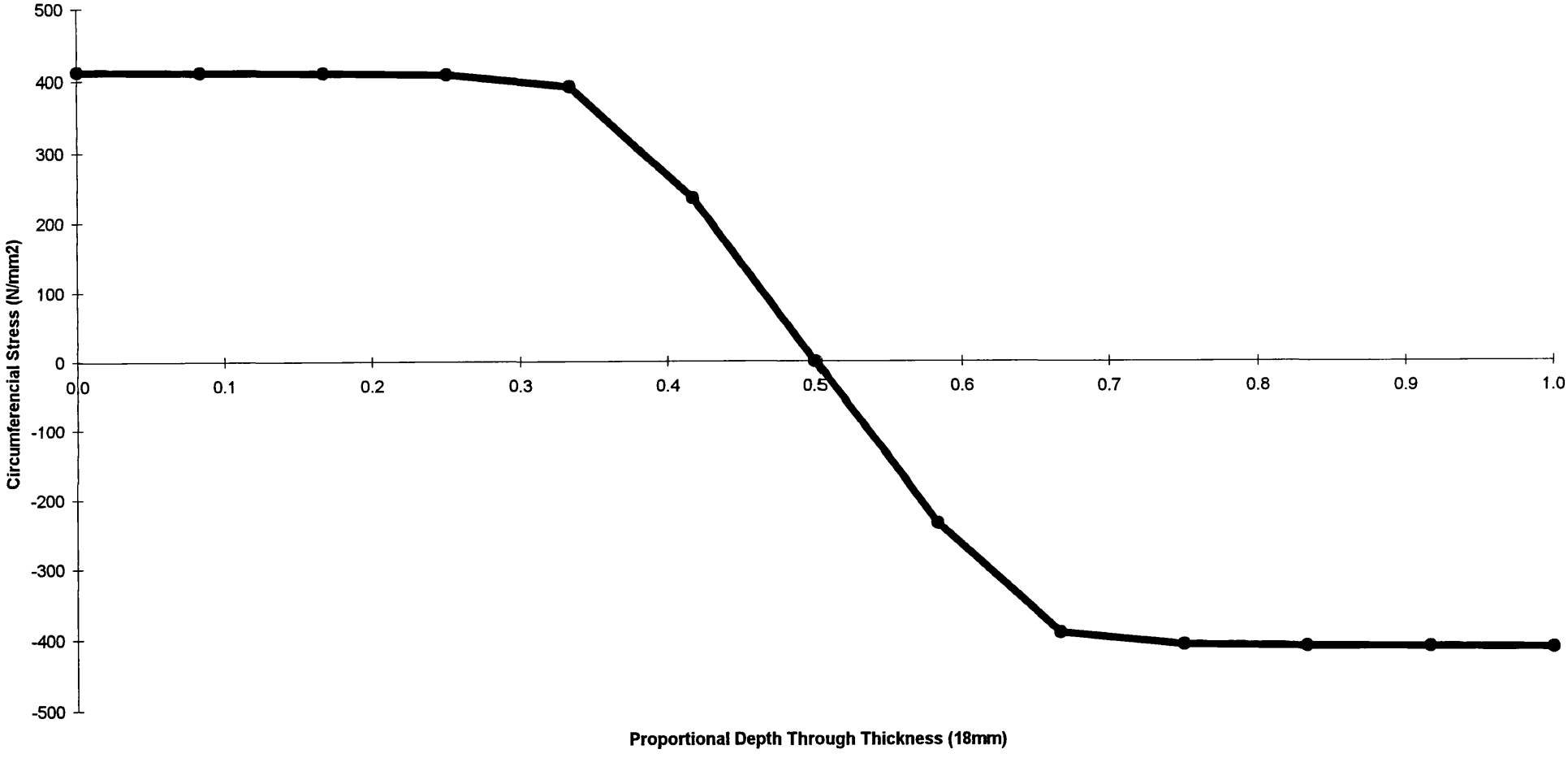


*Fig. A2.2.1.2, Model 2(ortho), bending back during cold forming , location 1 in Fig. 4.21*

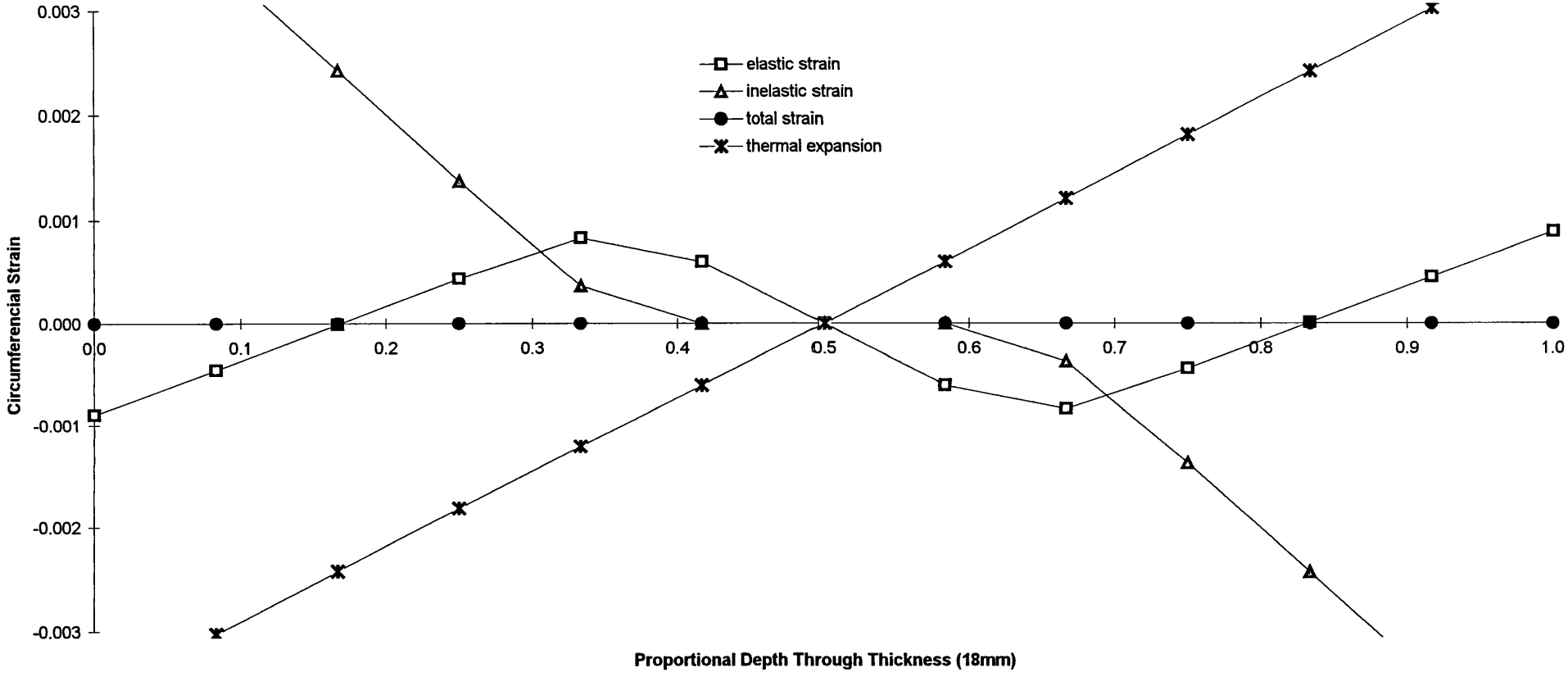


*Fig. A2.2.1.3, Model 2(ortho), spring back in cold forming simulated with thermal expansion, location 1 in Fig. 4.21*

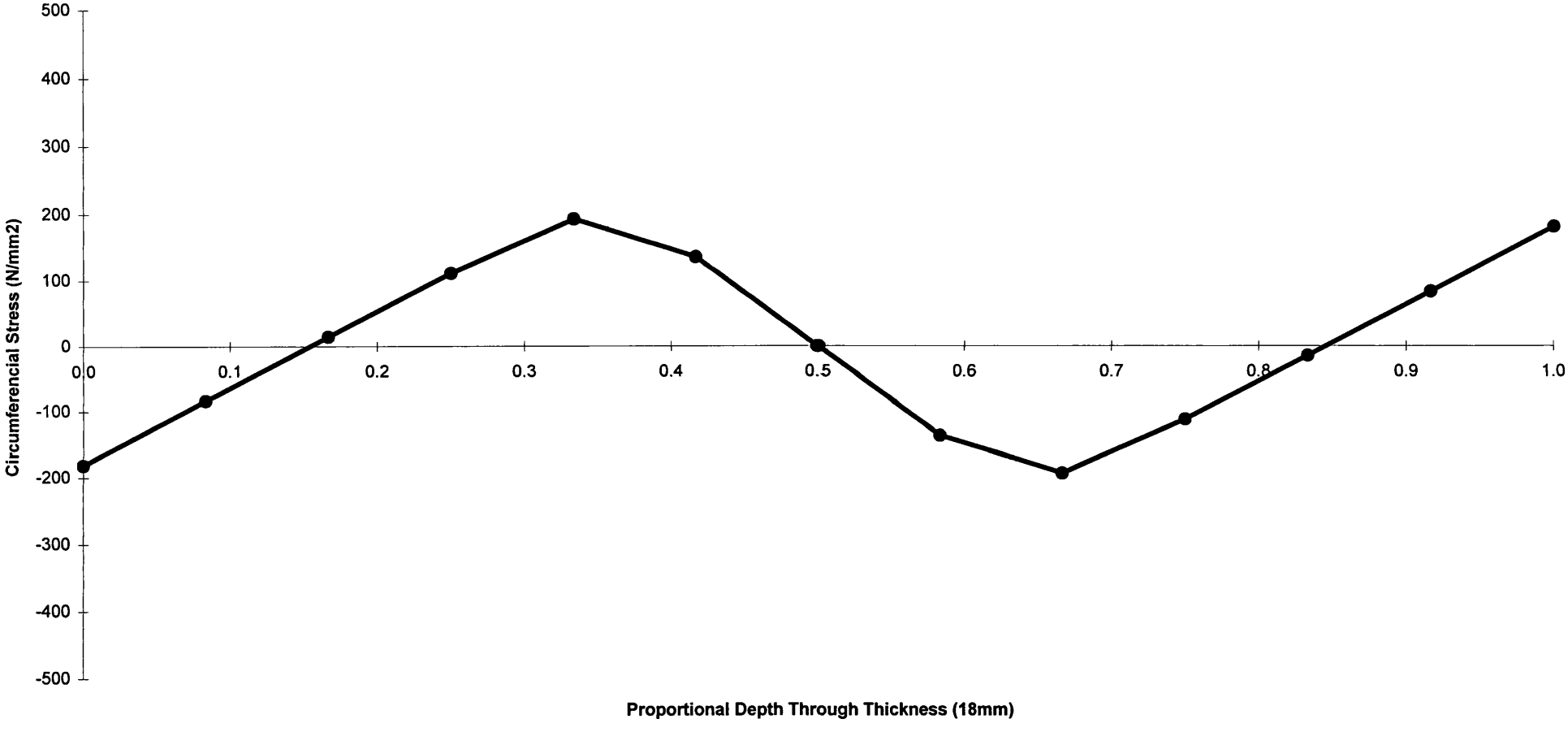


*Fig. A2.2.1.4, Model 2(ortho), spring back in cold forming, location 1 in Fig. 4.21*

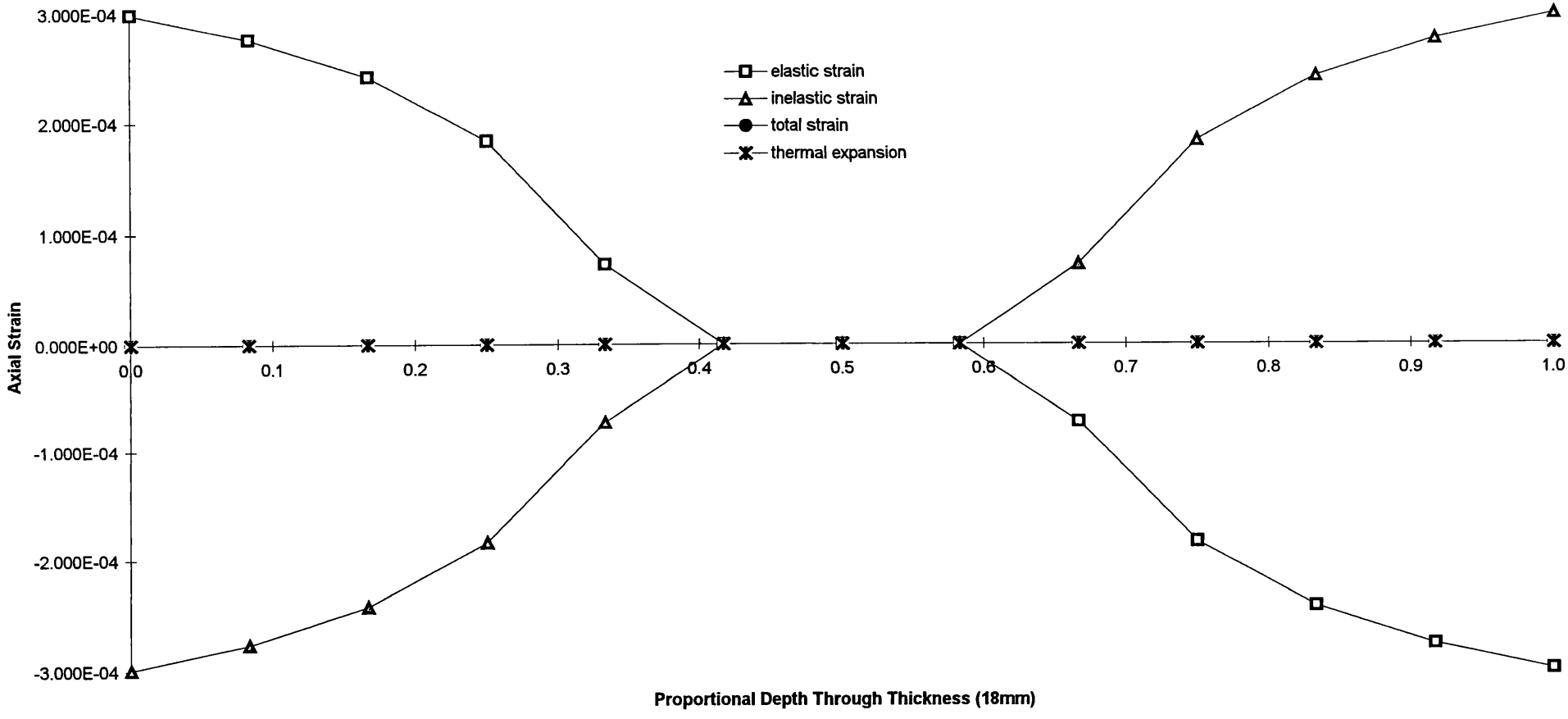


*Fig. A2.2.1.5, Model 2(ortho), bending back during cold forming simulated with thermal exoansion, location 1 in Fig.4.21*

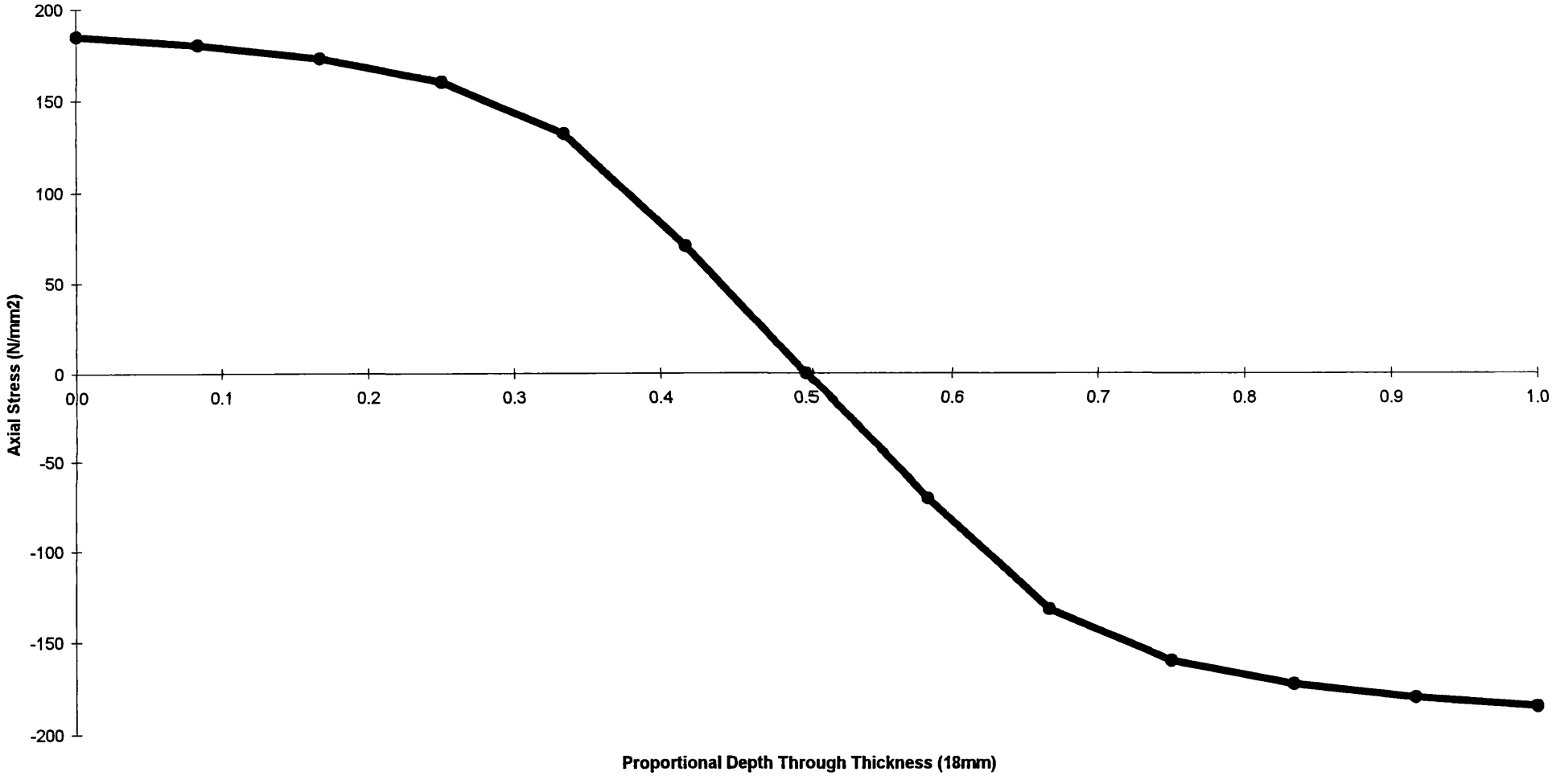


*Fig. A2.2.1.6 , Model 2(ortho), bending back during cold forming , location 1 in Fig. 4.21*

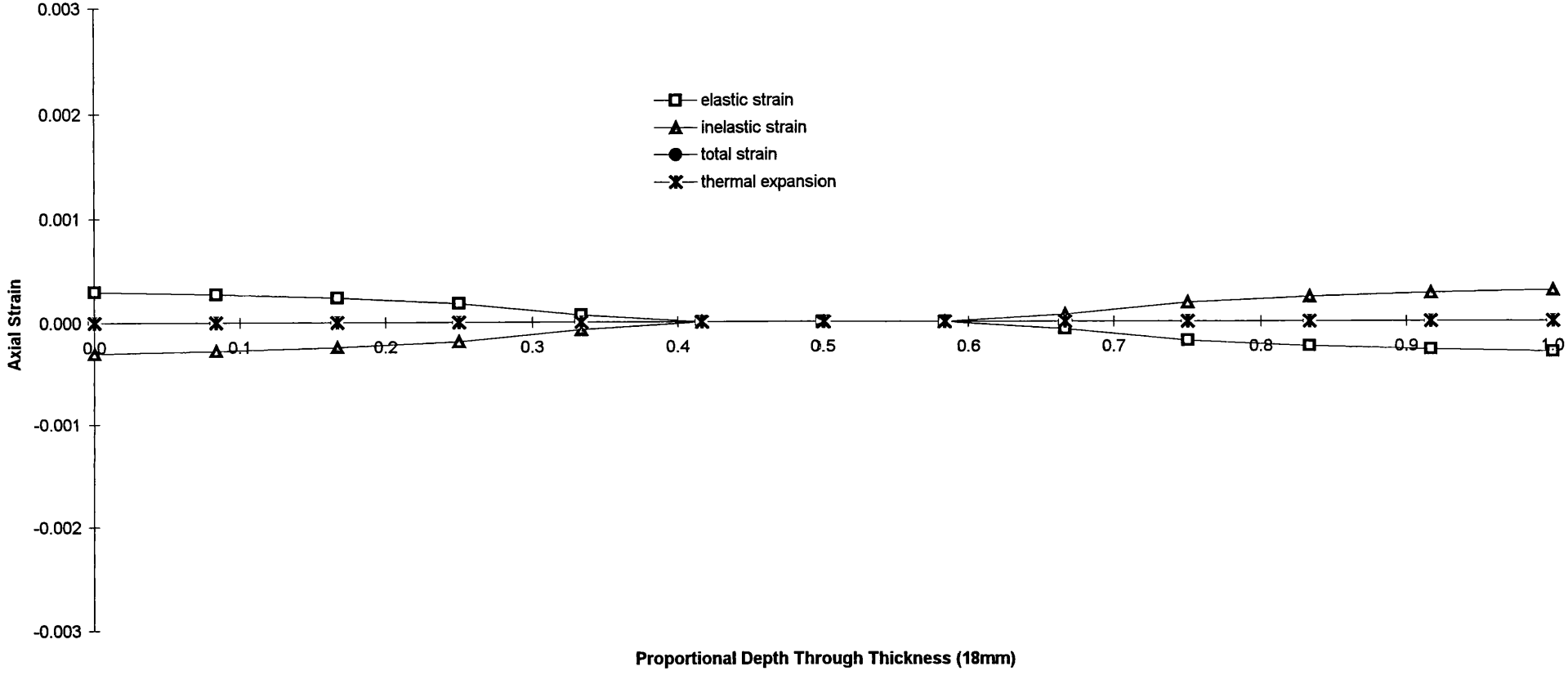


*Fig. A2.2.1.7, Model 2(ortho), spring back in cold forming simulated with thermal expansion, location 1 in Fig. 4.21*

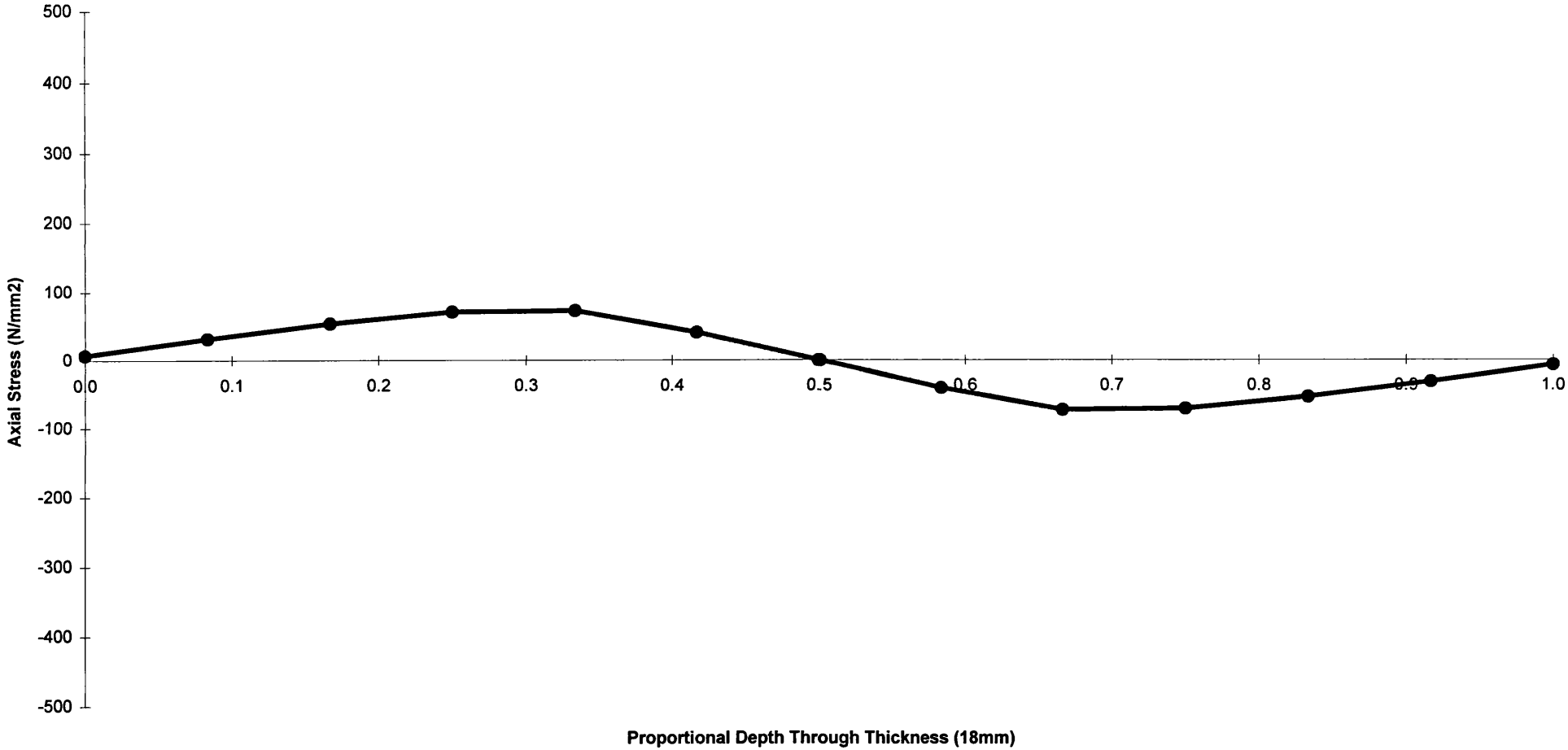


*Fig. A2.2.1.8, Model 2(ortho), spring back in cold forming, location 1 in Fig. 4.21*

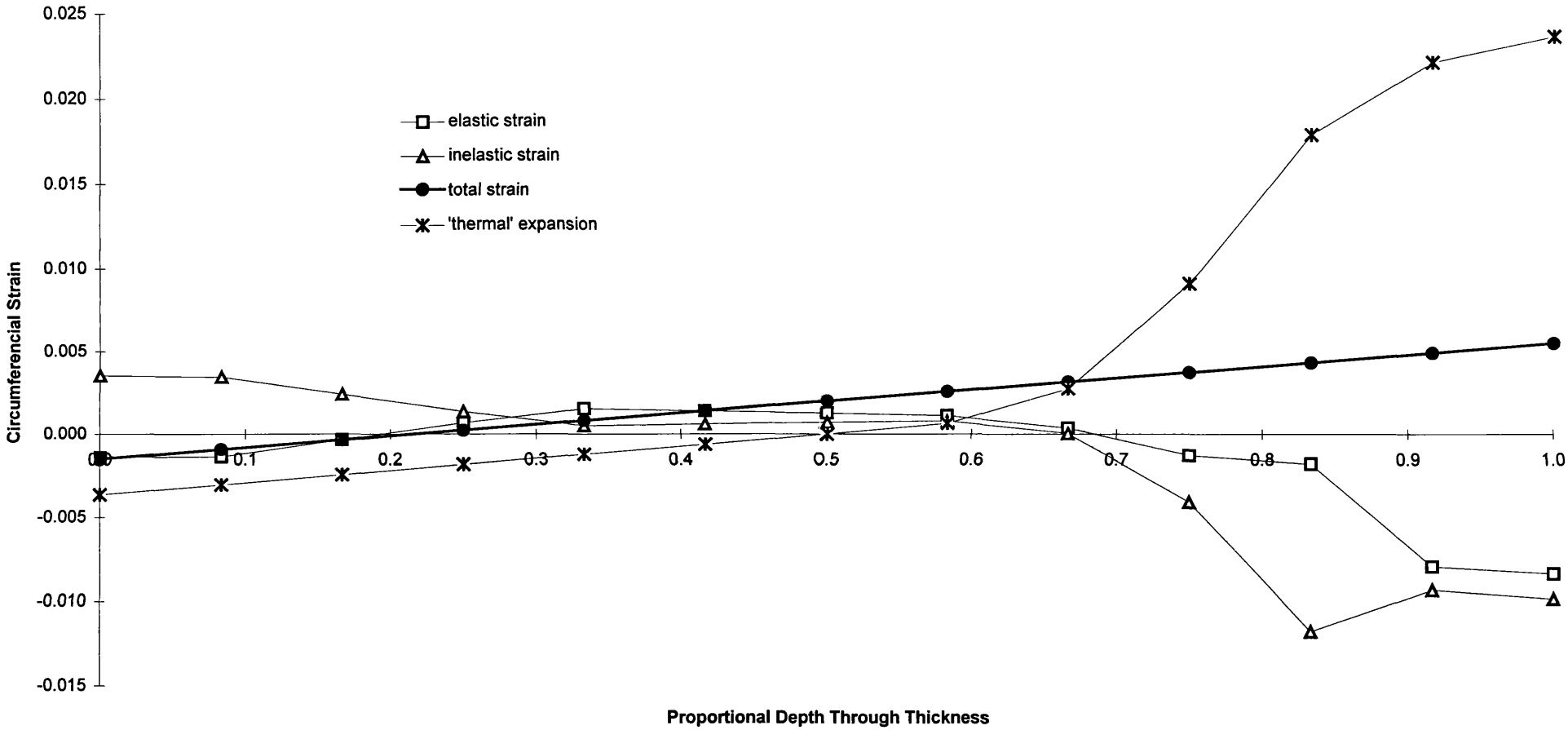


*Fig. A2.2.2.1, Model 2(ortho), thermal expansion in the welding steps, location 1 in Fig.4.21*

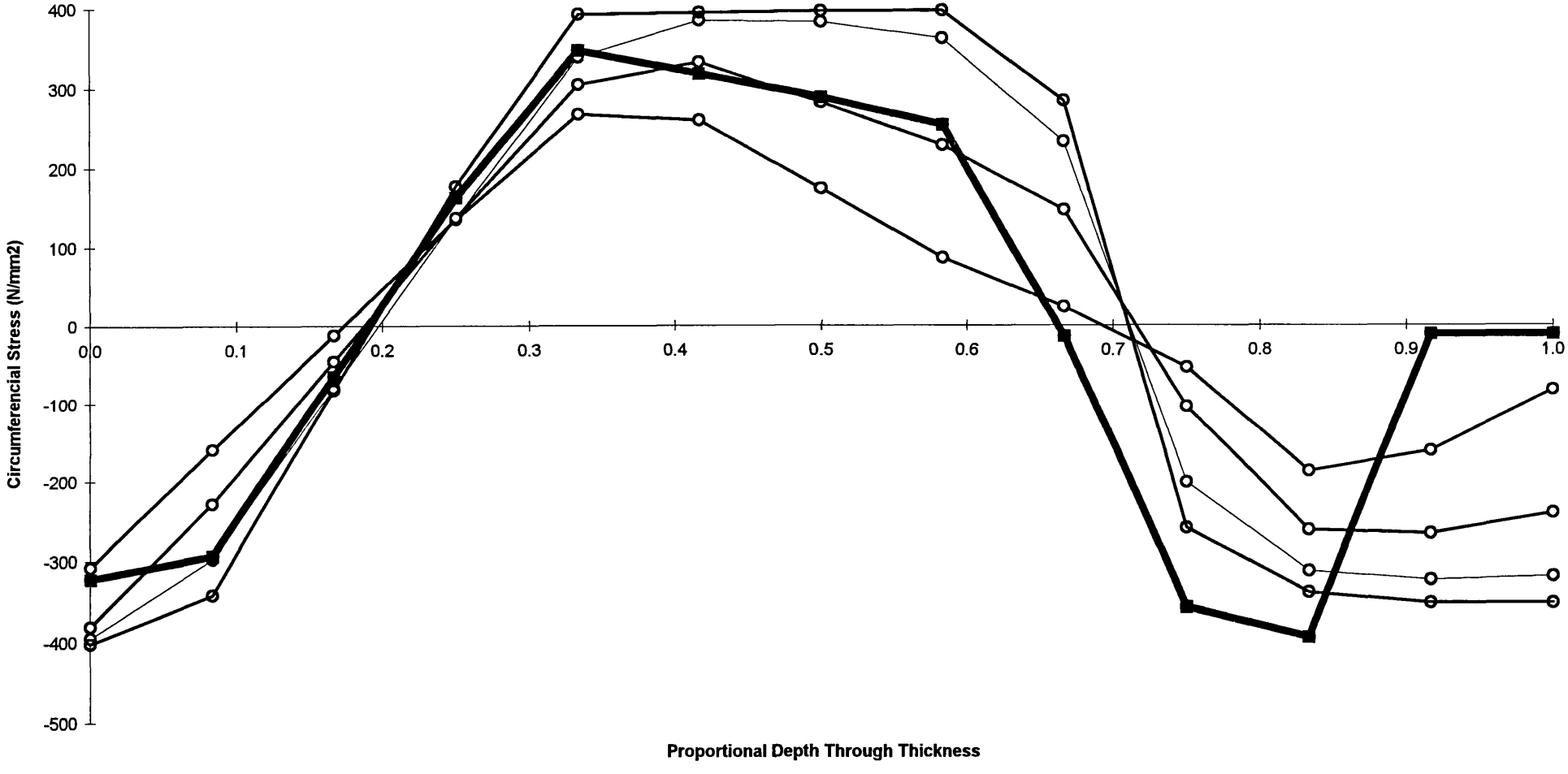


*Fig. A2.2.2.2, Model 2(ortho), thermal expansion in the welding steps, location 1 in Fig. 4.21*

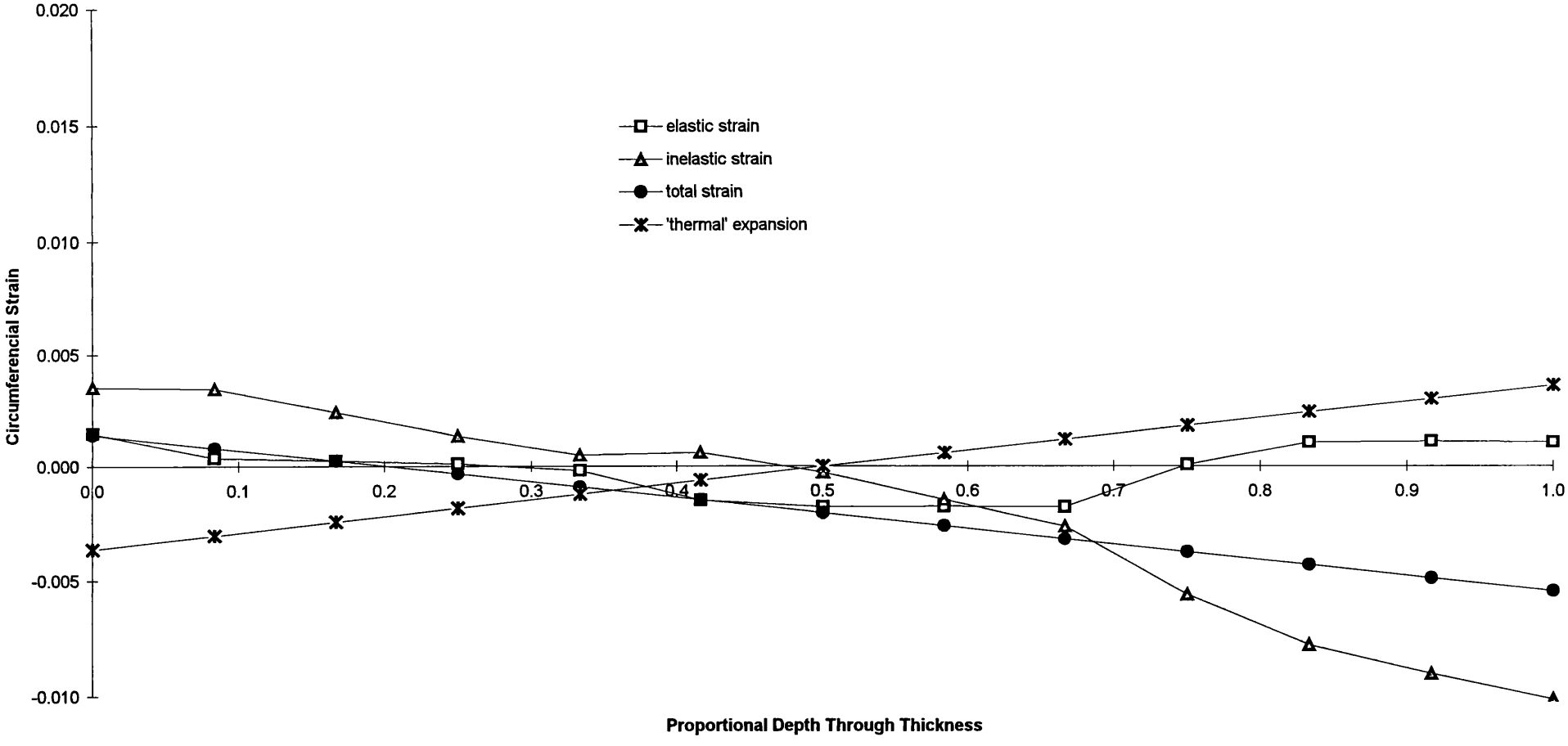


*Fig. A2.2.2.3, Model 2(ortho), thermal contraction in the welding steps, location 1 in Fig. 4.21*

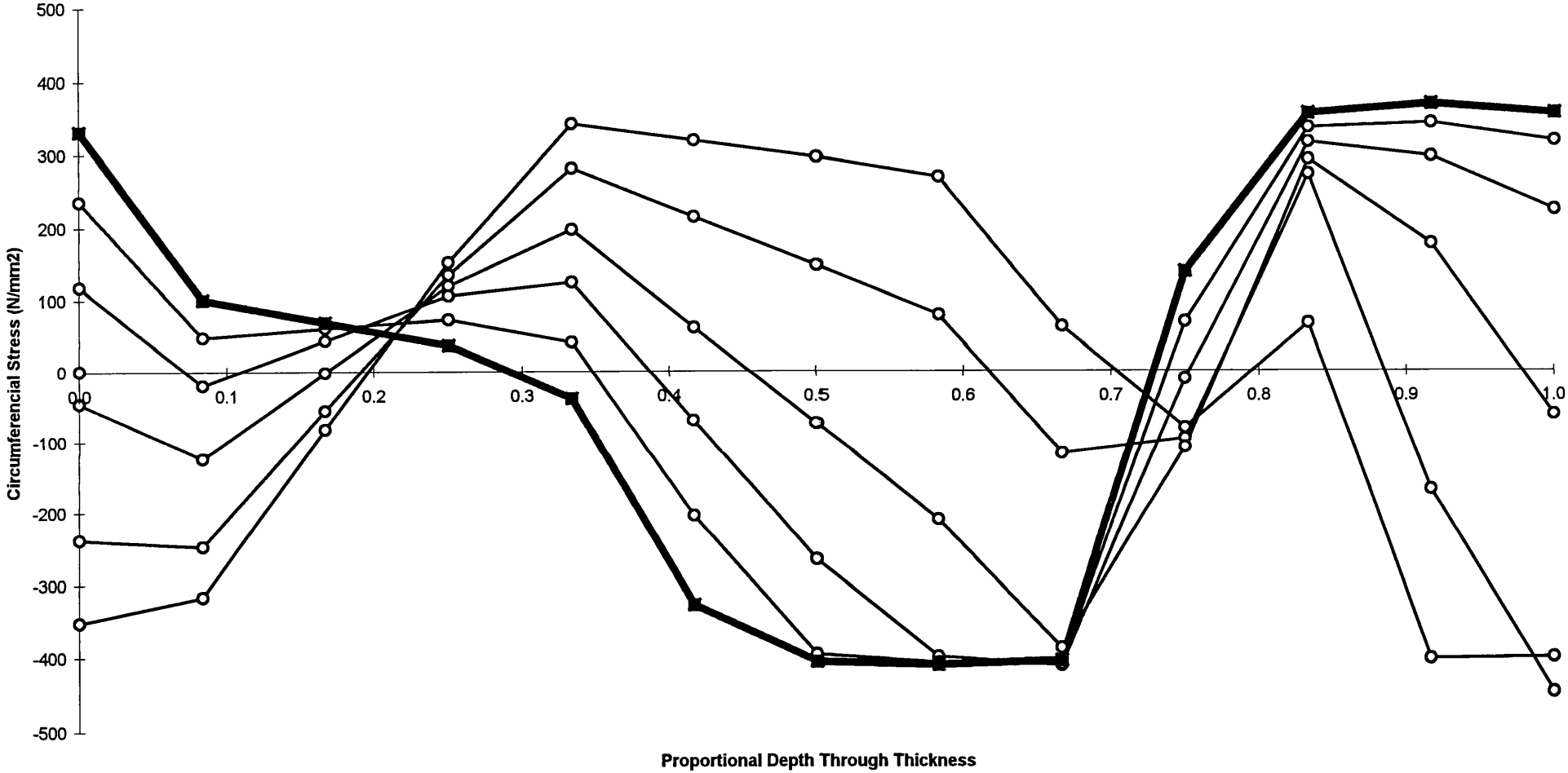


*Fig. A2.2.2.4, Model 2(ortho), thermal contraction in the welding steps, location 1 in Fig. 4.21*

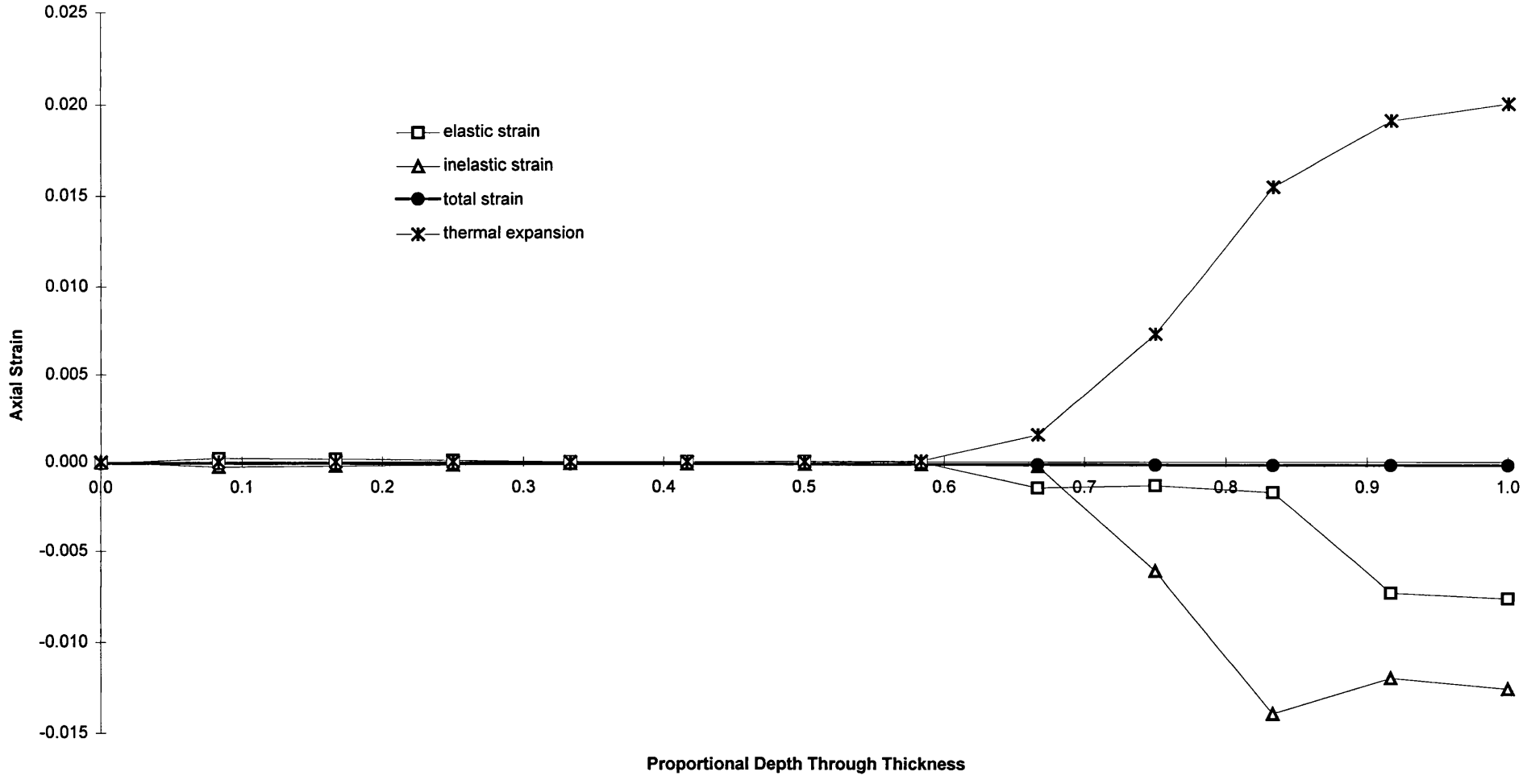


*Fig. A2.2.2.5, Model 2(ortho), thermal expansion in the welding steps, location 1 in Fig.4.21*

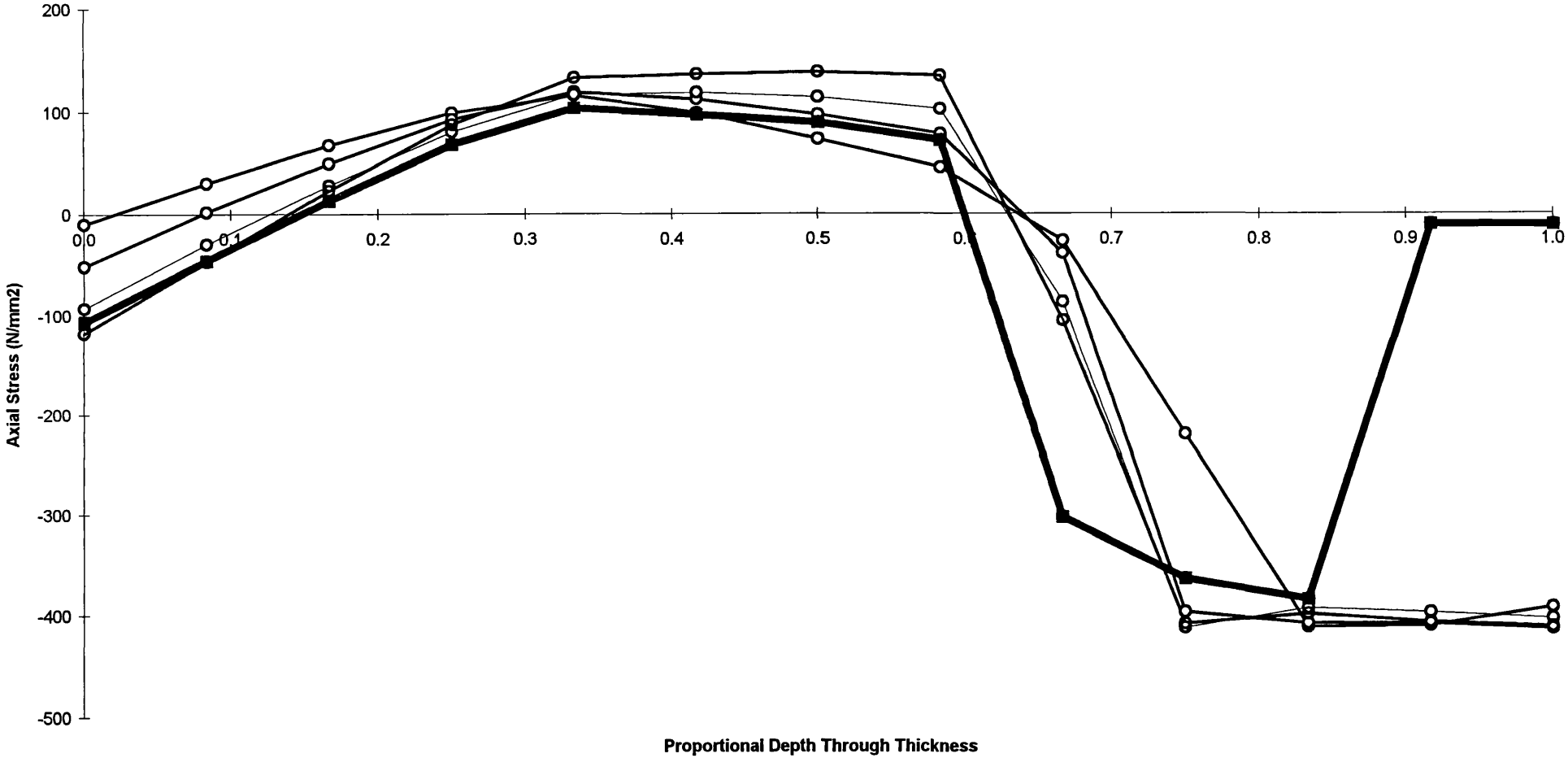


*Fig. A2.2.2.6, Model 2(ortho), thermal expansion in the welding steps, location 1 in Fig. 4.21*

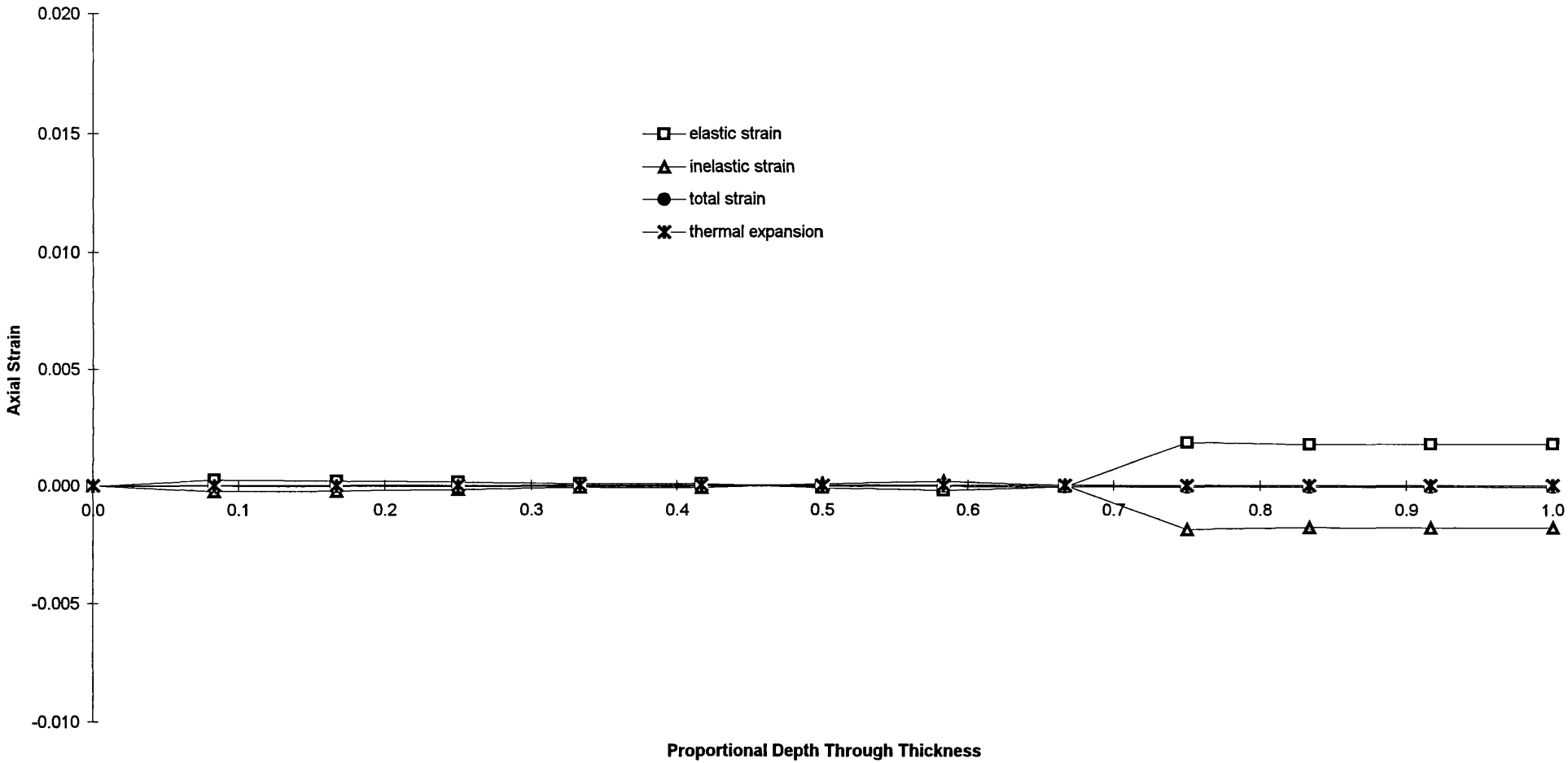


*Fig. A2.2.2.7, Model 2(ortho), thermal contraction in the welding steps, location 1 in Fig. 4.21*

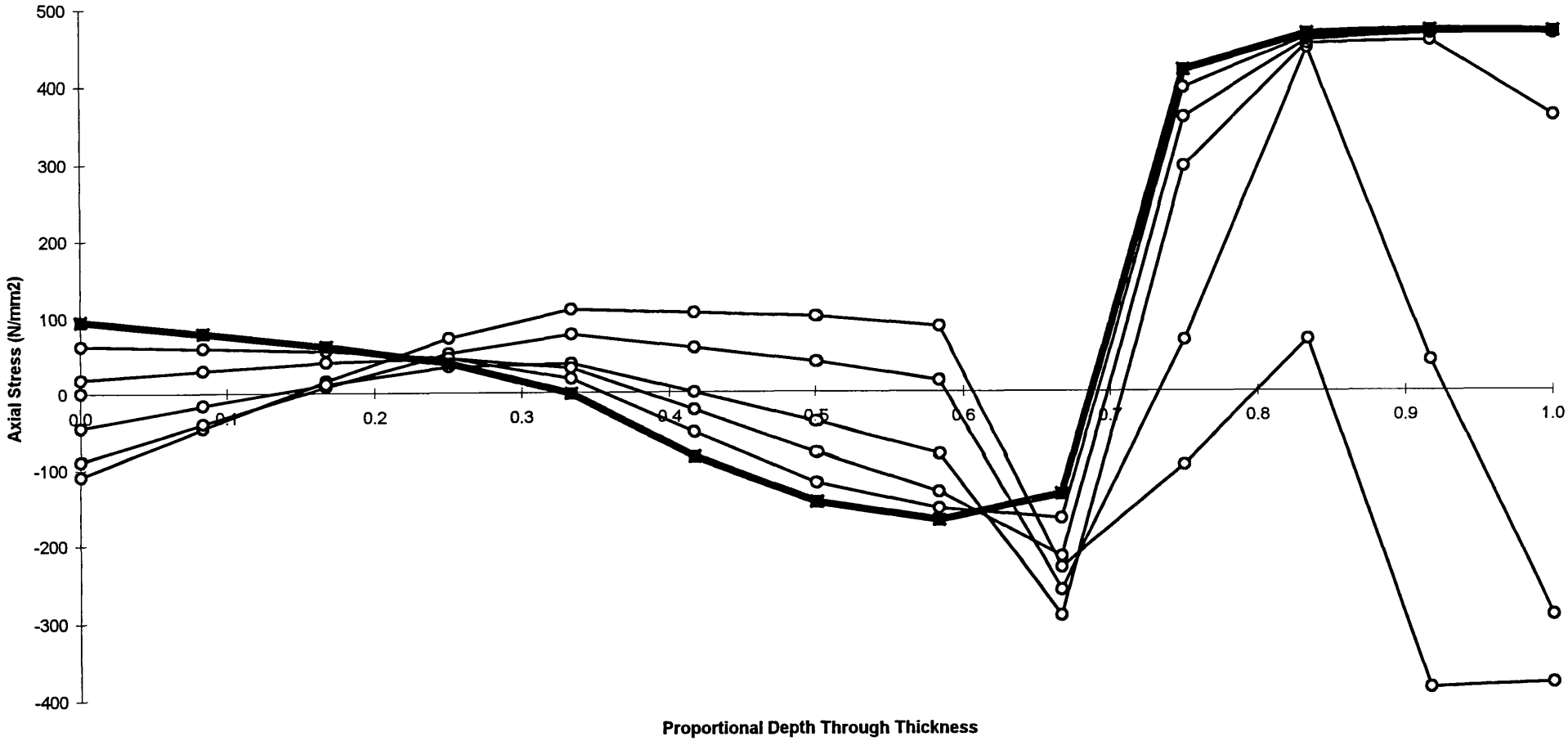


*Fig. A2.2.2.8, Model 2(ortho), thermal contraction in the welding steps, location 1 in Fig. 4.21*

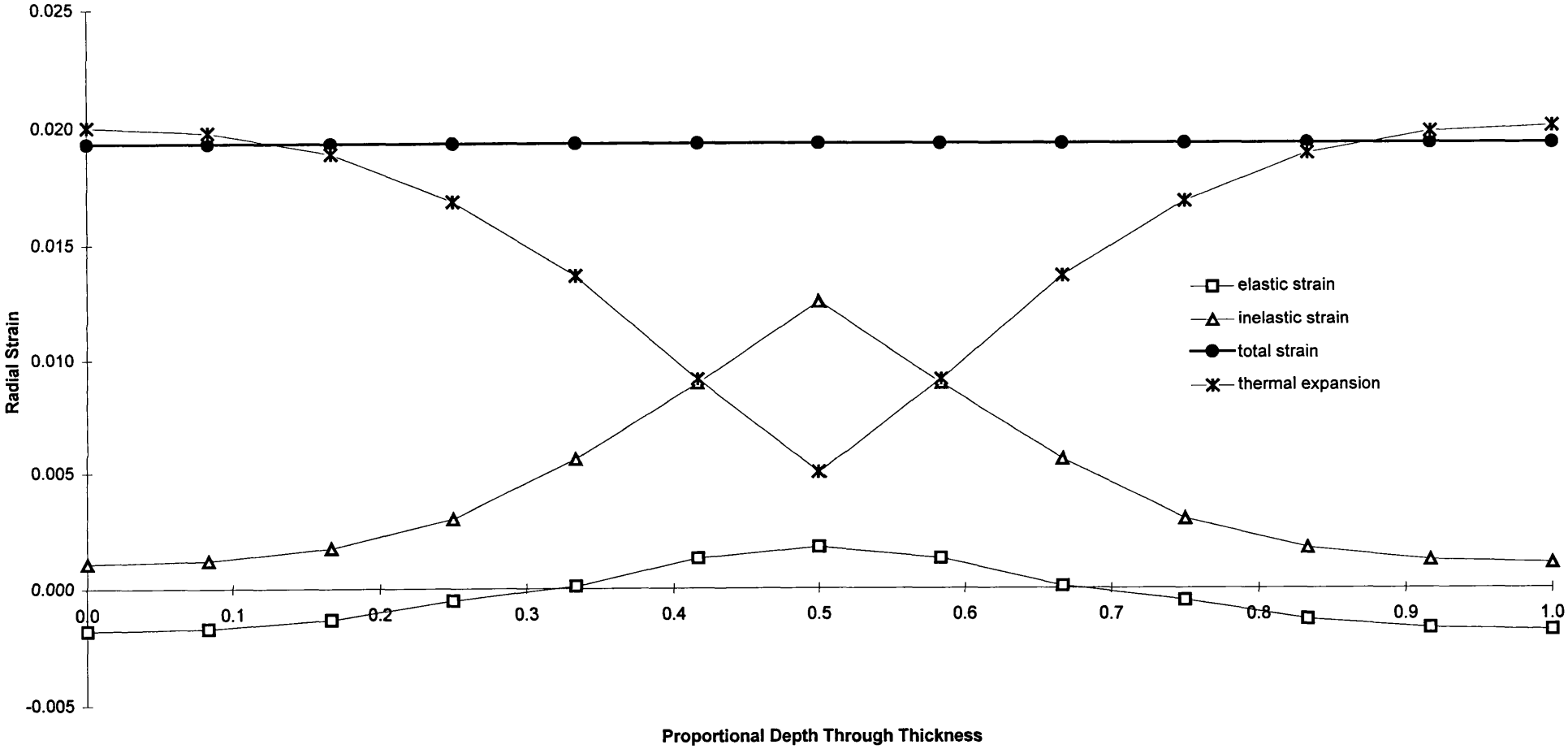


*Fig. A2.2.3.1, Model 2(ortho), thermal expansion in the welding steps, location 2 in Fig.4.21*

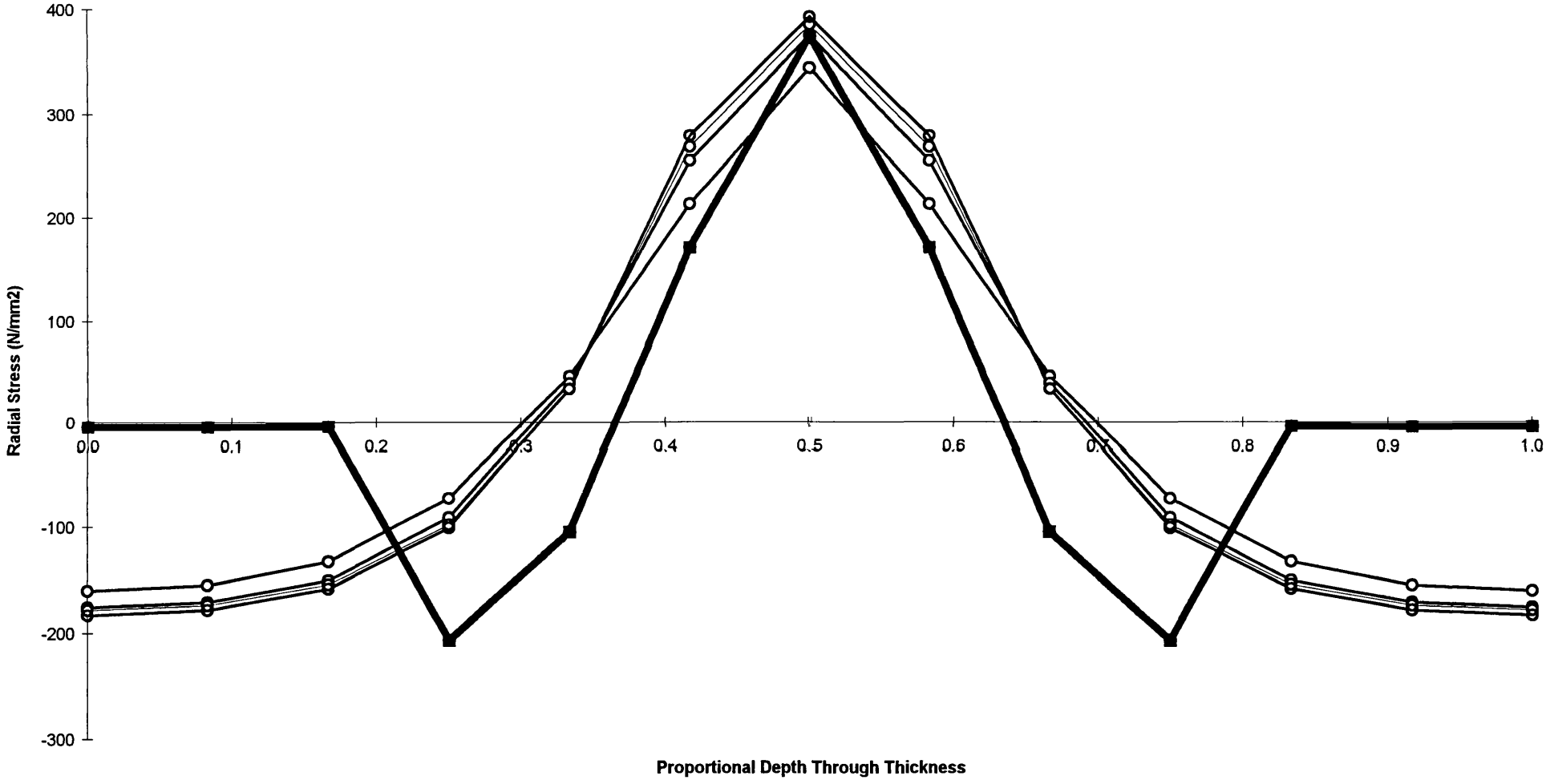


*Fig. A2.2.3.2, Model 2(ortho), thermal expansion in the welding steps, location 2 in Fig. 4.21*

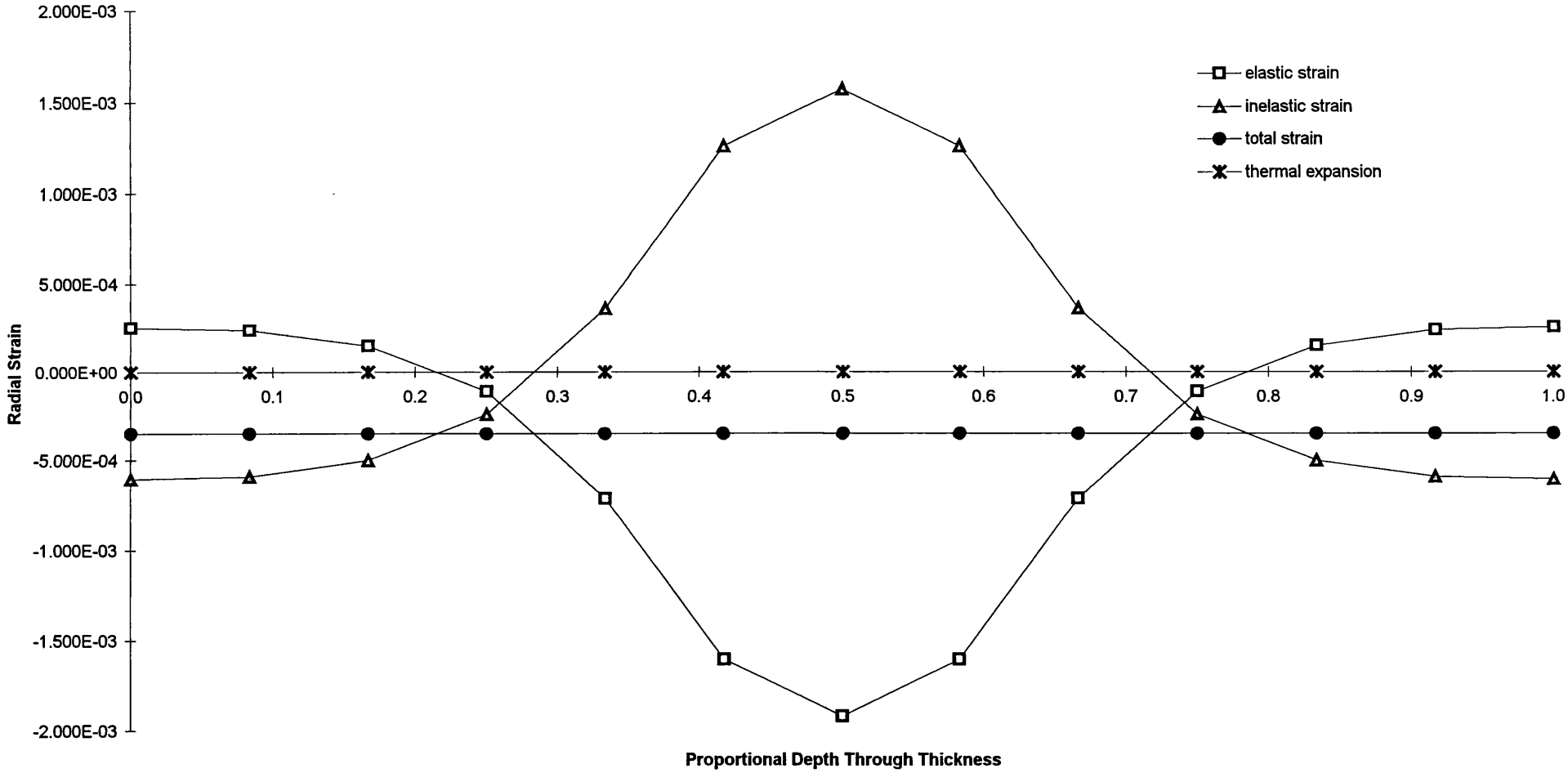


*Fig. A2.2.3.3, Model 2(ortho), thermal contraction in the welding steps, location 2 in Fig. 4.21*

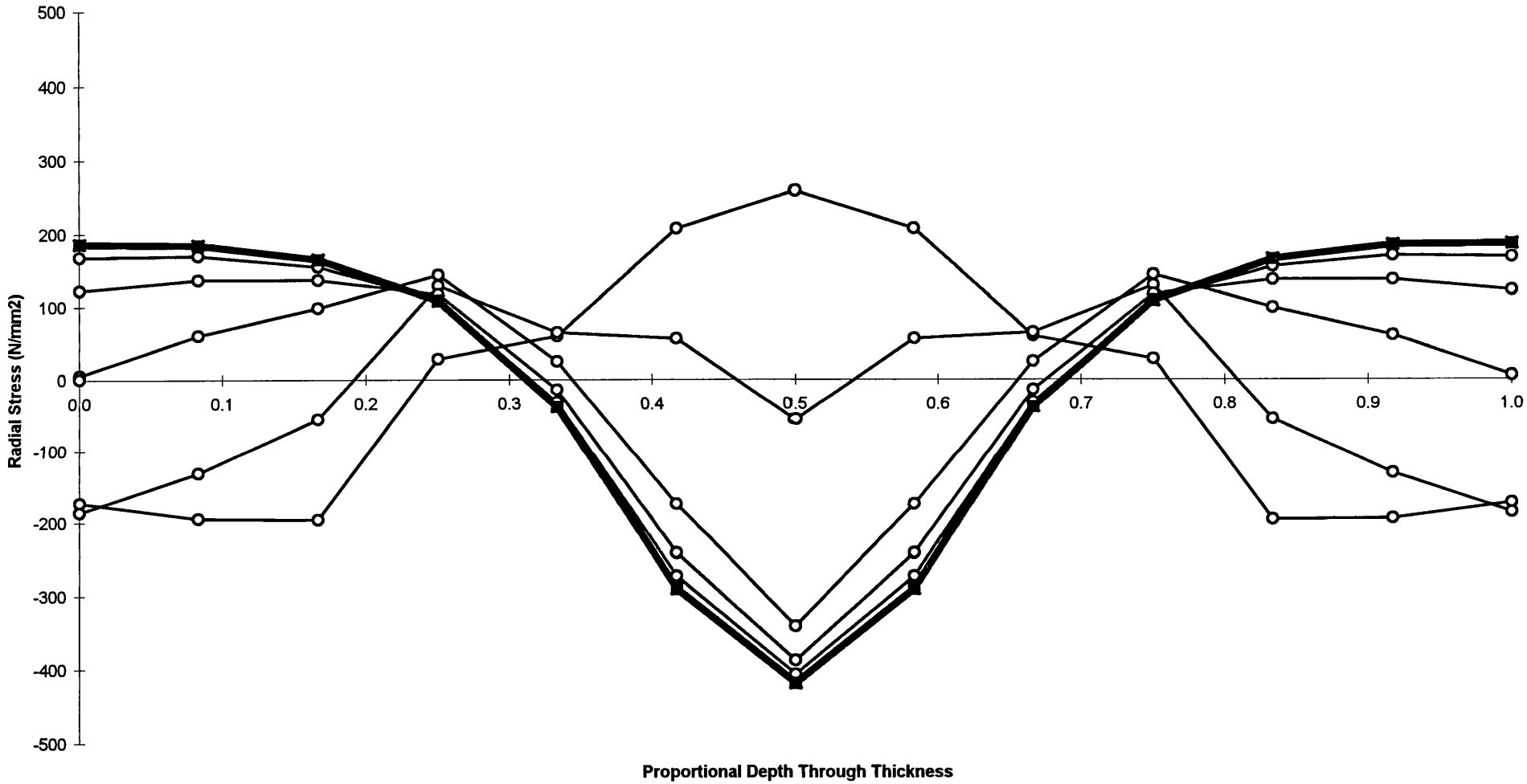


*Fig. A2.2.3.4, Model 2(ortho), thermal contraction in the welding steps, location 2 in Fig. 4.21*

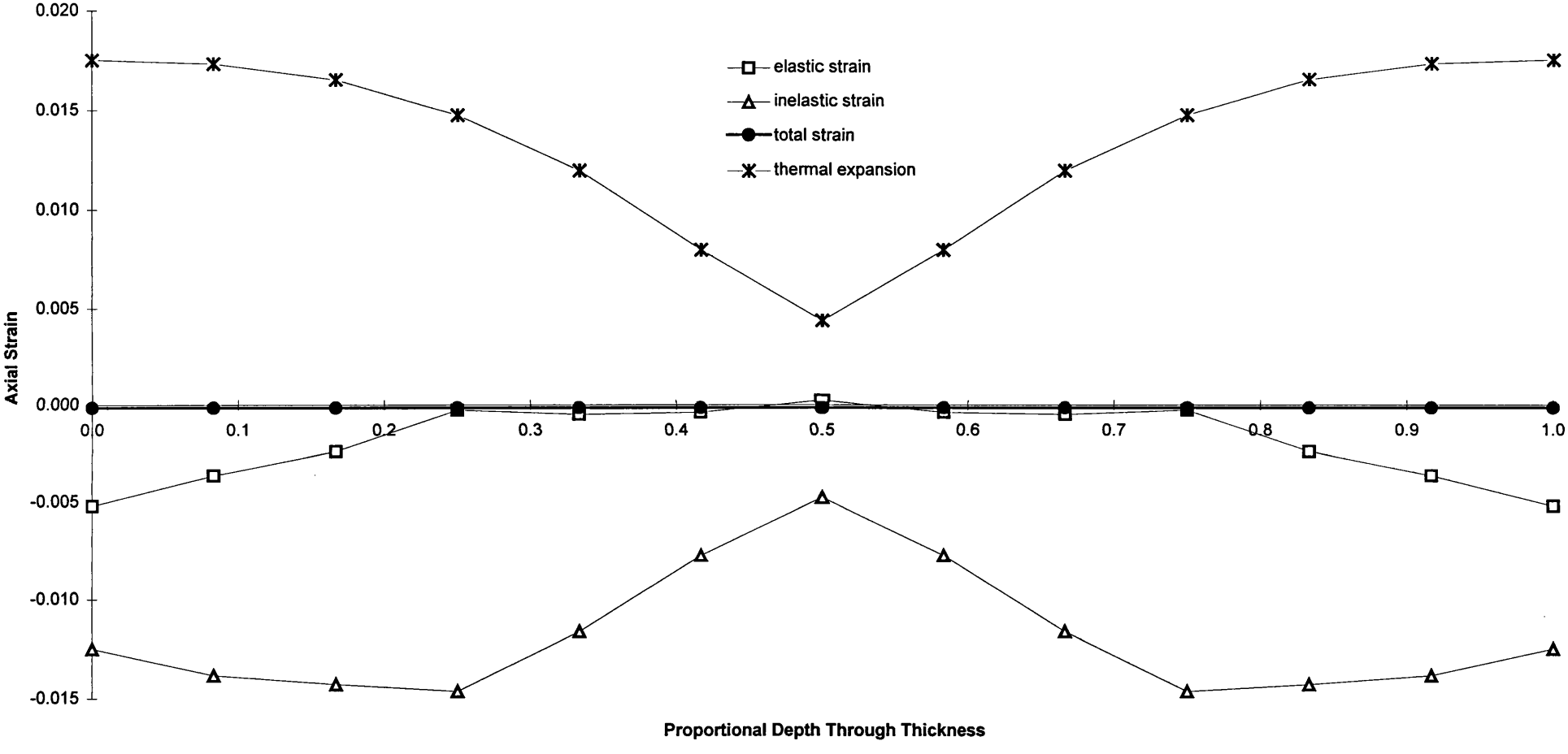


*Fig. A2.2.3.5, Model 2(ortho), thermal expansion in the welding steps, location 2 in Fig.4.21*

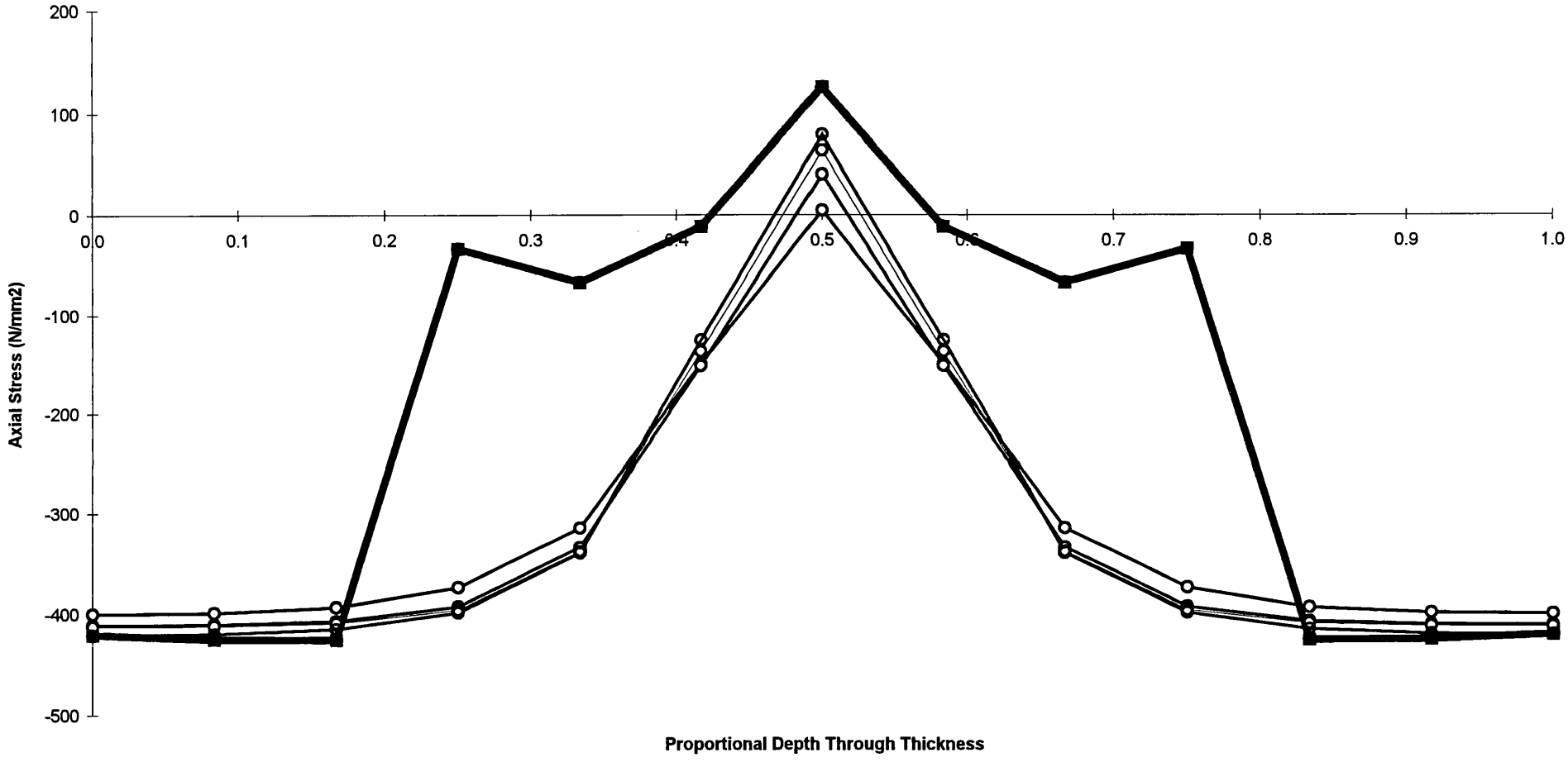


*Fig. A2.2.3.6, Model 2(ortho), thermal expansion in the welding steps, location 2 in Fig. 4.21*

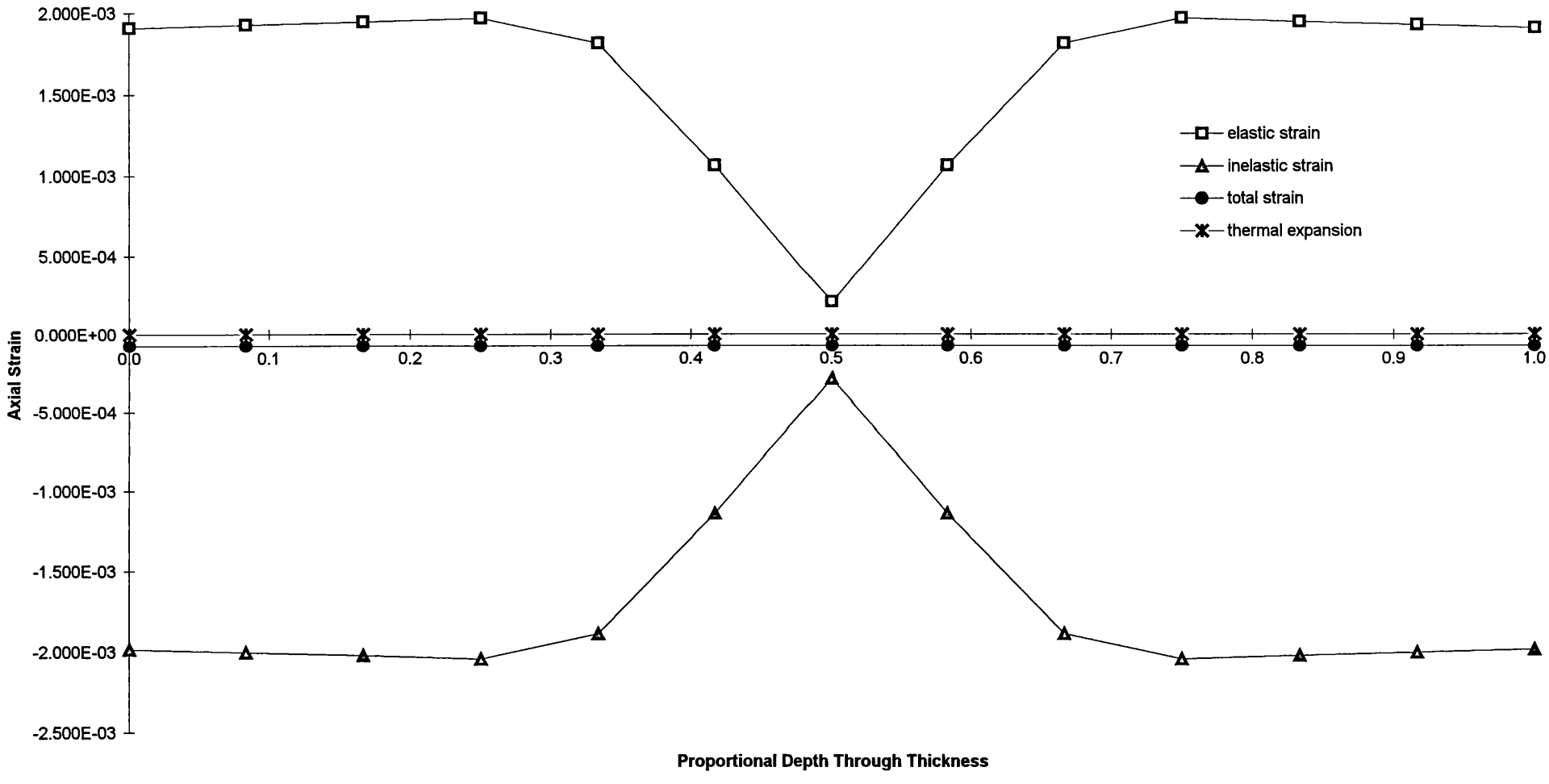


*Fig. A2.2.3.7, Model 2(ortho), thermal contraction in the welding steps, location 2 in Fig. 4.21*

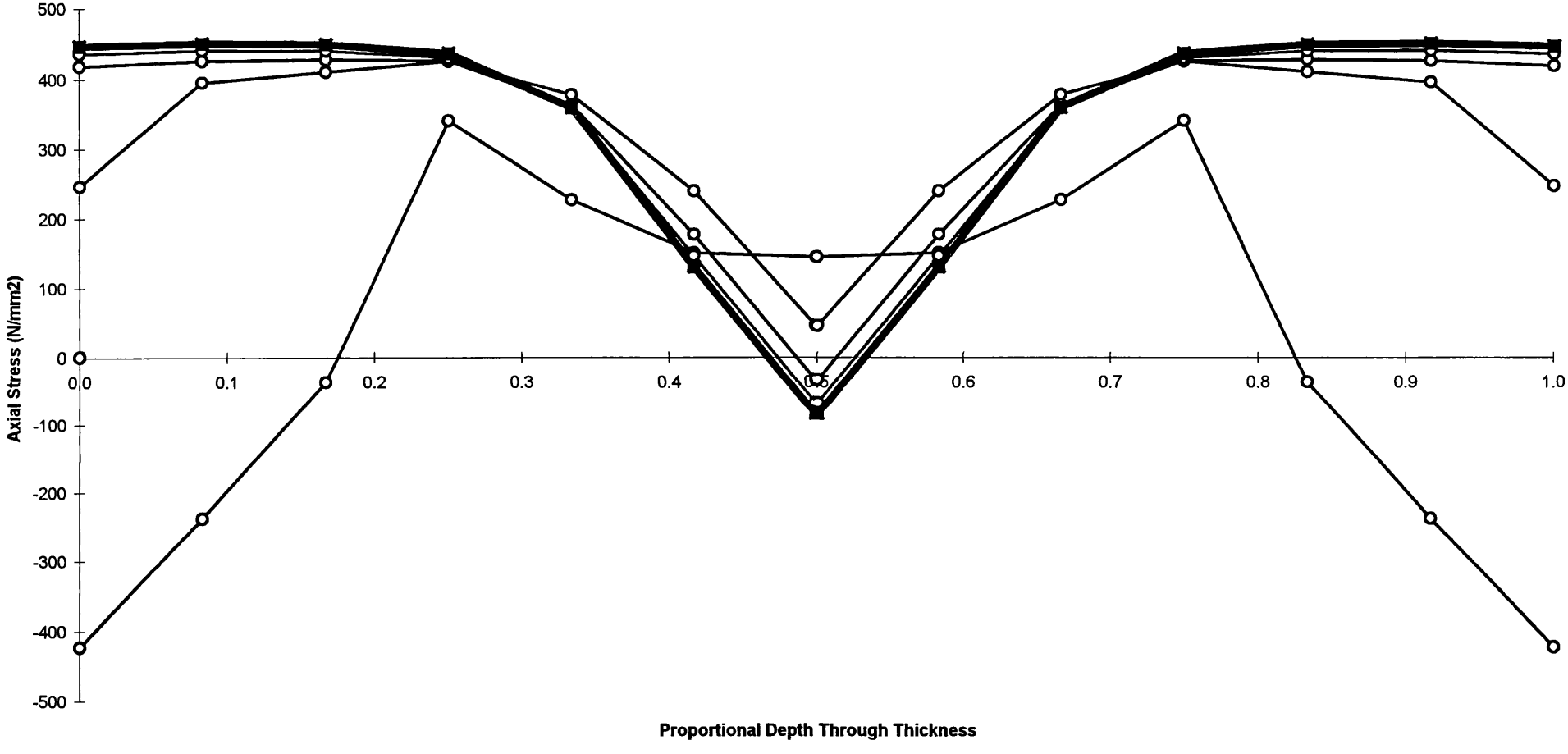


*Fig. A2.2.3.8, Model 2(ortho), thermal contraction in the welding steps, location 2 in Fig. 4.21*

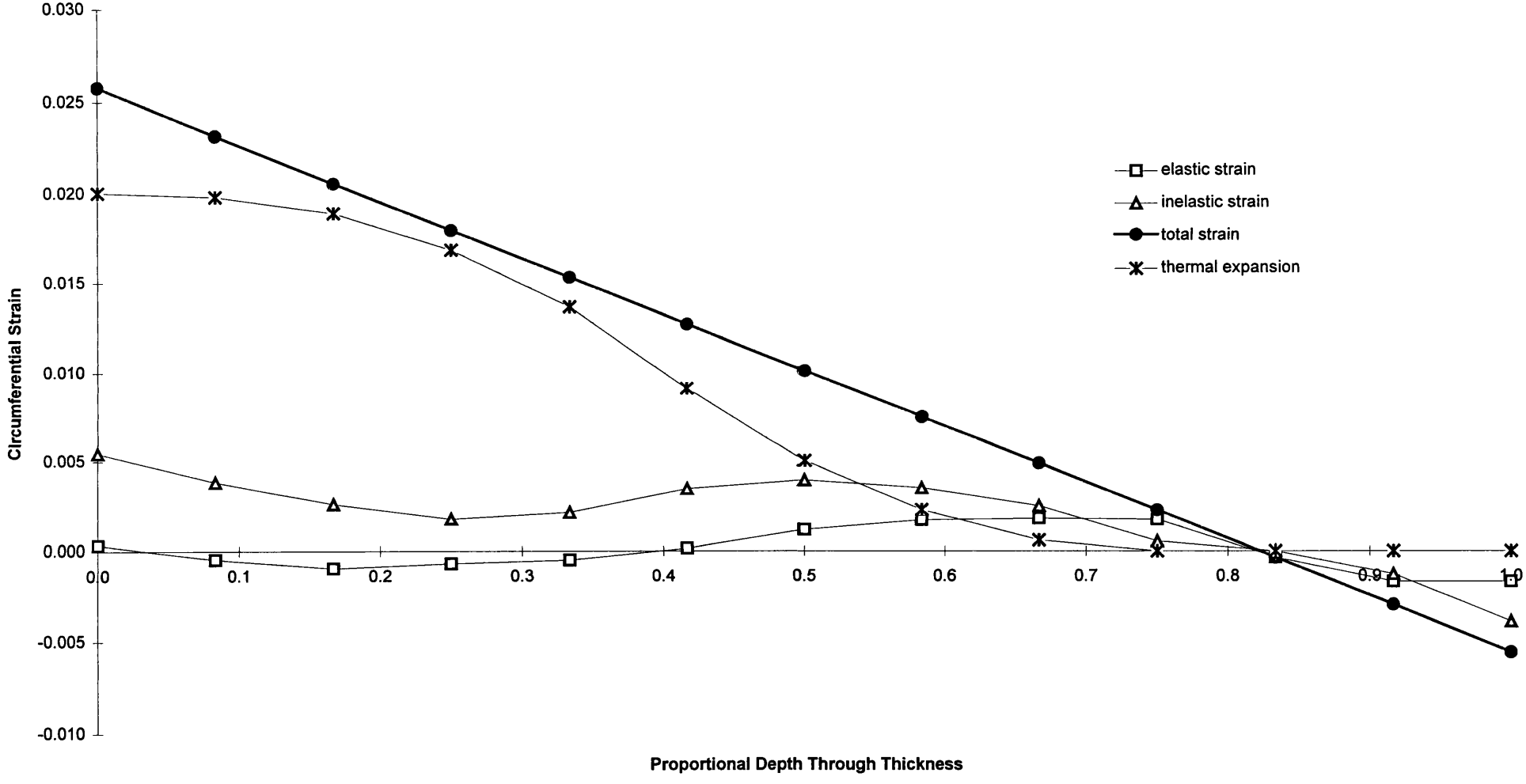


*Fig. A2.2.4.1, Model 2(ortho), thermal expansion in the welding steps, location 3 in Fig.4.21*

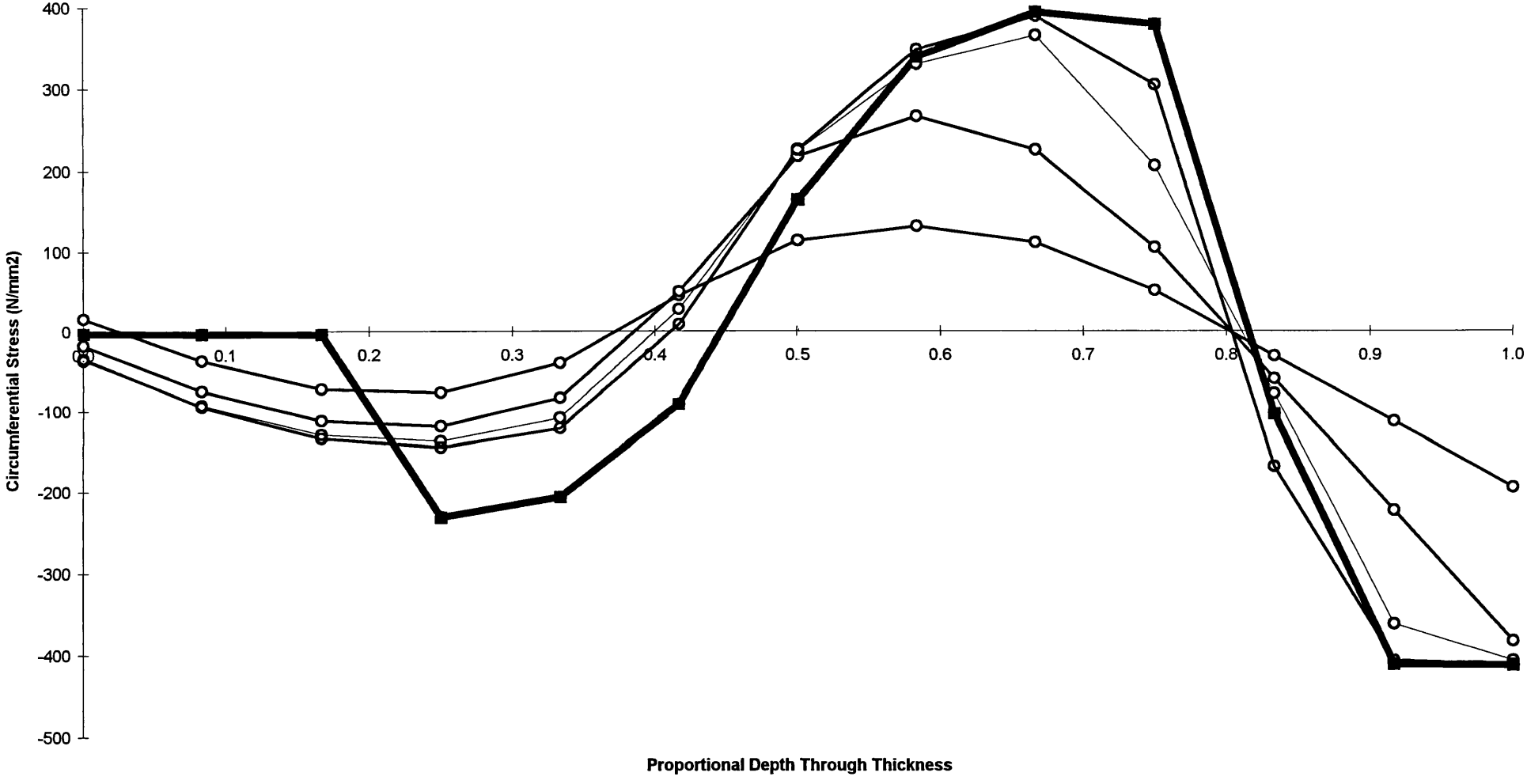


*Fig. A2.2.4.2, Model 2(ortho), thermal expansion in the welding steps, location 3 in Fig. 4.21*

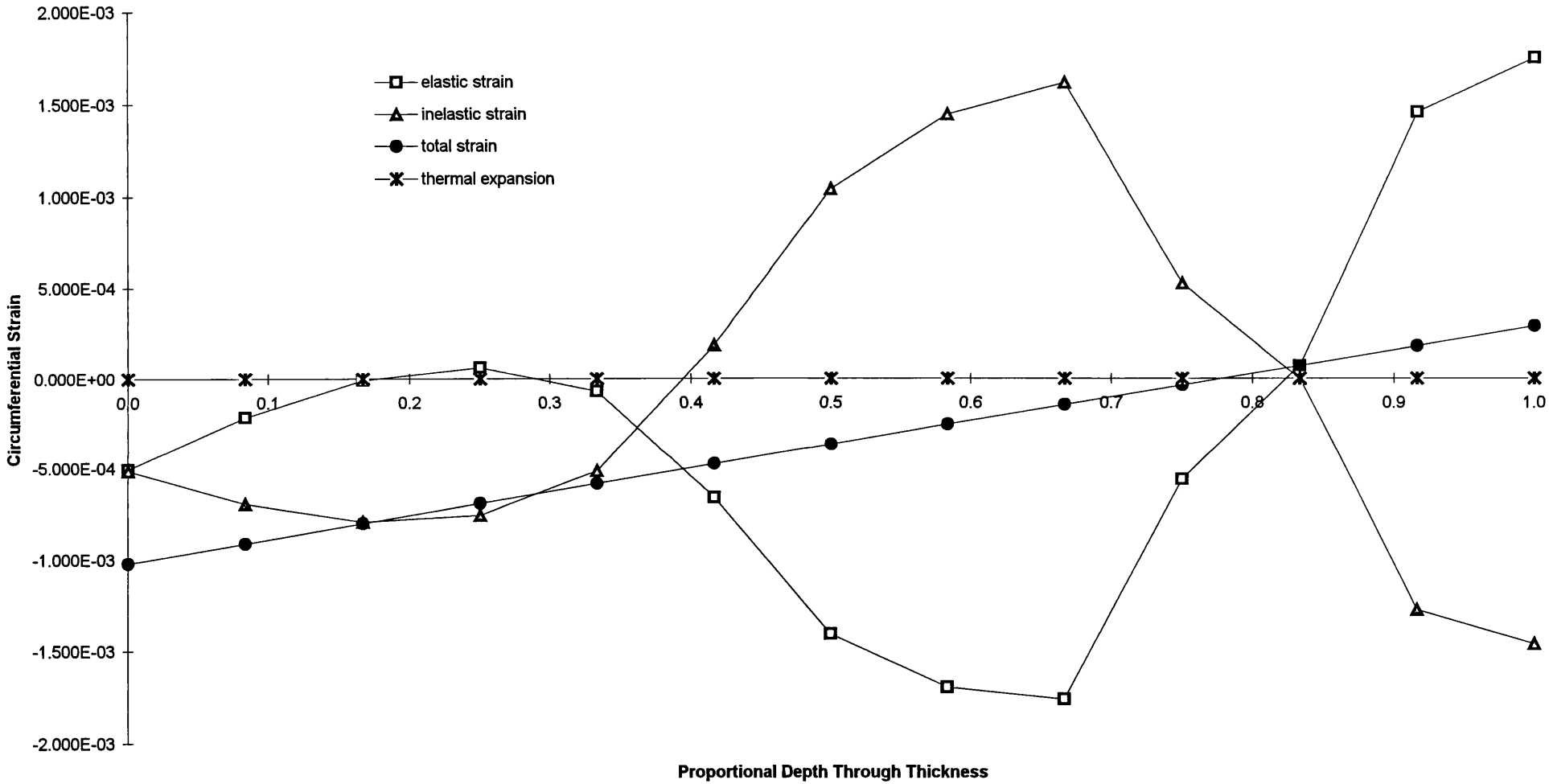


*Fig. A2.2.4.3, Model 2(ortho), thermal contraction in the welding steps, location 3 in Fig. 4.21*

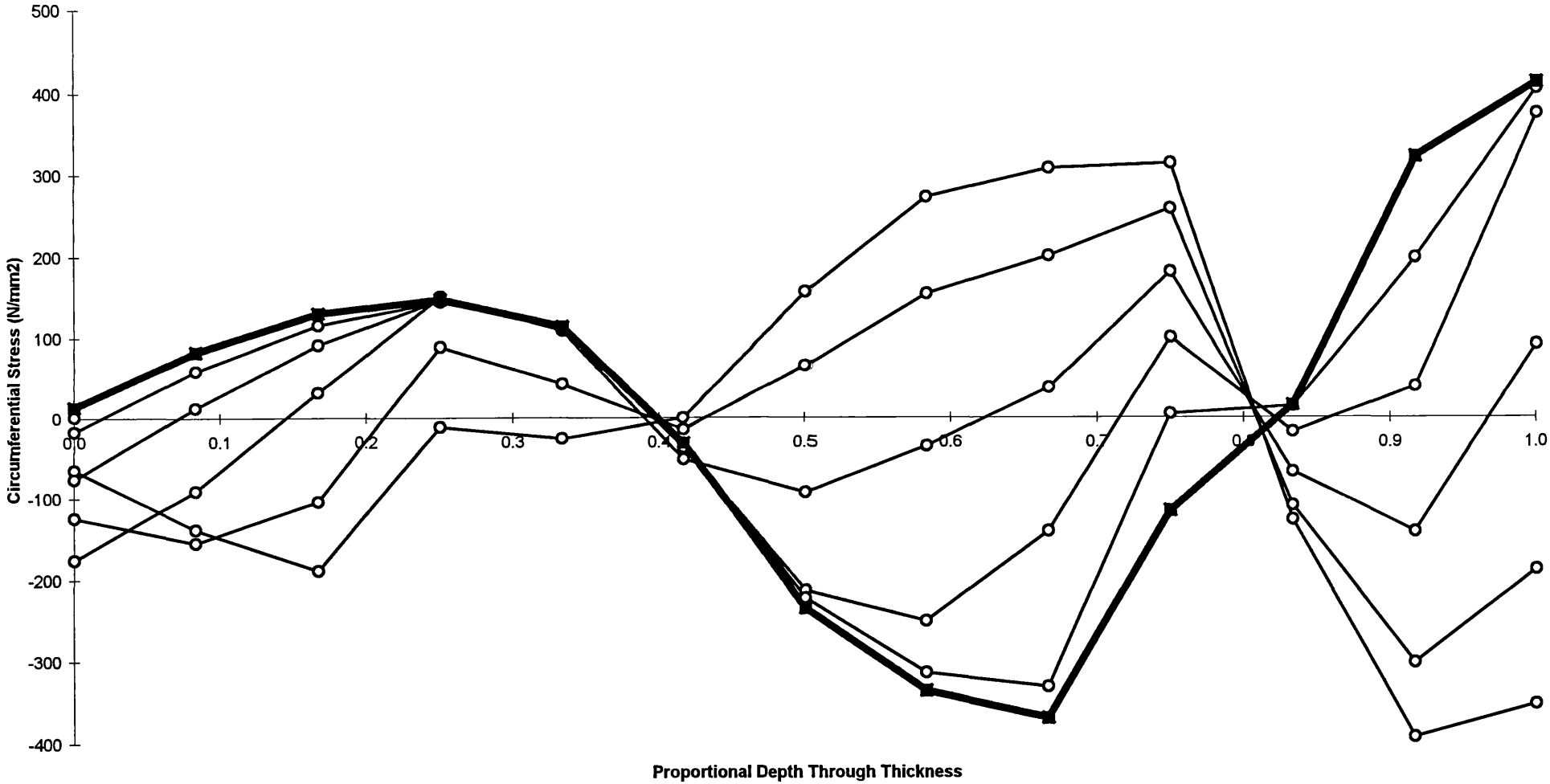


*Fig. A2.2.4.4, Model 2(ortho), thermal contraction in the welding steps, location 3 in Fig. 4.21*

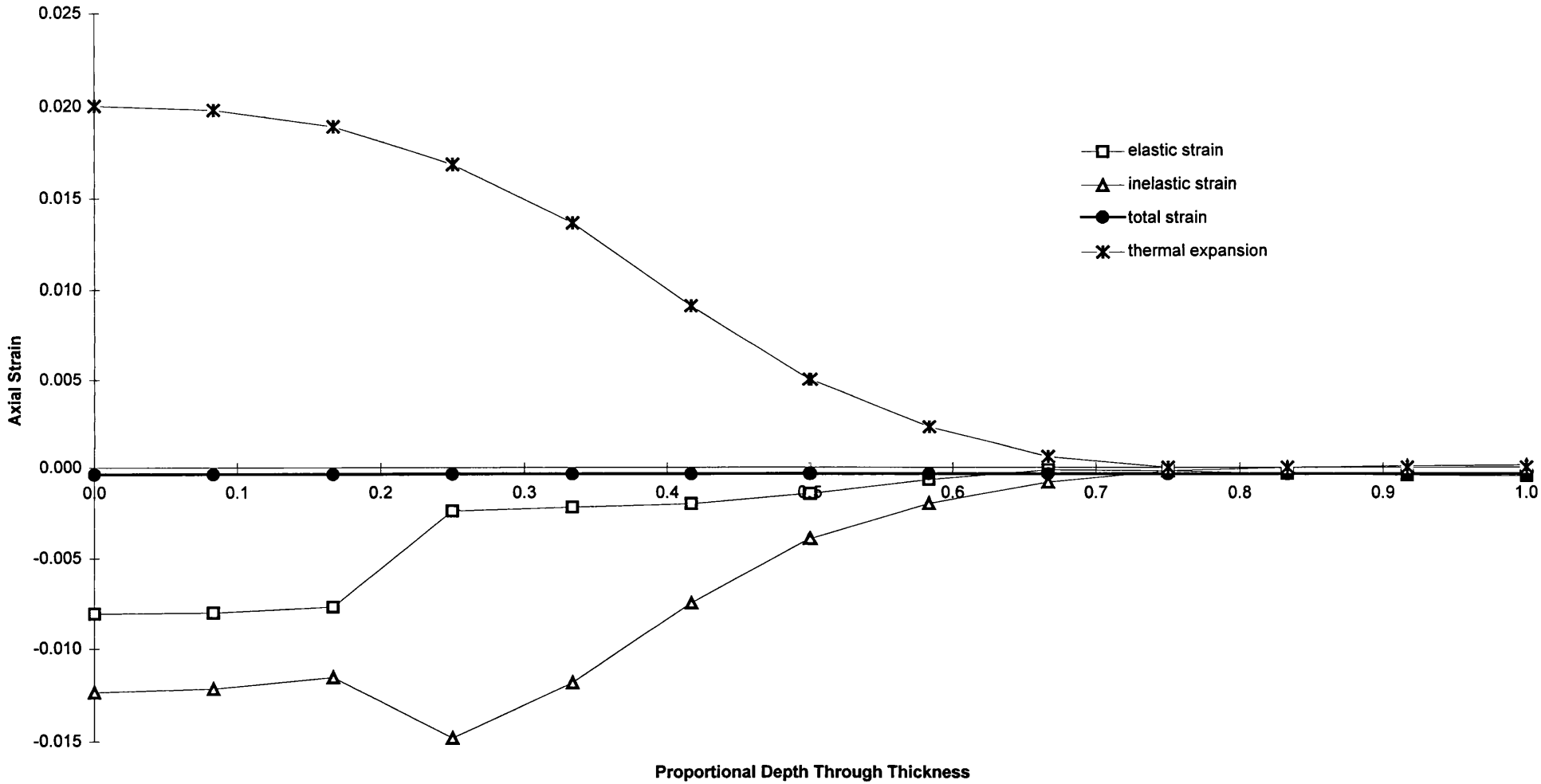


*Fig. A2.2.4.5, Model 2(ortho), thermal expansion in the welding steps, location 3 in Fig.4.21*

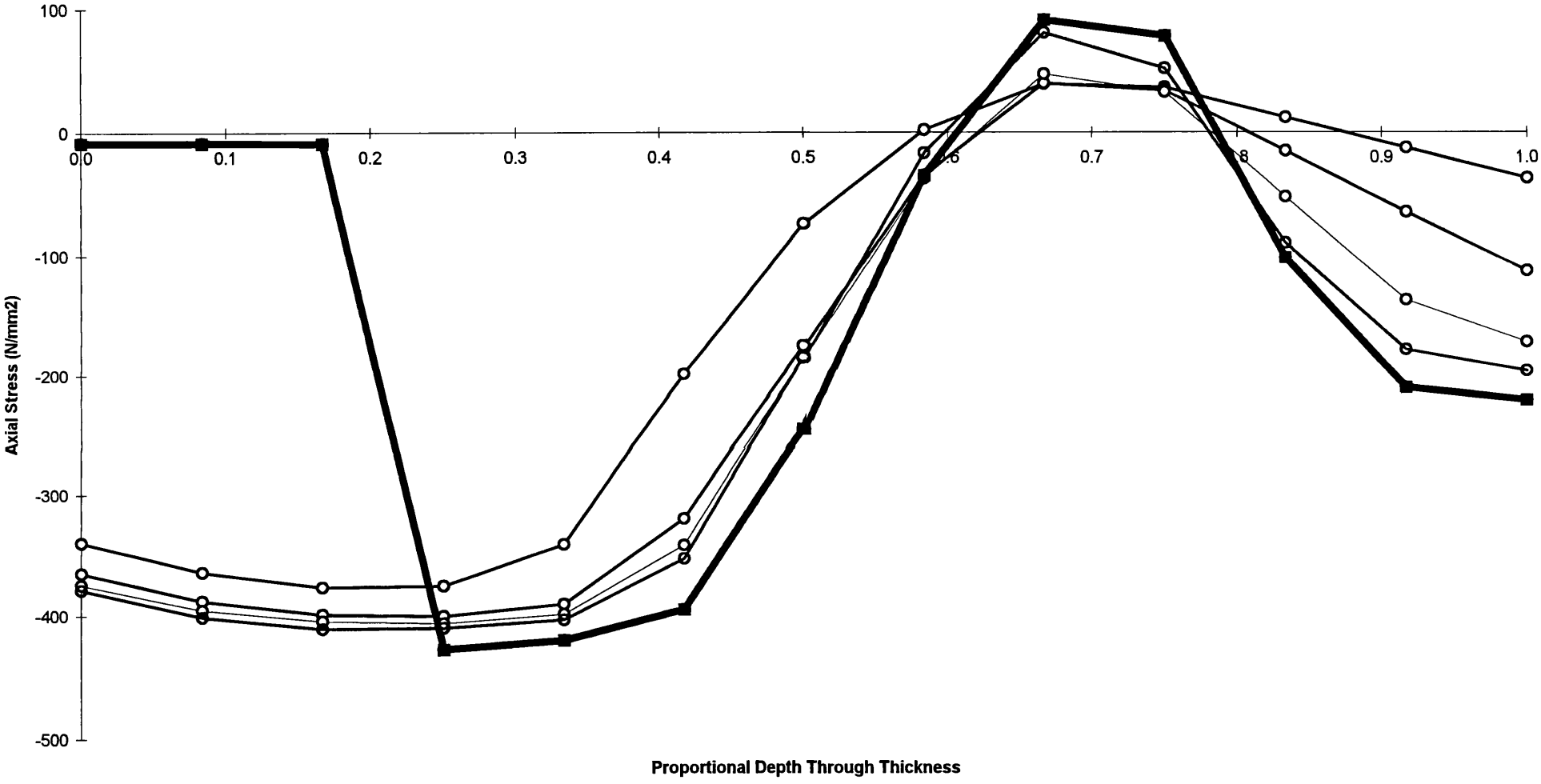


*Fig. A2.2.4.6, Model 2(ortho), thermal expansion in the welding steps, location 3 in Fig. 4.21*

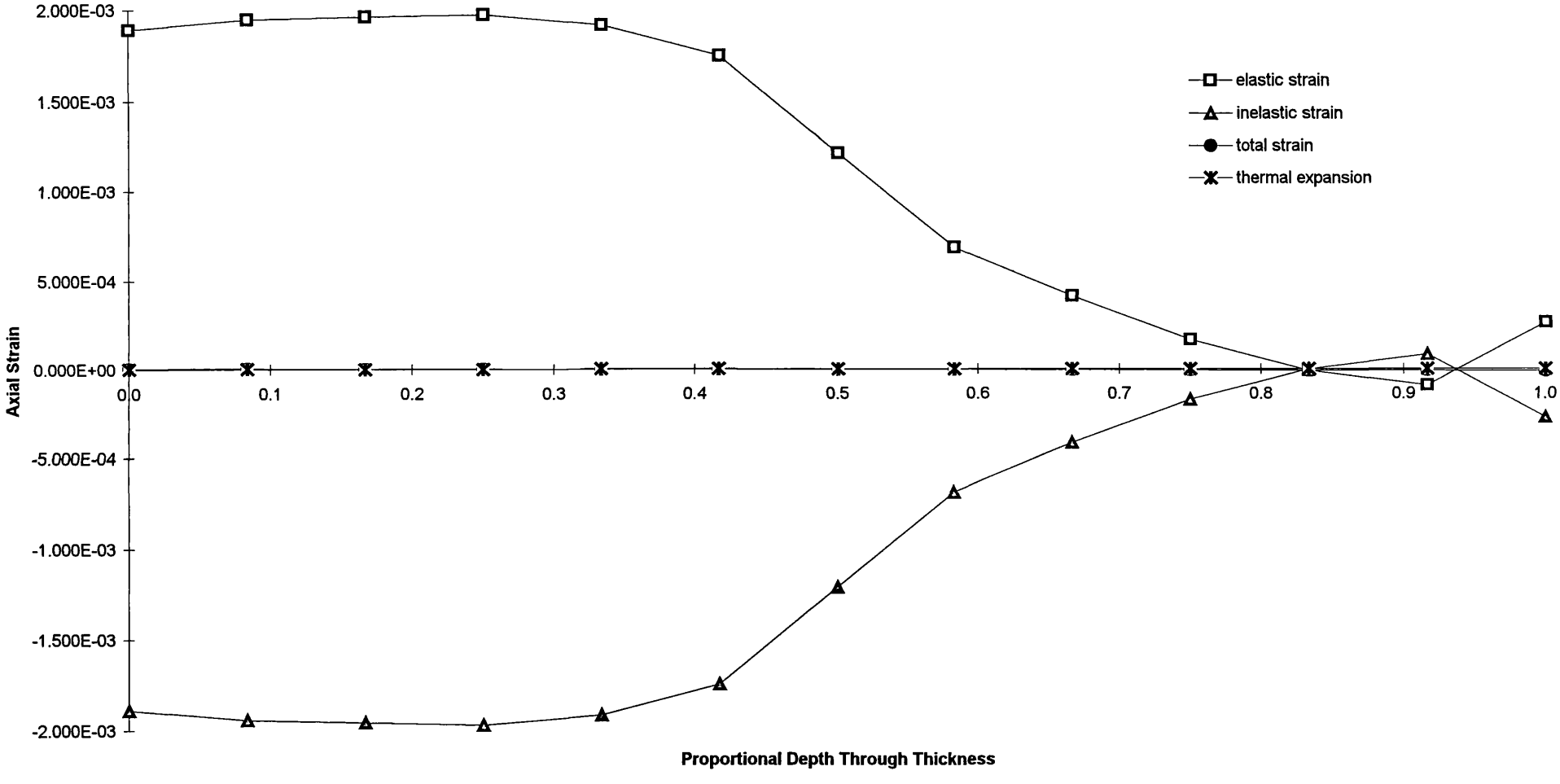


*Fig. A2.2.4.7, Model 2(ortho), thermal contraction in the welding steps, location 3 in Fig. 4.21*

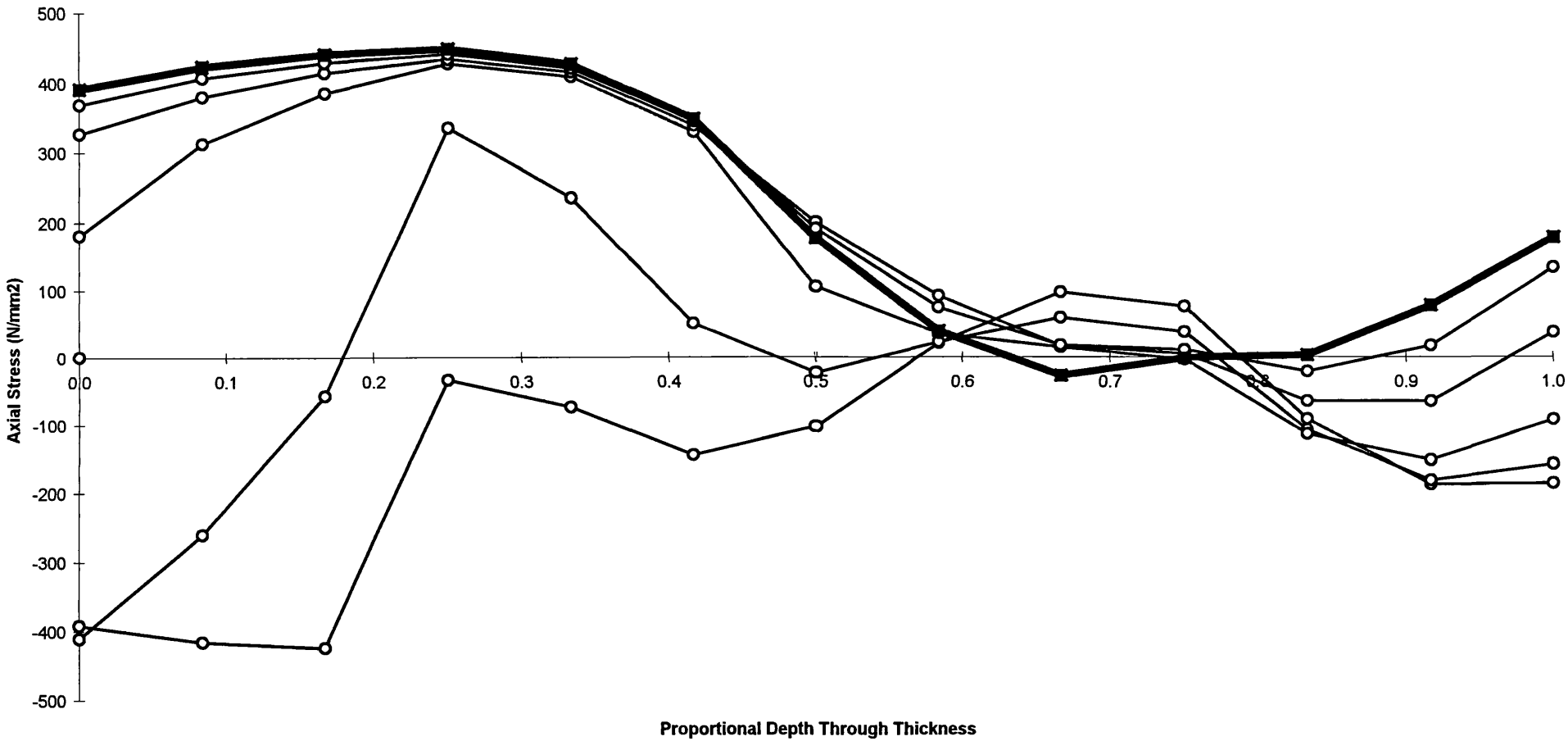


*Fig. A2.2.4.8, Model 2(ortho), thermal contraction in the welding steps, location 3 in Fig. 4.21*

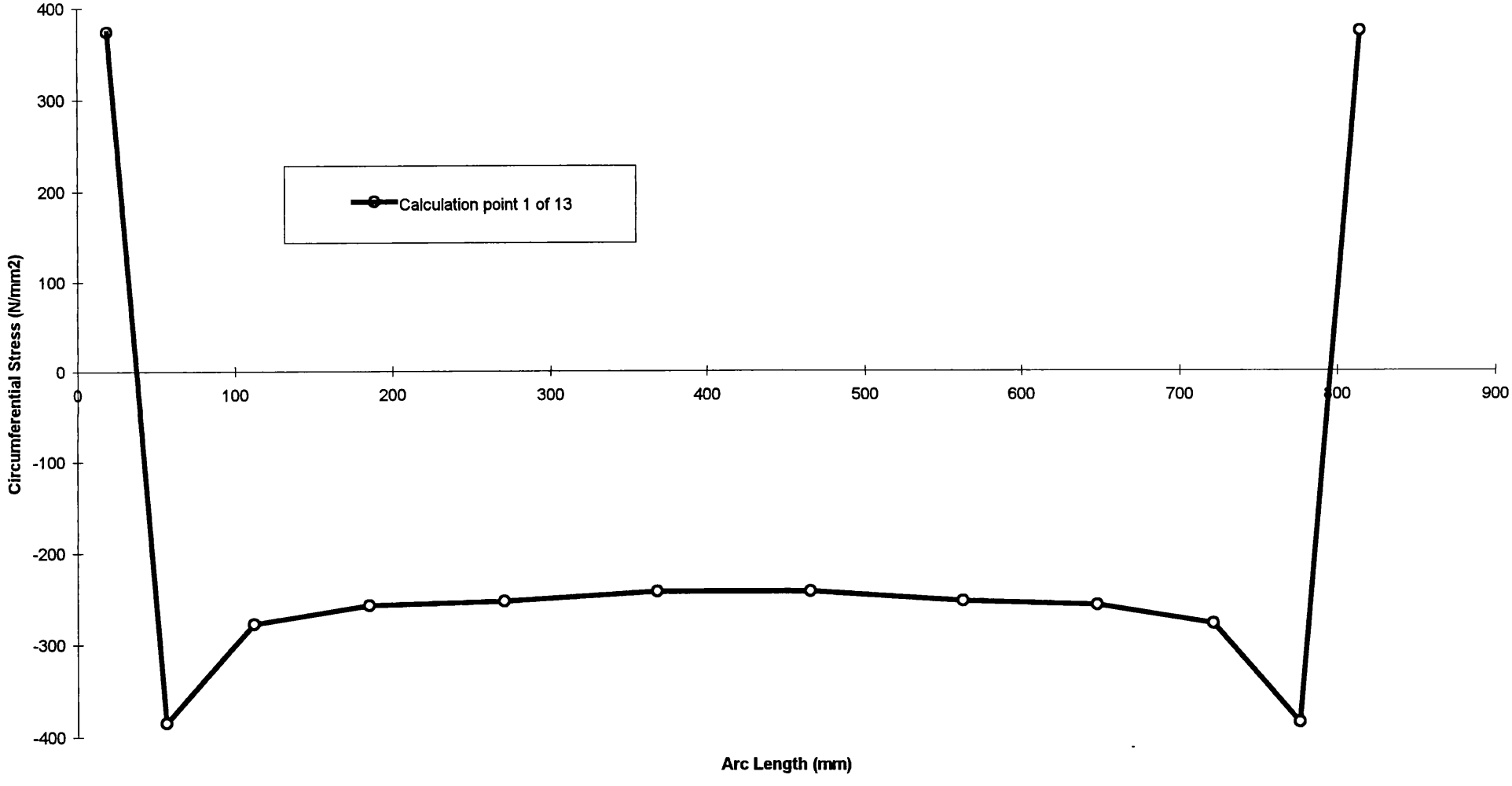


*Fig. A2.2.5.1, Model 2(ortho), Inter frame circumferential residual stress.*

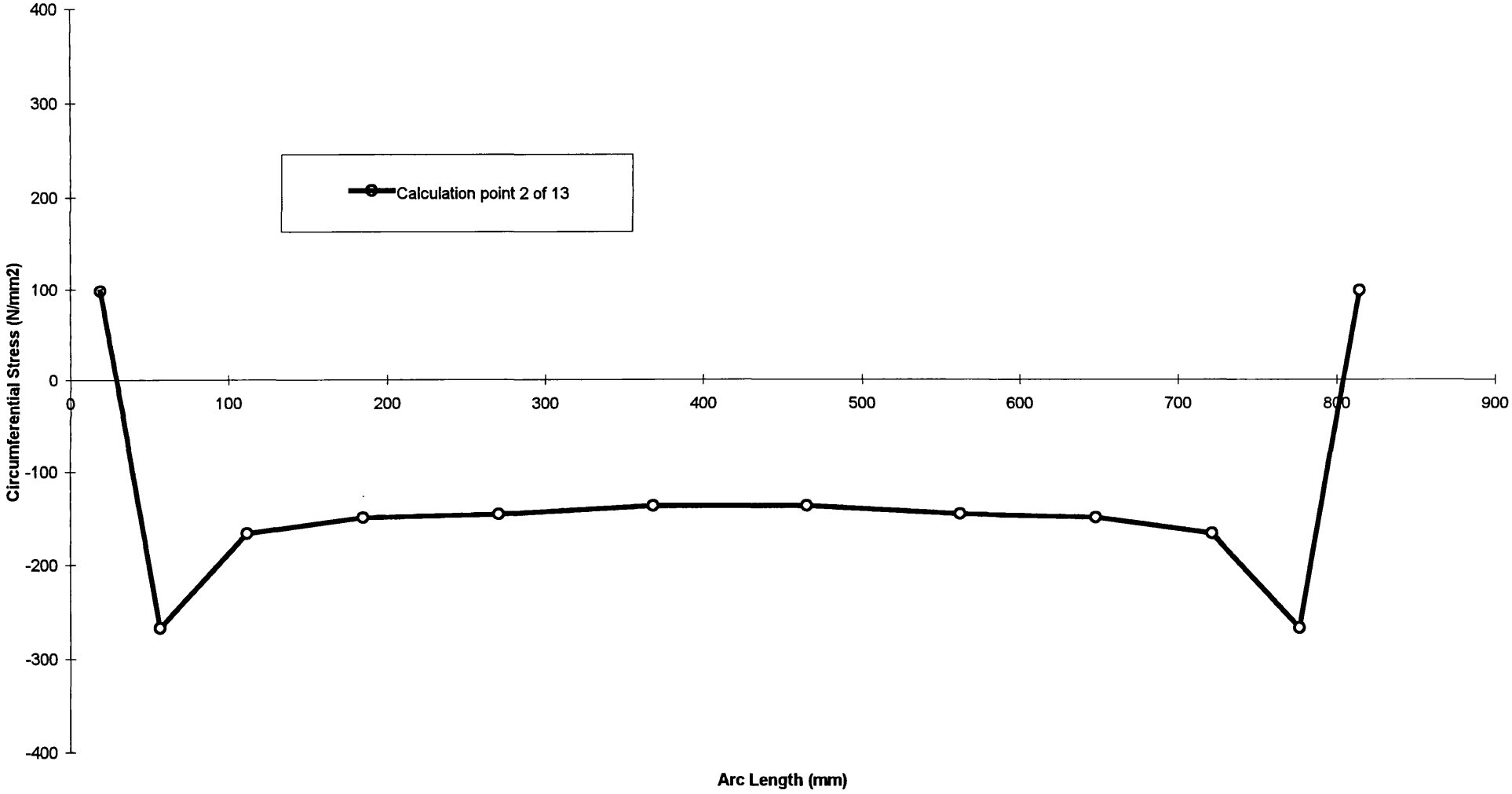


*Fig. A2.2.5.2, Model 2(ortho), inter frame circumferential residual stress.*

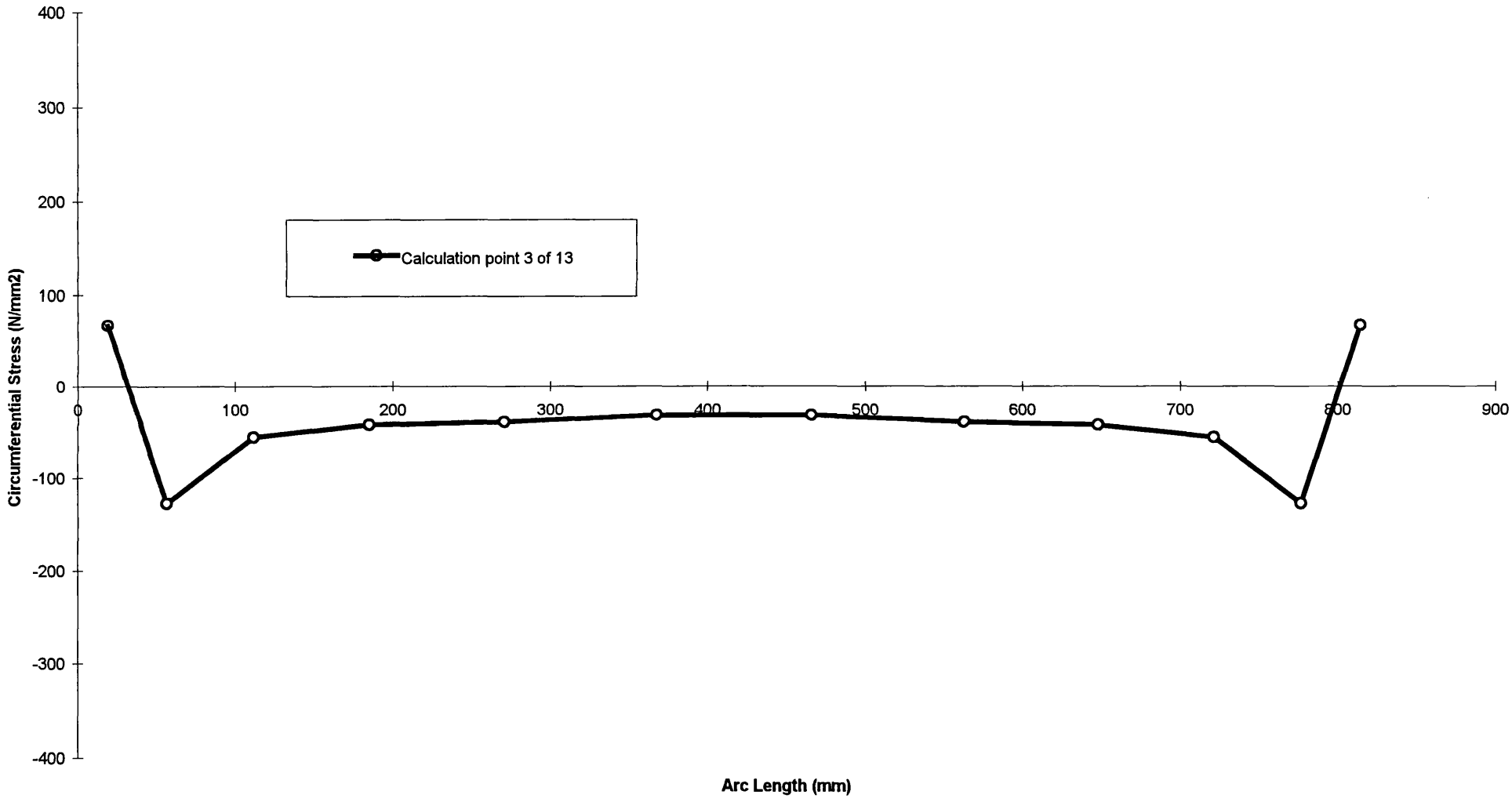


*Fig. A2.2.5.3, Model 2(ortho), inter frame circumferential residual stress.*

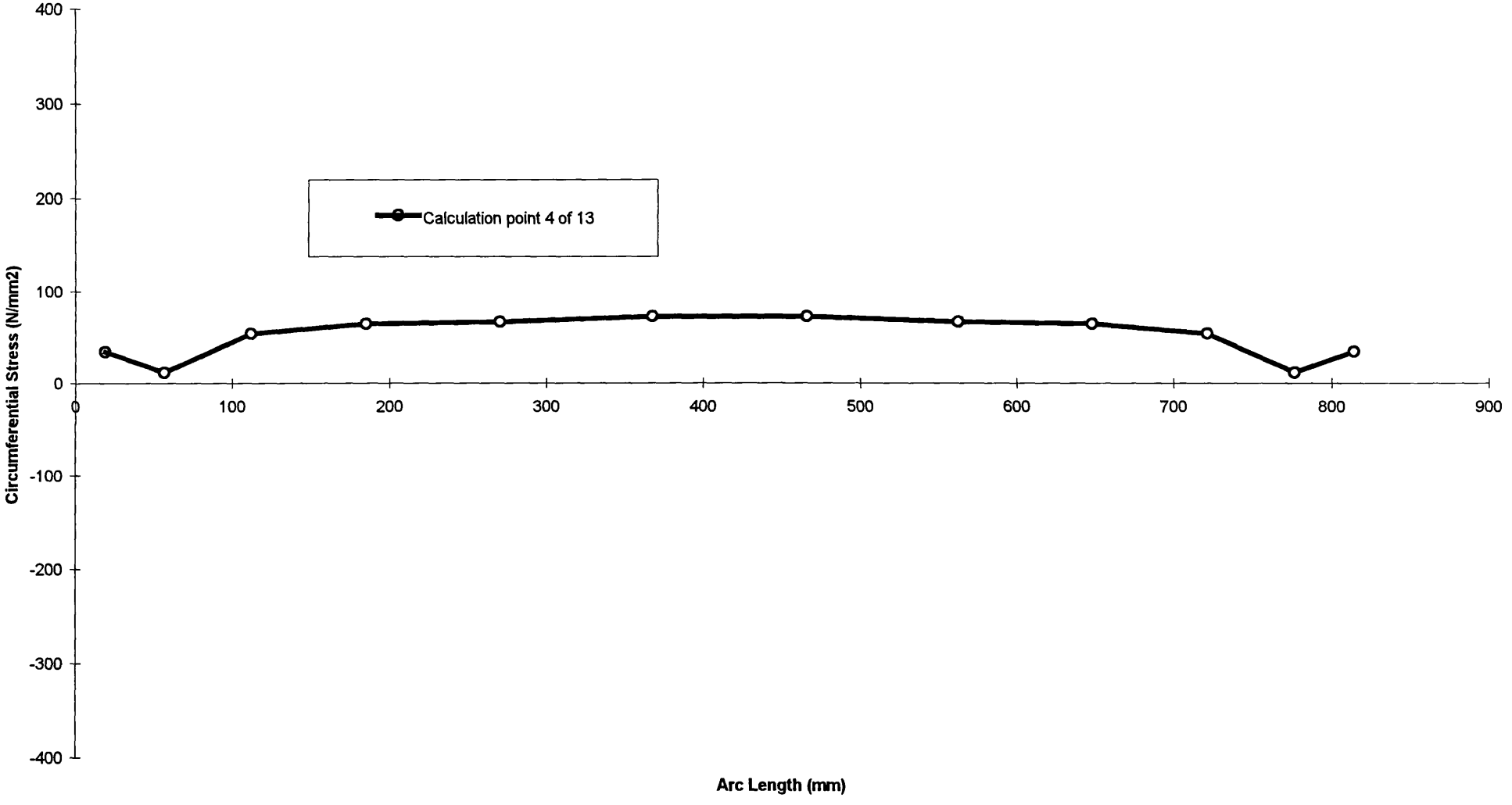


*Fig. A2.2.5.4, Model 2(ortho), inter frame circumferential residual stress.*

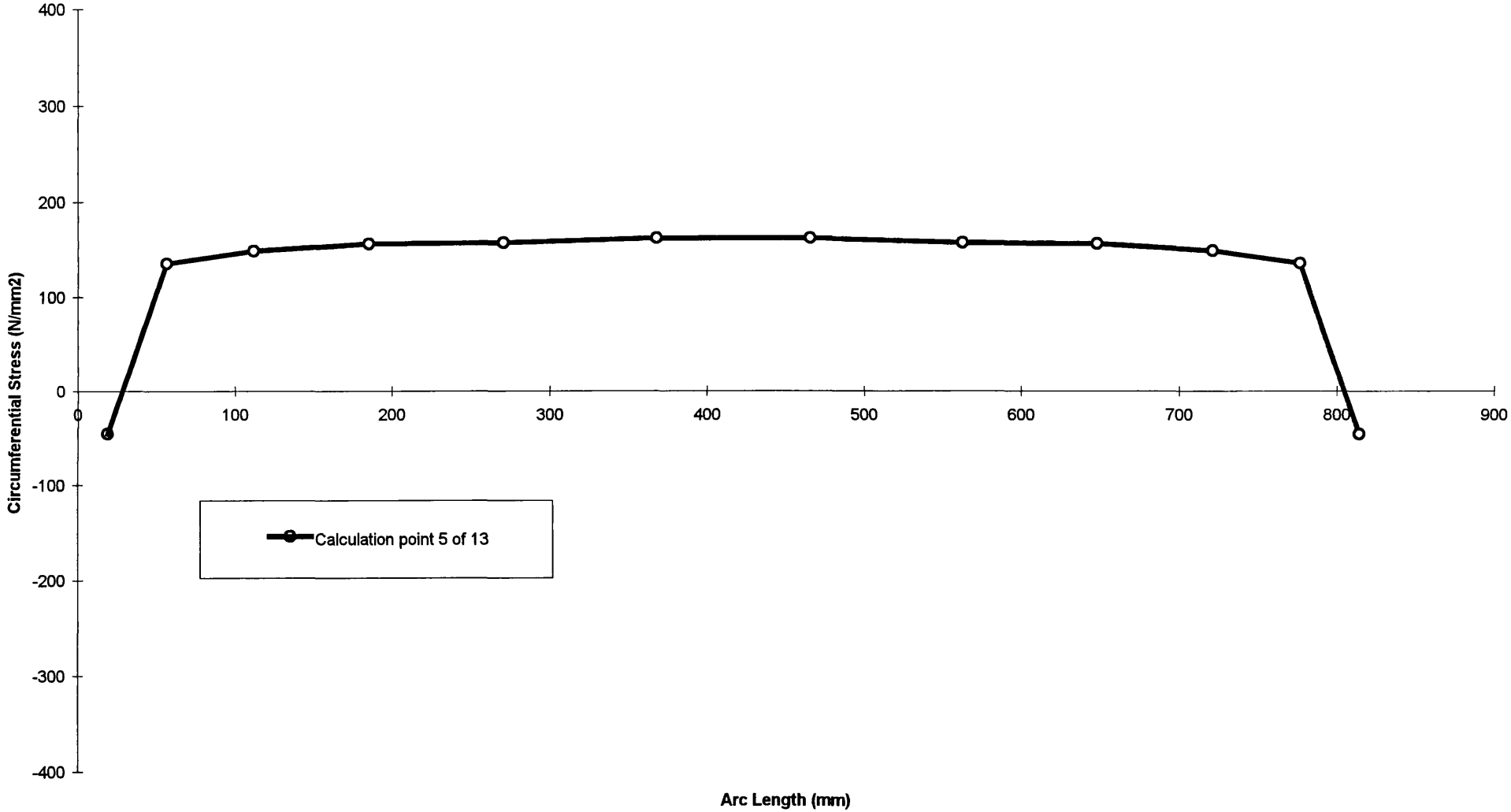


*Fig. A2.2.5.5, Model 2(ortho), inter frame circumferential residual stress.*

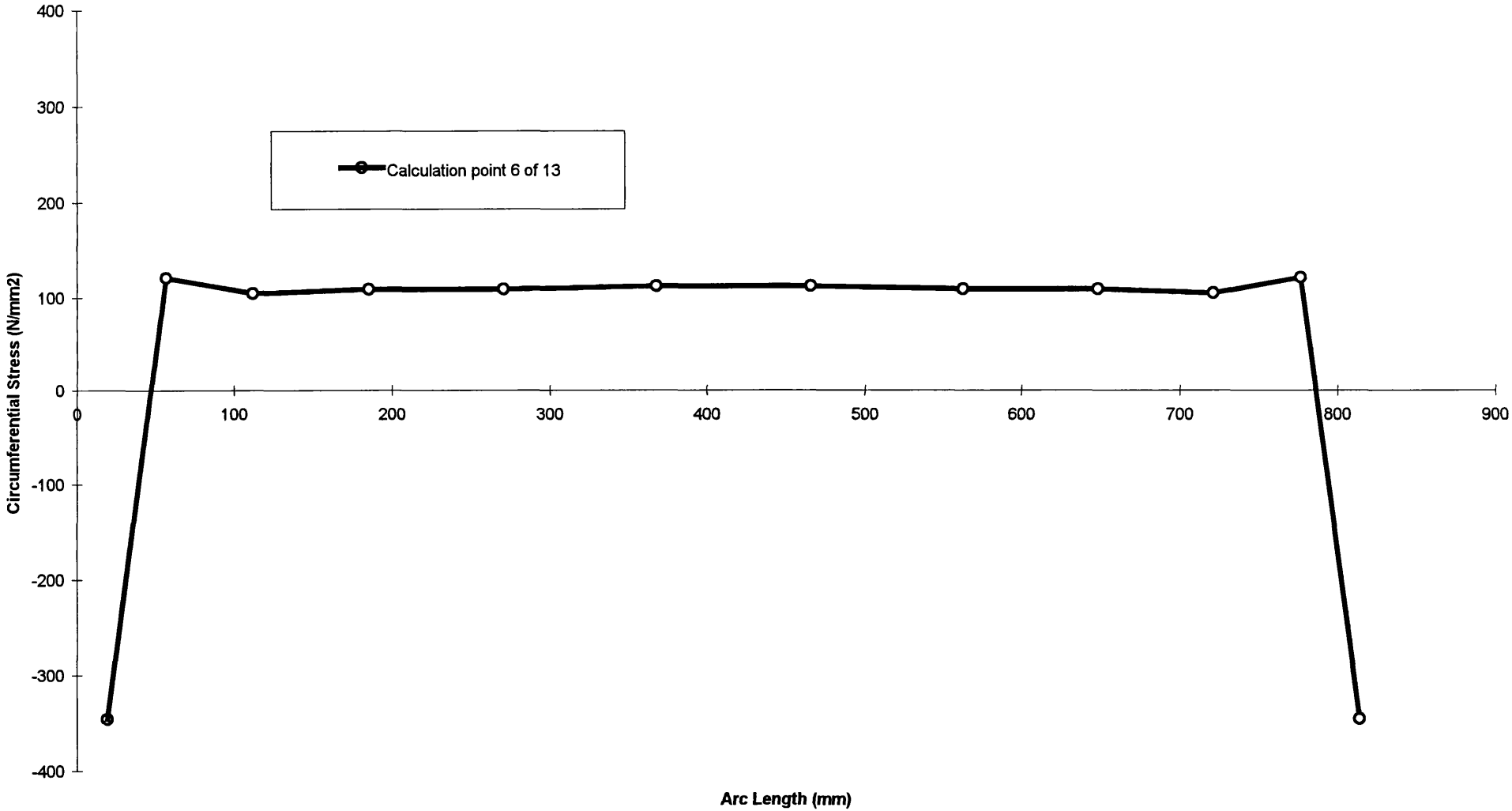


*Fig. A2.2.5.6, Model 2(ortho), inter frame circumferential residual stress.*

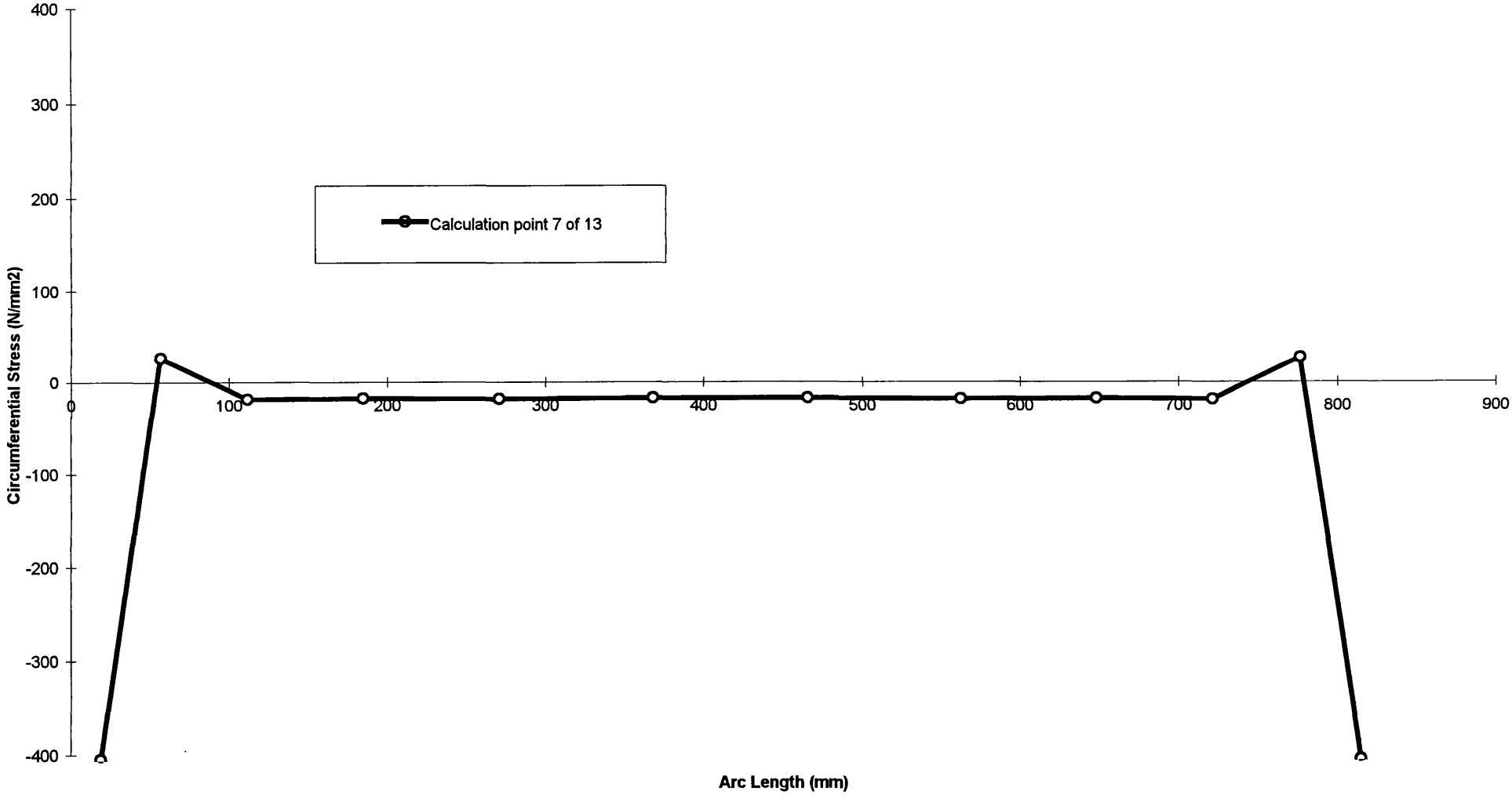


*Fig. A2.2.5.7, Model 2(ortho), inter frame circumferential residual stress.*

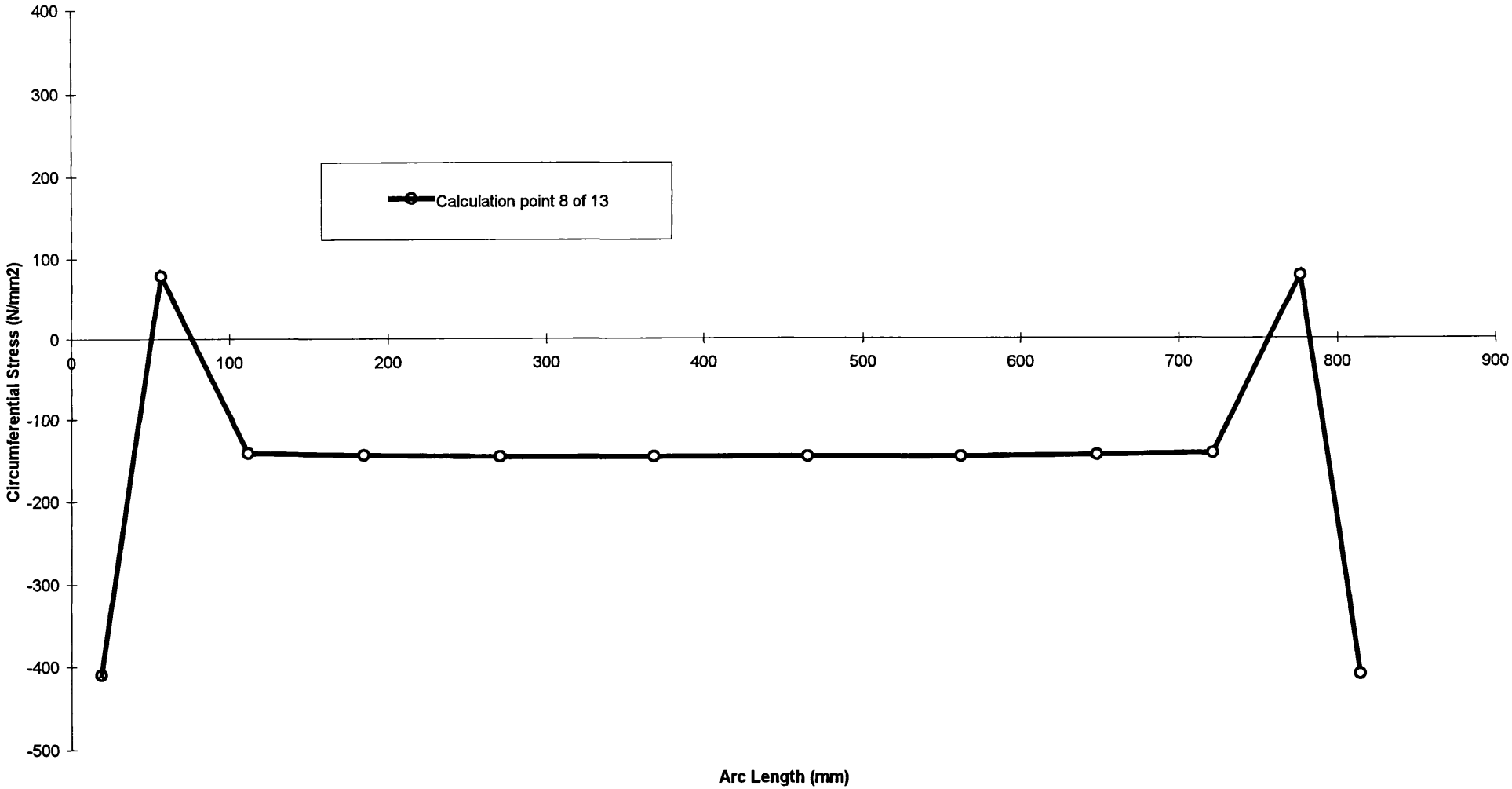


*Fig. A2.2.5.8, Model 2(ortho), inter frame circumferential residual stress.*

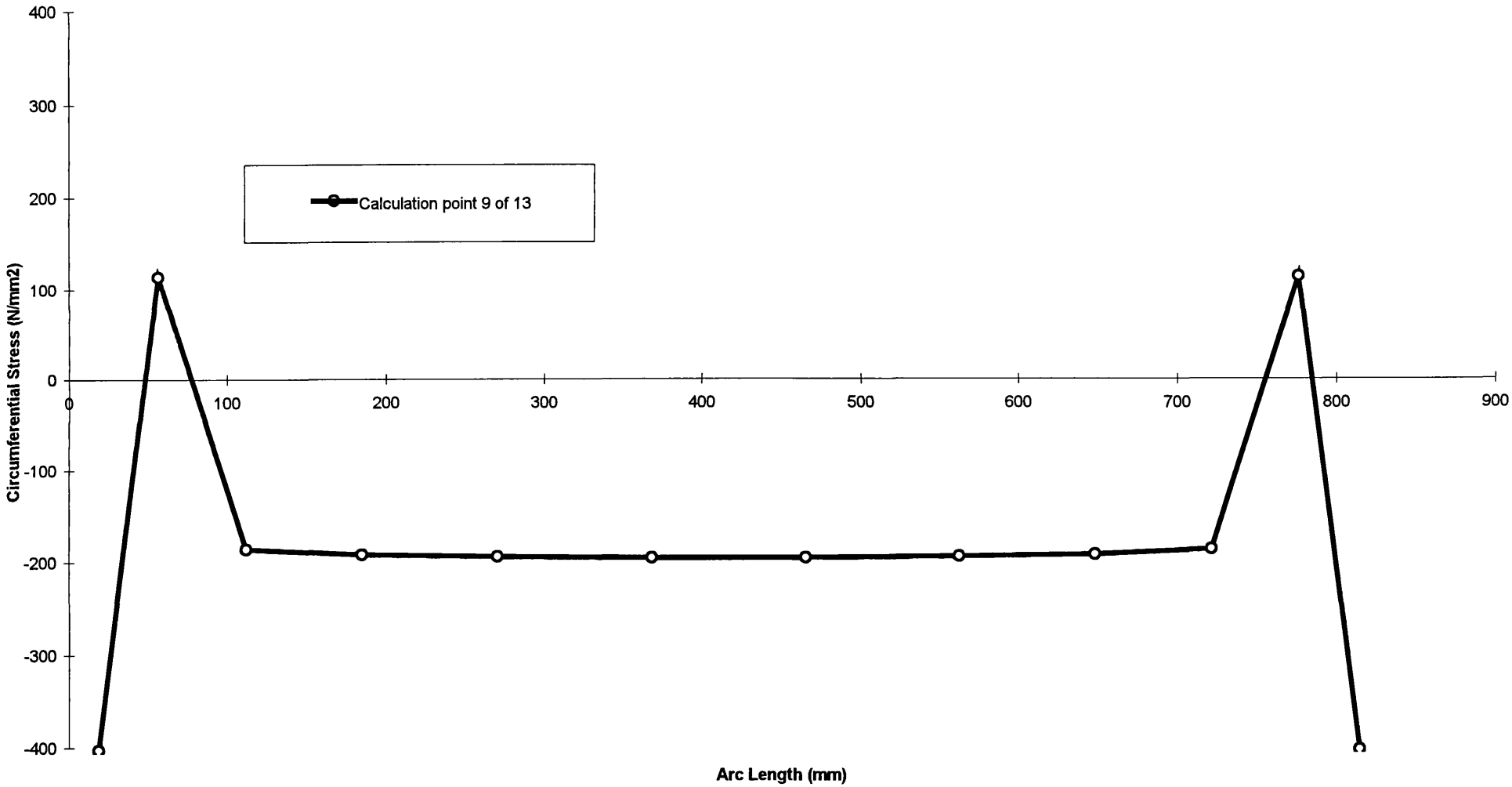


*Fig. A2.2.5.9, Model 2(ortho), interframe circumferential residual stress.*

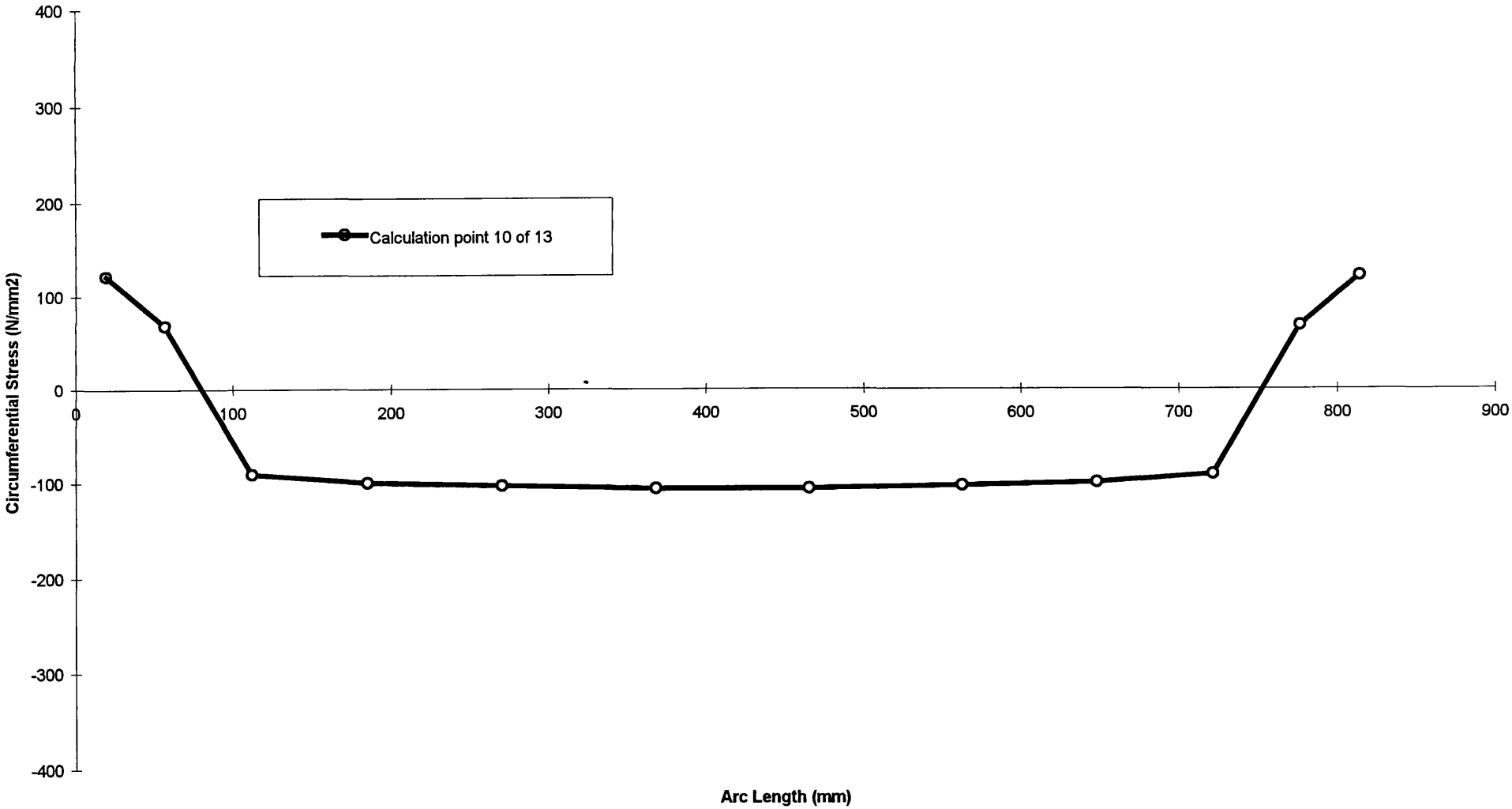


*Fig. A2.2.5.10, Model 2(ortho), inter frame circumferential residual stress.*

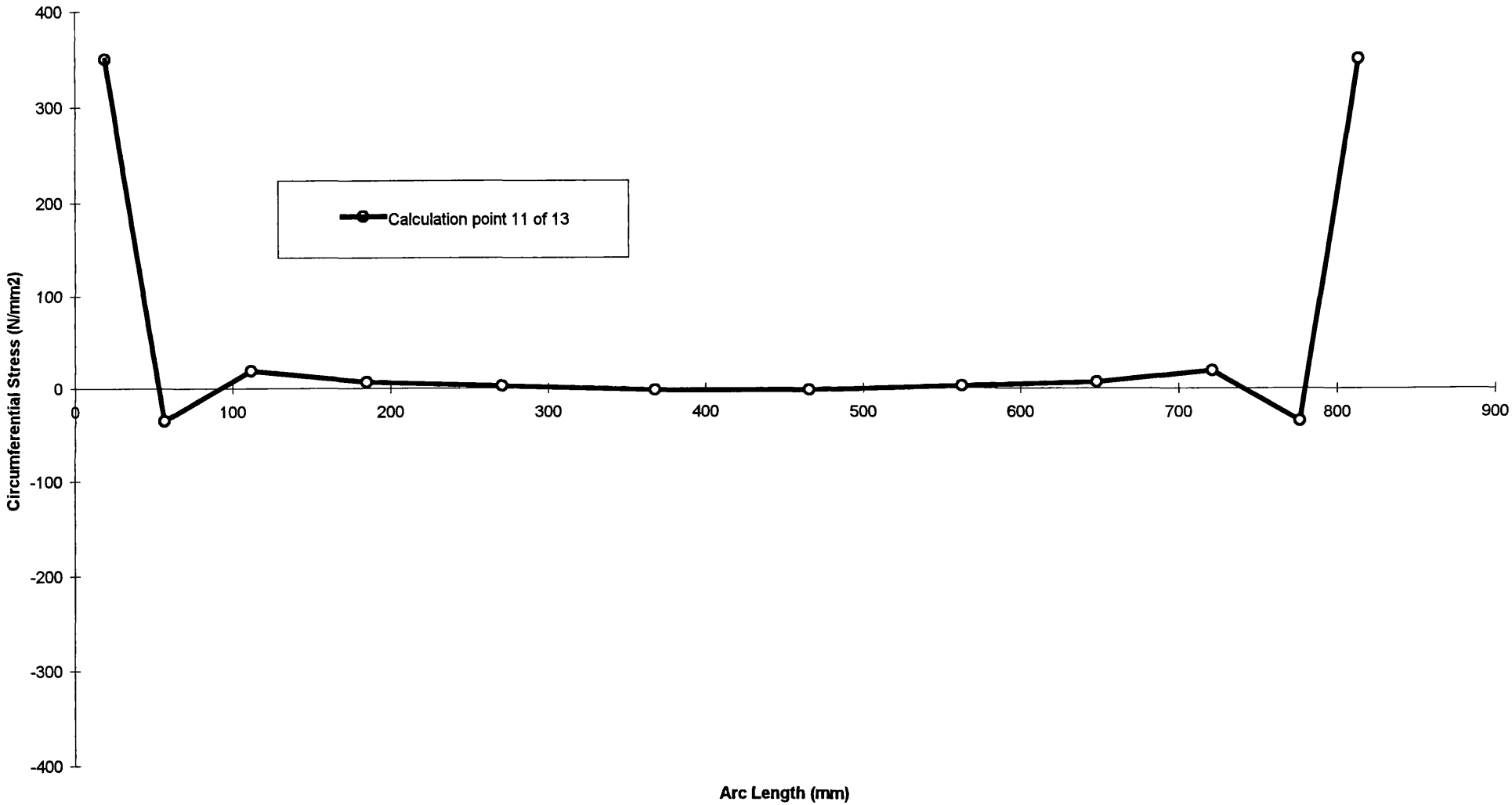


*Fig. A2.2.5.11, Model 2(ortho), inter frame circumferential residual stress.*

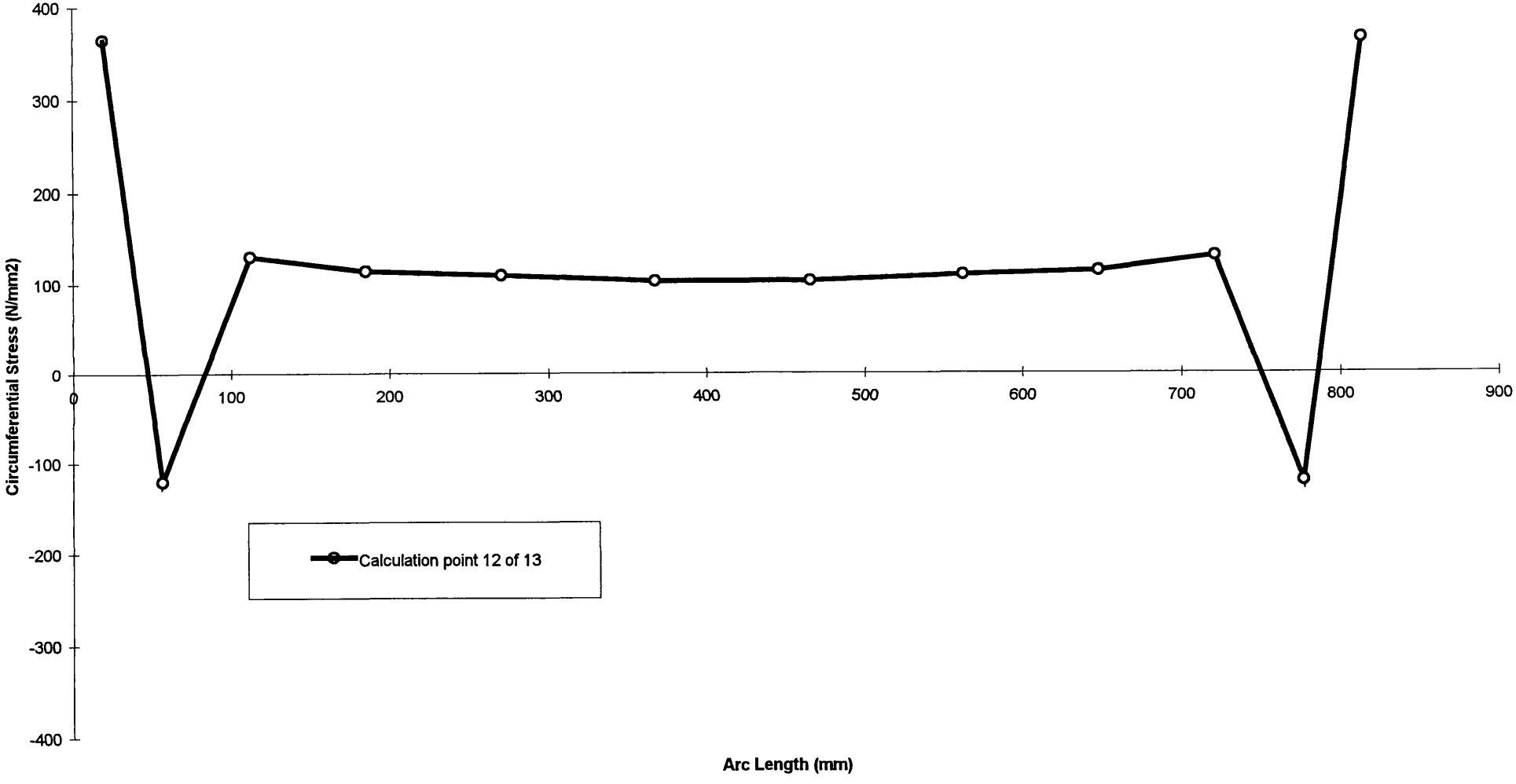


*Fig. A2.2.5.12, Model 2(ortho), inter frame circumferential residual stress.*

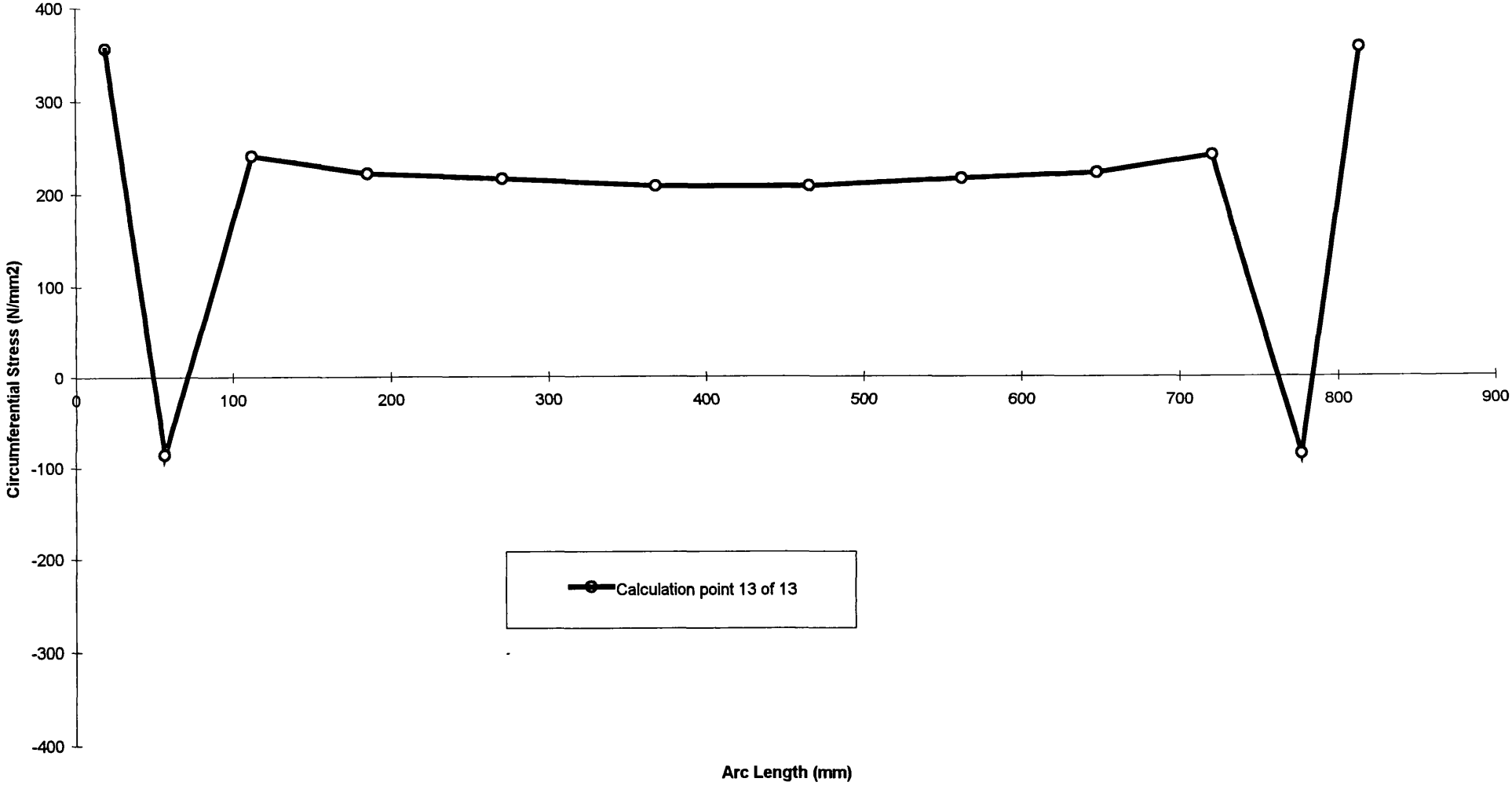


*Fig. A2.2.5.13, Model 2(ortho), inter frame circumferential residual stress.*

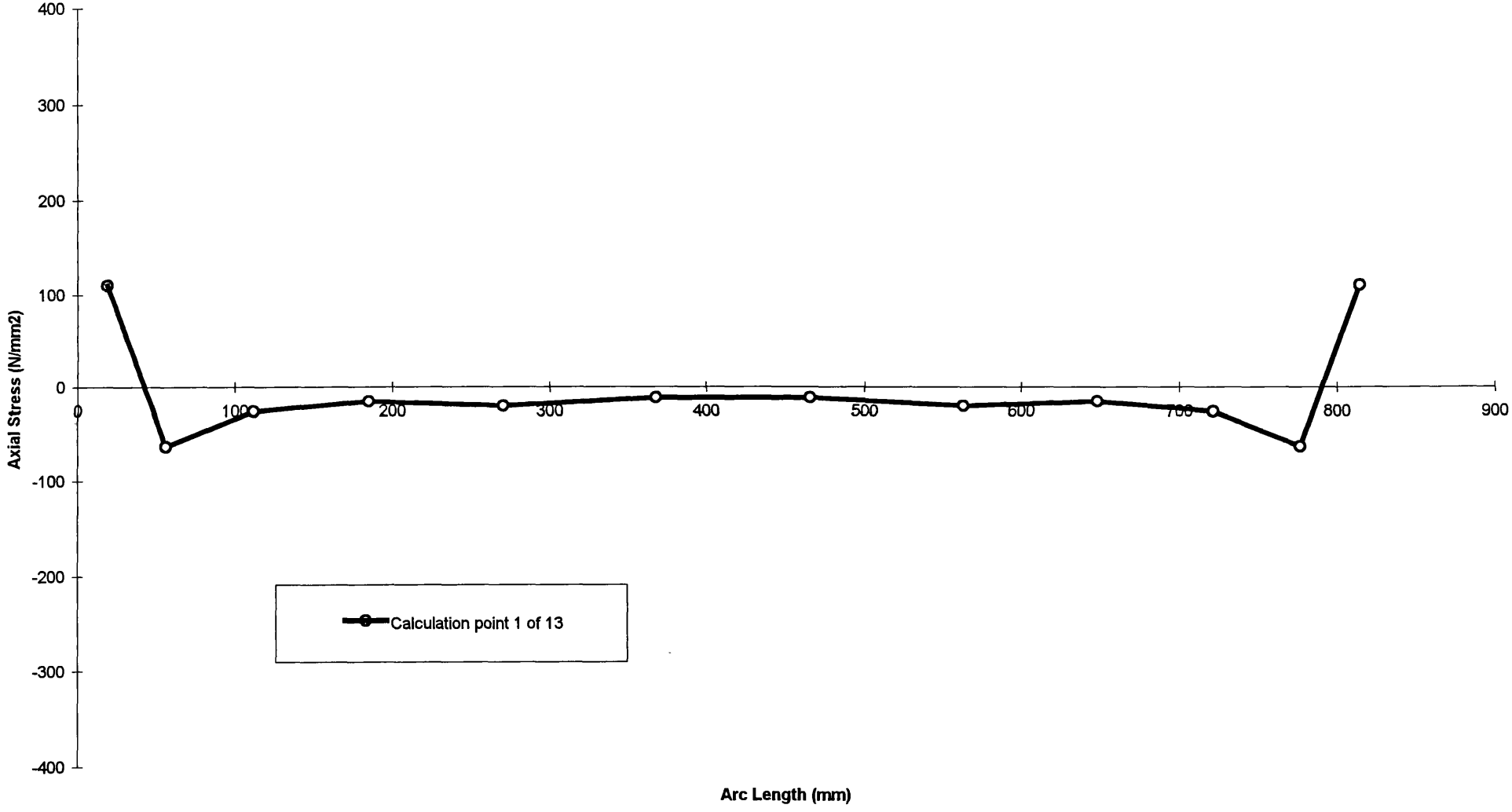


*Fig. A2.2.6.1, Model 2(ortho), Inter frame axial residual stress.*

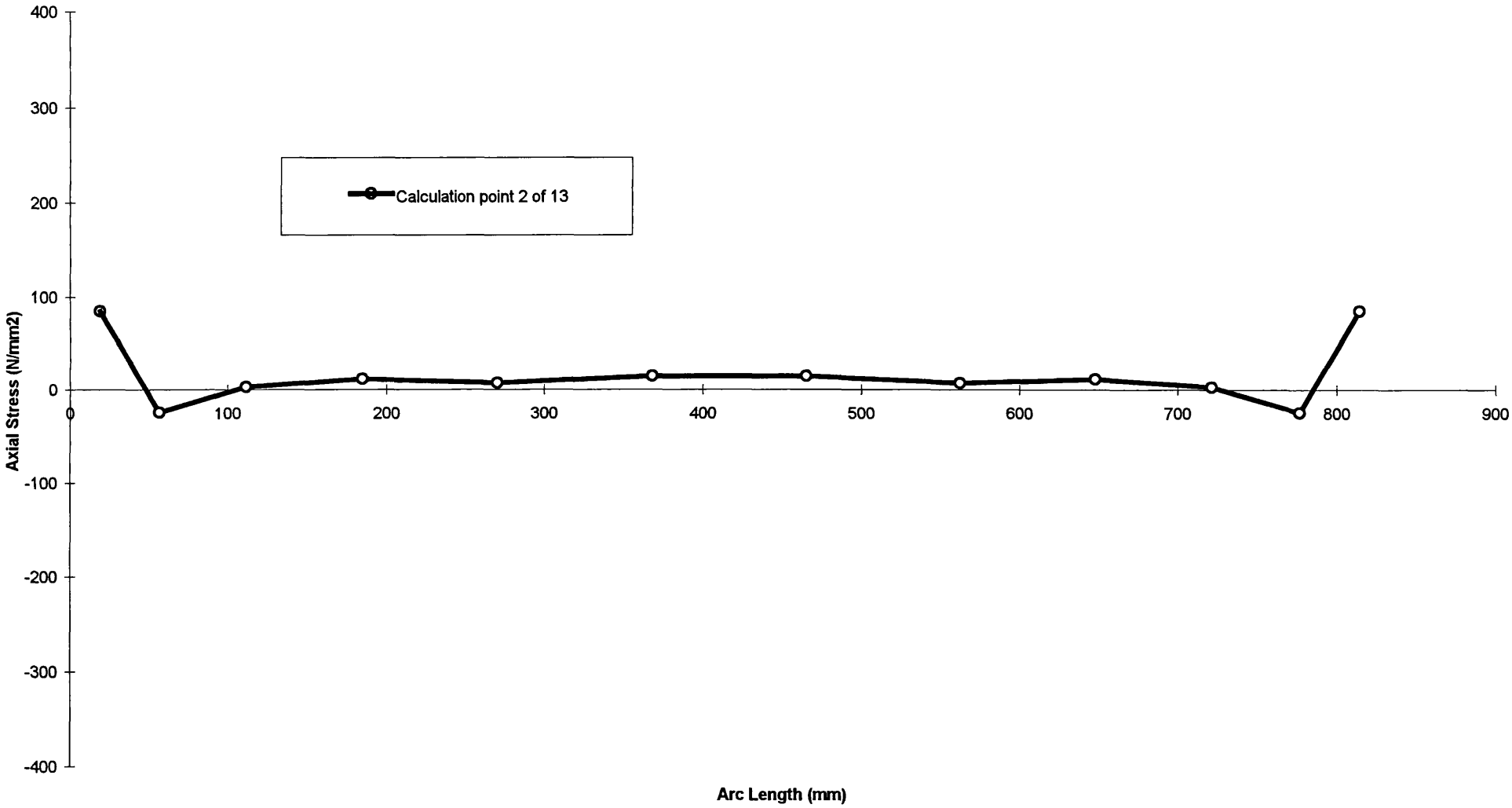


*Fig. A2.2.6.2, Model 2(ortho), inter frame axial residual stress.*

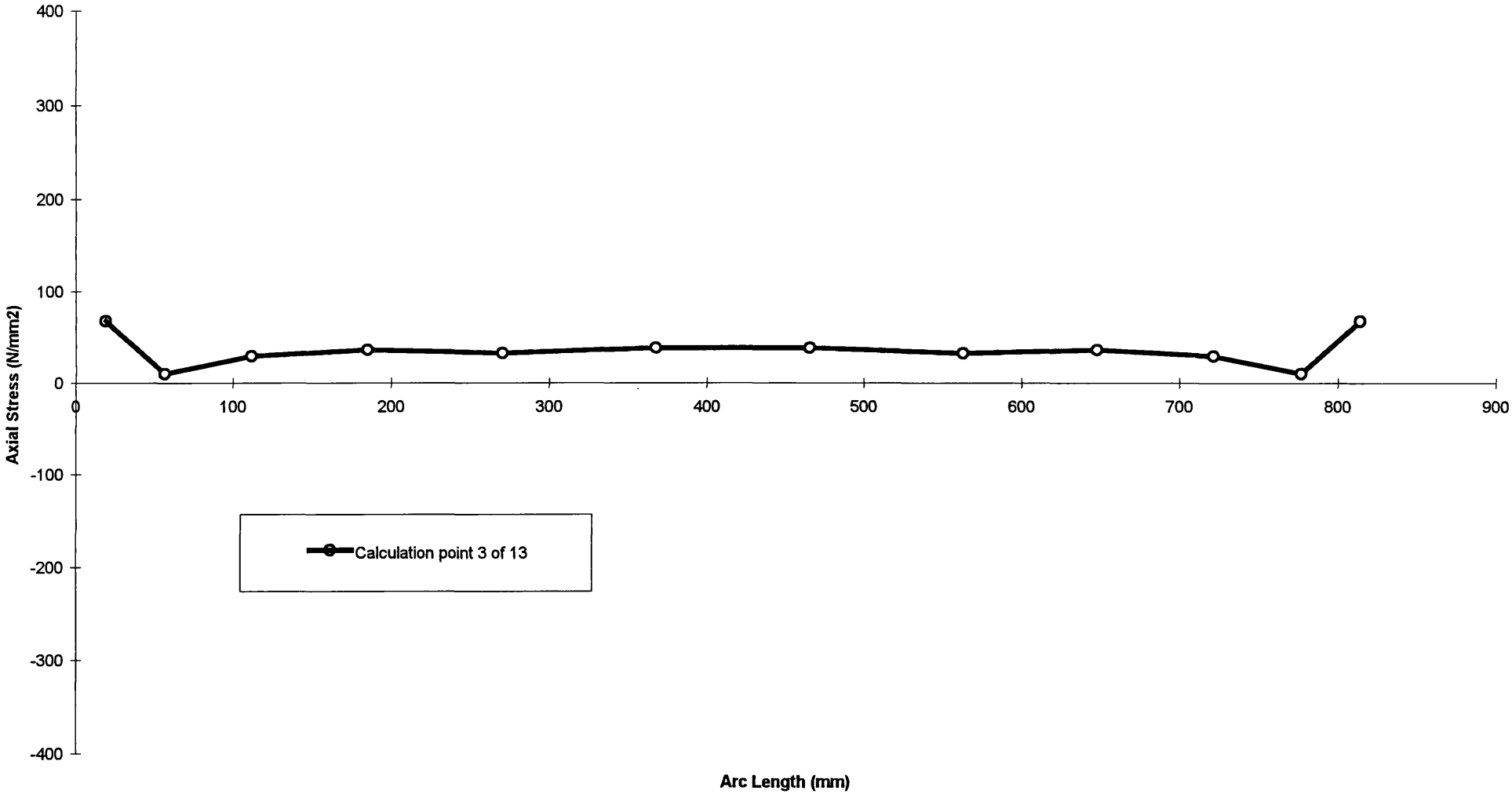


*Fig. A2.2.6.3, Model 2(ortho), inter frame axial residual stress.*

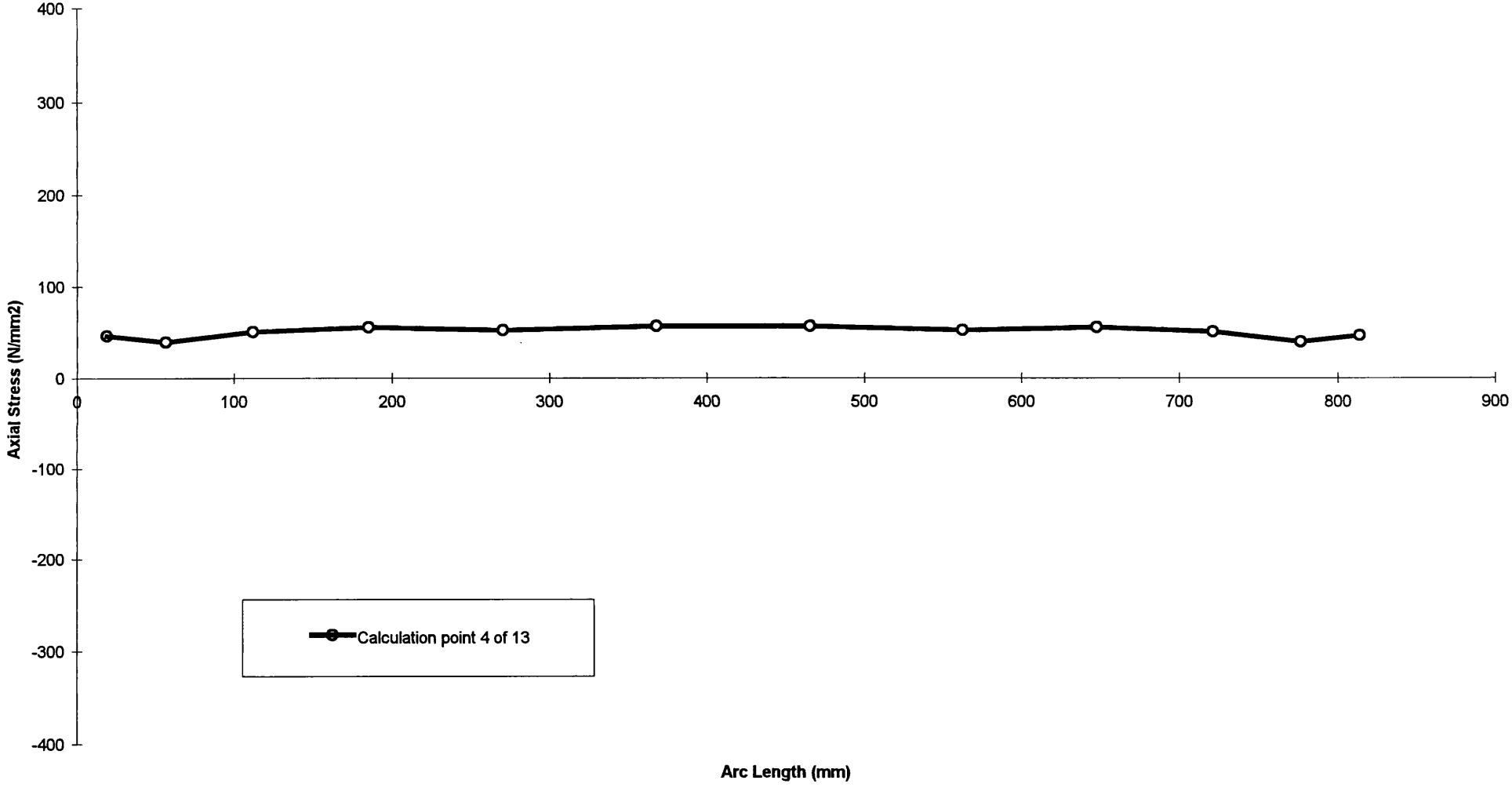


*Fig. A2.2.6.4, Model 2(ortho), inter frame axial residual stress.*

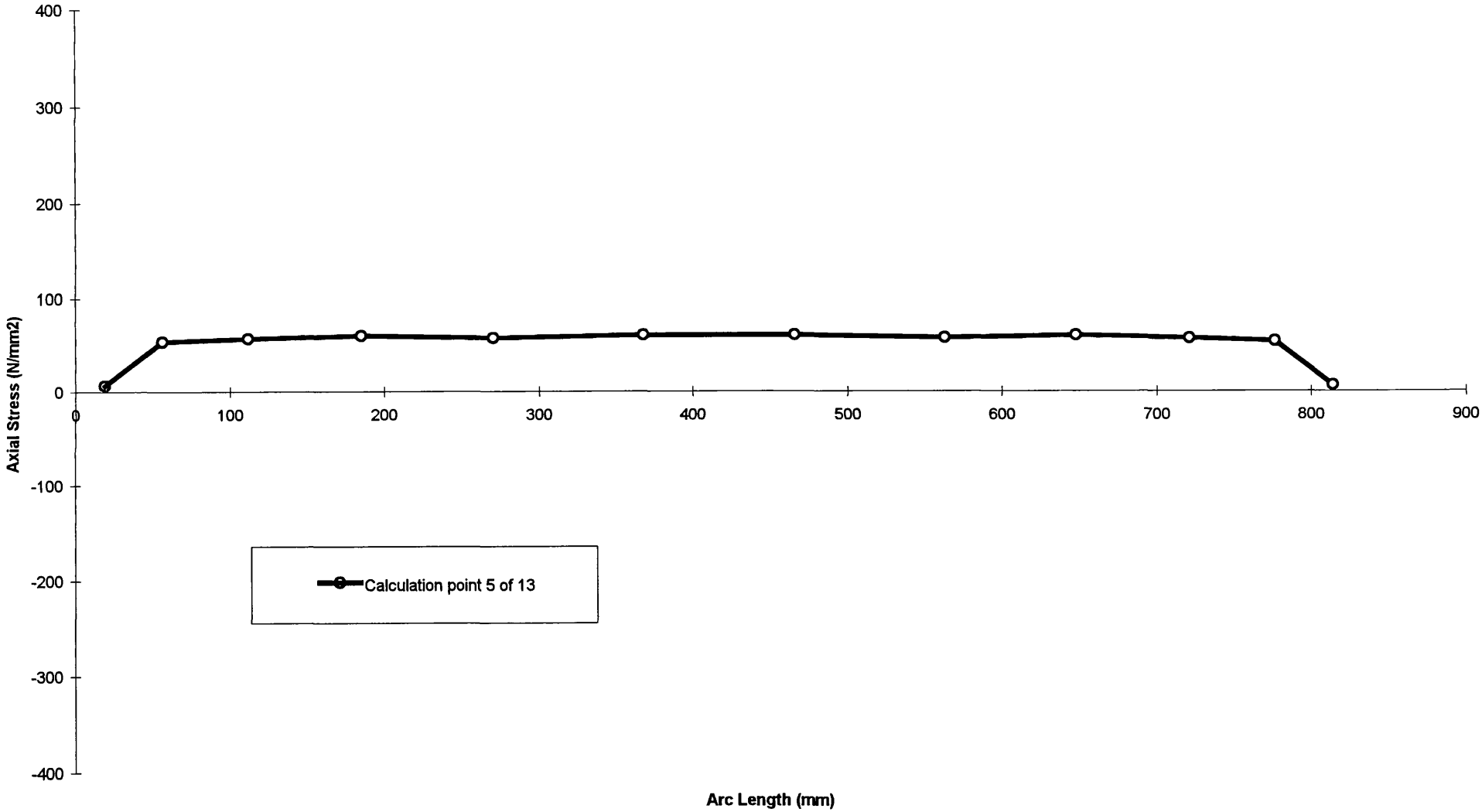


*Fig. A2.2.6.5, Model 2(ortho), inter frame axial residual stress.*

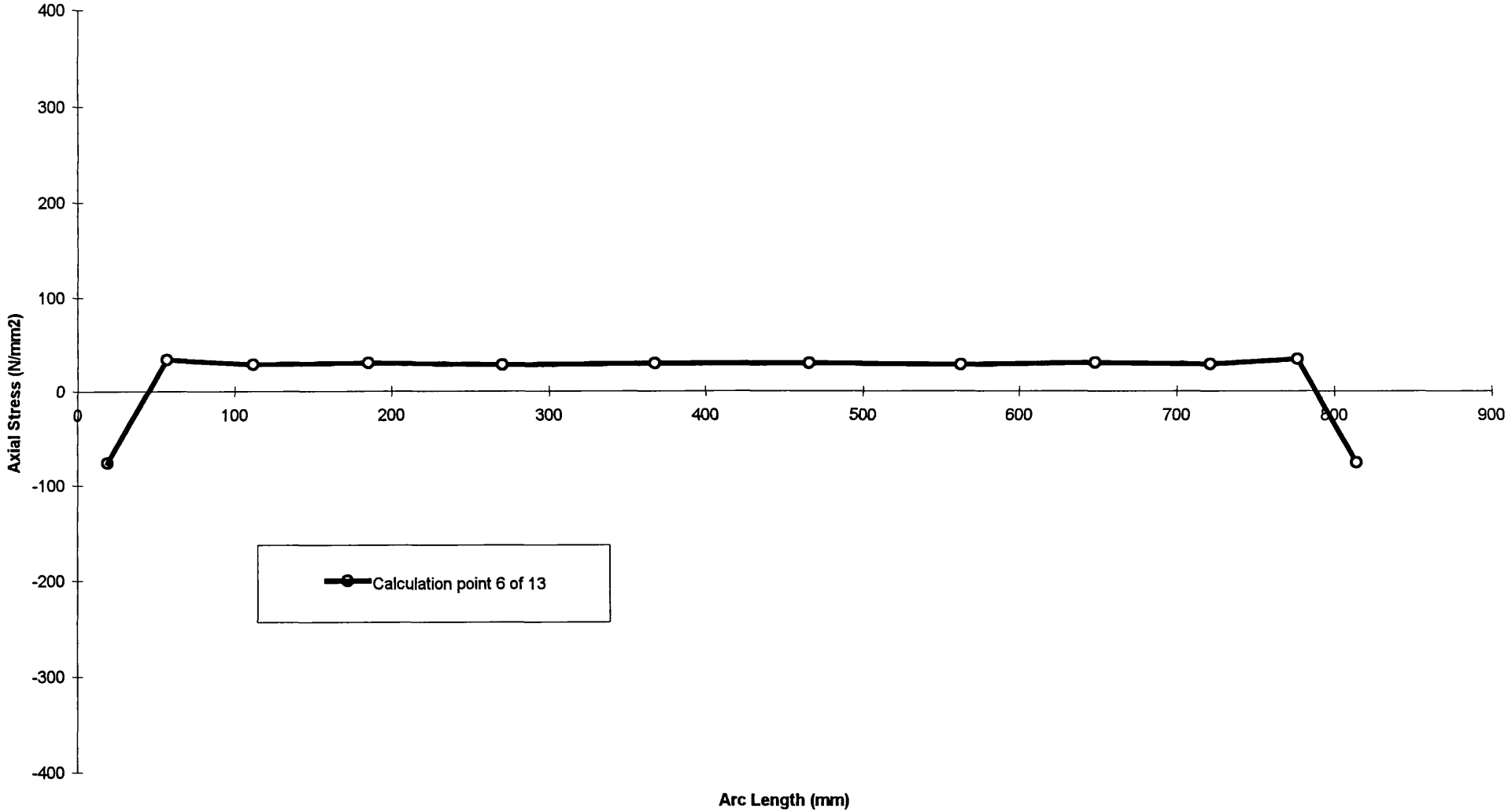


*Fig. A2.2.6.6, Model 2(ortho), inter frame axial residual stress.*

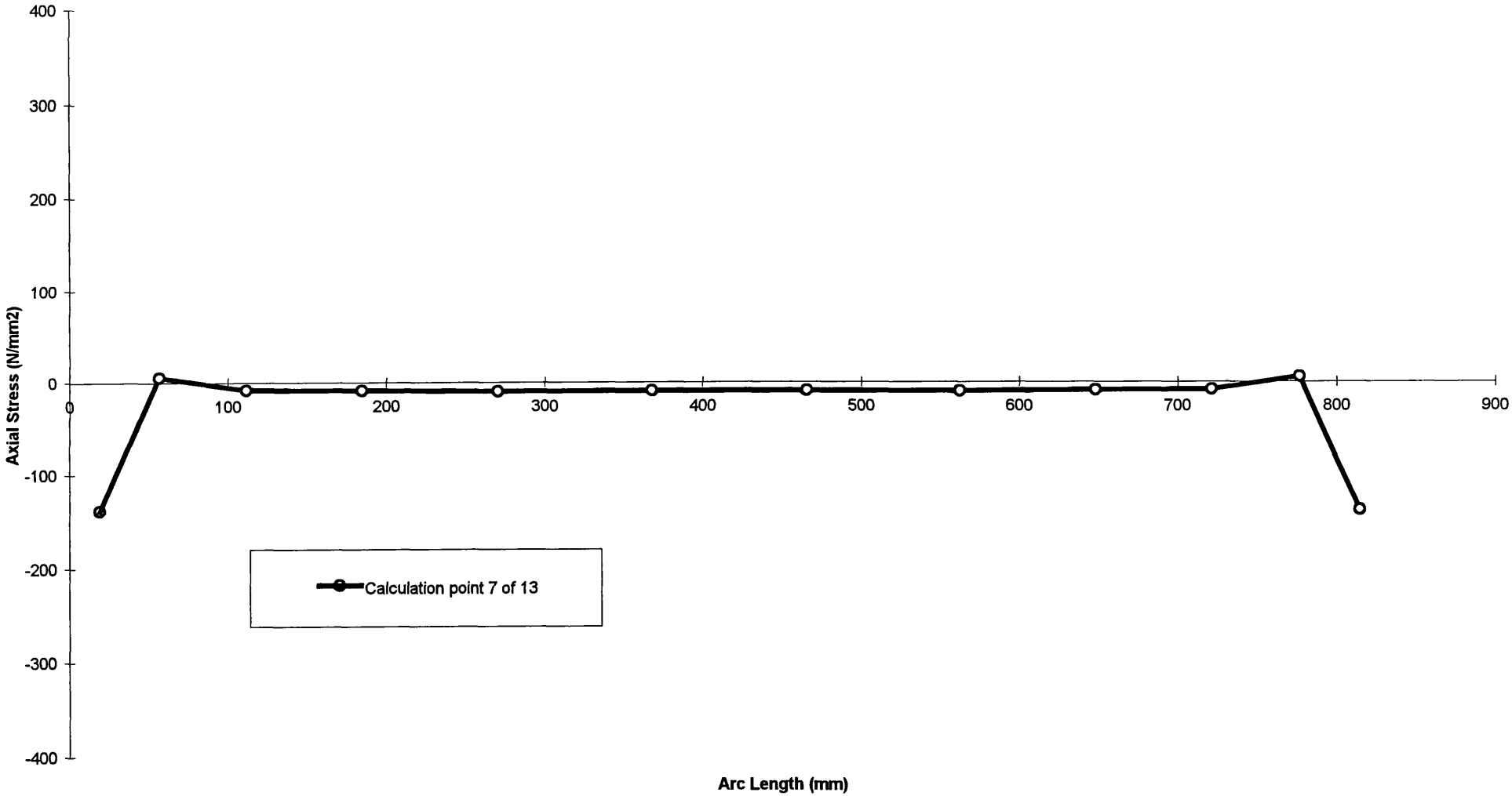


*Fig. A2.2.6.7, Model 2(ortho), inter frame axial residual stress.*

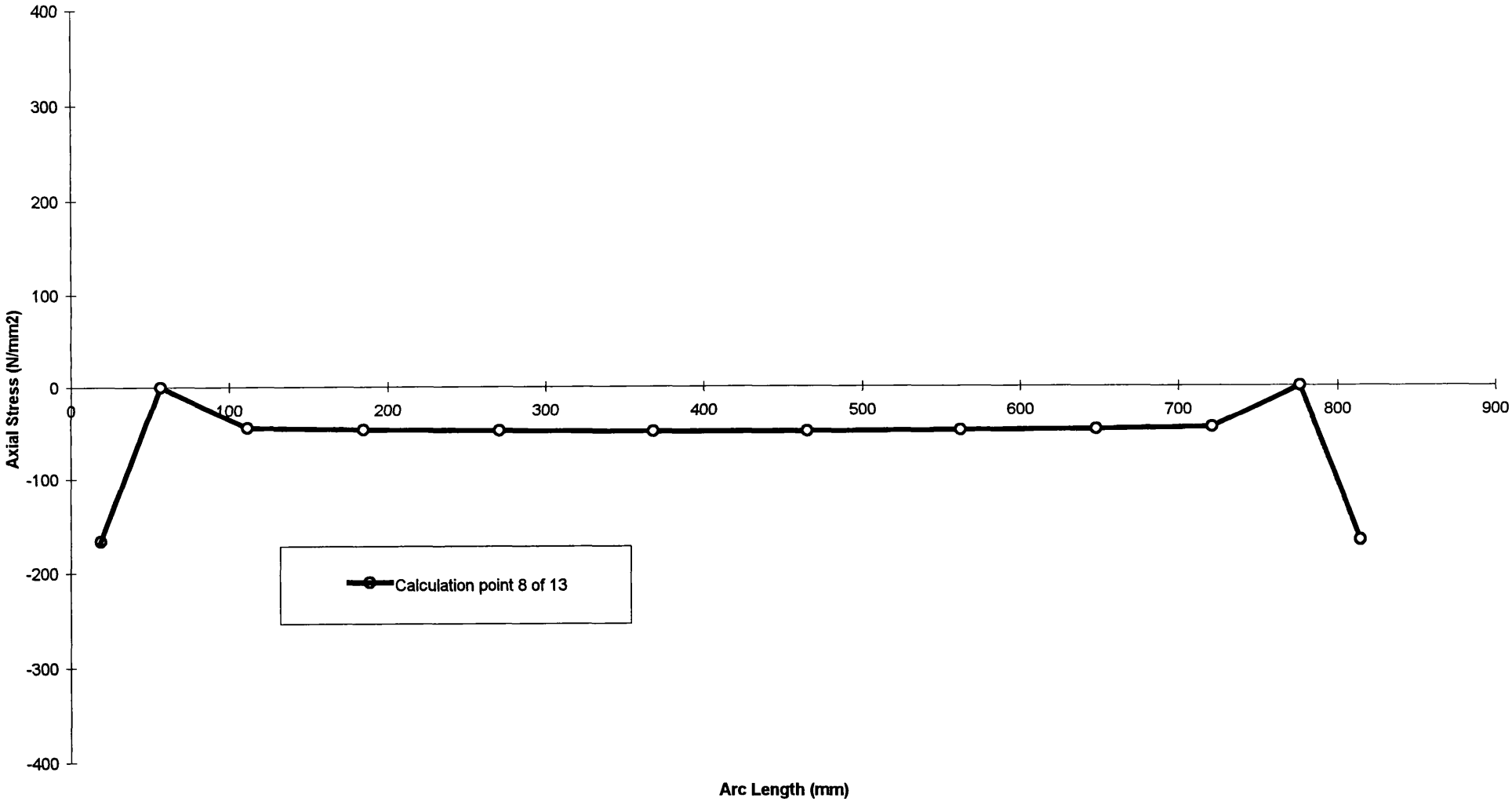


*Fig. A2.2.6.8, Model 2(ortho), inter frame axial residual stress.*

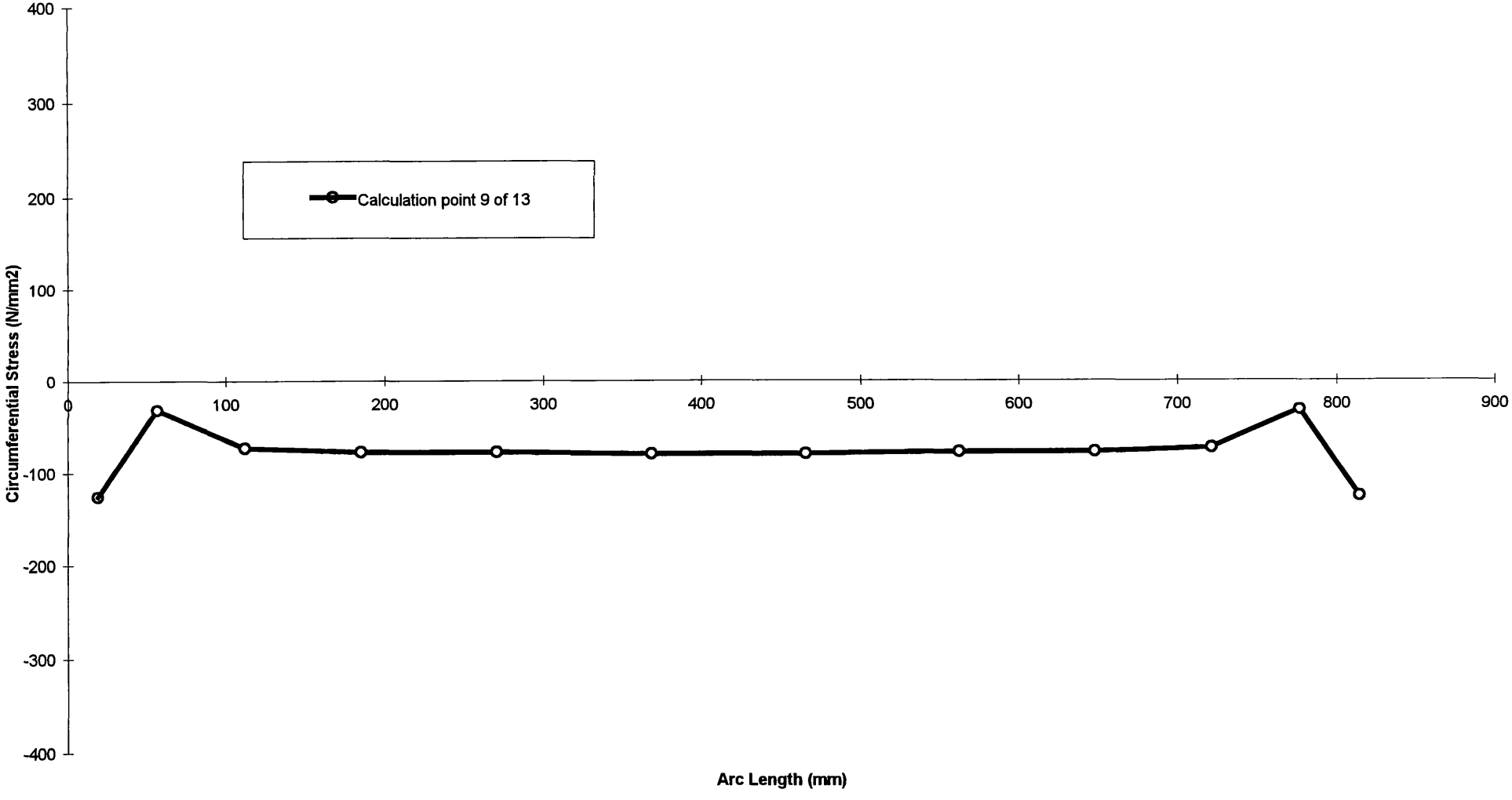


*Fig. A2.2.6.9, Model 2(ortho), interframe axial residual stress.*

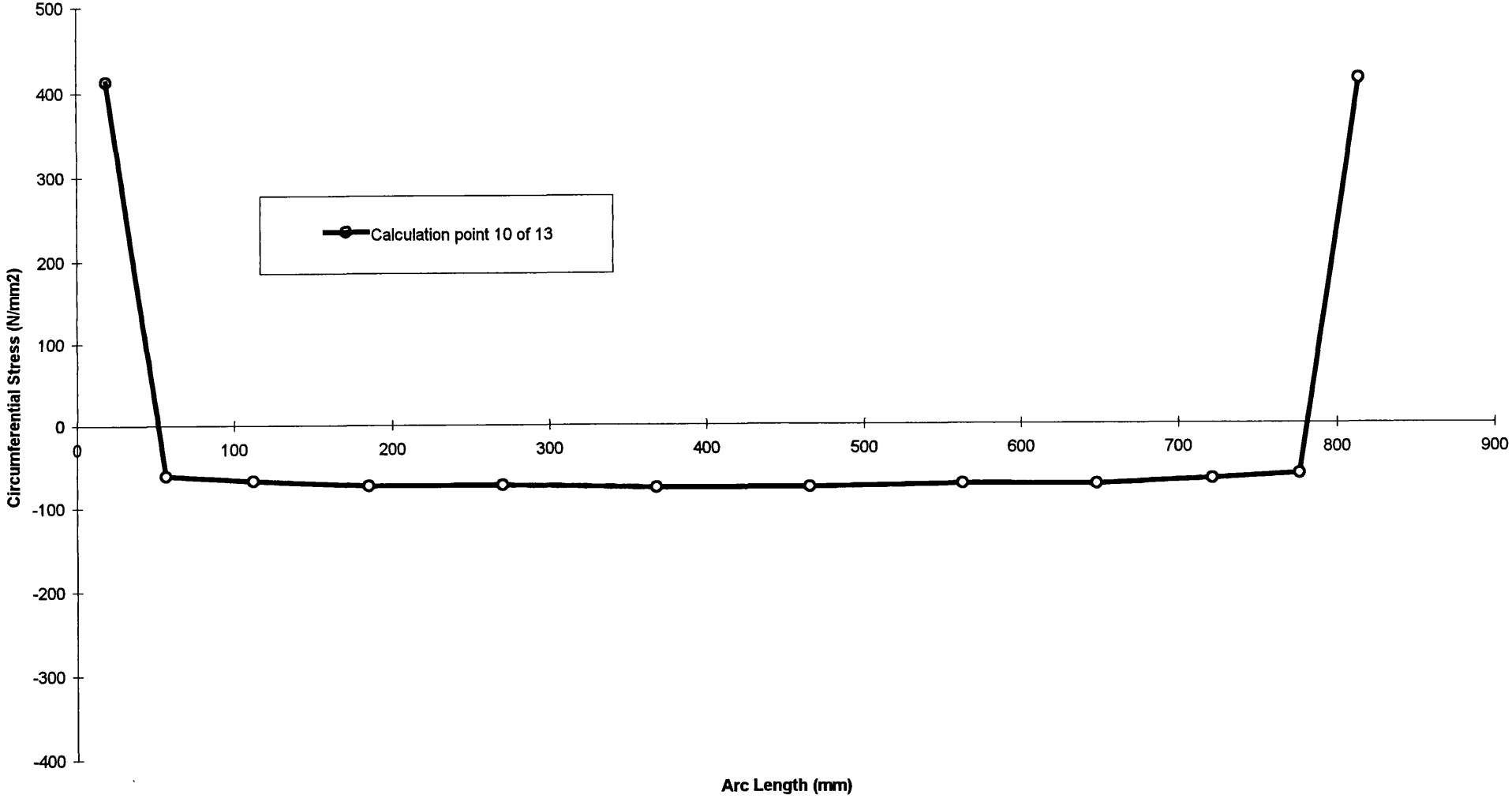


*Fig. A2.2.6.10, Model 2(ortho), inter frame axial residual stress.*

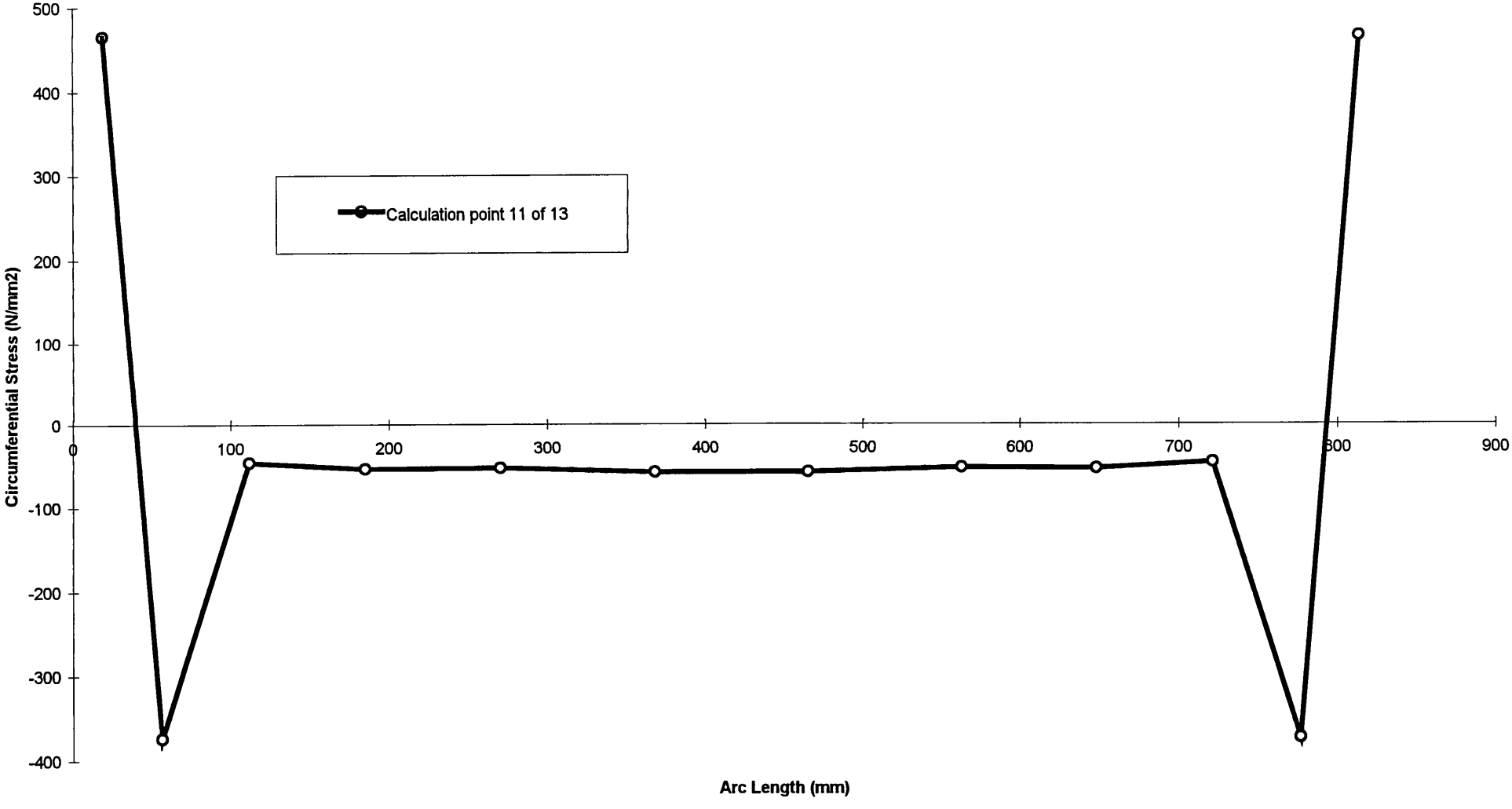


*Fig. A2.2.6.11, Model 2(ortho), inter frame residual stress.*

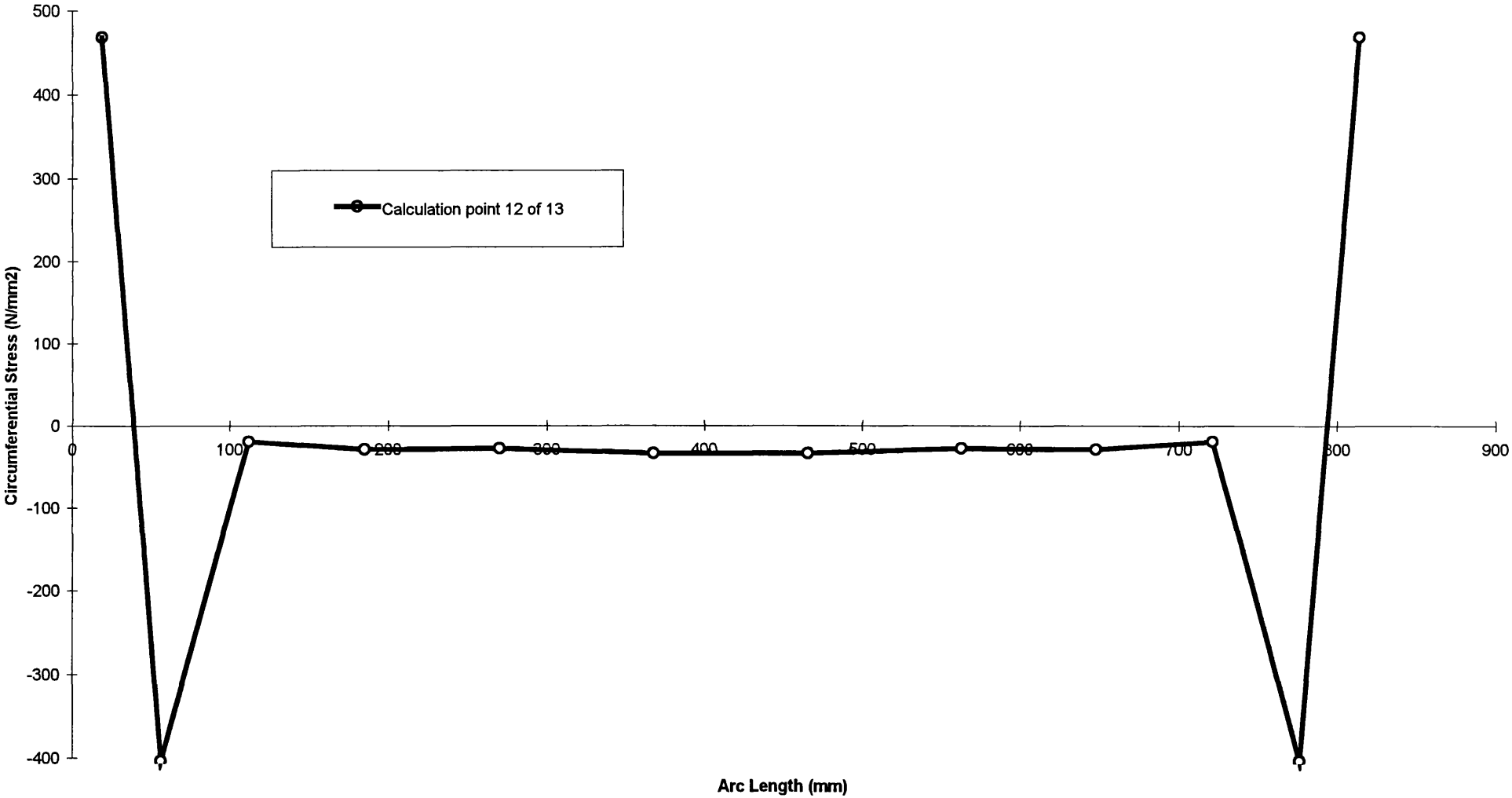


*Fig. A2.2.6.12, Model 2(ortho), inter frame residual stress.*

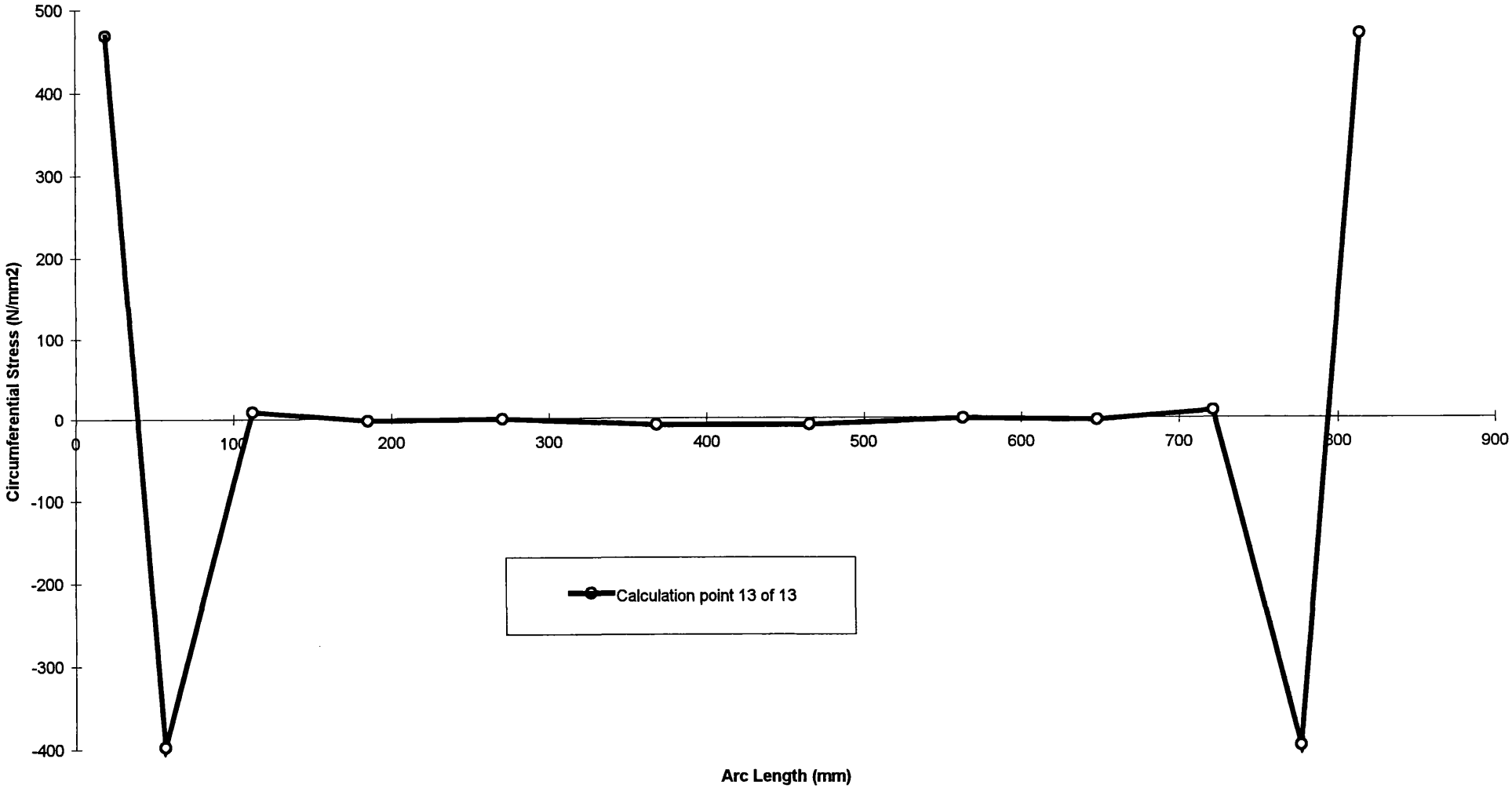


*Fig. A2.2.6.13, Model 2(ortho), inter frame residual stress.*

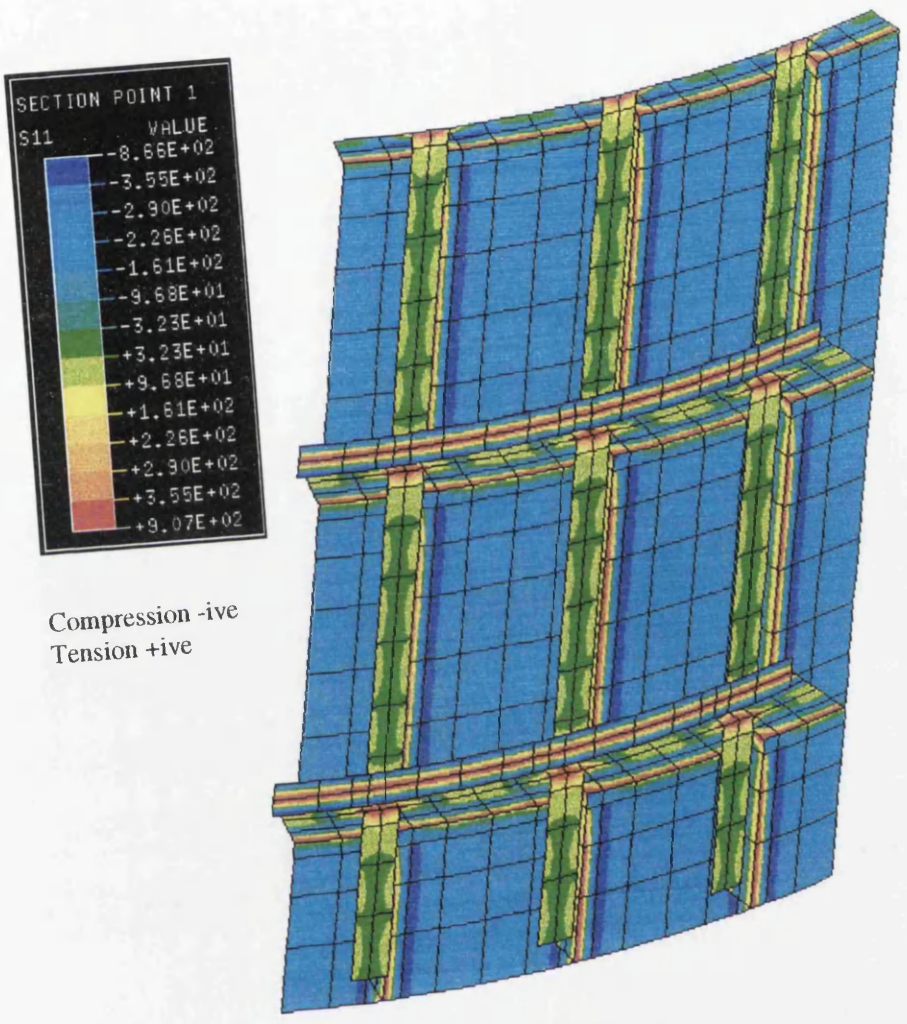


*Fig. A2.2.7.1, Model 2(ortho), circumferential residual stress at layer 1 (the far surface of all elements in the diagram) after the cold forming and welding steps.*

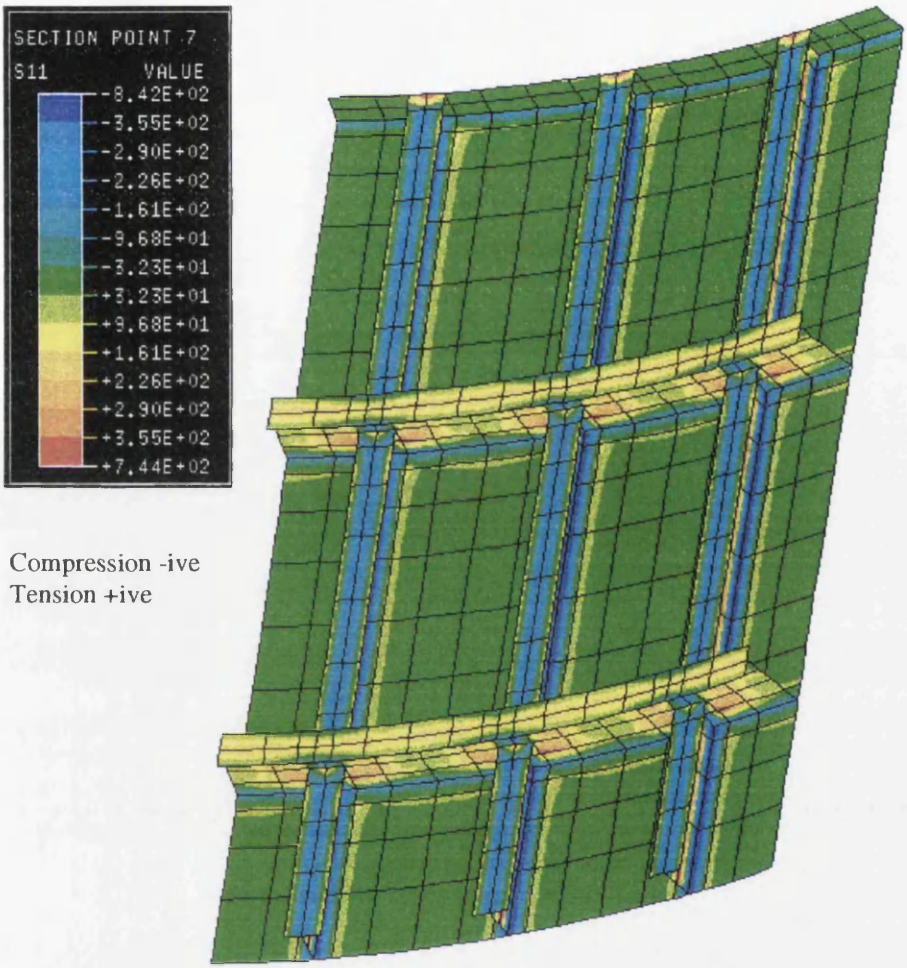


*Fig. A2.2.7.2, Model 2(ortho), circumferential residual stress at mid thickness after the cold forming and welding steps.*

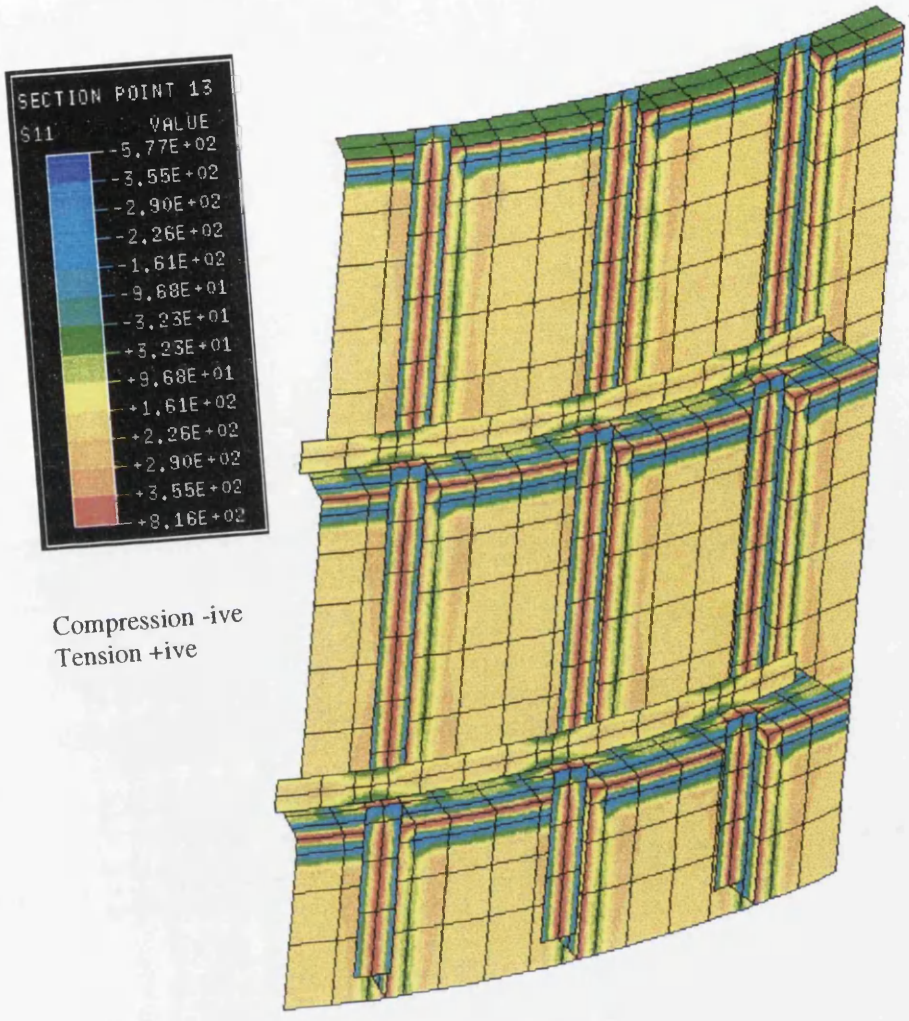


*Fig. A2.2.7.3. Model 2(ortho), circumferential residual stress at layer 13 (the near surface of all elements in the diagram) after the cold forming and welding steps.*

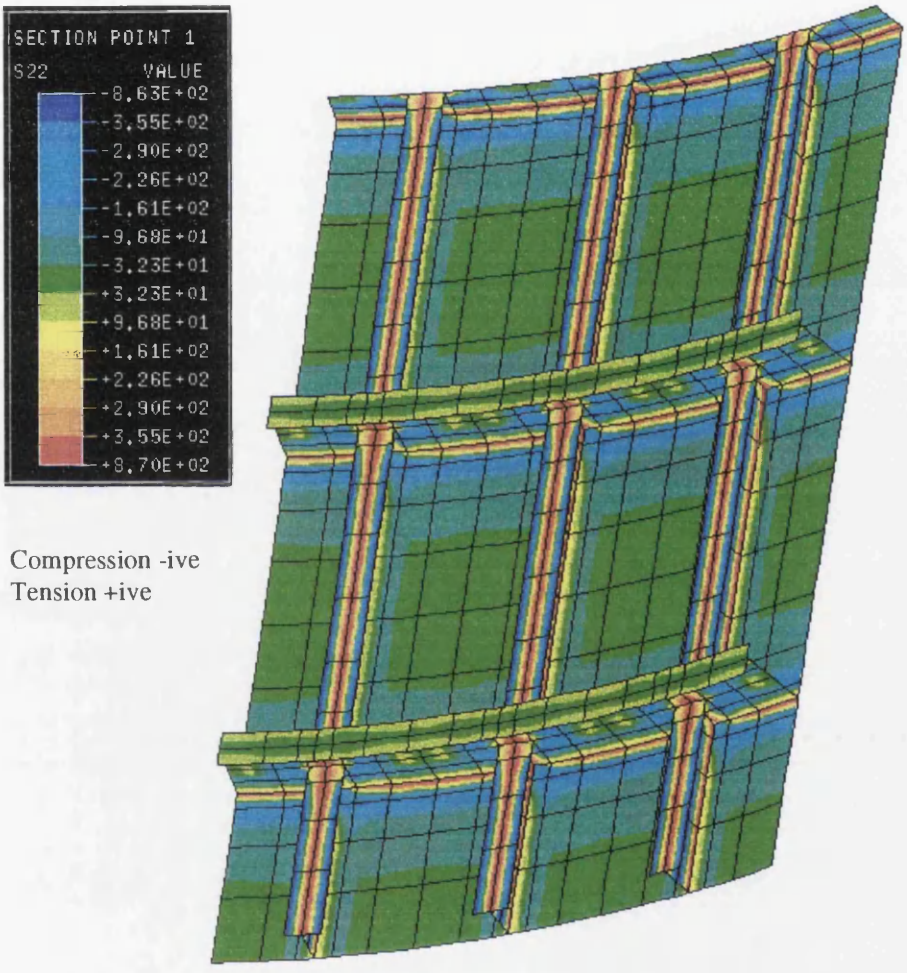


*Fig. A2.2.7.4. Model 2(ortho), axial residual stress at layer 1 (the far surface of all elements in the diagram) after the cold forming and welding steps.*

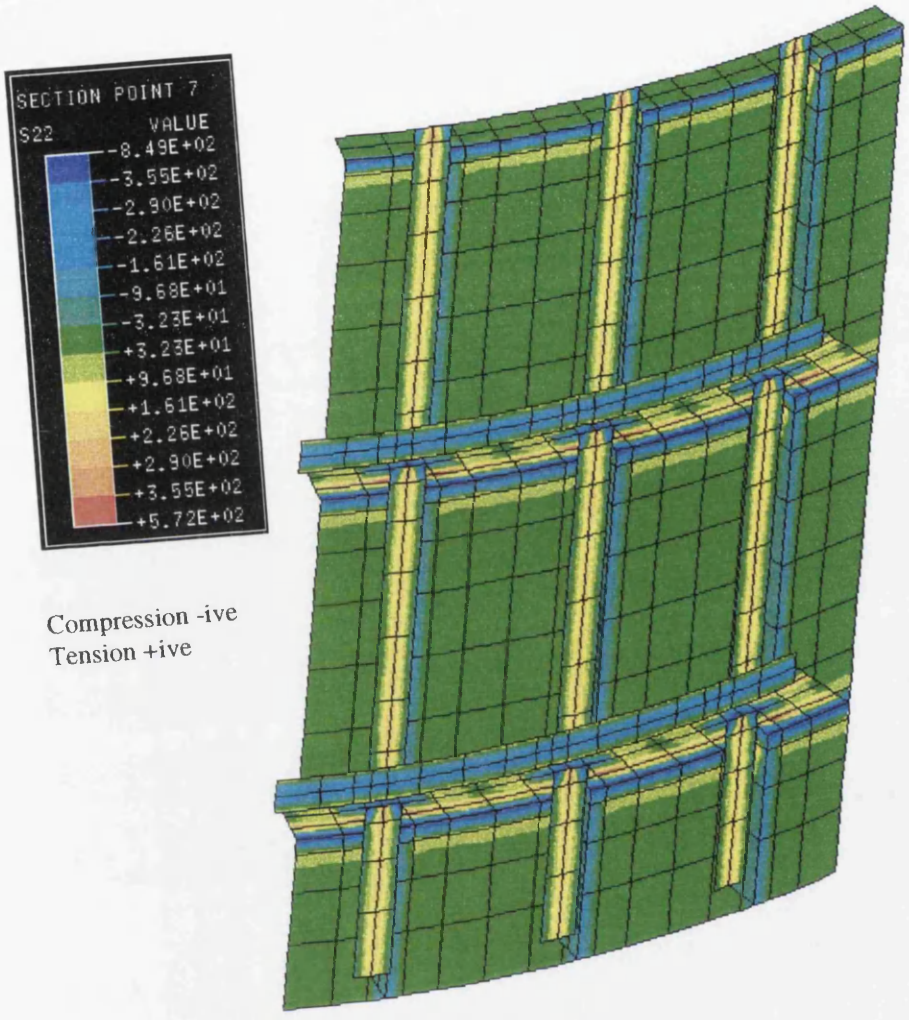


*Fig. A2.2.7.5, Model 2(ortho), axial residual stress at mid thickness after the cold forming and welding steps.*

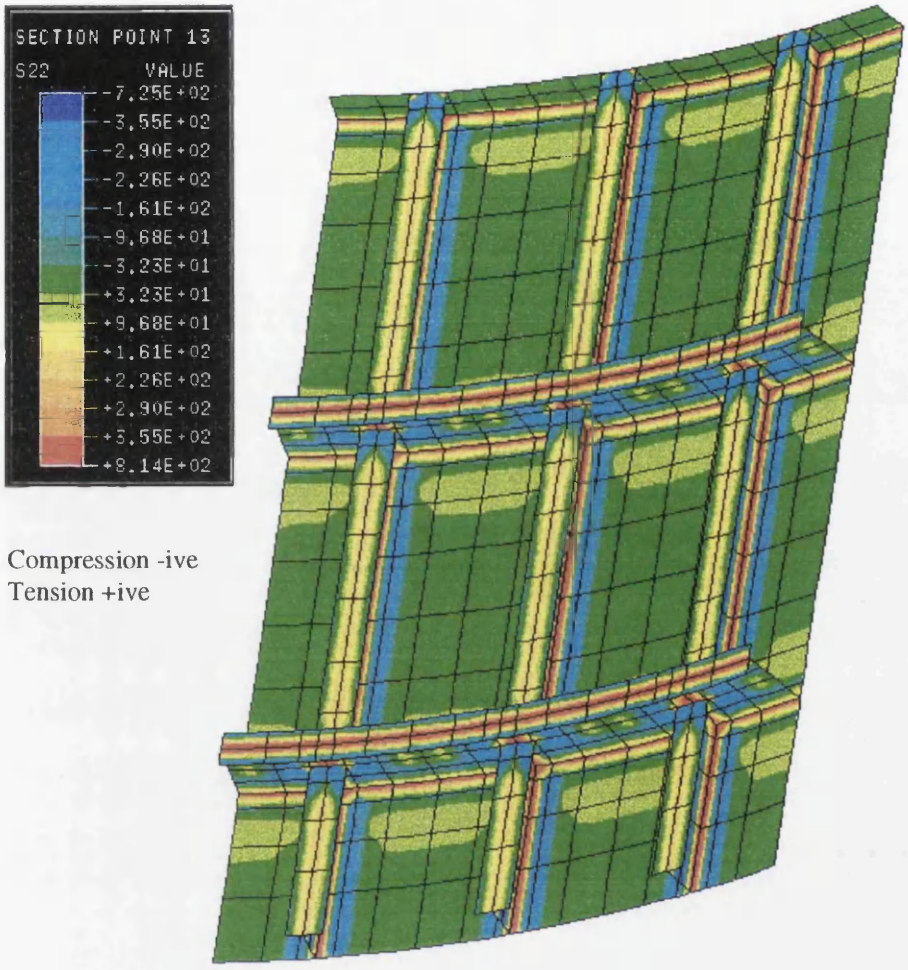


*Fig. A2.2.7.6, Model 2(ortho), axial residual stress at layer 13 (the near surface of all elements in the diagram) after the cold forming and welding steps.*

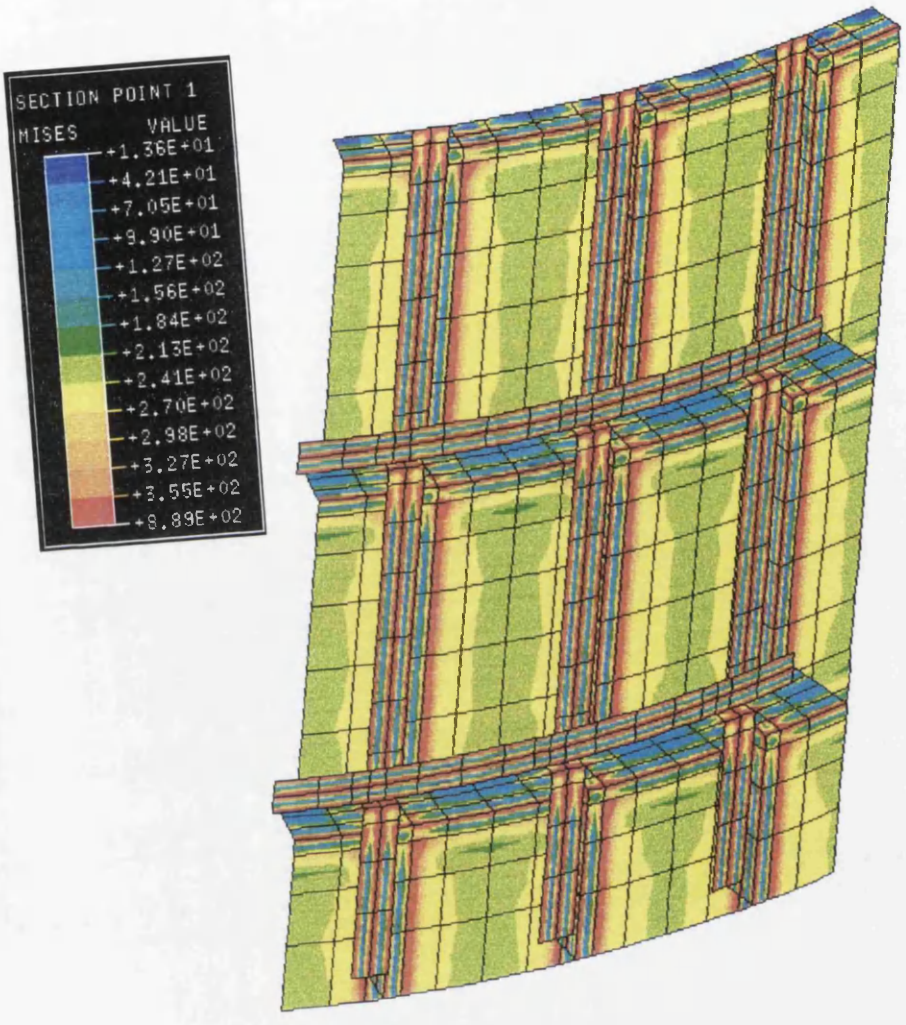


*Fig. A2.2.7.7, Model 2(ortho), Von Mises equivalent stress after the cold forming and welding steps at layer 1 (the far surface of all elements in the diagram).*

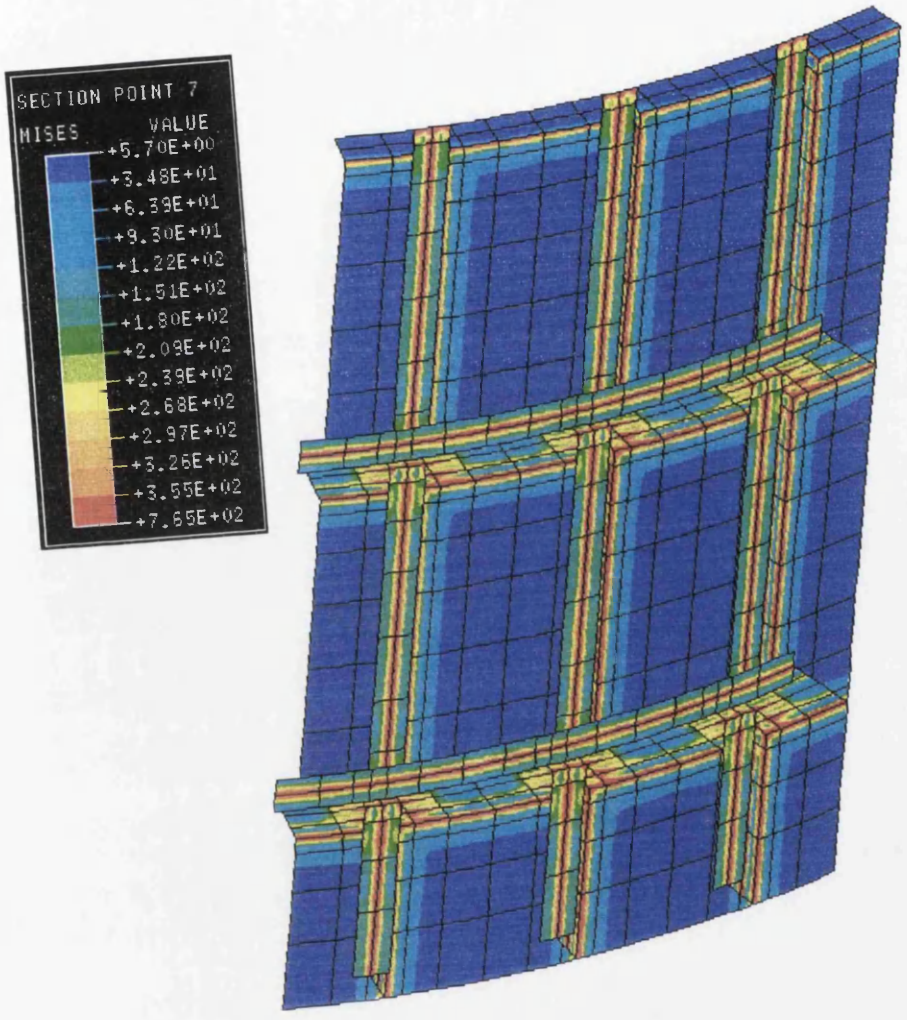


*Fig. A2.2.7.8, Model 2(ortho), Von Mises equivalent stress at mid thickness after the cold forming and welding steps.*

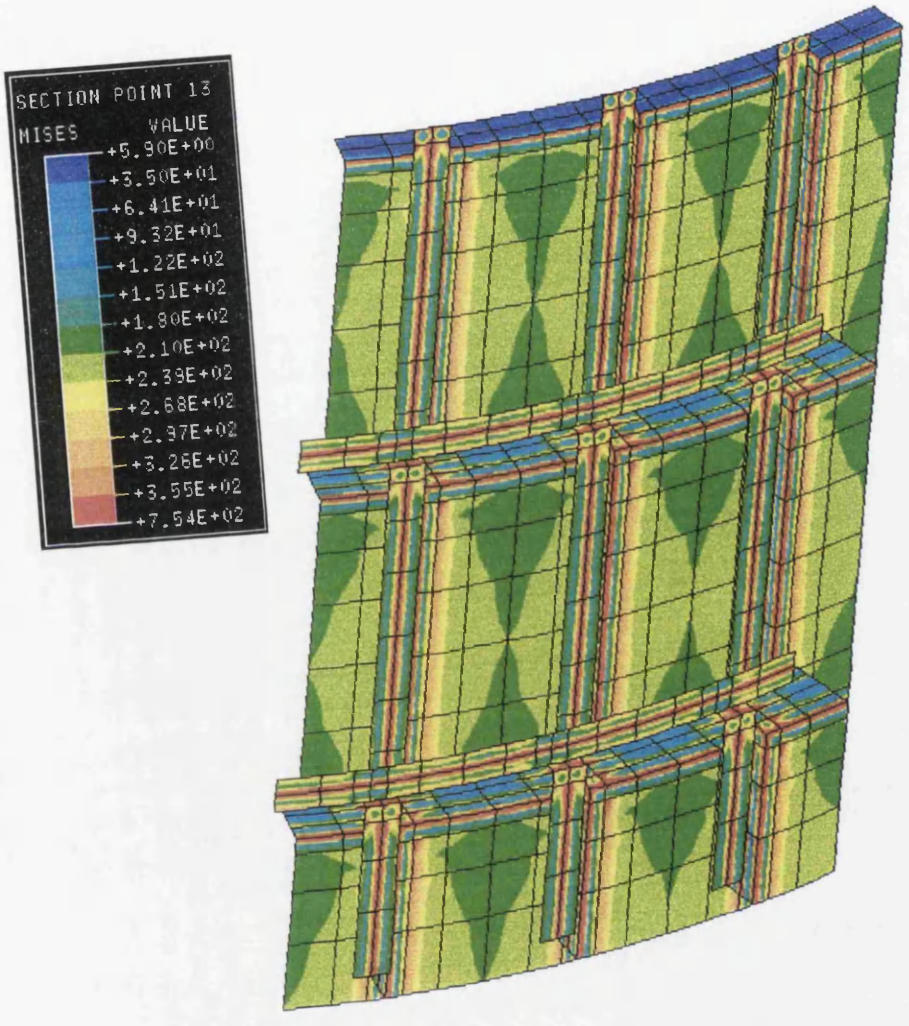


*Fig. A2.2.7.9, Model 2(ortho), mises equivalent stress at layer 13 (the near surface of all elements in the diagram) after the cold forming and welding steps.*


Compression -ive
Tension +ive

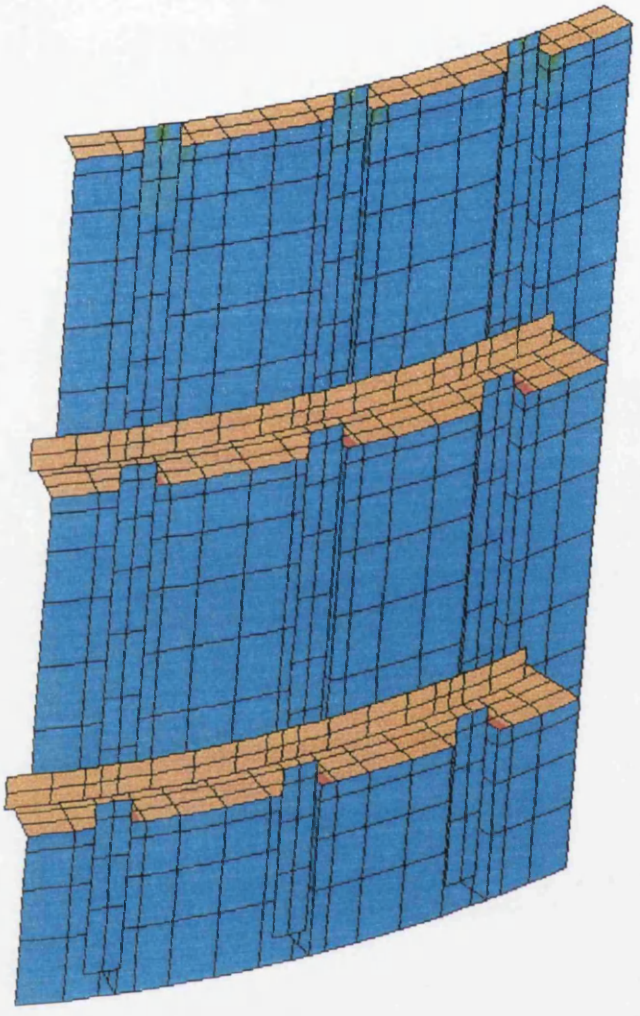

*Fig. A2.2.7.10, Model 2(ortho), Axial stress at mid thickness for the case* ***without*** *residual stress, after the axial loading step.*

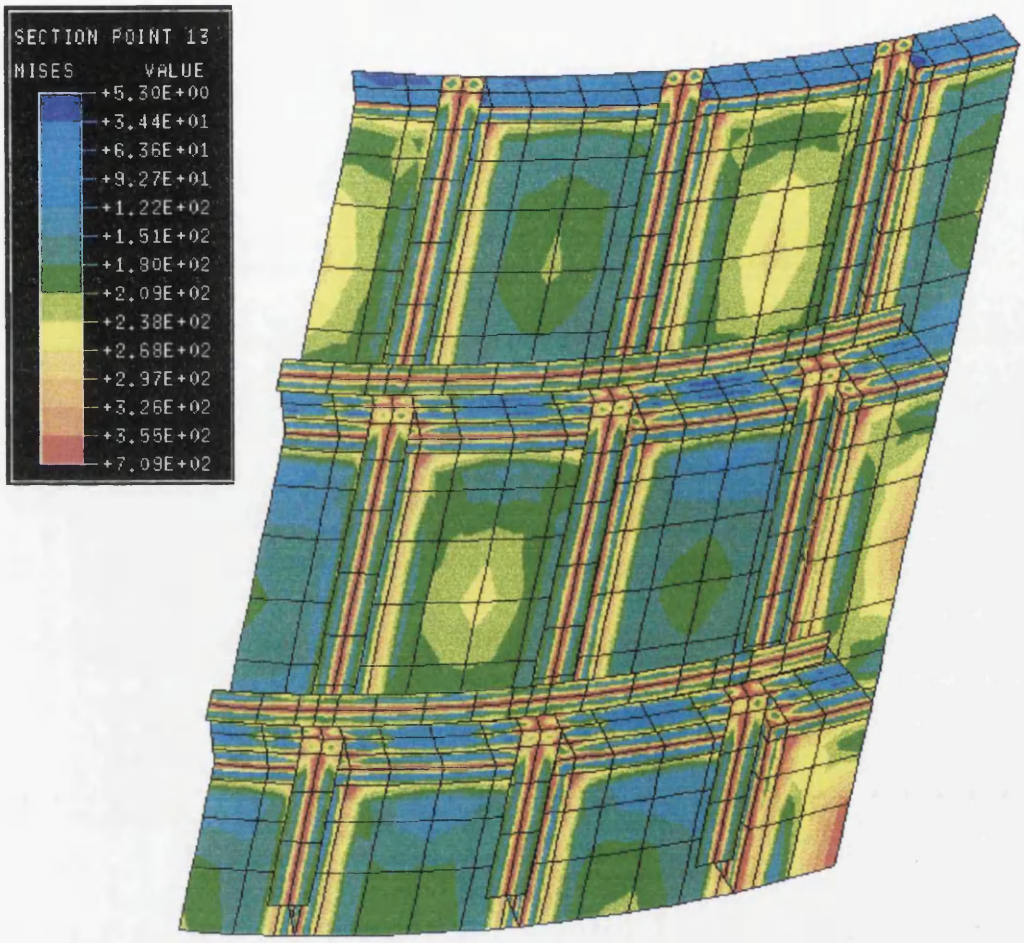


*Fig. A2.2.7.11, Model 2(ortho), Von Mises equivalent stress at layer 13 (the near surface of all elements in the diagram) after cold forming, welding, and axial loading steps, during the surface pressure buckling step, at the point of buckling (see point B, Fig. A2.2.8.1)*

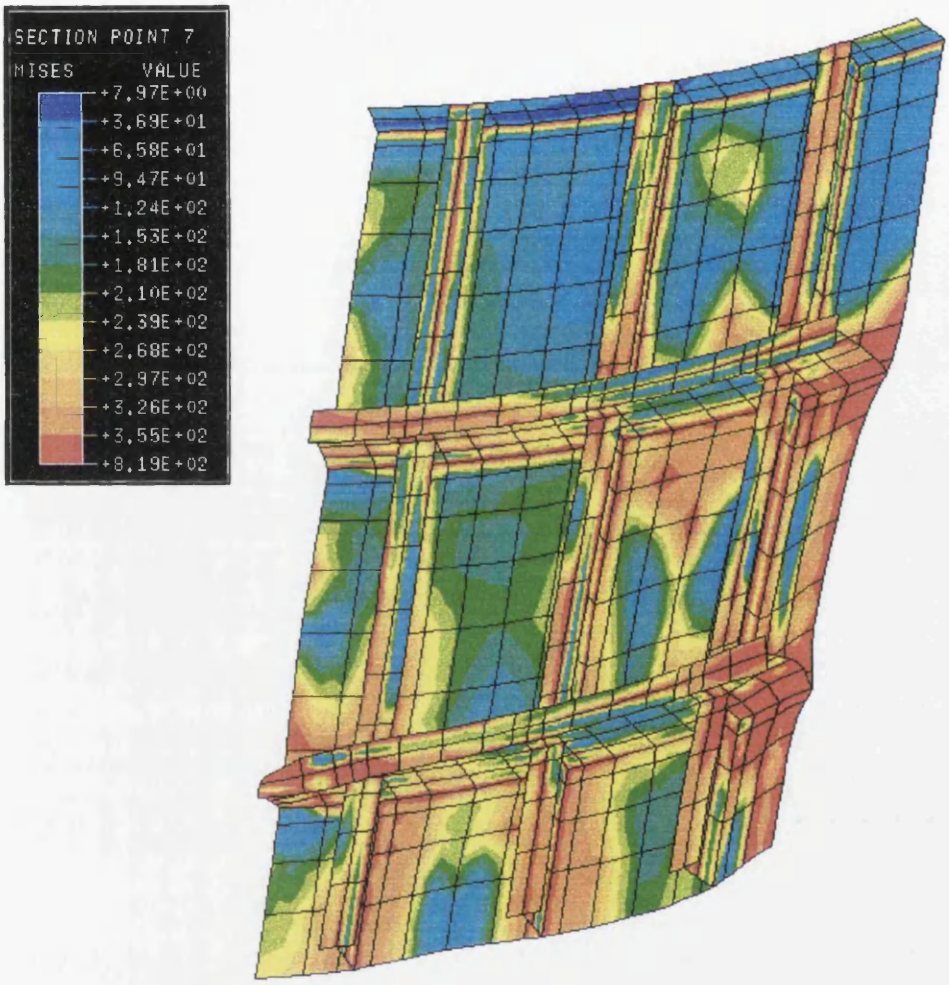


*Fig. A2.2.7.12, Model 2(ortho), Von Mises equivalent stress at mid thickness after cold forming, welding, axial loading and surface pressure buckling steps, at the large displacement buckling stage.*

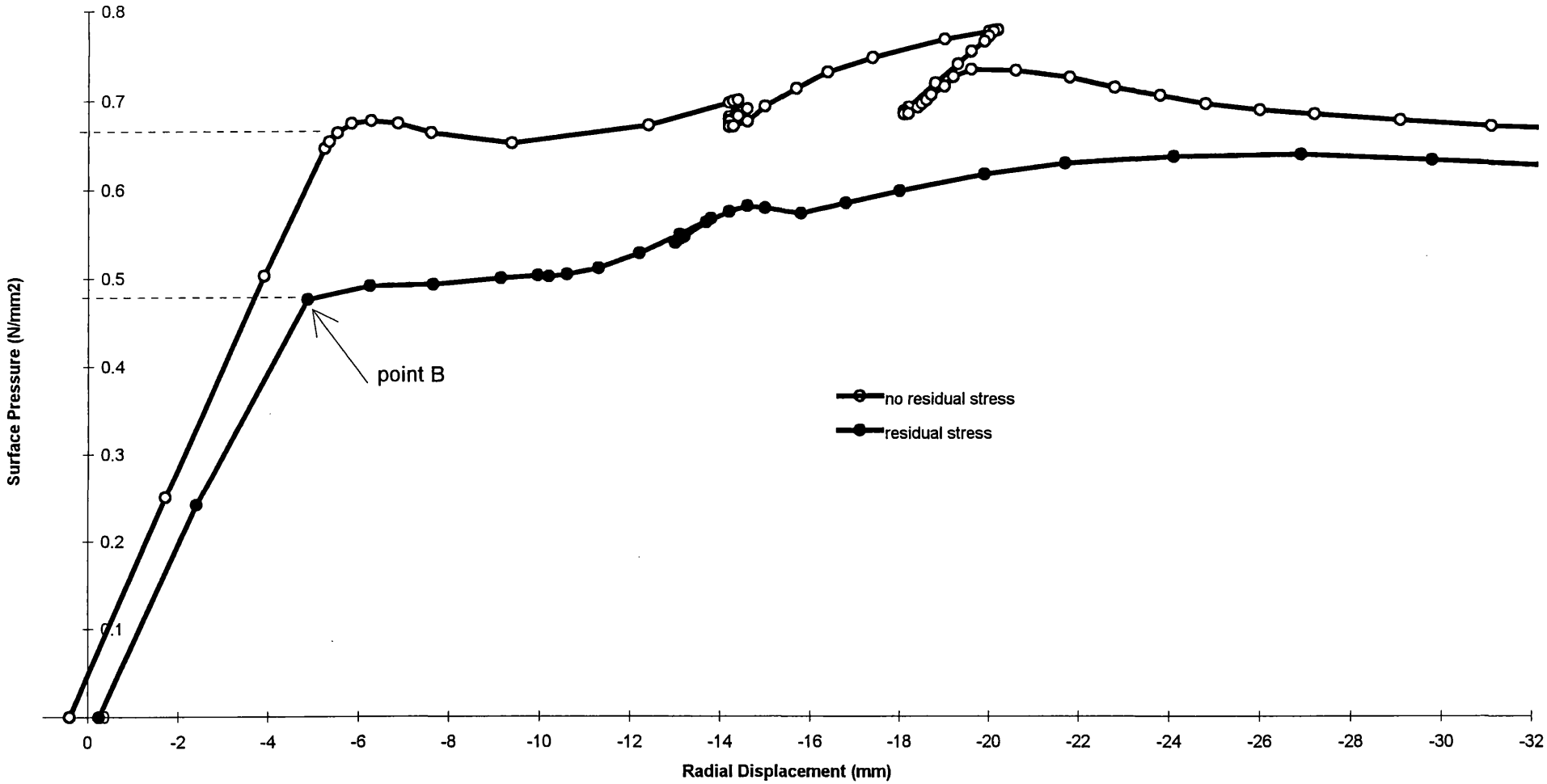


*Fig. A2.2.8.1, Model 2(ortho) load displacement path, welding and cold forming residual stresss.*

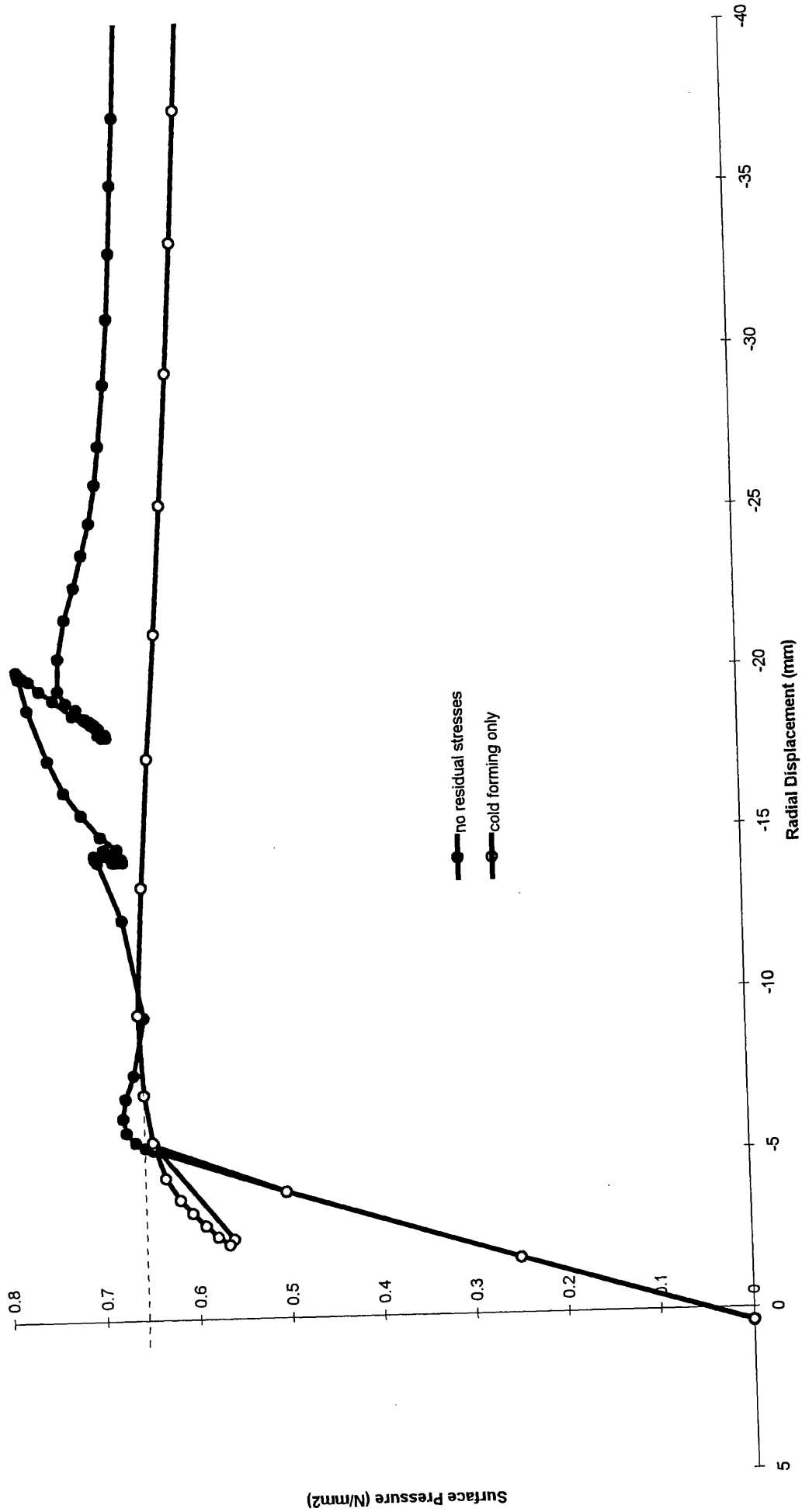


*Fig. A2.2.8.2, Model 2(ortho), cold forming residual stress.*

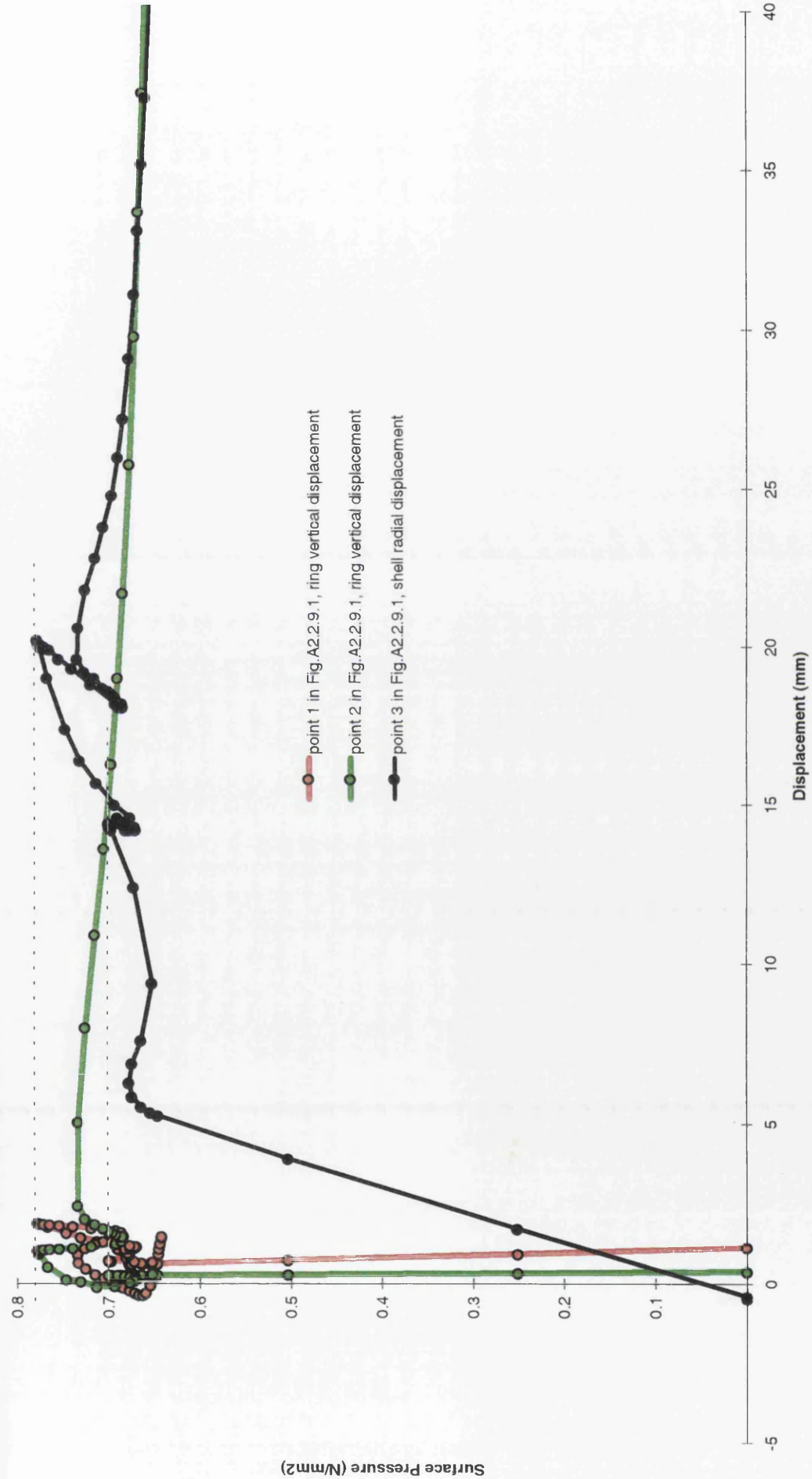


*Fig. A2.2.8.3, Model 2(ortho), shell radial displacement and ring axial displacement, no residual stress.*

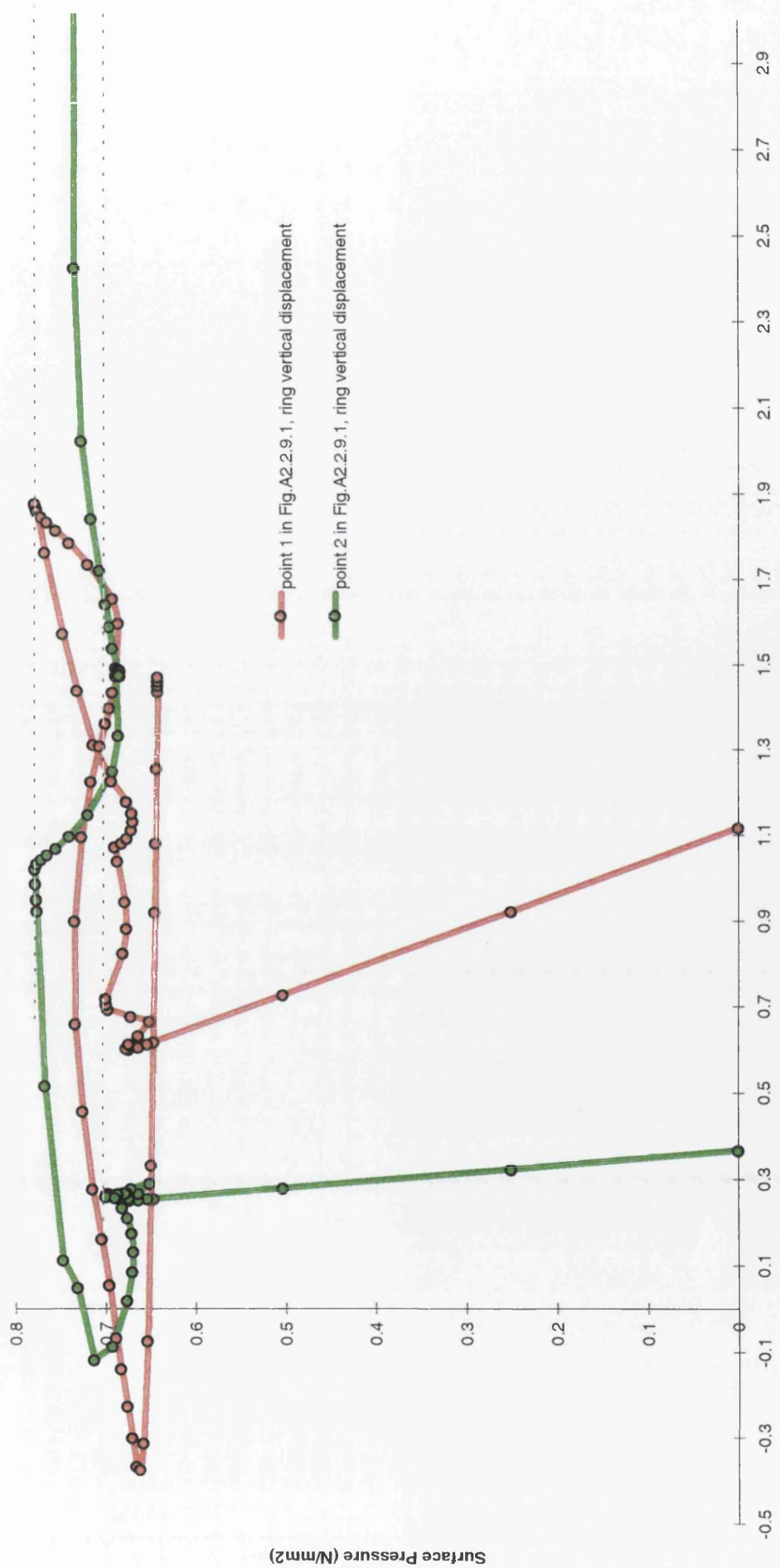


*Fig. A2.2.8.4, Model 2ortho, ring axial displacement, no residual stress.*

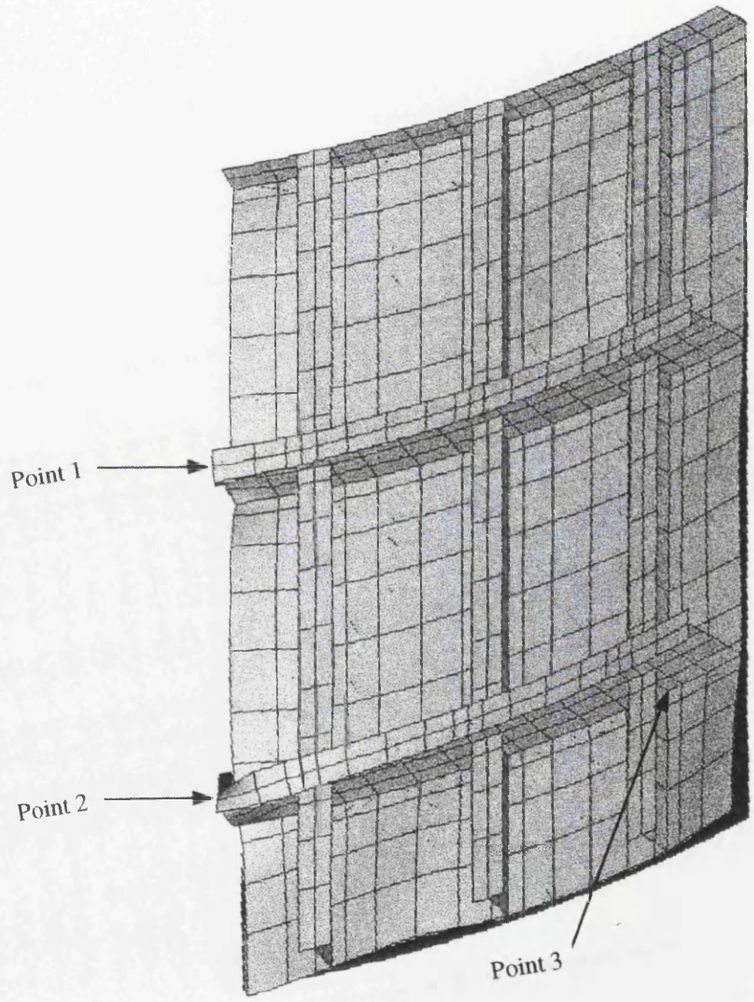


*Fig. A2.2.9.1, Model 2(ortho) without residual stress, displaced shape at the large displacement buckling stage.*

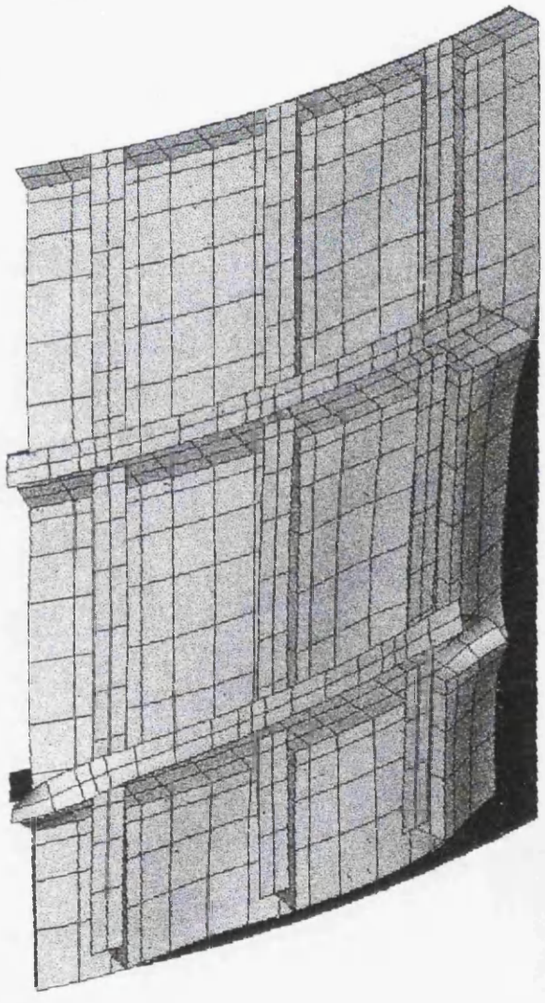

*Fig. A2.2.9.2. Model 2(ortho) with cold forming and welding residual stress, displaced shape at the large displacement buckling stage.*

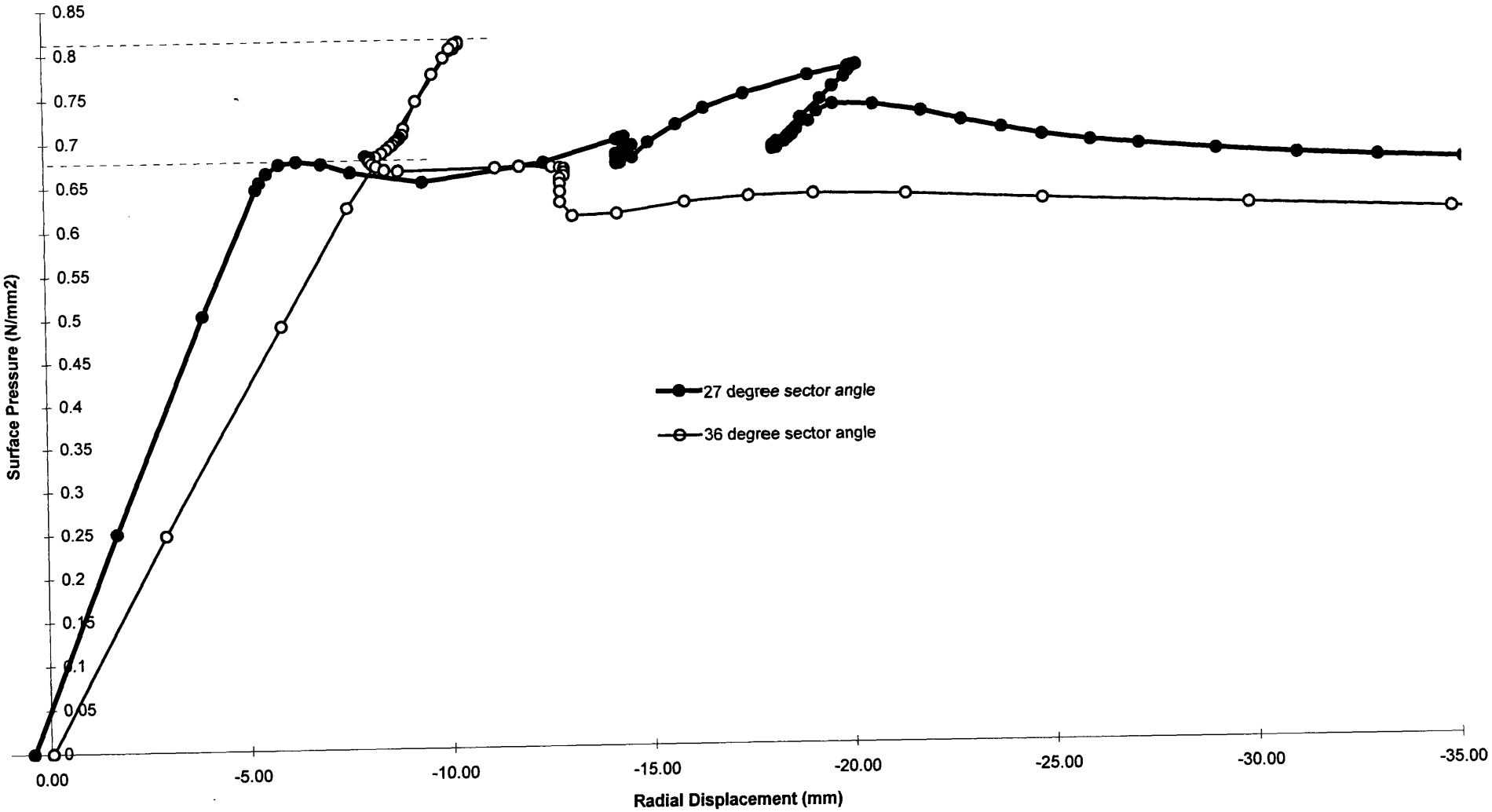


*Fig A2.3.1.1, Model 2(ortho), load displacement paths for 27 degree and 36 degree sector angle models without residual stress.*

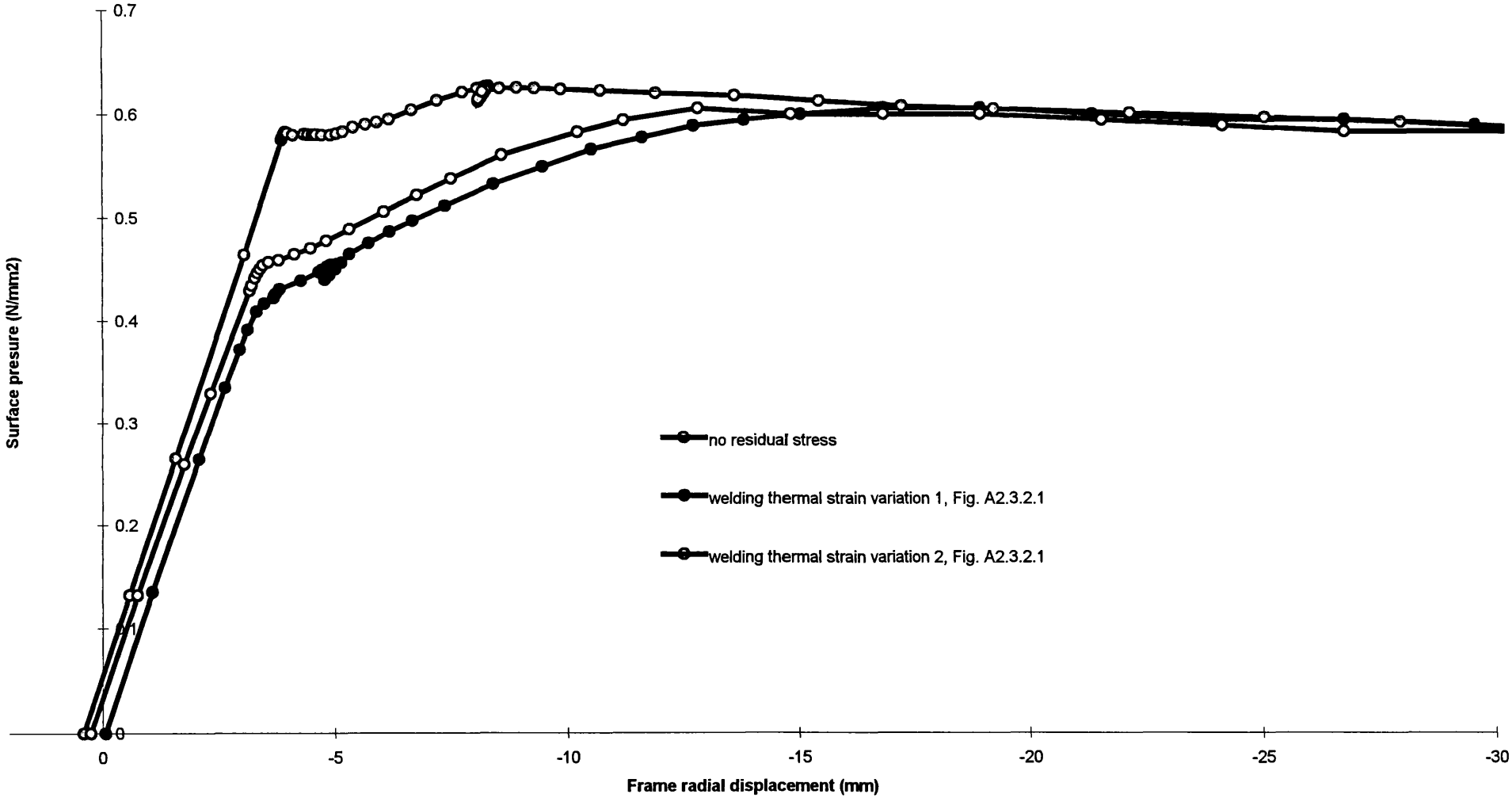


*Fig. A2.3.2.2, load displacement paths for the welding thermal strain variations in Fig. A2.3.2.1.*

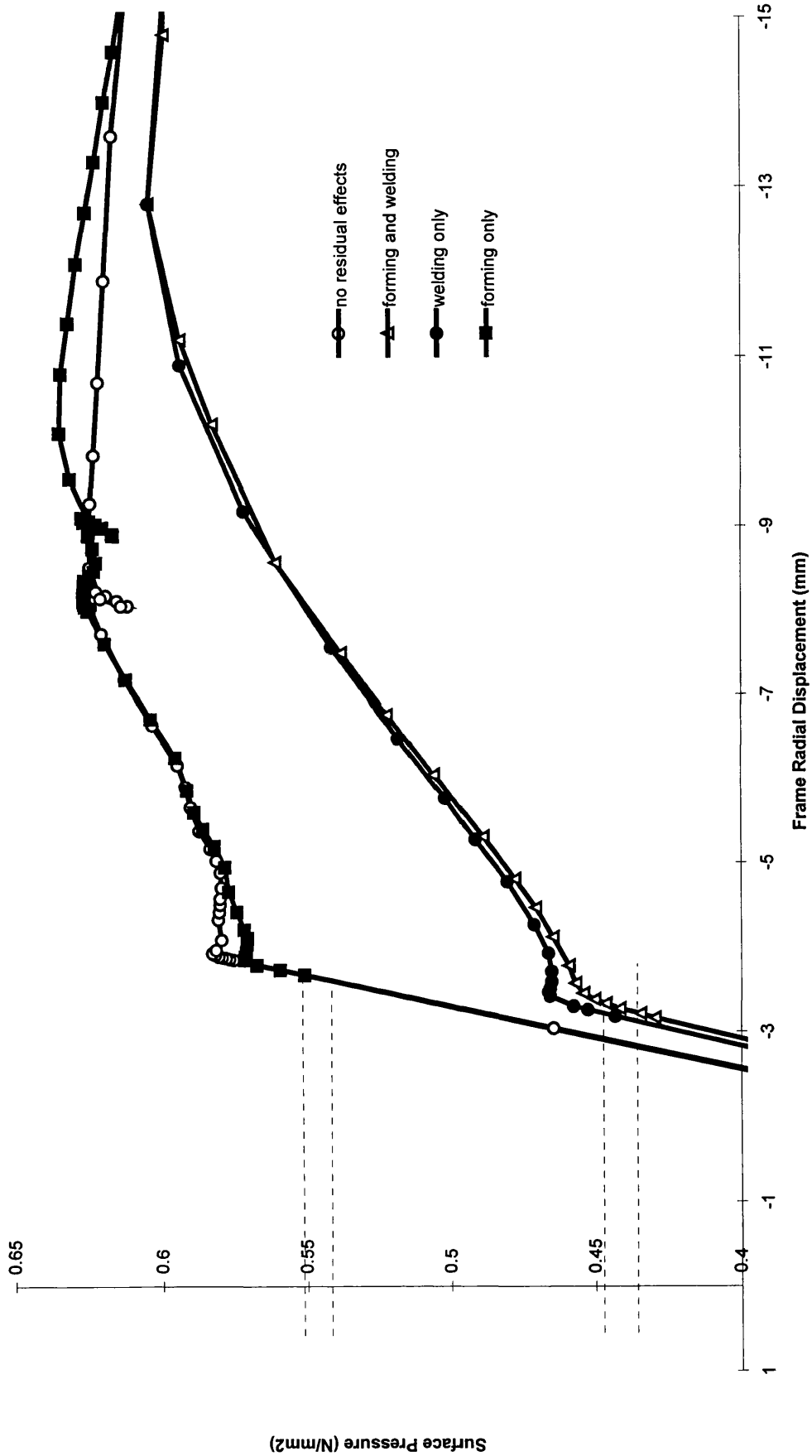


*Fig. A2.3.3.1, The effect of different combinations of residual stress types on load - displacement behaviour.*

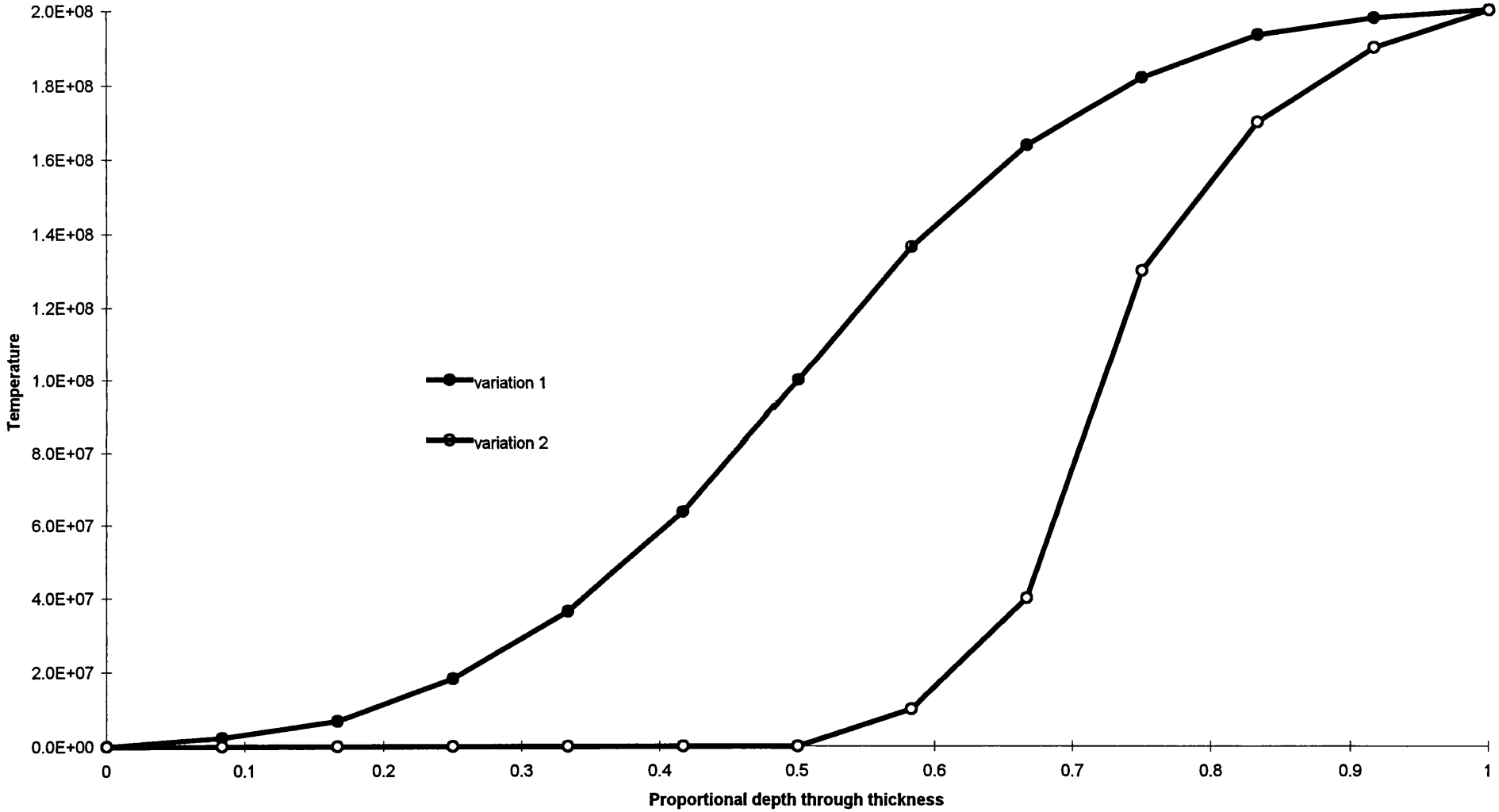


*Fig. A2.3.2.1, Different distributions of welding temperatures.*

# Appendix 3 : Torsional buckling plots.

# Appendix 3

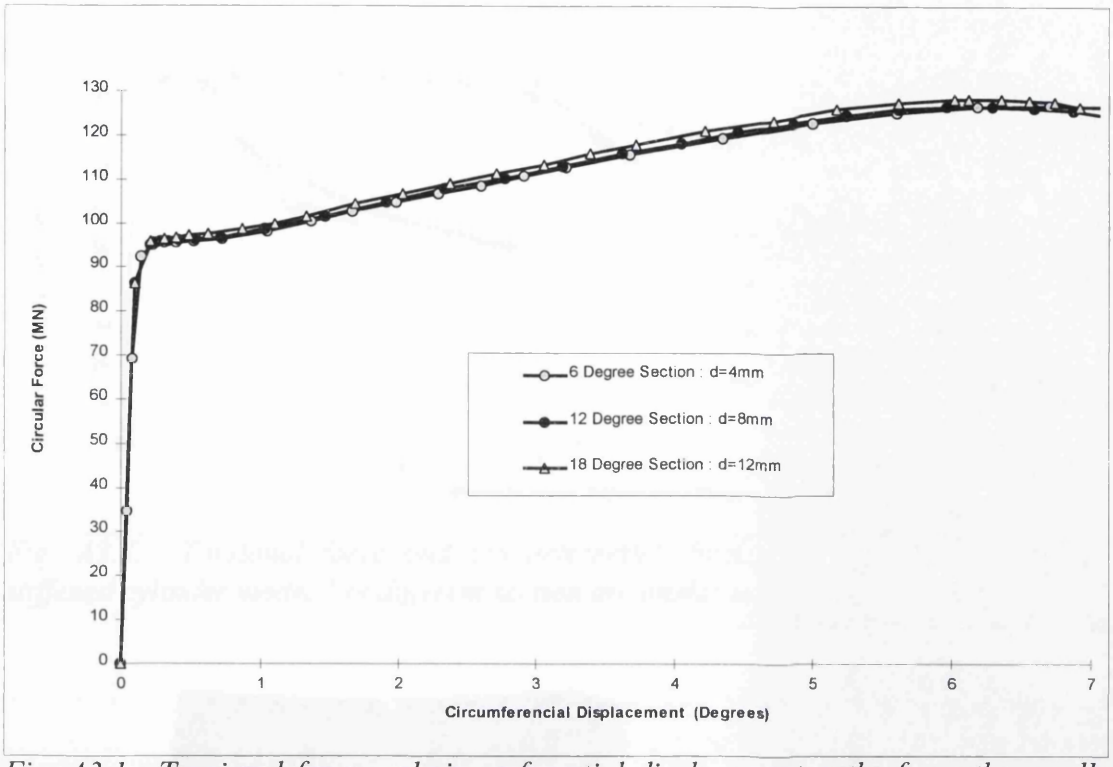


*Fig. A3.1. Torsional force and circumferential displacement paths for orthoganally stiffened cylinder model 1 of different section angles under torsional load.*

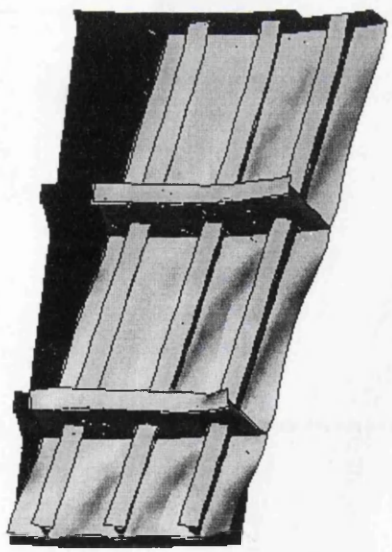

*Fig. A3.2. model 1, 18° section, buckled shape.*

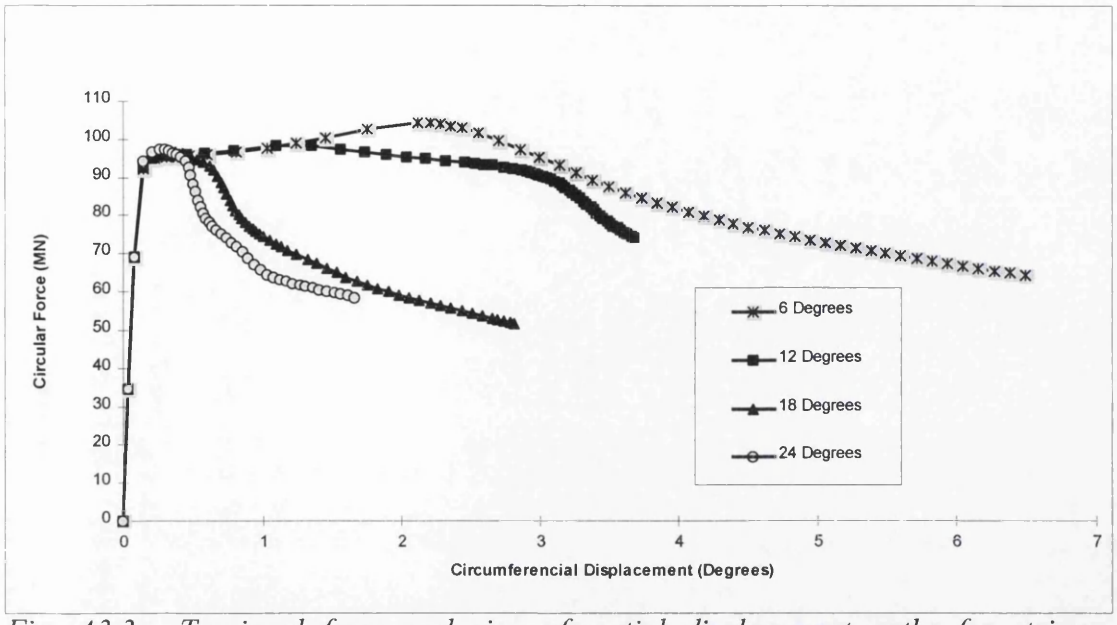


*Fig. A3.3. Torsional force and circumferential displacement paths for stringer stiffened cylinder model 2 of different section arc angles under torsional load.*

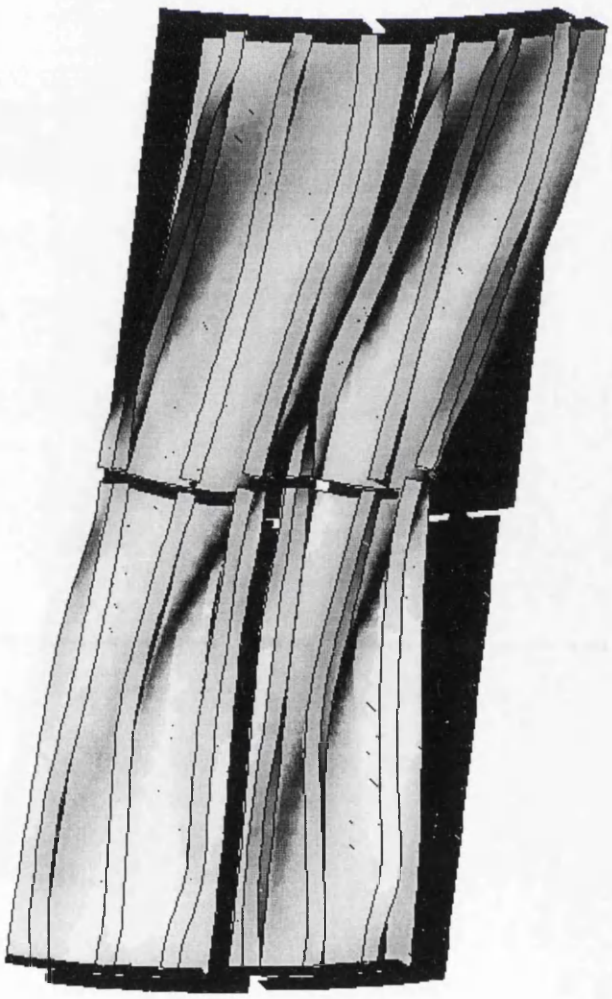

*Fig. A3.4. Model 2, 18° section, buckled shape, two circumferential waves, full axial length.*

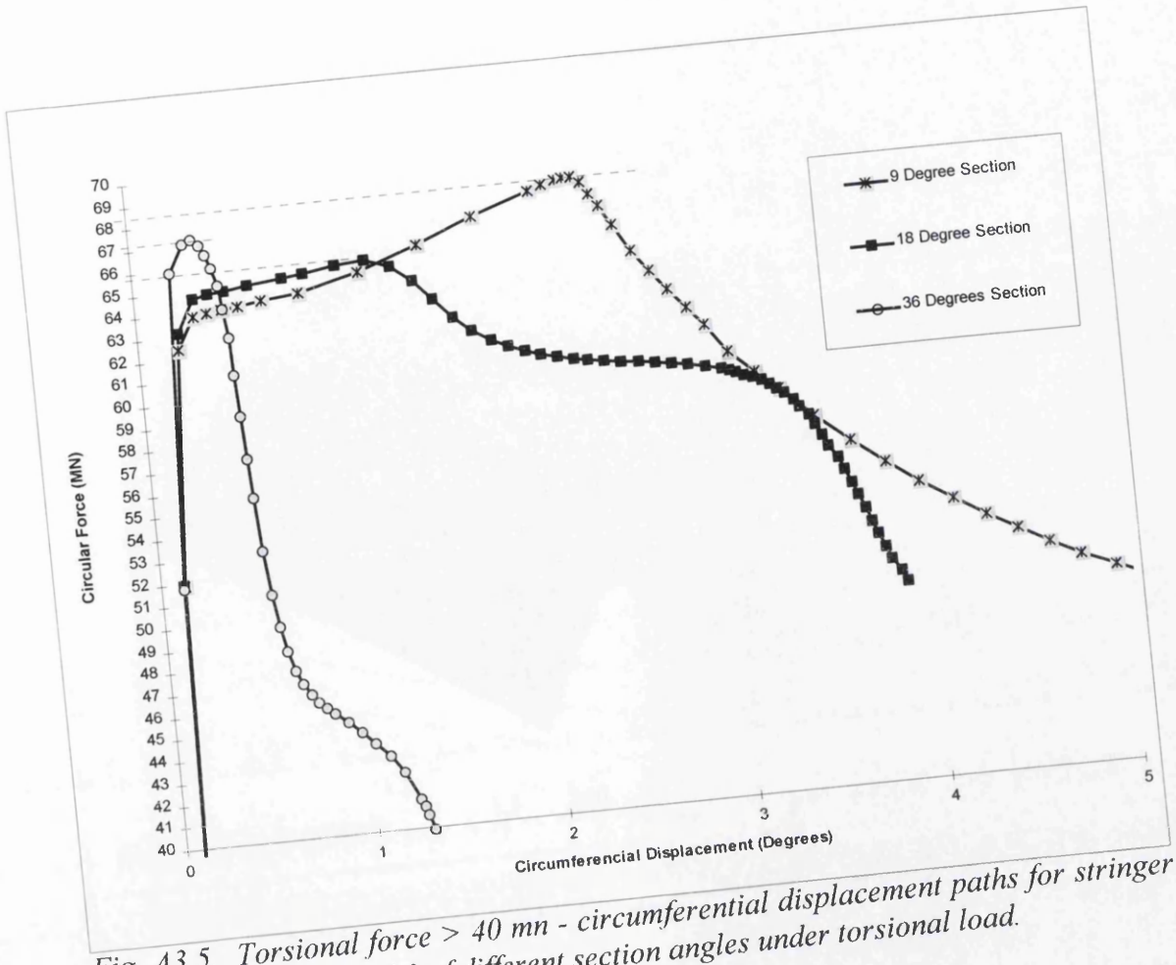


*Fig. A3.5. Torsional force > 40 mn - circumferential displacement paths for stringer stiffened cylinder model 3 of different section angles under torsional load.*

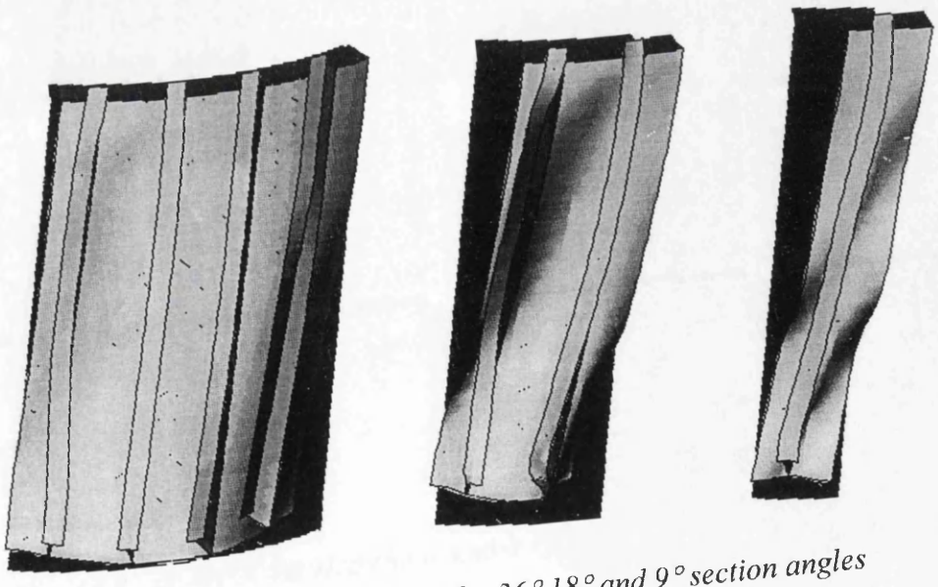

*Fig. A3.6. model 3, buckled shape for 36°, 18° and 9° section angles*

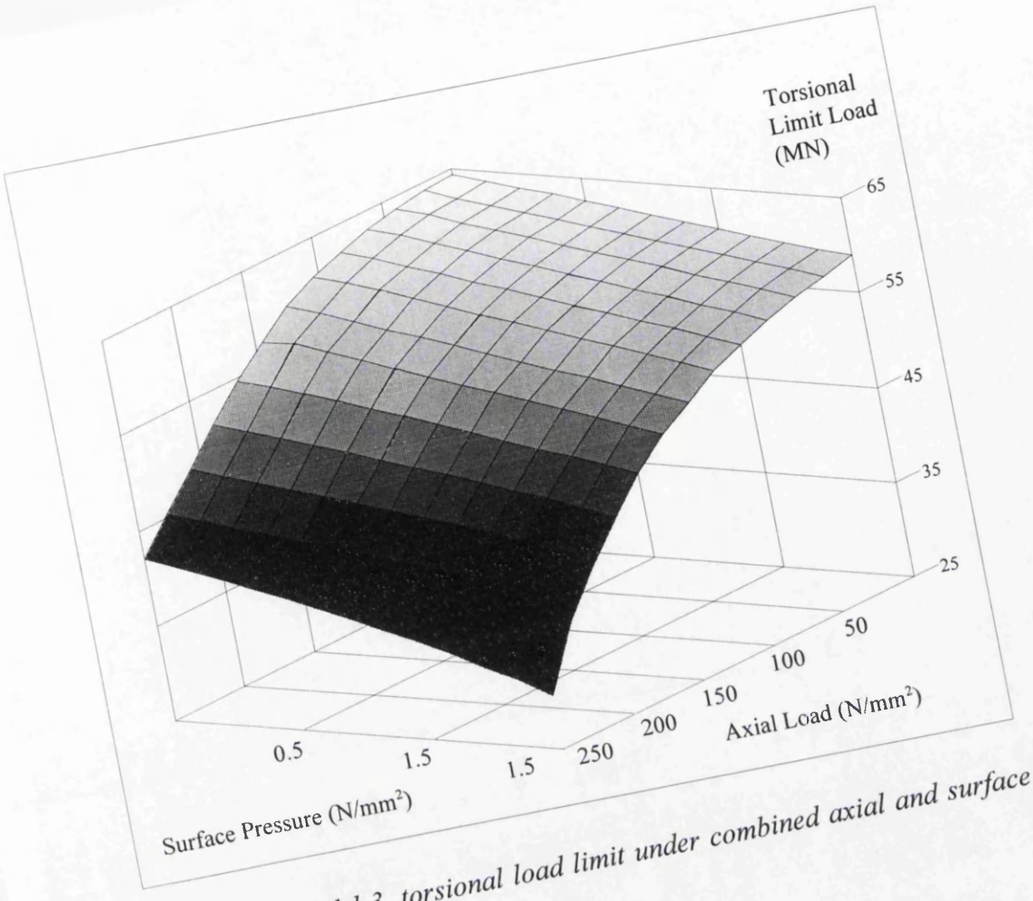


*Fig. A3.7. Model 3, torsional load limit under combined axial and surface pressure loading*

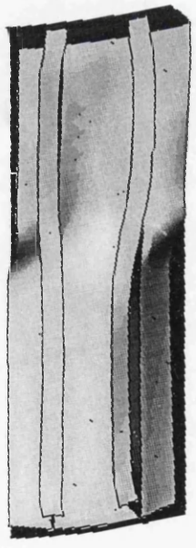

*Fig. A3.8. model 3, buckled shape under combined axial and torsional load*